Characterization of the Eastern Mediterranean surface dynamics : Insights from drifter assimilation and machine learning techniques

Georges Baaklini

SORBONNE UNIVERSITÉ
CRÉATEURS DE FUTURS DEPUIS 1257

CNRS
National Council for Scientific Research

Characterization of the Eastern Mediterranean surface dynamics: Insights from drifter assimilation and machine learning techniques

by

Georges BAAKLINI

A thesis submitted for the
degree of Doctor of Oceanography

in the
Faculté des Sciences et Ingénierie
ED129

June 2022

Jury members

Pascale	BOURUET-AUBERTOT	*President*
Anne	MOLCARD	*Reviewer*
Joaquim	BALLABRERA	*Reviewer*
Julien	BRAJARD	*Co-director*
Leila	ISSA	*Co-director*
Milad	FAKHRI	*Director*
Laurent	MORTIER	*Director*

Acknowledgements

I would like to express my sincere appreciation to my two supervisors: Laurent Mortier and Milad Fakhri, for their guidance and encouragement throughout the thesis work. Without their trust, this project could not have seen the light. Deep and sincere gratitude goes to my co-directors, Julien Brajard and Leila Issa, for their professionalism and your dedication, dynamism, vision, and motivational research.

I would also like to acknowledge the jury members: Anne Molcard, Joaquim Ballabrera and Pascale Bouruet-Aubertot, for evaluating our modest work. They raised many precious points that have led me to the completion of this thesis. This research was made possible by a grant from the National Council for Scientific Research of Lebanon (CNRS-L). This work was also partially funded by ALTILEV (in the framework of the PHC-CEDRE project).

The assimilation part would not have been possible without the collaboration with Milena Menna and Pierre-Marie Poulain from the National Institute of Oceanography and Applied Geophysics (OGS), who provided the necessary in-situ data.

I was fortunate to have the chance to work with Roy El Hourany, who taught me the machine learning method used in the thesis; I greatly benefited from his keen scientific insight. I am also grateful for the valuable conversations with Ananda Pascual, Alexandre Stegner, Dan Hayes, Jean-Luc Duvenon, Pierre Testor, Christophe Herbaut and Marie-Noelle Houssais. Their suggestions and constructive comments guided and helped us to improve the work.

I am indebted to Jean-Benoit Charrassin, Dany Thomas, Céline Le Helley, Nathalie Ortlieb, Bilal Amiri, Migueline Guillaume, and Eric Fourlon; for providing the administrative help throughout the thesis journey. I am also particularly grateful to Carlos Mejia, Julien Vincent, and Micheal Fields, who assured me of the necessary technical support during the Ph.D.

Special thanks go to all the members of the Laboratoire d'Océanographie et du Climat: Expérimentations et Approches Numériques (LOCEAN) and those of the Centre National des Sciences Marines (NCSM) for making my working days fun and enjoyable. Big thanks are due to Sara Sergi and Alberto Baudena for helping me, especially in my first steps at the start of the Ph.D.

Lastly, a warm expression of thanks is due to my parents, Sami and Rima, and all my family members for their unconditional love, encouragement, and prayers. Last but not least, I would like to thank my loving and patient Gina Fifani for her unconditional support during the Ph.D. journey.

To my grandmother, in loving memory.

Abstract

An accurate estimation of the surface circulation is crucial because of its direct impact on physical and bio-geochemical water properties. However, currents estimation remains challenging because the stream field is affected by quickly changing flows. This problem increases in the Eastern Mediterranean Sea, where in-situ observations are relatively scarce and the inaccuracies of altimetric observations increase. Therefore, some of the mesoscale features are still debated or unknown, especially in the Levantine Basin.

The thesis goal is to characterize these highly-evolving mesoscale features in the Mediterranean sea. In the first part of the thesis, we present a variational assimilation method that merges satellite altimetry with drifter observations to improve the surface circulation representation along and around the assimilated drifters' trajectories. We assess the method's efficiency by comparing the velocities resulting from assimilation with independent in-situ observations and ocean color images. We use the corrected velocities to characterize short-term and local events occurring in the Levantine Basin.

However, because of the significant spatio-temporal gaps in drifters' coverage, the assimilation does not allow a continuous investigation of all the mesoscale patterns and their long-term variabilities in the basin. In the second part of the thesis, we use machine learning techniques to build a catalog of the several circulation regimes in the Levantine Basin, providing a long-term characterization of these features. We also try to explain the possible reasons behind previous contradictory assessments about some features, such as the Mid-Mediterranean Jet.

The obtained results in the thesis improve the knowledge of the main mesoscale features' characteristics, behaviors, and tendencies. The thesis applications could take advantage of other in-situ observations and of future altimetric missions like SWOT, promising to mitigate some of the actual altimetric shortcomings.

Résumé

Une estimation précise de la circulation de surface est cruciale en raison de son impact direct sur les propriétés physiques et bio-géochimiques du du milieu marin. Cependant, l'estimation des courants reste un défi car le champ de circulation est affecté par des flux qui changent rapidement. Ce problème s'accentue en Méditerranée orientale, où les observations in-situ sont relativement rares et où les imprécisions des observations altimétriques augmentent. Par conséquent, certaines des caractéristiques de méso-échelle sont encore débattues ou inconnues, en particulier dans le bassin levantin.

L'objectif de la thèse est de caractériser ces strucutres méso-échelles hautement évolutives dans la mer Méditerranée. Dans la première partie de la thèse, nous présentons une méthode d'assimilation variationnelle qui fusionne l'altimétrie satellitaire avec les observations des bouées pour améliorer la représentation de la circulation de surface le long et autour des trajectoires des bouées assimilées. Nous évaluons l'efficacité de la méthode en comparant les vitesses résultant de l'assimilation avec des observations in-situ indépendantes et des images couleur de l'océan. Nous utilisons ensuite les vitesses corrigées pour caractériser les événements locaux et à court terme qui se produisent dans le bassin du Levant.

Cependant, en raison des lacunes spatio-temporelles importantes dans la couverture des bouées, l'assimilation ne permet pas une investigation continue de toutes les structures mésoéchelles et de leurs variabilitées à long terme dans le bassin. Dans la deuxième partie de la thèse, nous présentons des techniques de "machine learning" qui seront utilisées pour construire un catalogue des différents régimes de circulation dans le bassin levantin, permettant ainsi la caractérisation à long terme de ces structures. Nous essayons également d'expliquer les raisons possibles derrière les évaluations contradictoires précédentes de certaines structures, comme par exemple, le "Mid-Mediterranean Jet".

Les résultats obtenus dans cette thèse améliorent la connaissance des caractéristiques, des comportements et des tendances des principales structures méso-échelle. Les applications de la thèse pourraient tirer profit d'autres observations in-situ et de futures missions altimétriques comme SWOT, promettant ainsi de pallier certaines des lacunes actuelles de l'altimétrie.

Contents

List of Figures

List of Tables

Abbreviations

ADT	**A**bsolute **D**ynamic **T**opography
AMC	**A**sia **M**inor **C**urrent
AW	**A**tlantic **W**ater
CE	**C**yprus **E**ddie
CHL	**C**hlorophyll
CMEMS	**C**opernicus **M**arine **E**nvironment **M**onitoring **S**ervice
CINEL	**C**irculation and water mass properties in the **N**orth **E**astern **L**evantine
CTD	**C**onductivity **T**emperature **D**epth
DUACS	**D**ata **U**nification and **A**ltimeter **C**ombination **S**ystem
EGYPT	**E**ddies and **G**yres **P**ath **T**racking
EKE	**E**ddy **K**inetic **E**nergy
EM	**E**astern **M**editerranean
EMDW	**E**astern **M**editerranean **D**eep **W**ater
HAC	**H**ierarchical **A**scendant **C**lassification
IE	**I**erapetra **E**ddie
KaRIn	**Ka**-band **R**adar **In**terferometer
LE	**L**attakia **E**ddie
LEE	**L**ibyo **E**gyptian **E**ddies
LIW	**L**evantine **I**ntermediate **W**ater
MDT	**M**ean **D**ynamic **T**opography
MFS	**M**editerranean **F**orecaste **S**ystem
MKE	**M**ean **K**inetic **E**nergy
MME	**M**ersa **M**atruh **E**ddies
MMJ	**M**id **M**editerranean **J**et
MMS	**M**ean **S**ea **S**urface

SAR	**S**ynthetic **A**perture **R**adar
Shke	**S**hikmona eddie
SLA	**S**ea **L**evel **A**nomaly
SOM	**S**elf **O**rganizing **M**ap
SST	**S**ea **S**urface **T**emperature
SSH	**S**ea **S**urface **H**eight
SWOT	**S**urface **W**ater **O**cean **T**opography

Chapter 1

Introduction

1.1 Importance of surface ocean circulation

Surface currents have a continuous and direct impact on the distribution of physical and biogeochemical water properties. For example, the surface circulation can transport terrigenous material or chemicals from the industry originating from rivers and nutrient-rich coastal waters into the more oligotrophic open sea (Escudier et al., 2016; Lehahn et al., 2007; Levy and Martin, 2013; Taupier-Letage et al., 2003). This surface circulation is perturbed by loop-like patterns with nearly closed streamlines that are the so-called oceanic eddies. Eddies whose horizontal scales exceed the local deformation radius belong to the mesoscale. Inside such eddies, physical and biogeochemical properties like temperature, salinity, and carbon, can differ from those in the surrounding waters. The water inside the eddy can be, therefore, transported by the eddy drift without significant mixing over large distances (Bonaduce et al., 2021; Chelton et al., 2011, 2007; Zhao et al., 2018). Moreover, mesoscale dynamics are associated with vertical exchanges that are important for the transport of heat from the atmosphere to the deep ocean and for the primary production (Escudier et al., 2013; Griffies et al., 2015; Pascual et al., 2004).

Understanding and monitoring mesoscale surface circulation is thus crucial and faces significant challenges. Contrary to large scales that are today accurately monitored using satellites altimetry with nadir-pointing radar instruments, the study of the mesoscale is still not adequately resolved by altimetry which could lack accuracy in small-scale areas and near the coasts. The Mediterranean Sea is one example where the mesoscale dynamics and the shape of the surface circulation are poorly resolved by present satellite altimetry.

1.2 The Mediterranean Sea

The Mediterranean sea, or *Mare medi terraneum* in Latin, is a quasi-enclosed basin surrounded by the Middle East and Asia Minor in the east, north Africa in the South, and the European continent in the North. The sea is divided into two parts, the Eastern and Western Mediterranean, connected by the Sicily channel. It is a strait of around 150 km width and 600 m depth that plays a crucial role in connecting and regulating the exchanges between the Western and Eastern Mediterranean Basins (Menna et al., 2019). It is characterized by an anti-estuarine circulation, with a surface inflow and

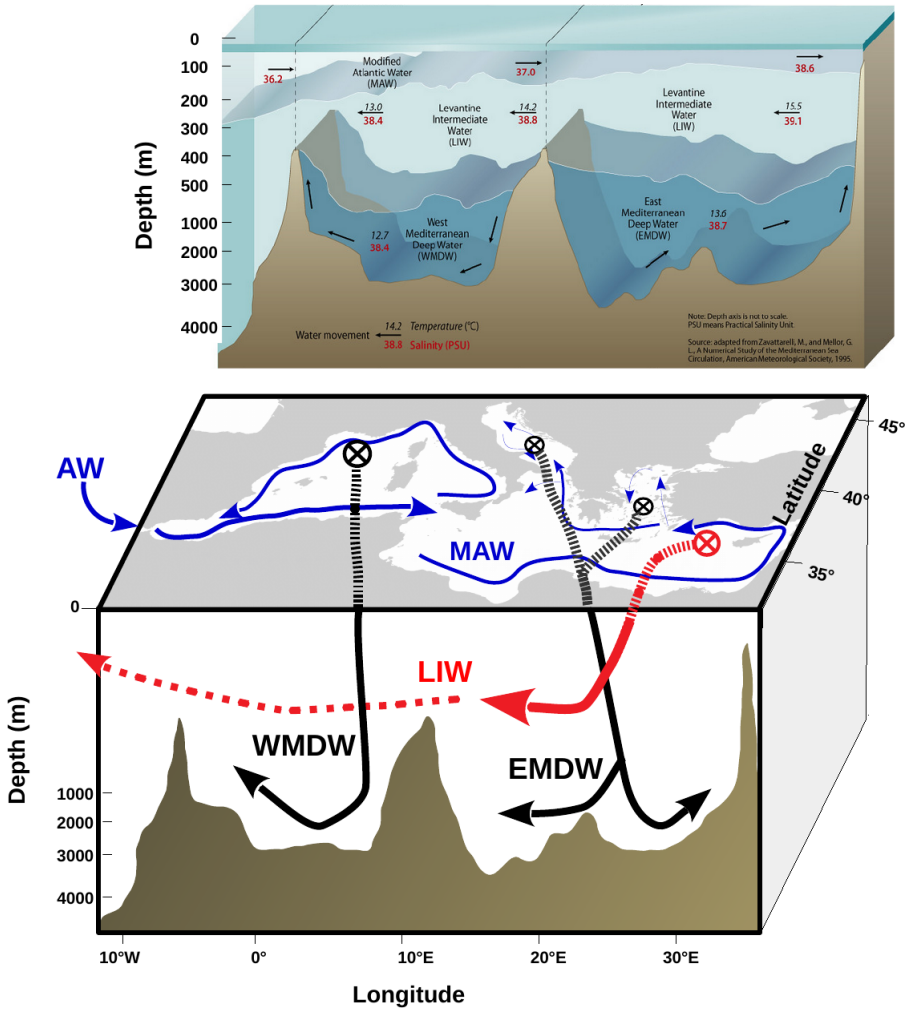

FIGURE 1.1: The upper panel shows the vertical distribution of the different water masses and their average temperature and salinity in the Mediterranean sea. The lower panel presents a schematic representation of the Mediterranean overturning circulation. When flowing in the upper layer of the Mediterranean, the Atlantic Water (AW) changes its physical properties. It's therefore called the Modified Atlantic Water (MAW), circulating throughout the Mediterranean and forming a gyre in each of the Eastern and the Western Mediterranean. In the Eastern Mediterranean, the Levantine Intermediate Water (LIW) is formed by convection events occurring in the Rhodes gyres, while convections in the Agean and Adriatic seas form the Eastern Mediterranean Deep Water (EMDW). In the Western Mediterranean, the deep water (WMDW) is formed by convection processes occurring in the Gulf of Lion.

deep outflow system at the Gibraltar Strait (Bergamasco and Malanotte-Rizzoli, 2010). This circulation is driven by the evaporation rate that exceeds the precipitation (Tanhua et al., 2013), and it is thus directly affected by global warming. Although representing only 0.82 % of the world ocean, it harbors between 4 % to 18 % of marine species. It is considered a "biodiversity and climate warming hot-spot" (Bianchi and Morri, 2000), which is highly exposed to many threats in particular because of the highly populated coasts. Indeed, besides the warming affecting its hydrographic properties (temperature

and salinity), the Mediterranean is also subjected to human-induced marine pollution, transported and mixed by the currents over large distances. Hydrographic measurements showed three main water masses permanently present in the whole Mediterranean (see fig. 1.1). The first layer is the Modified Atlantic Water (MAW), formed by the Atlantic Water entering the basin and occupies the subsurface between 30 and 200 m in-depth, with a salinity of 38.6 PSU. In the Western Mediterranean, the deep water is known as the Western Mediterranean Deep Water (WMDW), characterized by a temperature of 12,7 °C and salinity of 38.4 PSU. It is mainly formed in the Gulf of Lions and particularly triggered by the atmosphere with strong local winds (Rixen et al., 2005). In the Eastern Mediterranean, the deepest water mass below 800 m is the so-called Eastern Mediterranean Deep Water (EMDW). It is relatively cold (13.6 °C), and its salinity is around 38.7 PSU. EMDW is mainly formed by the strong cooling in the Adriatic and the Aegean Seas. The water masses separating AW and the two deep water masses are the Levantine Intermediate Water (LIW). The latter is present in the two Basins and represents $\sim$ 26 % of the total water. It has the highest salinity (38.8-39.0 PSU) and is formed by the intense evaporation that increases the salinity of the MAW in summer in the Levantine Basin. LIW constitutes an important fraction of the Mediterranean outflow into the Atlantic Ocean at the Gibraltar Strait (Alhammoud et al., 2005; Lascaratos et al., 1999; Ovchinnikov, 1984).

1.3 Mediterranean surface circulation and main mesoscale eddies in the Levantine

More particularly, the negative water balance, with evaporation exceeding precipitations, induces a continuous inflow of the Atlantic Water (AW) through the Gibraltar Strait to compensate for the water loss. While flowing through the Gibraltar Strait eastward in the Western Basin and the Eastern Basin after crossing the Sicily Channel, this inflow of AW becomes saltier and denser. Because of the Coriolis effect, the AW circulates anticlockwise along the continental slope, forming a large basin-scale cyclonic gyre, subdivided into two sub-gyres in the Western and the Eastern Basin interconnected by the Sicily Channel. The AW inflow in the Western Basin along the North African coast forms the Algerian current, which bifurcates into two branches while reaching the Tunisian coasts. One branch enters the Tyrrhenian Sea and progresses along the

coasts forming the Westen gyre. The other branch progresses into the Sicily channel (Jouini et al., 2016), and flows into the Eastern Basin along the Libyo-Egyptian coast and further on, forming the Eastern Gyre.

The southern part of the two gyres is perturbed by eddies, such as in the Algerian Basin, where instabilities of the coastal Algerian Current over the steep bathymetry generate such eddies with increasing kinetic energy (Sutyrin et al., 2009; Testor et al., 2005). The formed eddies can reach a diameter of 50-100 km and extend to thousands of meters down to the bottom (Taupier-Letage et al., 2003). They can perturb the along-slope flow by blocking and spreading the coastal AW further offshore.

In the eastern part, the coastal AW current continues its anticlockwise flow, and similarly the West, it is unstable. Indeed, the AW interacts with several semi-permanent mesoscale features characterized by their high eddy kinetic energy (more than 700 cm^2/s^2)(Gerin et al., 2009; Poulain et al., 2013; Pujol and Larnicol, 2005). These features have been described as separate building blocks: the anticyclonic Ierapetra eddy (southeast of Crete), Mersa-Matruh eddies off the Egyptian coasts, the Shikmona eddies, and Cyprus eddy, and the cyclonic Rhodes gyre (Matteoda and Glenn, 1996; Rio et al., 2007) (see fig. 1.2). Unlike the Western Basin, which does not exhibit such semi-permanent structures, these features have a prominent role in shaping the surface circulation in the Eastern Basin. However, these authors were aiming to characterize these features as *independant* separate blocks and put little focus on their variability and interactions, including with the AW inflow, which may have led to some controversies about the general circulation and, in particular, the so-called Mid-Mediterranean Jet (MMJ).

1.3.1 Ierapetra eddy (IE)

The Ierapetra eddy (IE), located in the southeast corner of Crete, is one of the largest and longest-lived mesoscale eddies of the Eastern Mediterranean Sea. IE is mainly generated by the Etesian wind stress curl (Larnicol et al., 2002). It is formed and intensified in late summer till early autumn and can persist for several months or last the whole year before merging with the new anticyclone formed in the following summer. Consequently, this merging may increase the IE lifetime, which can exceed two years (such as the IE formed in 2005). We note that during 20 years of monitoring, IE formation was not observed in three years only (Ioannou et al., 2017; Mkhinini et al., 2014). IE can either remain

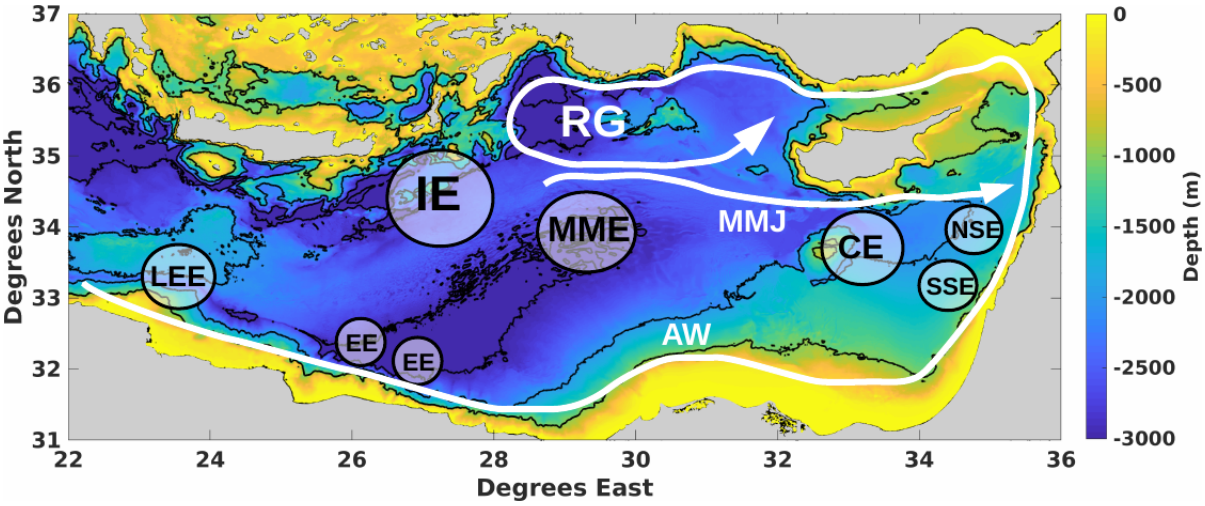

FIGURE 1.2: A schematic representation of the main structures present in the Levantine Basin (AW: Atlantic Water, RG: Rhodes gyre, IE: Ierapetra eddy, EE: Egyptian eddies, LEE: Libyo-Egyptian eddies, MME: Mersa-Matruh eddies (also known as Herodotus trough eddies), MMJ: Mid-Mediterranean Jet, CE: Cyprus eddy, NSE: North Shikmona eddies, SSE: South Shikmona eddies). All is overlayed on a bathymetry map.

stationary or drift towards the Libyan slope (Hamad et al., 2005). Due to its robust and coherent structure and the significant temperature and sea surface height signals, IE can be identified using different observational tools, including satellite altimetry, in-situ measurements, and sea surface temperature images. It can also be rather well reproduced by high-resolution models (Alhammoud et al., 2005).

1.3.2 Mersa-Matruh eddies (MME)

Mersa-Matruh eddies (MME), also known as Herodotus Trough Eddies (HTE), are formed offshore the Libyan and Egyptian coasts. The coastal current in this area is unstable, generating Mersa-Matruh large eddies that perturb the along-slope circulation and sometimes feed the IE (Hamad et al., 2005). These eddies are mainly formed in spring and summer and can reach large diameters (up to $\sim$ 100-250 km). MME drifts seawards while the 3000 m Herodotus plain traps and prevents the coastal vertically-extended eddies from propagating further to the east, thus causing an accumulation of these eddies in this area (Alhammoud et al., 2005; Elsharkawy et al., 2017). We note that MME and IE are the most dominant semi-permanent mesoscale features in the Eastern Mediterranean (Menna et al., 2012).

1.3.3 Shikmona eddies (Shke)

Shikmona eddies (Shke) represents a complex system composed of several cyclonic and anticyclonic eddies with varying size, position, and intensity (Gertman et al., 2007; Mauri et al., 2019; Menna et al., 2012). Similar to MME, Shke is not an area of eddy formation but an area where previously formed eddies tend to accumulate and/or merge (Hamad et al., 2005). The near-shore instabilities can spread the MAW seaward to feed the Shke or generate small eddies that can detach from the coast and propagate westward toward the center of the Levantine Basin (Alhammoud et al., 2005; Millot and Taupier-Letage, 2005). The continuous appearance and disappearance of such small eddies can largely influence the dominance of Shke. However, monitoring these eddies remains challenging because of their fast-evolving nature and the warm surface layer that can cover their thermal signature.

1.3.4 Cyprus eddy (CE)

The Cyprus eddy (CE) is another remarkable feature governing the circulation in the Eastern Levantine Basin. Its influence extends to about 400 m of depth. CE is one of the most intense dynamic features of the open sea. Unlike the MME and Shke, it is not an area of eddies accumulation (Zodiatis et al., 2005). CE could extend eastward, engendering a large anticyclonic structure with $\sim$ 100 km of diameter (Menna et al., 2012). CE formation could be related to the interaction between the surface currents and the topography in the region of the Eratosthenes seamount (Gerin et al., 2009).

We should note that other mesoscale structures exist in the Eastern Levantine but are less frequently observed. Among these, we mention the Lattakia Eddy (LE) taking place between Cyprus and Syria. LE is a cyclonic eddy generated by the interaction of the northward coastal current along the Lebanese and Syrian coasts with a mid-Mediterranean jet (Zodiatis et al., 2003), and/or between Shke and the coastline (Hamad et al., 2005), and/or by the topography (Gerin et al., 2009).

1.3.5 Mid-Mediterranean jet (MMJ)

The Mid-Mediterranean jet (MMJ) is a cross-basin flow of the MAW in the Eastern Basin (see fig. 1.2). Its existence is somewhat controversial. Some authors consider the MMJ

as an artifact caused by the deviation of the coastal MAW, driven from one offshore eddy to another. In other terms, it is the result of the "paddle-wheel" effect due to the high mesoscale activity across the Eastern Levantine (Millot and Gerin, 2010). As a matter of fact, no remarkable jet is present in the Mediterranean Forecast System (MFS) simulations (Manzella et al., 2001) or in XBT campaigns (Horton et al., 1994; Zervakis et al., 2003) or by the sizeable drifter data set released during the EGYPT/EGITTO program between September 2005 and July 2007 (Millot and Gerin, 2010), or even when using high-resolution numerical models (Alhammoud et al., 2005).

Nevertheless, other observations have been interpreted as a flow in the middle of the basin with an average speed ranging between 10-19 cm/s (Amitai et al., 2010; Poulain et al., 2012). More recently, SST anomaly images, drifter tracks, and the geostrophic currents computed from the ADT fields showed an occasional MMJ flowing toward the north of the Lebanese coasts between 2016 and 2017 (Mauri et al., 2019). The investigation of SST and altimetry images between 2000 and 2015 considered that the MMJ is triggered by the surface cold water pushed by northerly winds, reaching the northern periphery of the Lybio-Egyptian coasts and the high vorticity off the LEE that pushes the MMJ toward the middle of the Eastern Basin (Ciappa, 2021).

Current estimations remain challenging because the velocity field is affected by rapid changes and small-scale flows. Moreover, the above-listed eddies are energetic structures that can interact, split or merge and induce smaller-scale structures (shear-eddies and filaments) (d'Ovidio et al., 2004; Laxenaire et al., 2018; Le Vu et al., 2018; Taupier-Letage et al., 2003), which makes the estimation of a well-defined current crossing the basin rather challenging. Historically, Nielsen (1912) was a pioneer in describing the surface circulation in the Mediterranean as a simple basin-wide cyclonic gyre in which the strongest current is close to the coast. And despite the massive increase of observations with modern observational tools that has allowed improving the description of the surface circulation and the understanding of the mechanisms generating the mesoscale features, Nielsen's schemata should still be considered inspirational.

1.4 Tools used for observing the surface circulation

1.4.1 In-situ observations

1.4.1.1 Moorings

Moorings are a collection of devices attached to a wire, anchored on the seafloor with an acoustic release allowing an Eulerian way of measuring physical, chemical properties and ocean currents. Glass balls and syntactic foam floats are used to hold the mooring line stretched. They are equipped with attached instrumentation that often includes CTD (conductivity, temperature, depth sensors), optical sensors to measure various parameters such as Oxygen or fluorescence, and current meters. Usually, moorings are not reaching the surface, which forbids real-time data transmission, and data are recovered only when the mooring itself is recovered.

1.4.1.2 Drifters

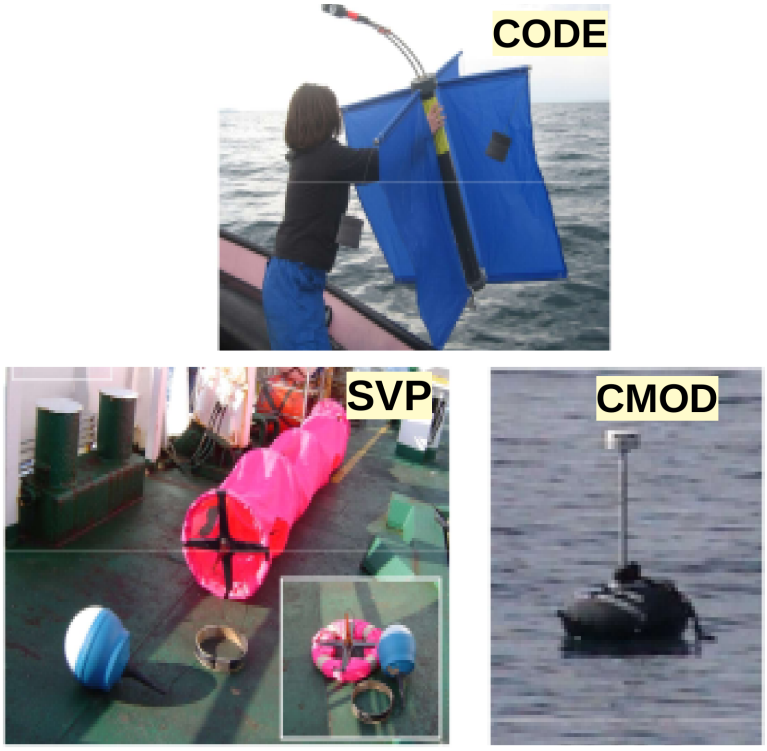

FIGURE 1.3: Different types of drifters that were deployed in the Eastern Mediterranean (CODE, SVP and CMOD) (Menna et al., 2017)

Surface drifters are simple in-situ autonomous platforms. They are sometimes called Lagrangian drifters since the location of the measurements they make moves with the flow. They are used to investigate surface ocean currents and other parameters like temperature or salinity. Once they are released, they follow almost langrangianly the surface ocean layer velocity current thanks to a so-called 'drogue'. Due to their positive buoyancy, these Lagrangian tools restrain them along with the two-dimensional flow at the surface or near-surface of the ocean (Poulain et al., 2012). Drifters have the advantage of providing an accurate description of the current circulation. In the Mediterranean sea, there were many types of deployed drifters (see fig. 1.3):

CODE drifter: It consists of a vertical, 1-m-long tube with four drag-producing vanes extending radially from the tube over its entire length and four small spherical surface floats attached to the upper extremities of the vanes to provide buoyancy. A small antenna for satellite tracking and data transmission is attached to the top of the tube and extends about 37 cm above sea level (Poulain, 1999).

Surface Velocity Program (SVP) Drifter: The hull has a diameter of 35 cm and is attached to a drogue consisting of a cylindrical tube connected to the surface buoy. It measures ocean currents at 15 m depth.

The CMOD drifter: The Compact Meteorological and Oceanographic Drifter (CMOD) is a 60-cm-long cylindrical hull with a floatation collar.

The drifter type used in the thesis is Surface Velocity Program (SVP) drifters, which are the standard design of the Global Drifter Program (Lumpkin and Pazos, 2007). Although being accurate, all the drifters are affected in one way or another by the wind. The wind impact on the drifter is mainly due to the emergence of the antenna that transfers data above sea level. The SVP design minimizes the wind impact on the drifter because the surface buoy is tethered to the drogue at 15 m depth, reducing thus the wind drag on the buoy itself (Poulain et al., 2012).

1.4.1.3 Argo-floats

Firstly introduced in 1999, the Argo-floats are autonomous drifting profilers capable of rising and descending in the ocean according to a pre-programmed schedule. By changing its buoyancy, the Argo drifter dives to its targeted depth, the parking depth,

where it follows the current for several days (see fig. 1.4). The profiler then ascends to the surface by increasing its volume while measuring temperature, conductivity, and pressure. Once the float reaches the surface, the data are transmitted to the shore via satellite before returning to the parking depth (Della Penna and Gaube, 2019). A typical Argo cycle is ten days (nine days at parking level, and one day descend to the profiling depth and ascend to the surface). In the Mediterranean, MedArgo is the official Argo Regional Centre (MED-ARC) for the Mediterranean and Black Seas, with around 80 operating floats deployed in the frame of the program. Due to the shallow bathymetry and the LIW core between 300 and 400 m in most of the Mediterranean Basin, MedArgo profilers executed cycles of 5 days with a parking depth near 350 m and maximum profiling depths of 700 m. They provide deeper profiling by diving to 2000 m every ten cycles (Poulain et al., 2007; Sánchez-Román et al., 2017).

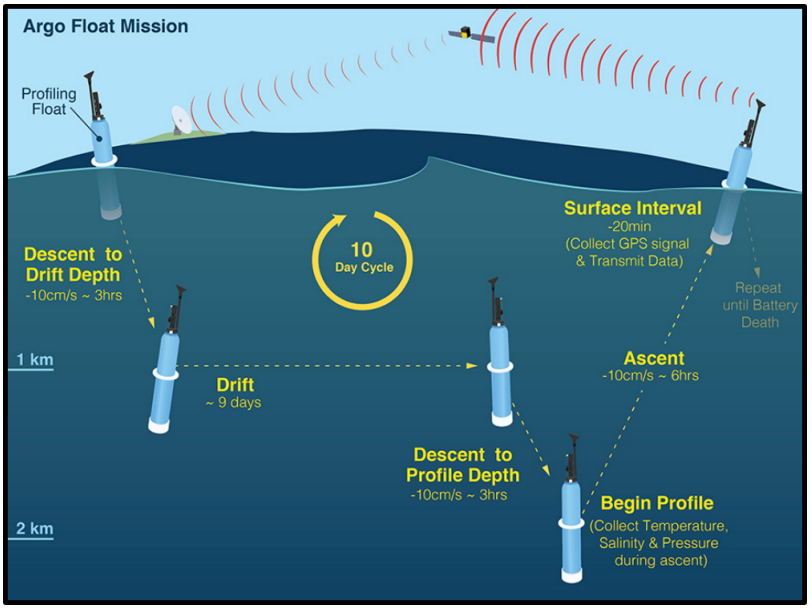

FIGURE 1.4: Schematic representation of the typical profiling mission that Argo floats repeats every 10 days. In the Mediterranean, the MedArgo profilers execute cycles of 5 days (Jayne et al., 2017).

1.4.1.4 Gliders

Gliders are robotic underwater vehicles that perform saw-tooth trajectories (Testor et al., 2019). In some way, gliders behave like Argo-floats having wings and controlling their attitude by moving internal weights, which allowing to have their velocities. The lift generated by the wings moving through the water converts vertical force into forwarding motion. It has the advantage of little human remote control while traveling. These robots

are uniquely suited for collecting data in remote locations and perfect for long-range and long-duration missions with high spatial and temporal resolution along their trajectory. Gliders can provide unique persistent fine resolution observations in the coastal and open ocean with a deployment duration that can last for almost one year.

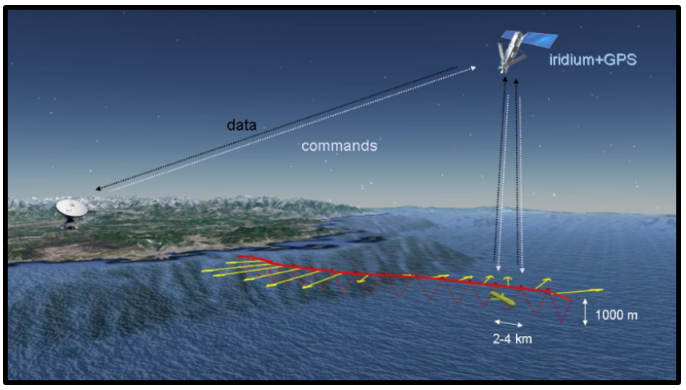

FIGURE 1.5: Schematic representation of a glider operation. The subsurface trajectory of the glider is presented in dark red, while the line in bright red represents its projection to the surface. The yellow vectors are the average current during each dive (Bosse, 2015).

Typically, gliders' profile from the surface to 200 or 1,000 m depth takes from 0.5 to 6 h to complete a cycle from the surface to this depth and back (see fig. 1.5). During this cycle, it travels a distance of 0.5 to 6 km at a speed of about 1 km/h, making measurements of pressure, temperatures, conductivity (to calculate salinity), vertically averaged currents, chlorophyll fluorescence, optical back-scatter, and sometimes more complex measurements such as micro-structure or acoustic ambient noise. Like Argo-floats, they send the data to the shore by satellite transmission, but unlike Argo-floats, they can receive command back from the shore for a possible reprogramming of their mission. The glider was imagined by Henry Stommel in 1989 and became available in early 2000. There are three main types of gliders commercially available: Two developed in the USA (the Slocum and the Seaglider) and one in France (the Seaexplorer). Each one has its technical characteristics but works quite the same way.

1.4.2 Numerical models

Numerical models are mathematical equations used to estimate surface currents. They can produce an estimation of different depths and/or provide high-resolution products. In the Mediterranean, there is the Mediterranean Monitoring and Forecasting Center that provides several regional numerical models to analyze and forecast physical and

biogeochemical variables (Tintoré et al., 2019). Although numerical models are efficient methods widely used in the physical ocean sciences, the simulation of the ocean currents in full detail remains very challenging. The dynamics are nonlinear, highly variable in space and time, and coupled to other complex systems such as the atmosphere. Moreover, the ocean models depend on the parameterizations of unresolved processes. For these reasons, models could still provide an inaccurate estimation of the surface flow (Haine, 2008).

1.4.3 Satellite observations

1.4.3.1 Ocean color

The ocean color observations are based on the detection of spectral variations in the water of the sunlight back-scattered out of the ocean. The reflectance varies after interacting with the water constituents because water contains photosynthetic pigments, primarily chlorophyll-a (chl-a), and an assemblage of other pigments (Groom et al., 2019). High-resolution chlorophyll images have shown that satellite color imagery can reveal very small swirling and filamentary patterns (see fig. 1.6). High-resolution ocean color images could therefore be an efficient tool for mesoscale features monitoring because they can detect their shape and location, leading to a good description of their evolution and possibly a better understanding of the physical processes driving their behaviors (Sarangi, 2012).

1.4.3.2 Altimetry

Satellite altimetry is a radar technique that measures the distance from the satellite to the ocean surface using a radar signal. The altimeter is placed on a satellite and emits a radar wave (signal) at the nadir to the earth's surface. Earth's surface reflects the emitted signal, and the satellite receives the reflected signal. The time elapsed between the emitting and receiving the radar signal is proportional to the satellite height. The distance with the instantaneous ocean's surface is determined by complex data processing. With a precisely determined orbit, the computed distances give the sea surface height (SSH) relative to a reference ellipsoid.

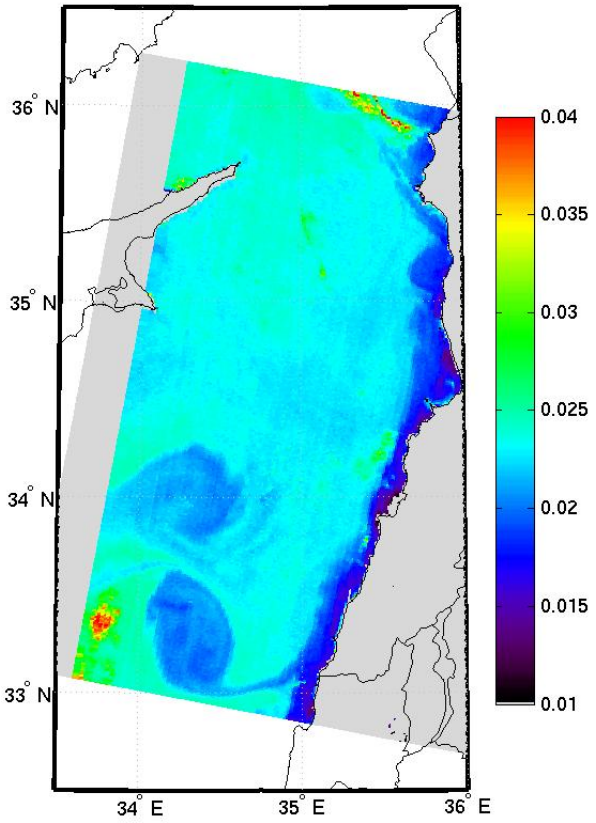

FIGURE 1.6: Satellite spectral reflectance image of the Eastern Levantine. It shows two mesoscale eddies offshore, interacting with the Lebanese coastal waters by a filament.

Satellite altimetry is considered revolutionary for the global ocean observing system and is used for several applications. One of the main satellite altimetry targets is to monitor the sea surface height (SSH) and (see below) the ocean surface current velocity, with a continuous accurate record of the global ocean surface topography and current velocity since the TOPEX/Poseidon mission in 1992 which the accuracy reached 2-3 cm. Indeed, the uninterrupted spatio-temporal coverage provided by altimetry satellites since the early '90s allows oceanographers to study the sea-level change from meso to global scales for more than 25 years (Bosch et al., 2014; Fu and Cazenave, 2000; Hamlington et al., 2013; Willis, 2010). While a radar altimeter measures SSH along the satellite's ground tracks, it produces a one-dimensional SSH profile. This profile has relatively high-resolution along-track sampling (6-7 km) but leaves large cross-track gaps (200-300 km). Data from several satellites are merged to produce two-dimensional maps at moderate resolution. Their spatial resolution after two-dimensional gridding is limited to wavelengths larger than about 150 km, resolving relatively large eddies and focusing on large and mesoscale activity (Ducet et al., 2000). Detecting large-scale

and mesoscale activity by altimetry is very important because they dominate the ocean circulation signal, and monitoring them helps not only in analyzing their dynamics but also in understanding their role in redistributing heat, nutrients, and oxygen (Wunsch, 1999).

Altimetry limitations

Although merging the data from several altimetry missions helps to improve the representation of the mesoscale features (Pascual et al., 2007), their present resolution remains insufficient for addressing small-scale ocean circulation. Moreover, further errors and inaccuracies are additional limiting factors, especially in the coastal areas where satellite information is degraded (within 20-50 km from land, Cipollini et al. (2010)). Many factors cause these inaccuracies, such as land contamination, but also inaccurate tidal and geophysical corrections, inaccurate Mean Dynamic Topography (MDT) (see section .1.4.4), and incorrect removal of high-frequency atmospheric effects at the sea surface (Caballero et al., 2013). The problem is accentuated in the Mediterranean Sea, where precise knowledge of MDT is still an issue, due to the presence of narrow straits, a high number of islands, and the small Rossby radius of deformation in the Mediterranean (around 10 km), which, overall, makes altimetry unable to capture some important small features of the Mediterranean surface circulation (Rio et al., 2014). As a consequence of the coarse resolution in both space and time of the altimeters, the relatively poor MDT, and the fact that mesoscale structures are moving, eddies can be missed, misplaced, or even created (Mkhinini et al. (2014), Ioannou et al. (2017)).

1.4.4 How does satellite works

The altimeter measurement allows to retrieve the SSH, which is the height from the reference ellipsoid to the instantaneous sea surface.

$$SSH = (Satellite\ altitude - h - corrections) \tag{1.1}$$

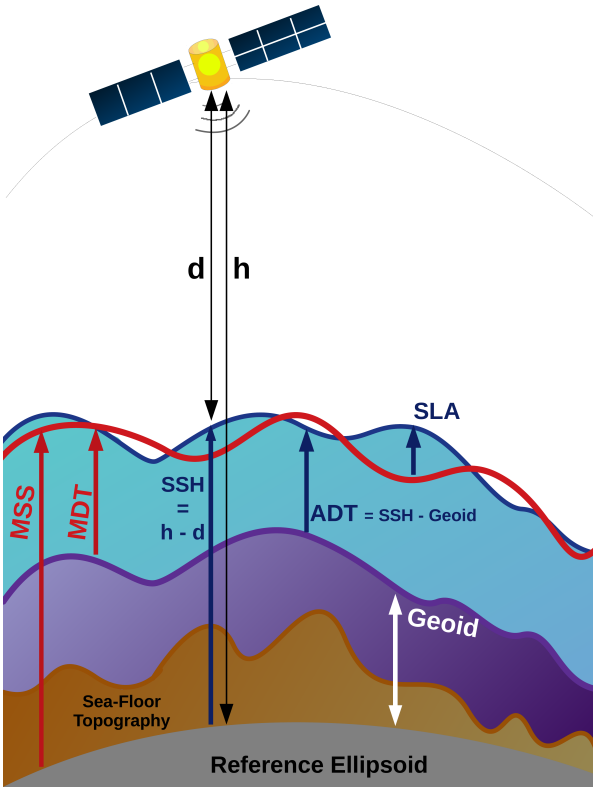

FIGURE 1.7: A schematic representation of the altimetry measuring system and the different notions for the sea level.

In the fig. 1.7, the reference ellipsoid is an algebraic reference surface close to the Earth shape, while the geoid is an equipotential reference surface for the Earth gravity field. In other words, the marine part of the geoid is the shape the ocean surface would take if it was at rest under the influence of the gravity and rotation of Earth alone in the complete absence of other forces.

The Mean Sea Surface (MSS) is a reference surface representing the SSH level averaged over several years. Subtracting the geoid from the MSS allows for obtaining the Mean Dynamic Topography (MDT).

$$MDT = MSS - geoid \tag{1.2}$$

Unlike the MSS, the MDT is not computed using altimetry only. Altimetric data are combined with other data (in-situ, gravimetric satellites) to determine the geoid precisely and to subtract it from the MSS. The Absolute Dynamic Topography (ADT) is obtained either by subtracting the geoid from the altimetric Sea Surface height (SSH) above the reference ellipsoid or by adding the MDT and adding it to the altimetric Sea Level

Anomalies (SLA).

$$ADT = SSH - geoid \tag{1.3}$$

SLA also called (Sea Surface Height Anomalies) is the sea surface height (SSH) with respect to a Mean Sea Surface (MSS).

$$SLA = SSH - MSS \tag{1.4}$$

1.4.5 Geostrophic current equations

The Navier-Stokes equations are non-linear differential equations that describe fluid movement. It is based on the second law of Newton applied to a continuous medium, stating that the acceleration of an object is related to the net force and inversely related to its mass (see eq.1.5).

$$\rho\left(\frac{\partial \vec{v}}{\partial t} + (\vec{v}.\nabla)\vec{v}\right) = -\nabla P + F + \mu.\nabla^2\vec{v} \tag{1.5}$$

where the first term represents the variation of the velocity with time. The second term is convective acceleration, which is the velocity variation rate due to the change of position of the fluid particle in the fluid flow field. The third term is the pressure gradient, where the direction of the force is from higher to lower pressure. F represents the external forces applied to the fluid, such as gravity and Coriolis. The last term represents viscosity, which is the internal stress acting on the fluid. The left side of the equation describes the acceleration, while the right side describes all the forces acting on the fluid. The geostrophic current exists when the Coriolis and Pressure gradient are the only two dominating forces. It occurs on a large scale and outside turbulent boundaries where the acceleration and the viscosity forces can be neglected. The resulting current is orthogonal and on the right (left) of the pressure gradient in the northern hemisphere (southern).

The zonal (u) and meridional (v) components of the geostrophic current are easily obtained from the altimetry (see fig. 1.8) by the following equations:

$$v = \frac{g}{f}\frac{\partial n}{\partial x} \tag{1.6}$$

$$u = -\frac{g}{f}\frac{\partial n}{\partial y} \tag{1.7}$$

where g is gravity, f is the Coriolis parameter, and n is the height of the sea surface above a level surface obtained from altimetry.

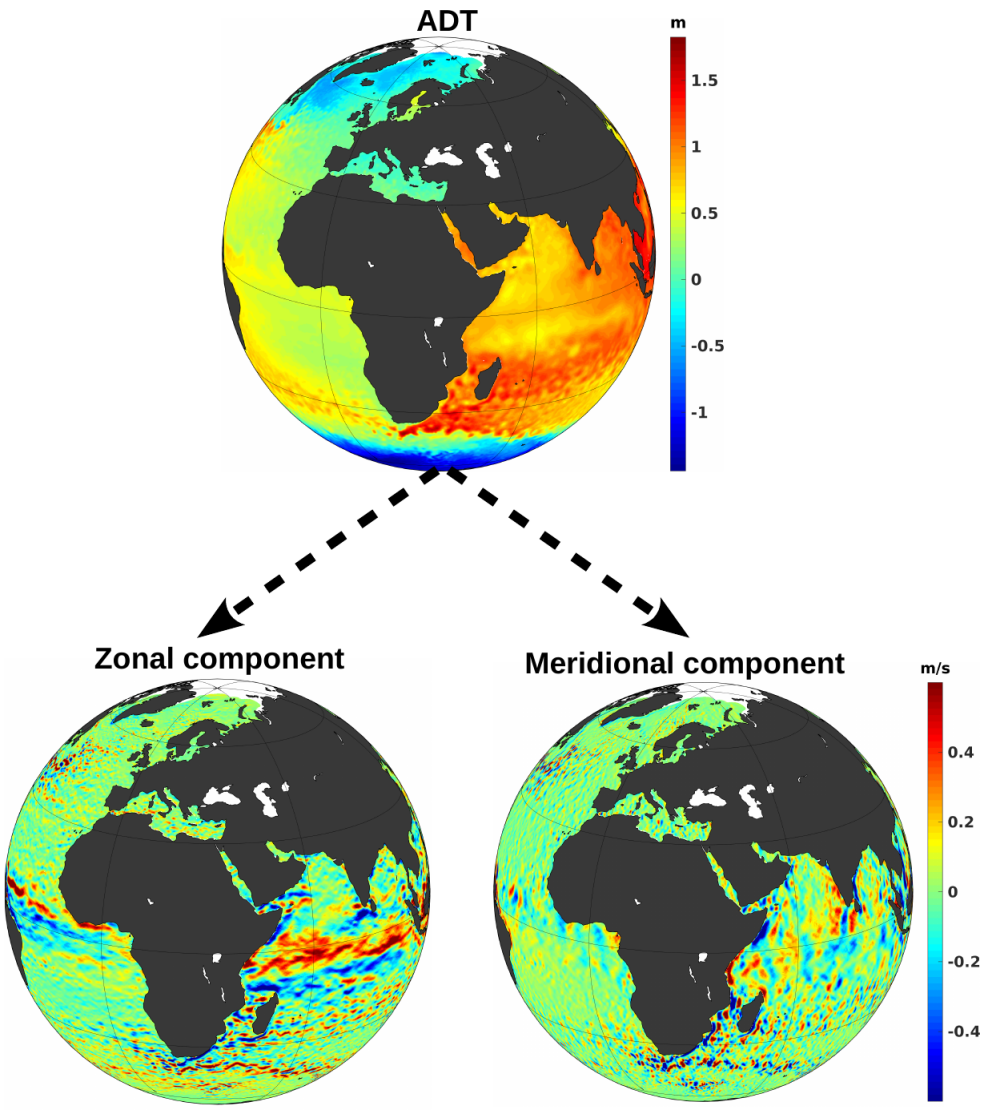

FIGURE 1.8: ADT-derived geostrophic current in 31^{st} of December 2020. The upper panel is a map of ADT measurements provided bycthe satellite altimetry. The ADT was used to derive the zonal and meridional components of the geostrophic current mapped in the lower panel.

1.5 Data assimilation

As previously mentioned in section 1.4.3.2, the use of altimetry to study the surface currents is efficient, but sometimes there is still some lack of accuracy. On the other hand, in-situ observations from surface drifters or other platforms do not provide continuous spatio-temporal coverage. Different approaches can be used to improve the Eulerian velocities (obtained from altimetry) with other observations like Lagrangian ones (Isern-Fontanet et al., 2017). One of the widely used methods is the statistical approach, which is conditioned by the availability of large data sets. Combining altimetry with large drifters observations has been successfully done previously :e.g. in the Gulf of Mexico Berta et al. (2015); Carrier et al. (2014); Muscarella et al. (2015), the Black Sea Kubryakov and Stanichny (2011); Stanichny et al. (2016), the North Pacific Uchida and Imawaki (2003). In the Mediterranean sea, Poulain et al. (2012), Menna et al. (2012) applied Pseudo-Eulerian statistics using regression models to improve its surface circulation representation.

Another common method is to use in-situ observation positions to modify the state of a dynamical model. In this context, there are two main approaches to data assimilation: Variational assimilation, based on optimal control theory, or statistical ones, based on optimal statistical estimation. Sequential methods relying on optimal interpolation have been tested successfully in blending in-situ position data and several types of operational models, such as General Circulation Models with simplified stratification (Molcard et al., 2005, 2003). In the variational assimilation approach, velocity corrections are obtained by minimizing an objective function measuring the difference between observations and their corresponding model variables. The gradient of this objective function is computed by the integration of the adjoint model. Variational methods relying on adjoint computations and that take into account the temporal variation of the observations are called 4D-Var. (Kamachi and O'Brien, 1995; Mead, 2005; Nodet, 2006). Other methods assimilate the drifters' velocities instead of their positions, such as (Carrier et al., 2014; Muscarella et al., 2015).

In the Mediterranean sea, Taillandier et al. (2006b) used an advection model to obtain drifter positions assuming that velocities were time-independent. This method has allowed the development of the Lagrangian Variational Analysis (LAVA) algorithm. It was applied to correct model velocity fields using drifter trajectories (Taillandier et al.,

2006a, 2008) and later customized to several other applications such as model assimilation (Chang et al., 2011; Taillandier et al., 2010). It was also applied to estimate surface currents in the Gulf of Mexico (Berta et al., 2015).

More recently, Issa et al. (2016) used variational assimilation that blends altimetry with drifters' observations. It proved its efficiency in the Eastern Levantine region, specifically between Lebanon and Cyprus. It was based on matching observed drifters' positions with those predicted by a simple advection model, taking into account the wind effect and imposing a divergence-free constraint on the velocity correction. The velocity correction was done in a time-continuous manner by assimilating at once an entire trajectory of drifters using a sliding time window. Sensitivity analyses showed that the velocity improved significantly even with only a few drifters, and it needed very few computational resources and converged quickly.

1.6 Machine learning technique in oceanography

Because altimetry provides such extended datasets, besides basic statistical analysis, advanced statistical methods can be applied to characterize the surface circulation from these datasets. One of these methods is the Self Organizing Map (SOM), a high-performance clustering method (Kohonen, 2013). It is an efficient tool to classify and extract features previously applied in different fields. In the oceanographic field, the SOM is relatively new. It has already been applied to characterize the inter-annual, seasonal, and event-scale variability of surface wind and Sea Surface Temperature patterns (Richardson et al., 2003), and to analyze phytoplankton pigments concentrations (El Hourany et al., 2019). The tool was also efficient for the characterization of the coastal areas by combining high-resolution numerical models with radars observations (Ren et al., 2020), or radar with ADCP data set, such as in the West Florida Shelf Liu et al. (2007), and the Long Island Sound tidal estuary (Mau et al., 2007). In the Mediterranean, SOM was applied in the Adriatic sea using HF radar measurements (Mihanović et al., 2011). SOM was also able to provide a prediction of the surface current in the shallow coastal area (Kalinić et al., 2017) and to identify phytoplankton functional types in the Mediterranean Sea using a bioregionlization approach (Basterretxea et al., 2018; El Hourany et al., 2019). By using a 46 years long high-resolution model simulation (Jouini et al., 2016), SOM allowed decomposing the surface circulation in the Sicily

Channel into modes reflecting the variability of the surface circulation in space and time at seasonal and inter-annual scales. This work has been inspirational for our own work.

1.7 Thesis motivation and objectives

Lebanon is a small country of 10452 km^2 with a 220 km long coastline located in the heart of the Middle East at the eastern edge of the Levantine Basin. Urbanism, demographic explosion, and industries along its coast are menacing its whole marine environment, its ecosystems, and its populations. Like in many other Mediterranean countries, the Lebanese coastal waters are threatened permanently by land-based sources of pollution with strong concern about the impact of industry, domestic sewage, agricultural runoffs, and tourism. The presence of various outflows inside the same coastal zone, with their complex interactions and the large influence of the large-scale circulation, enhances the difficulties to discriminate the sources to assess an efficient environmental policy (Fakhri et al., 2011).

Key information for reducing marine pollution and, hence, prioritizing political actions against land-based sources is the knowledge about surface circulation. Ocean currents do not simply act to dilute and disperse harmful material released into the sea but can also connect pollution sources to vulnerable sites (fragile ecosystems, fishing grounds, desalination plants, recreation sites). The established European Copernicus Marine Environment Monitoring Services (CMEMS, `http://marine.copernicus.eu/)`, which provide data access to the observations of the Sentinel satellite constellation and other marine data-based products, bring a new opportunity for environmental studies. Similarly, recent developments in "big data" mathematical techniques like modern assimilation, Lagrangian methods (Van Sebille et al., 2018), and clustering methods allow now to merge several types of observations and analyze large and complex datasets.

The Levantine marine science suffers from chronically weak multilateral cooperation, which translated into a much poorer understanding of the circulation than in the Western Basin. The knowledge gap on such a basic issue is worrying in terms of science but also for societal applications, as it hinders our capacity of mapping the connectivity patterns and, in turn, to deploy an effective strategy for reducing pollution at its sources and more generally for managing the marine space. The National Centre for Marine Sciences, or

the Centre National de la Recherche Scientifique du Liban (NCMR/CNRS-L), has set up collaborations with French universities to train doctoral students in the physical sciences of the ocean to address the major environmental issues for which it is responsible. In particular, it is about having the capacity to analyze the large datasets produced by CMEMS to better analyze and understand water quality data.

The addressed research questions in this thesis are summarized as follows: Is it possible to improve the representation of the Levantine Sea? Are we able to detect new events of mesoscale activity missed by the actual observations (altimetry, models) by improving the sea surface circulation representation? What are the reasons behind the contradictory assessments about the MMJ's existence? Does the complex bathymetry of the Levantine Sea impact surface circulation? Is there any seasonal, inter-annual variability or trends of the mesoscale features? To answer those questions, we will use variational assimilation and machine learning techniques. As a first step, the altimetric and in-situ data will be merged using data assimilation techniques to produce improved estimations of surface currents. The assimilation assessment will be done by comparing with other in-situ observations. This approach will allow more precise characterization of local events occurring in the Levantine Basin showing again the small-scale variability importance. However, this data merging allows the investigation of only some intermittent and short-term mesoscale activity because of the significant spatio-temporal gaps in drifters coverage in the Mediterranean (Tintoré et al., 2019). Indeed, for several years, no drifters were deployed in all of the Eastern Mediterranean, and when deployed, the covered area was limited compared to the total area (see fig. 1.9). To analyze the long-term variability of the surface dynamics, an extended altimetry dataset will be decomposed into clusters using a machine learning technique, the self-organizing map (SOM). A catalog of the several circulation regimes allows us to improve the understanding of the mechanisms driving the surface dynamics in the Levantine Sea.

The thesis is structured as follows:

In chapter 1, we have presented a general overview of the study framework and this thesis objectives and motivations.

In chapter 2, we present the variational assimilation method used for the short-time scale analysis and the data used. We then show the sensitivity tests conducted to tune the hyperparameters included in the assimilation algorithm.

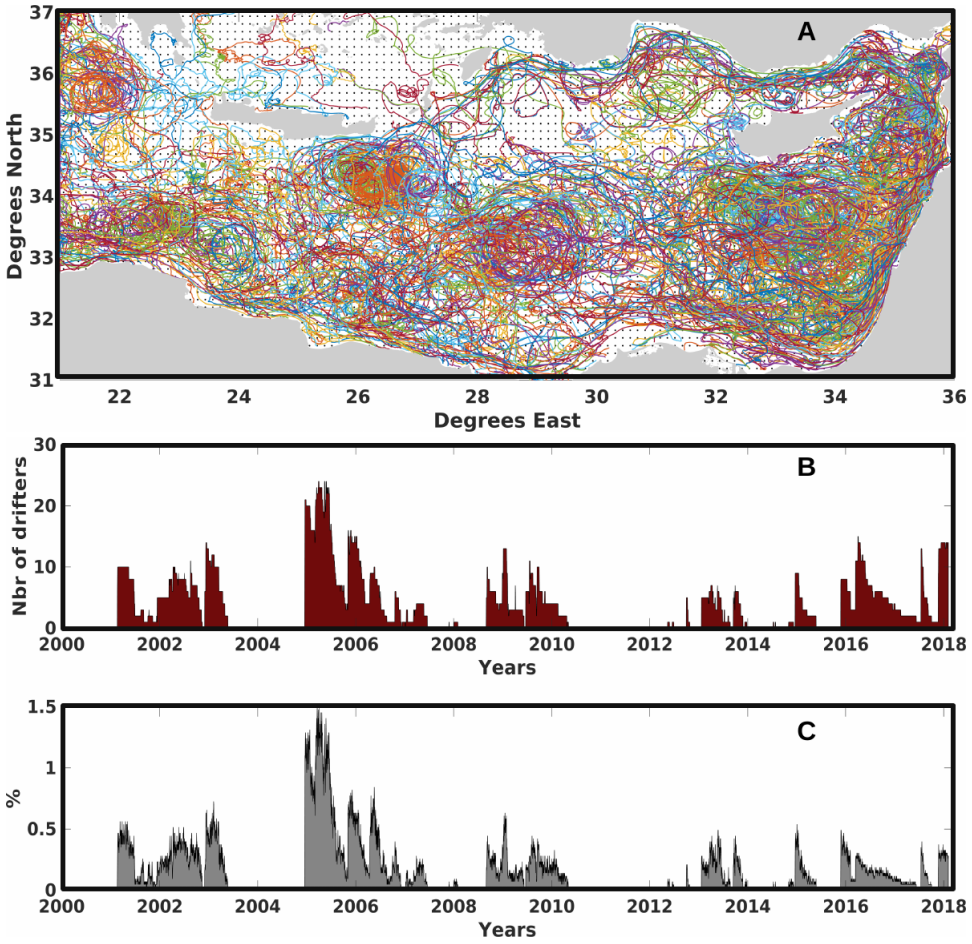

FIGURE 1.9: The upper panel presents the trajectories of the total drifters released in the Eastern Mediterranean between 2000 and late 2018, overlaid on the altimetric grid points represented in dark dots. The daily variation of the available drifters is presented in panel B, while panel C shows the percentage of the grid covered by those drifters compared to the total grid points.

In chapter 3, we provide an objective validation of the assimilation algorithm. The assessment of the validation impact is done based on the comparison with available in-situ data (current meters, gliders, and independent drifters) and satellite ocean color images.

In chapter 4, we assimilate the full drifters' dataset provided by the EGITTO/EGYPT campaign in 2006. The resulting corrected velocity fields allow analyzing the mesoscale activity of the Western Levantine by tracking the two strongest eddies present: the Ierapetra eddy and Libyio-Egyptian eddies.

In chapter 5, we assimilate drifters from NEMED and CINEL campaigns in 2009 and 2017, respectively, to characterize the activity of the Cyprus eddy, the so-called North Shikmona and South Shikmona eddies present in the Eastern Levantine.

In chapter 6, we present the machine learning self-organizing map (SOM) and Hierarcihal Ascendant Classification (HAC) method that will be used for the decomposition of the surface circulation and the sensitivity tests conducted for its optimization.

In chapter 7, we use the developed machine learning method to analyze the long-term variability of the Levantine surface circulation by decomposing 26 years of altimetric data into five clusters that reflect the different circulation patterns. By analyzing the spatio-temporal variation frequencies of these clusters, we build a catalog of the several regimes of circulation in the main mesoscale features in the Levantine Basin and analyze some physical factors that are controlling these regimes.

The thesis limitations and perspectives are drawn in chapter 8.

Part I

Local events analysis using a variational assimiation approach

Chapter 2

Data and methods

In the first part of the thesis, we use the variational assimilation to improve the characterization of short-term events occurring in the Levantine Sea. In this chapter, we will detail the assimilation method. It is a variational approach (Issa et al., 2016) that minimizes a cost function $\mathcal{J}$, which measures the distances between the observations positions (drifter) and those predicted by an advection model. The assimilation algorithm blends altimetry, wind, and drifter positions to obtain a corrected surface velocity field. First, we present the data used in the algorithm, and then we will detail the method itself and its calibration.

2.1 Data

2.1.1 Altimetry data

Geostrophic surface velocity fields are processed by the DUACS (Data Unification and Altimeter Combination System) multi-mission altimeter data processing system and distributed by E.U. Copernicus Marine Service Information (CMEMS). The SLA computation provides the Absolute Dynamic Topography (ADT) and geostrophic currents. The gridded products are estimated by an optimal Interpolation that merges measurements from altimeter missions: Jason-3, Sentinel-3A, HY-2A, Saral/AltiKa, Cryosat-2, Jason-2, Jason-1, T/P, ENVISAT, GFO, ERS1/2. The interpolation provides a consistent and homogeneous database. Data were daily mapped at a resolution of $1/8^o$. In this part of the thesis, we used altimetry data corresponding to the periods of continuous drifters deployment in the Eastern Mediterranean, more precisely in 2006, 2009, and 2017.

2.1.2 Wind data

Six-hourly wind data were obtained from ECMWF ERA-Interim products (Dee et al., 2011) at 10 m above the surface. Data was re-sampled on a half an hour time step. Wind velocities were interpolated at a resolution of $1/8^o$ at the same grid point as the AVISO background data. The wind component is added to the geostrophic current provided by altimetry to bring the corrected velocity field obtained after assimilation closer to reality.

2.1.3 Drifters data

We present the EGYPT/EGITTO, CINEL, and NEMED campaigns, from which we used the deployed drifters for assimilation. All drifters were low-pass filtered using a Hamming filter with a cut-off period at 36 h to eliminate tidal and inertial variability. EGITTO/EGYPT drifters were interpolated at 0.5 h, compared to 6h for NEMED and CINEL drifters (doi:data/10.6092/7a8499bc-c5ee-472c-b8b5-03523d1e73e9).

EGYPT/EGITTO program

The EGYPT/EGITTO program (Eddies and Gyres Paths Tracking, (Taupier-Letage et al., 2007)) focused on the EM southern part spanning the period 2005-2007. It provided an extensive deployment of satellite-tracked drifters. Between 2005 and until 2007, 97 drifters were tracked by the global Argos System. Their time series were interpolated at 0.5 h (Poulain et al., 2013). Data were then low-pass filtered using a Hamming filter with a cut-off period at 36 h to eliminate high-frequency current components (tidal and inertial currents). (See the $\sim$ 2-years trajectories animation on SOUTHEASTERN MEDITERRANEAN SURFACE DRIFTER DATABASE: nettuno.ogs.trieste.it/doga/sire/egitto/database_egitto/movies/sep05-oct07.avi).

NEMED

The Surface Circulation in the Northeastern Mediterranean (NEMED) project from 2009 to 2010 was an observational program releasing drifters between Cyprus and the Middle East. A total of 31 drifters SVP were released between summer 2009 to spring 2010, using low-cost satellite-tracked drifters. Drifters time series were interpolated at 6 hours.

CINEL

The Circulation and water mass properties in the North Eastern Levantine project (CINEL), is a project in which drifters and gliders were operating in the eastern part of the Levantine sea starting from September 2016 lasting for more than one year. A total

of 16 drifters were released in the area between Cyprus and Lebanon. Two drifters were deployed each season in the coastal waters of Lebanon. In addition, another group of drifters was released along a meridional transect south of Cyprus.

From this data set, we will select the drifters that were stuck in eddies for several weeks (see table 2.1) to better inverstigate their activity in the chapters 4 and 5.

Targeted eddies	Id Argos	Lifetime
Ierapetra eddy	59748/59751	24/04/2006 - 20/08/2006
Libyo-Egyptian eddy	57312/59774/59777	01/04/2006 - 31/08/2006
South-Shikmona eddy	92058/92063	05/08/2009 - 30/09/2009
Cyprus eddy/ North-Shikmona eddy	No id available	01/03/2017 - 26/10/2017

TABLE 2.1: List of the eddies trapping drifters for several weeks in the Levantine Sea.

Mediterranean Forecasting System

The Mediterranean Forecasting System is a coupled hydrodynamic (from NEMO v3.6) and wave (provided by WaveWatch-III) model with data assimilation components implemented over the Mediterranean Basin. In-situ vertical temperature and salinity profiles (from XBT, CTD, Argo floats) are assimilated with satellite Sea Level Anomaly along-track data (from Jason1&2, Cryosat, Envisat, Altika). The product quality assessment is done by comparing with quasi-independent satellite and in-situ observations. The model spatial resolution is 1/16°, and the product is computed on 72 unevenly-spaced vertical levels. The depths levels are unevenly spaced, and the thickness varies from 3 m at the surface to 300 m at the bottom. The first level depth is at 1.5 m while the deepest one is at 5000 m (Tonani et al., 2008). The model will be used to evaluate the comparability between the currents at different depths in chapter 3. Afterward, the MFS velocity field at drifters depth (15 m) will be compared to the velocities before and after assimilation by characterizing mesoscale features in chapters 4 and 5.

2.2 Methodology

The correction is based on a variational assimilation method described in Issa et al. (2016). Observations of drifter's positions are available every Δt (Δt=6 hours for drifters

in the eastern Levantine and 0.5 hours for those in the western Levantine). The background surface velocity field, which will be assimilated with drifters, is prepared using the altimetry and the wind components. It is denoted by:

$$\mathbf{u}_m^b = \mathbf{u}^b(m\Delta t),\ m = 1, 2, \cdots M, \tag{2.1}$$

where this field is two dimensional $\mathbf{u}_m^b = (u_m^b, v_m^b)$, and where m is the integer time index. This field is corrected by matching observed drifter's positions with those predicted by an advection model.

The background velocity field ($\mathbf{u}_m^{\mathrm{b}}$) used is the sum of a geostrophic component provided by altimetry ($\mathbf{u}_m^{\mathrm{geos}}$) and an ageostrophic component accounting for the effect induced by the wind ($\mathbf{u}_m^{\mathrm{wind}}$)

$$\mathbf{u}_m^b = \mathbf{u}_m^{\mathrm{geos}} + \mathbf{u}_m^{\mathrm{wind}}. \tag{2.2}$$

This wind-induced velocity is computed by a regression model with parameters found by beta fitting (Poulain et al., 2009) (for drifters that are attached with a drogue).

$$\mathbf{U}_m^{wind} = 0.007 \exp(-27^o i) \times \mathbf{U}_m^{10} \tag{2.3}$$

where $\mathbf{U}_m^{wind} = u_m^{\mathrm{wind}} + iv_m^{\mathrm{wind}}$ is the drifter velocity due to the wind effect, and $\mathbf{U}_m^{10} = u_m^{10} + iv_m^{10}$ represents the wind velocity at 10 m above the surface. Both are expressed as complex numbers. The wind speed above the sea surface varies considerably at a very short time scale.

An incremental approach (Talagrand and Courtier, 1987) is used so that the minimization is done for the incremental corrections $\boldsymbol{\delta}\mathbf{u}$ invariant in time within the time window of size T_w. The objective function to be minimized is:

$$\begin{aligned}\mathcal{J}(\delta\mathbf{u}) = &\sum_{i=1}^{N_f} \sum_{m=1}^{\lfloor T_w/\Delta t \rfloor} ||\mathbf{r}_{\mathrm{i}}^{\mathrm{b}}(\mathbf{u}_{\mathrm{m}}^{\mathrm{b}}) + \delta\mathbf{r}_{\mathbf{i}}(\delta\mathbf{u}) - \mathbf{r}_{\mathrm{i,m}}^{\mathrm{obs}}||^2 \\ &+ \alpha_1 ||\delta\mathbf{u}||_{\mathbf{B}}^2 + \alpha_2 \sum_{j,k} (\nabla \cdot \delta\mathbf{u})^{\mathbf{2}},\end{aligned} \tag{2.4}$$

where N_f is the number of drifters, i is the index of the drifter, and Δt is the sampling time of the observations. $\mathbf{r}_{i,m}^{\mathrm{obs}}$ represents the observed position of drifter i at time $m\Delta t$.

The term $\mathbf{r}_i^b$ (resp. $\delta\mathbf{r}_i$) is the position of the drifter i estimated by an advection model calculated from the background field $\mathbf{u}_m^b$ (resp. from the incremental correction $\boldsymbol{\delta}\mathbf{u}$). The first term measures the misfit between the observations and the positions of drifters simulated considering the advection by the surface velocity field. The second component requires the corrected field to stay close to the background velocity. Here the $\mathbf{B}$-norm is defined as $||\psi||^2_{\mathbf{B}} \equiv \psi^T\mathbf{B}^{-1}\psi$, where $\mathbf{B}$ is the background error covariance matrix. The error covariance matrix $\mathbf{B}$ is obtained using the diffusion filter method of Weaver and Courtier (2001). The choice of the length scale R of the correction that enters in the error covariance matrix can be done in the context of the sensitivity analyses. The last component is a constraint on the geostrophic part of the velocity required to stay close to divergence-free. This term is added to ensure a physical correction, avoiding artifacts, especially near the coasts. The weights α_1 and α_2 correspond to the confidence given to the respective terms of the cost function, relative to the observation error term. Because the cost function is defined within a multiplicative constant, it is safe to set a standard confidence of one to the observation error term, assuming the standard deviation of the observation error distribution is the same and de-correlated from the other. The relative confidence in the background α_1 and the non-divergent constraint α_2 cannot be prescribed a priori. So they are determined empirically using sensitivity analyses. After the minimization, we compute a corrected velocity field:

$$\mathbf{u}_{\mathrm{m}}^{\mathrm{corr}} = \mathbf{u}_{\mathbf{m}}^{\mathbf{b}} + \delta\mathbf{u} \tag{2.5}$$

Because $\delta\mathbf{u}$ is constant inside a time window, a sliding window of time shift σ, is used to obtain smooth time-dependent velocity $\delta\mathbf{u}_k$ in $[k\sigma,\ k\sigma + \mathrm{T}_w]$, k= 0, 1, 2, $\cdots$.
The obtained corrected velocities are thus the results of the a superposition of the time dependent background field and the weighted corrections

$$\mathbf{u}^{\mathrm{corr}}(t_i) = \mathbf{u}^{\mathbf{b}}(t_i) + \sum_{k=0}^{N_w^i - 1} w_k \delta\mathbf{u}_k. \tag{2.6}$$

The weight w is inversely proportional to the distance between time t_i and the window position:

Hyperparameter	Definition
T_w	Temporal window size in which the incremental correction is constant
α_2	Divergence coefficient to keep the geostrophic velocity close to divergence-free
R	Length scale of the correction that enters in the error covariance matrix

TABLE 2.2: Presentation of the hyperparameters that will be tuned in each of the Eastern and Western Levantine by the sensitivity tests.

$$w_k = \frac{1}{|k - k^*| + 1}, \tag{2.7}$$

where k^* corresponds to the window centered at t_i . Note here that the weights are normalized to add to one.

2.2.1 Determination of hyperparameters through sensitivity studies

Sensitivity tests allow tuning the following hyperparameters: T_w, α_2 and R (see table 2.2). The length scale R variation does not affect the correction around the drifter but the length of the corrections around the assimilated drifter. Thus an independent drifter that was not assimilated (if possible) but was closely circulating is used for sensitivity studies. The determination of hyperparameters is based on the lowest distances (d) obtained after correction between the simulated drifter positions ($\mathbf{r}$) and the real observations ($\mathbf{r}^{obs}$) (see eq.2.8). Sensitivity tests were done for each part of the Levantine: the western (Chapters 3 and 4) and the eastern part (Chapter 5), where for each case, the hyperparameters are tuned based on minimizing d:

$$d(t) = \frac{1}{N_w} \sum_{j=1}^{N_w} ||\mathbf{r}_j(t) - \mathbf{r}_j^{obs}(t)||^2, \tag{2.8}$$

where N_w is the number of windows used during the simulation.

Western Levantine

Three drifters were circulating closely off the Libyan coasts between 8^{th} and the 27^{th} of May 2006 (1^{st} drifter: longitude 22.545 and latitude 33.3; 2^{nd} drifter: longitude 23.733 and latitude 33.263; 3^{rd} drifter: longitude 23.479 latitude 33.339). The positions of two drifters were assimilated (Argo number: 59777 and 59774) to simulate the position

evolution of the third one (57312) based on the surrounding velocity field. During all the sensitivity tests, the simulated drifter positions were reinitialized every three days to the position of the real drifter.

We opted for σ of a half-day to have a smoother correction. In the first experiment, to optimize T_w, the corrected velocity fields were obtained after assimilation with T_w of one, two, and three days. The other two parameters were constant and selected heuristically with α_2=0 and R= 20 km. From 8^{th} to 27^{th} of May 2006, the averaged-distances variations reveal that for T_w of two days, the simulated trajectories were the closest to the real observations. The improvement reached around $\sim$ 70% compared to the background, 5% and 9% more when compared to T_w of one and three days respectively (see fig. 2.1A).

After optimizing T_w with a selected temporal size of 2 days, the second parameter to tune is the divergence coefficient α_2 (fig. 2.1B). Like the previous experiments, R=20 km was heuristically selected. As a result, α_2 of 5×10^6 or null, the solution was modified by only $\sim$ 0.7%. Thus α_2 had a negligible effect on the resulting velocity field for the selected values.

In the last experiment, R was varied from 20 to 30 km with optimized T_w of 2 days and α_2 of 5×10^6. After simulating the trajectories of the independent drifter based on the resulting velocity field, R of 30 km gave the closest simulations to the observations, especially at the end of the window (see fig. 2.1C).

Eastern Levantine

The same approach was applied for the data set of the drifters in the Eastern Levantine, more precisely in the area between Cyprus and Lebanon. The drifters released were lower compared to the EGITTO/EGYPT campaign. Thus it was not possible to simulate the trajectory of an independent drifter because they were no multiple drifters circulating close to each other as in the previous experiment. Consequently, we selected only one drifter (OGS drifter identification number: 5310) that was trapped in a high vorticity area, the Cyprus eddy, to assimilate its trajectory from 18 until 26^{th} March 2009 (see fig. 2.2). The distances between the simulated positions obtained based on the surrounding corrected velocities and the observations of the same drifter were computed.

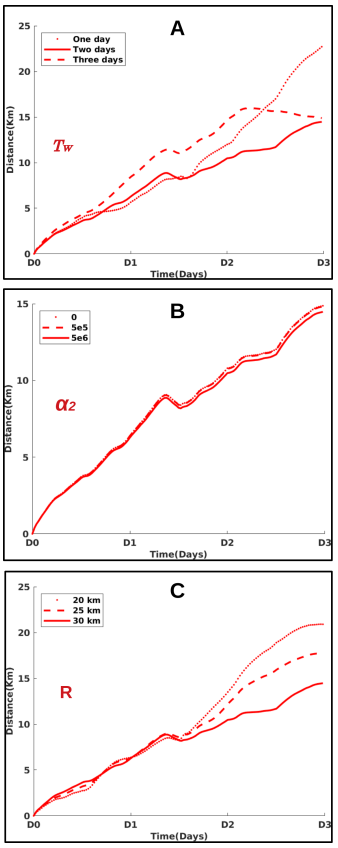

FIGURE 2.1: Temporal evolution of the distances between the simulated trajectories and the real drifter positions depending on the variation of the window size (A), the divergence coefficient (B) and the length scale of the correction (C).

Hyperparameter	Western Levantine	Eastern Levantine
T_w	*Two days*	*Two days*
α_2	5×10^6	5×10^6
R	30 km	20 km

TABLE 2.3: Summary of the tuned hyperparameters values in each of the Eastern and Western Levantine.

In all cases, we opted for a moving window (σ) that is equal to the previous experiment. Fig. 2.3A shows the distances resulting from the window size (T_w) of one and two days. For both cases, the maximum distance was less than 0.6 km. The variation of T_w size did not have a major impact on the assimilation. There was an improvement of 95 % compared to the background (95 % and 96 % for T_w of 2 and 3 days, respectively). The same results were obtained when comparing the divergence coefficient α in fig. 2.3B. The variations were homogeneous in all of the three cases with an improvement of 96 % (α= 5×10^5, 5×10^6, and 0). On the other hand, the tuning of the length scale of the correction (R) was not possible (they were no multiple drifters to simulate an

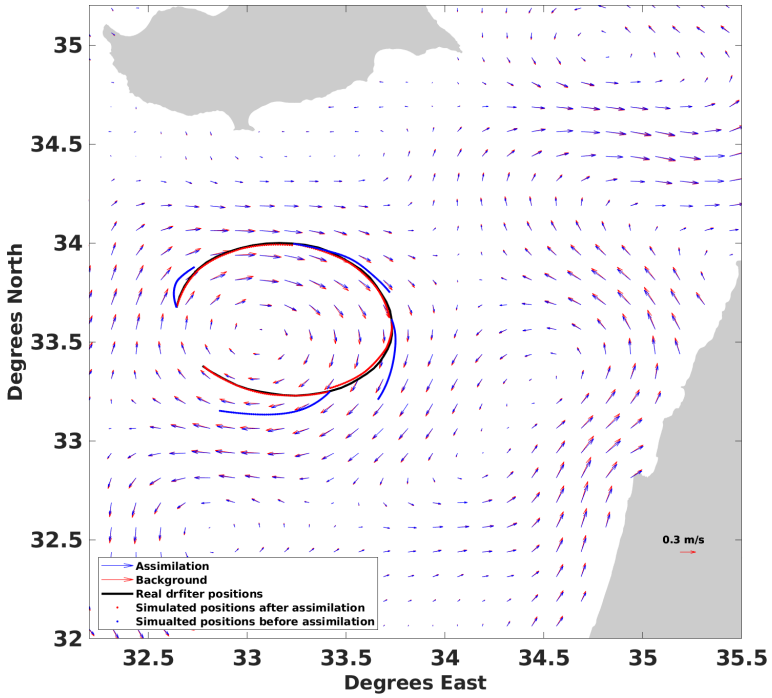

FIGURE 2.2: The trajectory of the simulated positions before (blue) and after correction (red), compared to the real observations.They are overlaid on the average velocity field of the background (blue) and assimilation (red).

independent one). Thus we opted for the same length R as in Issa et al. (2016) because it corresponds to the same area. Velocity fields of the Eastern Levantine, in 2009 and 2017, were thus assimilated with the following parameters: T_w of two days, R=20 km, and α=5 $\times$ 10^6 (see table 2.3).

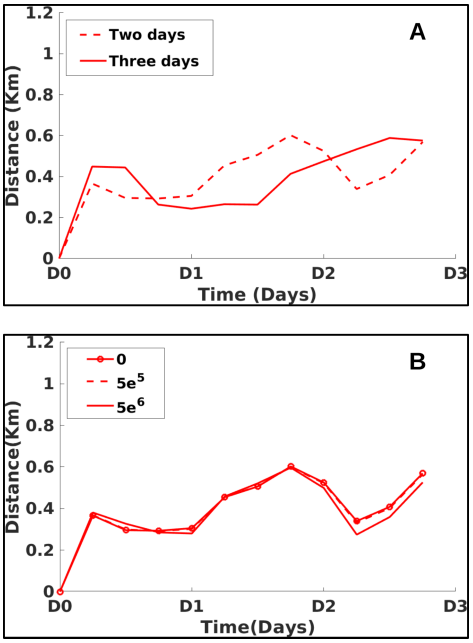

FIGURE 2.3: Temporal evolution of the distances between the simulated trajectories and the drifter real positions depending on the variation of the window size (A) and the divergence coefficient (B).

Chapter 3

Validation by comparison with independent observations

The previous chapter showed that the hyperparameters need to be tuned according to the studied area. After the sensitivity tests, we present an objective validation of the variational assimilation method when applied in the Levantine Basin. The assessment is done by comparing the corrected velocity fields with other independent observations. These observations are in-situ data (current meter, glider, and independent drifter) and ocean color images.

The metrics used for validation proved that the algorithm was able to improve the representation of the surface circulation even in a high vorticity area. Fig. 3.1 shows that after assimilating drifter positions trapped in an eddy detected at the same time from high-resolution chlorophyll images, the resulting streamlines from the corrected velocity field are more consistent with the eddy shape and location as revealed by the ocean color image.

A detailed presentation of these validations is presented in Baaklini et al. (2021) in Appendix A.

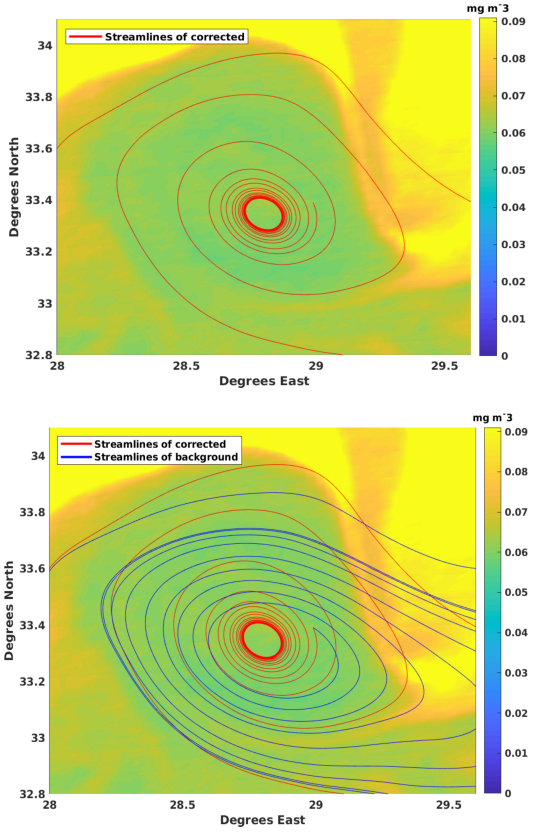

FIGURE 3.1: Velocity field streamlines after correction (upper panel) compared with the background (lower panel) overlaid on chlorophyll-a image of 20 May 2006.

Chapter 4

Characterization of local events in the Western Levantine

In this chapter, we applied the assimilation, presented and validated in the previous chapters, to characterize two of the most dominant features in the Eastern Mediterranean: the Ierapetra eddy (IE) and the Libyo-Egyptian eddies (LEE). In chapter 3, we used only a subset of the data from the EGYPT/EGITTO campaign (Eddies and Gyres Paths Tracking) for validation. Here we took advantage of all the drifters released to assimilate them. The corrected velocities obtained after assimilation will be used to characterize IE and LEE based on the diagnostics of Mean kinetic energy (MKE), eddy kinetic energy (EKE), and relative vorticity (ζ). These results will be compared with the background (altimetry only) and the geostrophic current retrieved from the Sea Surface Height of the Mediterranean Forecasting system MFS model. This comparison will allow evaluating the assimilation contribution in the characterization of short-time scale eddies activities compared to the conventional observational tools (altimetry and models).

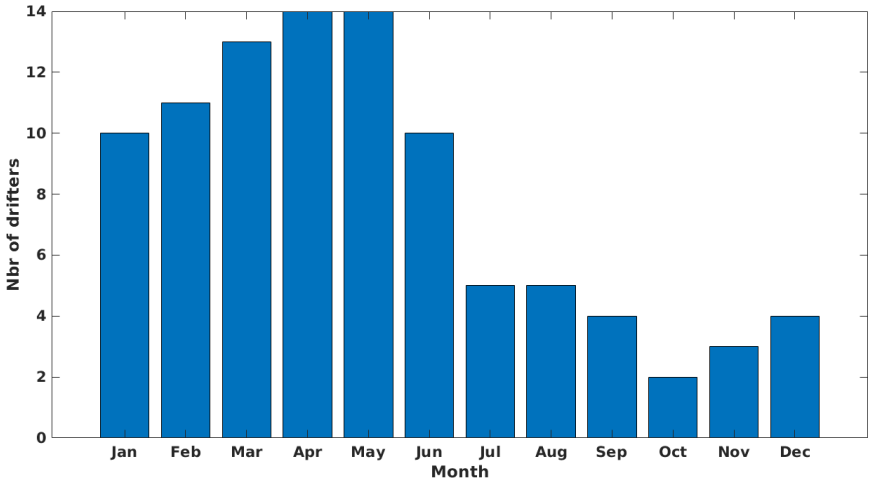

FIGURE 4.1: The number of drifters assimilated in each month of 2006. These drifters were released during the EGYPT/EGITTO campaign and circulating between Crete and off the Libyo-Egyptian coasts.

Fig. 4.1 shows the monthly variation of the number of drifters in the area between the Libyo-Egyptian coasts and Crete during 2006. The density of drifters was higher during the first months and reached a maximum of 14 per month in April and May, while only two drifters were available during October 2006. A detailed representation of the spatial distribution is presented in fig. 4.2. The studied area was divided according to the number of times a drifter circulated in each bin during 2006. It showed that the deployed drifter trajectories covered most parts of the area between the Libyo-Egyptian coast and Crete Island. The highest densities were observed off the Libyan coasts and in

the Ierapetra eddy area, with more than 600 observations. After assimilating all these available drifters, a new velocity field was obtained for 2006.

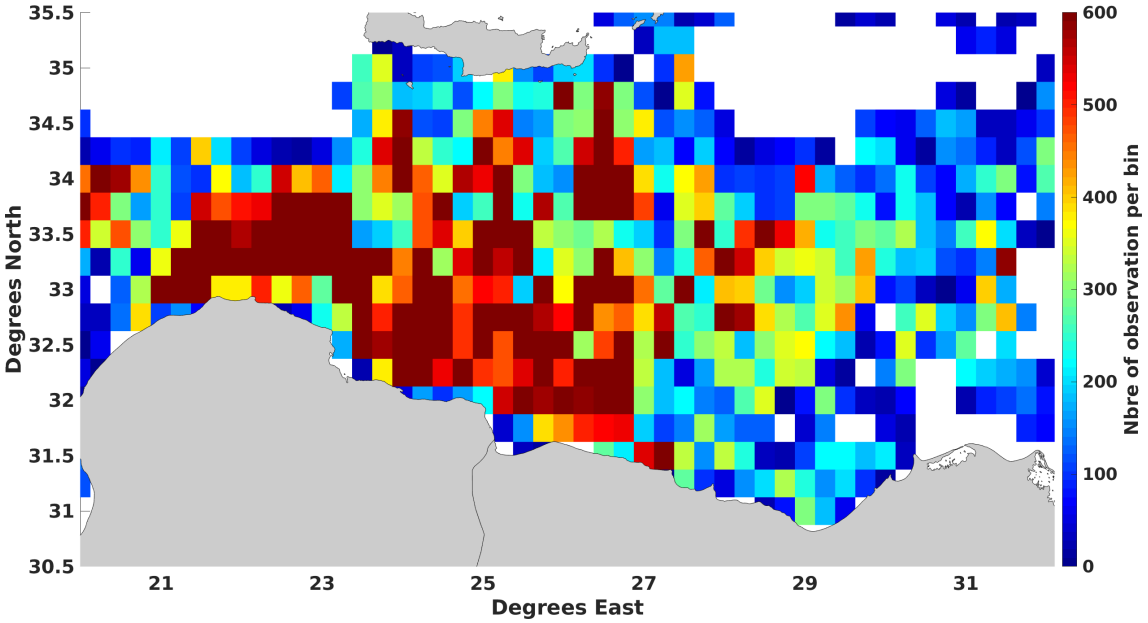

FIGURE 4.2: The observations density in each bin of the area between the Libyo-Egyptian coasts and Crete in 2006.

4.1 Metrics

Mesoscale eddies capture almost 80% of the total global kinetic energy, thus Mean Kinetic energy (MKE) and Eddy Kinetic Energy (EKE) are commonly used to analyze the mesoscale eddies (Ding et al., 2020):

4.1.1 Mean Kinetic Energy (MKE)

The kinetic energy per unit of mass of the mean flow (MKE, cm^2/s^2) is computed for the corrected, background, and MFS velocity fields. If u and v are the zonal and meridional velocity, respectively, MKE is:

$$MKE = \frac{1}{2}\left(|u|^2 + |v|^2\right) \tag{4.1}$$

where $|\ |$ is the time averaging of the component in a given bin.

4.1.2 Eddy Kinetic Energy (EKE)

The kinetic energy per unit of mass of the fluctuating flow knows as the Eddy Kinetic Energy (EKE, cm^2/s^2), is obtained from the following equation:

$$EKE = \frac{1}{2}\left(u'^{\,2} + v'^{\,2}\right) \tag{4.2}$$

where the prime indicates the residual velocity in a given bin ($u = |u| + u'$ and $v = |v| + v'$).

4.1.3 Relative vorticity (ζ)

The relative vorticity (ζ) is the vorticity of the fluid relative to Earth, describing thus the local spinning motion of the fluid:

$$\zeta = \frac{\partial v}{\partial x} - \frac{\partial u}{\partial y} \tag{4.3}$$

where positive (negative) ζ reveals cyclonic (anticyclonic) structures. It should be mentioned that the vorticity measured relative to absolute space is called absolute vorticity (η):

$$\eta = \zeta + f \tag{4.4}$$

where f is the Coriolis force.

4.2 Results

In this section, after assimilating all the available drifters, we used the resulting corrected velocities to characterize the activity of two main features in 2006, the Ierapetra eddy (IE) and Libyo-Egyptian eddies (LEE):

4.2.1 Ierapetra eddy

4.2.1.1 Mean Kinetic Energy

The MKE during 2006 of the area between the Libyo-Egytoian coasts and Crete, obtained after assimilation, is presented and compared to the background and the geostrophic velocities derived from the Sea Surface Height (SSH) of the Mediterranean forecasting system (MFS) in fig. 4.3. The Ierapetra eddy (IE) was present in all three velocity fields, showing high intensities during 2006. However, after assimilation, these intensities increased significantly in parts of IE. Consequently, the ring shape was distinctly present compared to other mesoscale structures in the area. To quantify the difference of IE intensity between the three products, we showed the MKE value in each bin of IE area as seen in fig. 4.4. For the MFS, more than 60% of the bins were less than 200 cm^2/s^2, and the local maxima did not exceed 500 cm^2/s^2. The assimilation mainly increased the density of pixels whose MKE exceeded 500 cm^2/s^2 from $\sim$ 8%, in the background velocities, to $\sim$ 20%. The maximum of MKE registered by the MFS was 329 cm^2/s^2, compared to 634 cm^2/s^2 for the background and 762 cm^2/s^2 after assimilation. The MKE of 2006 obtained from the drifter's velocities of the EGYPT/EGITTO showed that the IE was the dominant mesoscale feature with values more than 600 cm^2/s^2 (Gerin et al., 2009). The higher values obtained after assimilation were in agreement with the previous studies mentioning that altimetry tends to underestimate the MKE of the mesoscale structures in the Mediterranean (Poulain et al., 2012). These results show that the IE is the most intense structure in the Eastern Mediterranean, and still is underestimated by the previously used observations.

Seasonal comparison

Because IE is an eddy that mainly appears in late summer or autumn, we divided the corrected mean flow into two extended seasons: winter (from 1^{st} January to 30^{th} June 2006) and summer (from 1^{st} of July until 31^{st} of December 2006). Fig. 4.5 shows that the IE summer intensification was observed in all of the three velocity fields. The saturation and the spatial extension of all IE parts were seen by the MFS, corrected, and background velocities, with values exceeding 500 cm^2/s^2. Oppositely, during the winter, IE was not the most intense structure, but it was the MME further to the east

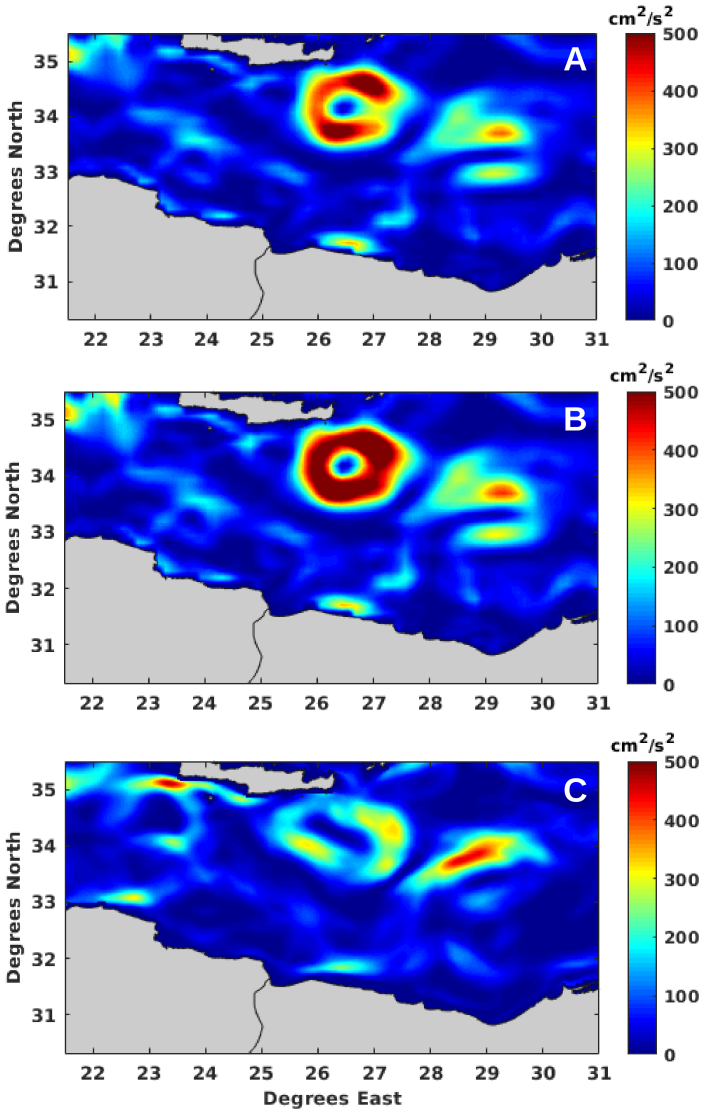

FIGURE 4.3: The annual Mean Kinetic Energy (saturated at 500 cm^2/s^2) in 2006 resulting from the background (A), corrected by assimilation (B), and geostrophic velocities derived from MFS (C).

(fig. 4.6). In both seasons, MFS (C) revealed smaller structures not observed in the other velocities, such as close to the west of Crete. It could be due to the higher resolution capable of detecting jets, meanders, or filaments that could be missed or smoothed by the altimetry or the corrected velocity fields. Indeed, the absence or the lack of observations to assimilate in these zones did not allow the assimilation to detect these structures (see fig. 4.2).

The seasonal comparison of the MKE value in each bin of IE revealed significant differences between summer and winter (see fig. 4.7). During the winter, most bins were weak, with more than 70% being less than 200 cm^2/s^2. Overall, the MKE values were similar in all the three compared, and the values of maximum MKE observed were also

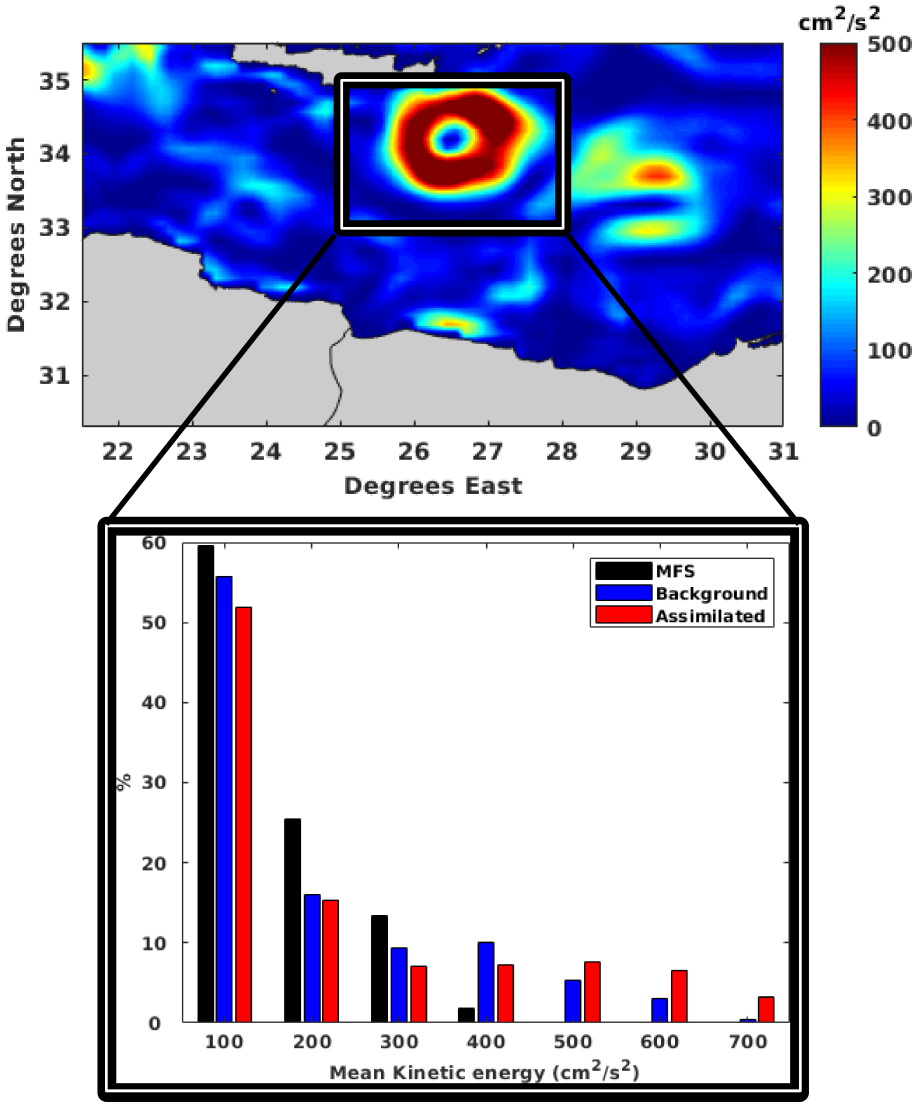

FIGURE 4.4: The area of Ierapetra eddy location (upper panel) overlayed on MKE derived from corrected velocities. Bin values of MKE are plotted in histograms (lower panel) for the three experimented velocity fields (corrected, background and MFS).

close (358 cm^2/s^2, 365 cm^2/s^2, and 385 cm^2/s^2 for corrected, background, and MFS velocities, respectively).

The summer intensification of IE was markedly noticed in fig. 4.7, where the number of bins with values more than 200 cm^2/s^2 increased significantly. The highest MKE values exceeded 1000 cm^2/s^2 in MFS, corrected and background velocities, meaning that the flow intensity grew more than three times in a time scale of a few months.

The density of bins with values exceeding 1000 cm^2/s^2 was around $\sim 1\%$ for the MFS but increased significantly, reaching $\sim$ 16% for the background and $\sim$ 20% for the assimilation. Similarly, the MKE local maxima was the highest in the corrected velocity

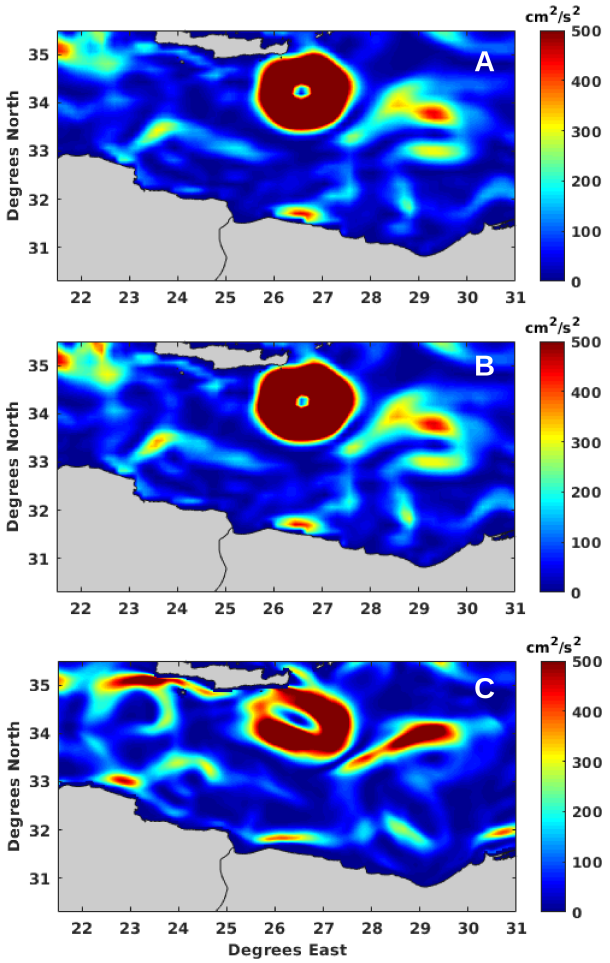

FIGURE 4.5: The Mean Kinetic Energy (saturated at 500 cm^2/s^2) for the extended summer resulting from the background (A), corrected (B), and geostrophic velocities derived from MFS (C).

field with $\sim$ 2140 cm^2/s^2, exceeding by more than 400 cm^2/s^2 ($\sim$ 1700 cm^2/s^2) the background, and 950 cm^2/s^2 for the MFS ($\sim$ 1170 cm^2/s^2). Previous studies have shown that MFS could underestimate the current velocities (De Dominicis et al., 2012; Lacorata et al., 2014), thus possibly explaining this weak flow observed in IE during the summer. Moreover, the maximum of MKE after correction exceeded those observed in Gerin et al. (2009), although using the same drifters (see table. 4.1). Indeed an eddy is characterized by velocity contours that vary depending on their distance from the eddy center. The contour flow intensifies with the increasing radius until reaching a maximum velocity Vmax before progressively decreasing. Accordingly, the drifters used in Gerin et al. (2009) could be circulating in the contours of relatively weaker intensity than V_{max}, while assimilating those drifters could increase the velocity field occurring 30 km around a drifter (including V_{max}) which explains the lowest values observed by the drifters compared to those of background and assimilation.

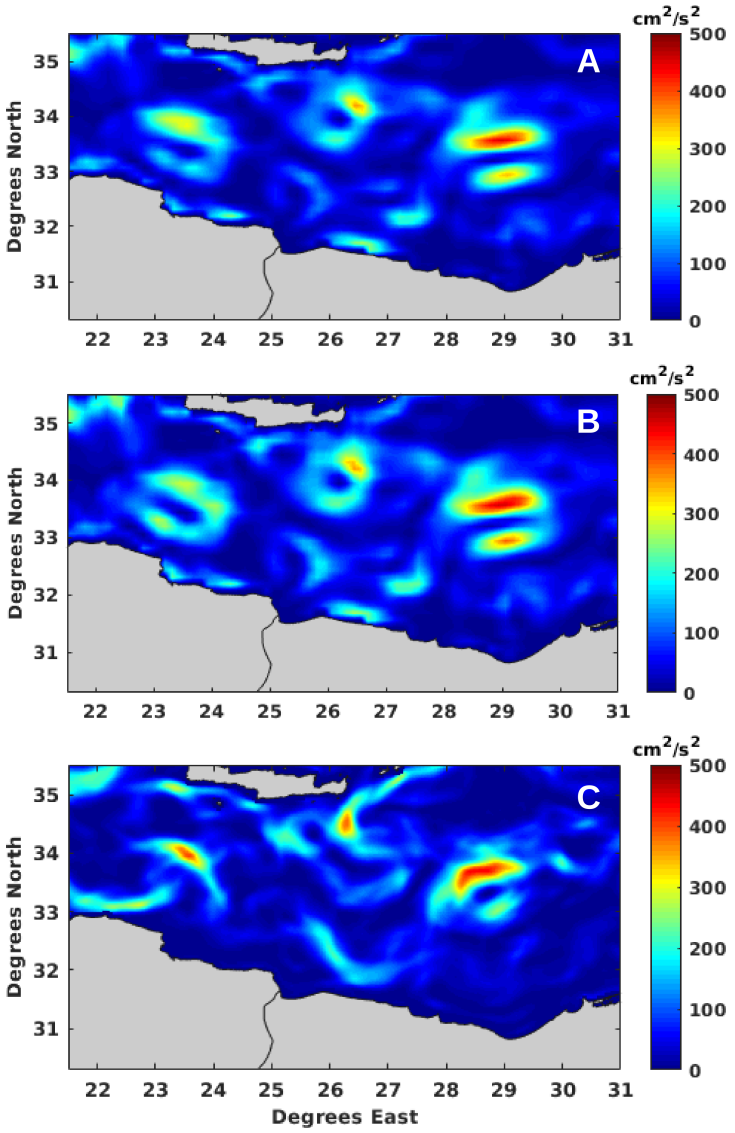

FIGURE 4.6: The Mean Kinetic Energy for the extended winter resulting from the background (A), corrected (B), and geostrophic velocities derived from MFS (C).

4.2.1.2 Eddy Kinetic Energy

The annual EKE average revealed high variations in the IE area (see fig. 4.8 (upper panel)). Additionally, high EKE was observed off the Libyan coasts and in the Mersa-Matruh area. The bins histogram in IE (lower panel) showed that no values exceeded 500 cm^2/s^2 in the MFS. On the other hand, the assimilation increased the frequency of bins with values exceeding 500 cm^2/s^2 when compared to the background.

Time	Corrected	Background	MFS	Gerin et al. (2009)
Summer	2140	1700	1170	1529
Winter	358	365	385	>250
All year	762	634	329	>600

TABLE 4.1: The MKE (cm^2/s^2) local maxima according to the compared velocities and the observations of Gerin et al. (2009) in the year 2006, the summer-autumn, and the winter-spring.

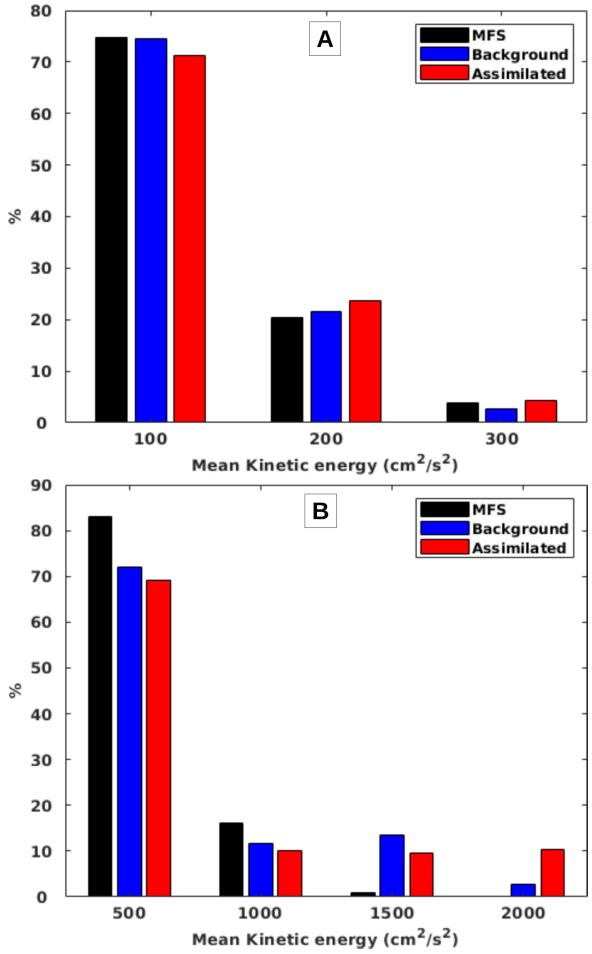

FIGURE 4.7: MKE binning for the corrected (by assimilation), background, and MFS velocity fields for the winter-spring (upper panel) and the summer-autumn (lower panel).

4.2.1.3 Relative vorticity

Starting from the 24^{th} of April and until 20^{th} of August 2006, two drifters were trapped in the Ierapetra eddy (IE) (Argo number: 59748, 59751), flowing in continuous circular trajectories. After assimilation, the resulting corrected velocities around the drifters' paths differed from the background even when averaging on for three months (see fig. 4.9).

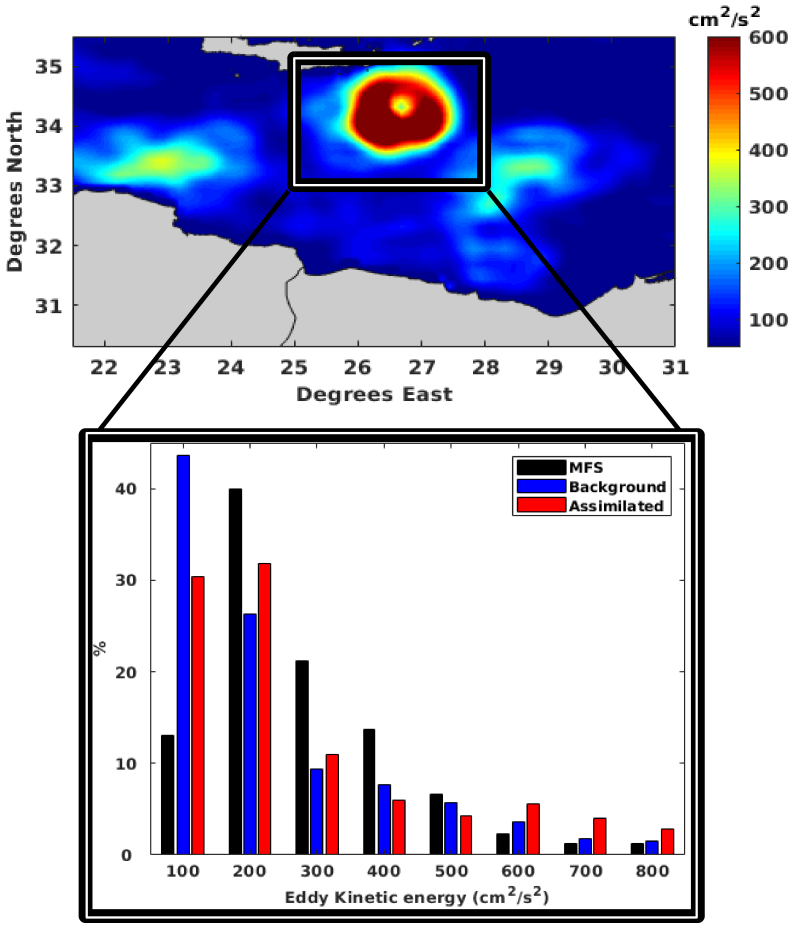

FIGURE 4.8: The area of Ierapetra eddy location (upper panel) overlayed on EKE derived from the corrected velocities. Bin values of EKE are plotted in histograms (lower panel) for the three experimented velocity fields (corrected, background and MFS).

Fig. 4.10 shows the resulting average relative vorticity (ζ) of the background (A), the corrected (B), and MFS (C) in the IE area. The corrected and background velocities revealed a clear anticyclonic feature with negative ζ. Oppositely, MFS showed a weak and spatially limited structure.

To better analyze the temporal evolution of IE, a Hovmöller diagram was shown in fig. 4.11, representing the temporal evolution of ζ after assimilation, compared to the background. The reference position (latitude 26.47° N longitude 34.07° E) of the Hovmöllers was identified from fig. 4.10, referring to the area of the lowest ζ values. Both Hovmöllers showed an active anticyclonic eddy from late April until the end of October, although some periods of weakening at the end of June. IE intensification started from the half of July until the end of October. To quantify this intensification, the local minima of ζ in each day was computed for the corrected velocities and compared to the

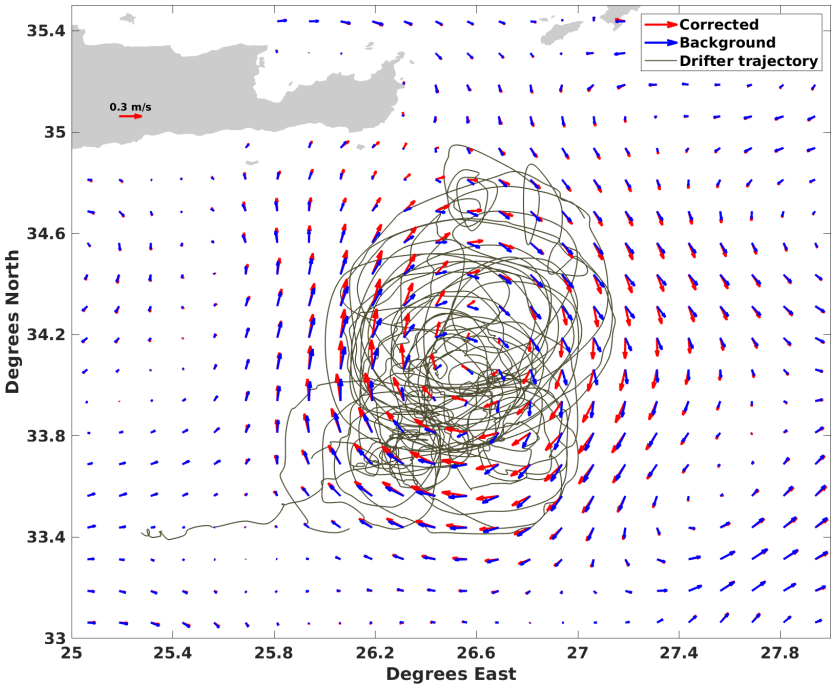

FIGURE 4.9: Average velocity field resulting from the background (blue) and the assimilation (red) in the Ierapetra eddy area between the 24^{th} of April and the 20^{th} of August 2006. The drifters' trajectories (Argo number: 59748, 59751) used in the assimilation are represented by the grey lines.

background (see fig. 4.12). At the start, IE had a local minimum of $\sim$ -3×$10^{-5}s^{-1}$ in both velocities. The difference was noticed starting from May, where after assimilation ζ fluctuated around -4×$10^{-5}s^{-1}$ while it varied around -3×$10^{-5}s^{-1}$ for the background. On the 17^{th} of July, ζ computed from the corrected velocities reached record values exceeding -7.5×$10^{-5}s^{-1}$ for around one month, from half July until half of August. This intensification was not observed for ζ computed from the background, where the lowest value reached was -4.3×$10^{-5}s^{-1}$, meaning that the assimilation almost doubled ζ. According to Ioannou et al. (2017), Coriolis is a standard threshold where ζ rarely reaches values lower than f. In a total of 22 years, ζ exceeded this threshold only three times, in 1995, 1999, and 2004. Fig. 4.12 shows that it was also exceeded at the end of July until the start of August. Thus the absolute vorticity η of IE changes from positive to negative when $|\zeta| > f$. A geostrophic current is symmetrically unstable when its absolute vorticity takes the opposite sign of the Coriolis parameter (where f is positive in the Northern Hemisphere) (Stone, 1966; Thomas et al., 2013). Consequently, such intensification of the vortex rotation could cause some symmetric instabilities, which could induce small scale and three-dimensional perturbations of IE borders (Kloosterziel and Van Heijst, 1991; Lazar et al., 2013; Teinturier et al., 2010).

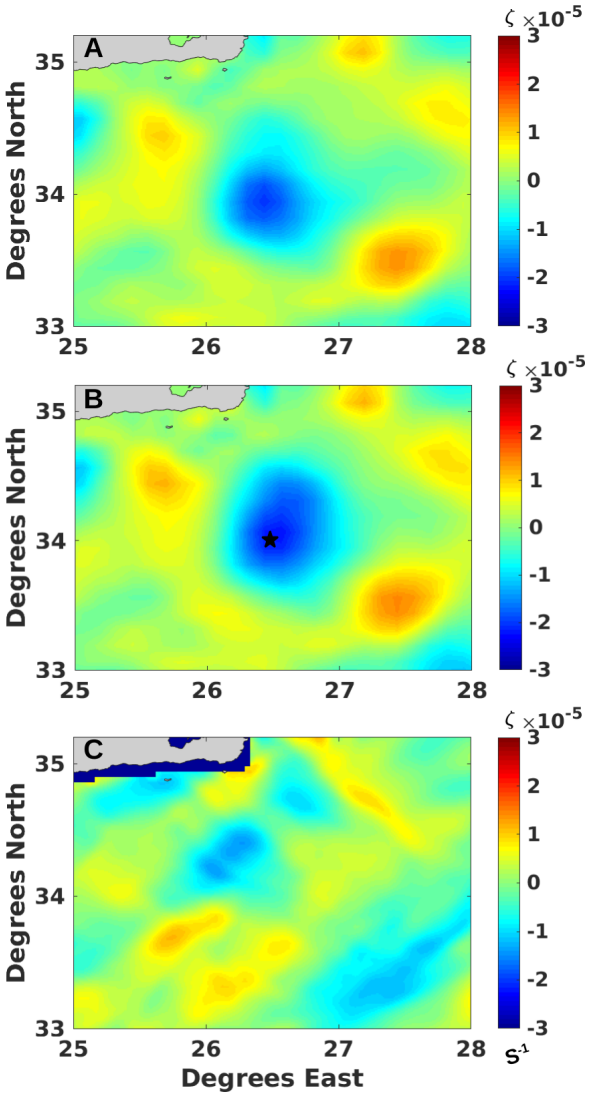

FIGURE 4.10: Relative vorticity (ζ) in the Ierapetra area obtained from the background (A) and corrected velocities (B) and MFS (C). The dark star in B represents the reference position of the Hovmöller diagram.

Ioannou et al. (2017) mentioned that the comparisons with in-situ observations showed an underestimation of the IE maximal velocity amplitude. Thus its real core vorticity is more intense. Our results confirm this underestimation of IE by altimetry, especially during the summer. Consequently, according to the corrected velocities, IE is more intense, and the -f threshold is more frequently exceeded by its real core vorticity.

Our previous results showed the temporal evolution of IE core, but it did not highlight its position evolution. In fig. 4.13, we tracked IE core by showing the daily lowest ζ position, starting from 16^{th} (start of intensification) until 27^{th} of July. Eddy core positions resulting from the background and assimilation are overlaid on the daily average velocity field. On the 16^{th} of July, there was no difference between the compared core positions

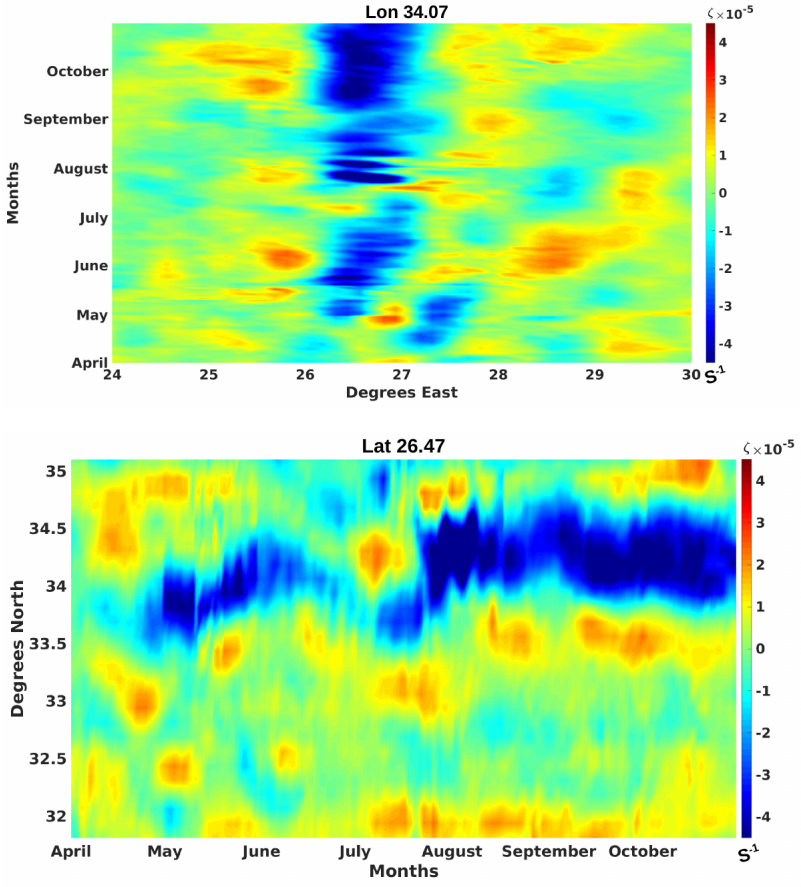

FIGURE 4.11: Hovmöller diagram of the relative vorticity (ζ) obtained from the corrected velocities along latitude 34.07° N (A), and longitude 26.47° (E) between the 1^{st} of April and until late October.

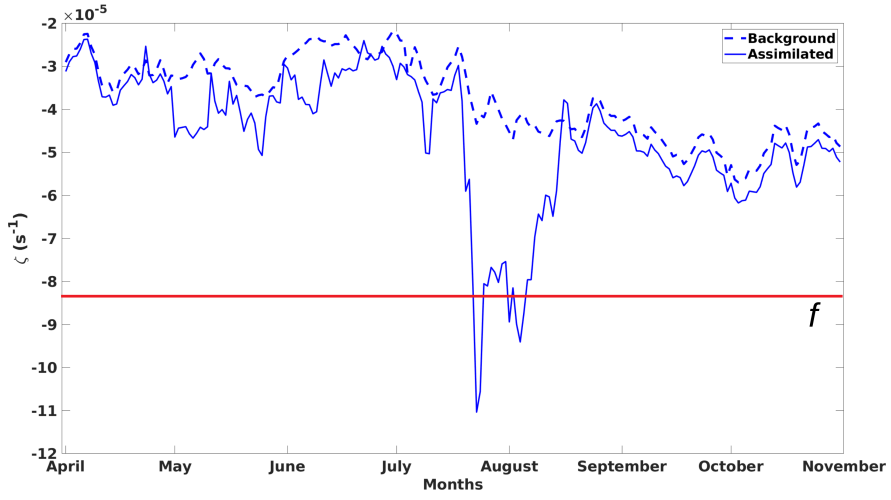

FIGURE 4.12: Temporal variation of the relative vorticity local minima in Ierapetra eddy computed from the background (dashed) and corrected (thick) velocity fields. The red line represents the threshold standard (-f) which is equal to the Coriolis force.

(longitude $\sim$ 26.1° E-latitude 33.8° N). But on the 19^{th}, the assimilation showed the formation of a new high vorticity zone off the Cretan east coasts. Thus on this date,

the location of the local minimum ζ has changed after assimilation further towards the northeast (longitude $\sim 27°$ E -latitude 34.6° N). Afterward, the newly formed eddy continued its intensification with a southwestward drift until merging with the previously existing eddy starting from the 25^{th} of July. Thus the intensification with values exceeding -7.5×$10^{-5}s^{-1}$, detected by the assimilation in fig. 4.12 corresponded to a newly formed eddy that drifted and merged with the previously existing one.

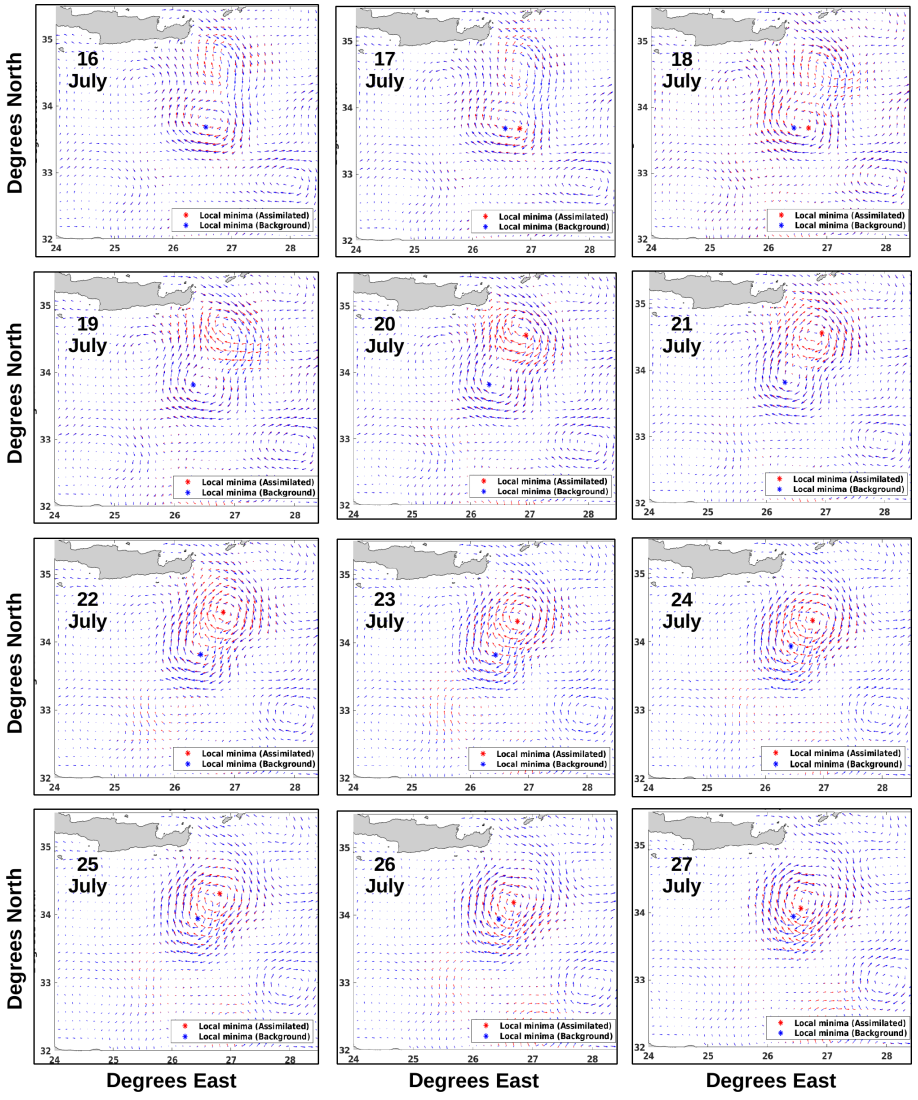

FIGURE 4.13: Eddy core represented by ζ local minima, tracked in the Ierapetra eddy area between 16^{th} and until 27^{th} of July 2006. The red (blue) star represents the local minima obtained from the assimilated (background) velocity field.

The apparition and merging phenomena showed by the assimilation were further investigated by comparing with contemporary chlorophyll images(see fig. 4.14). On the 16^{th} July, the daily chlorophyll image showed a big eddy (denoted E1) and a smaller one located more to the north, close to the Cretan coast (E2). These observations were

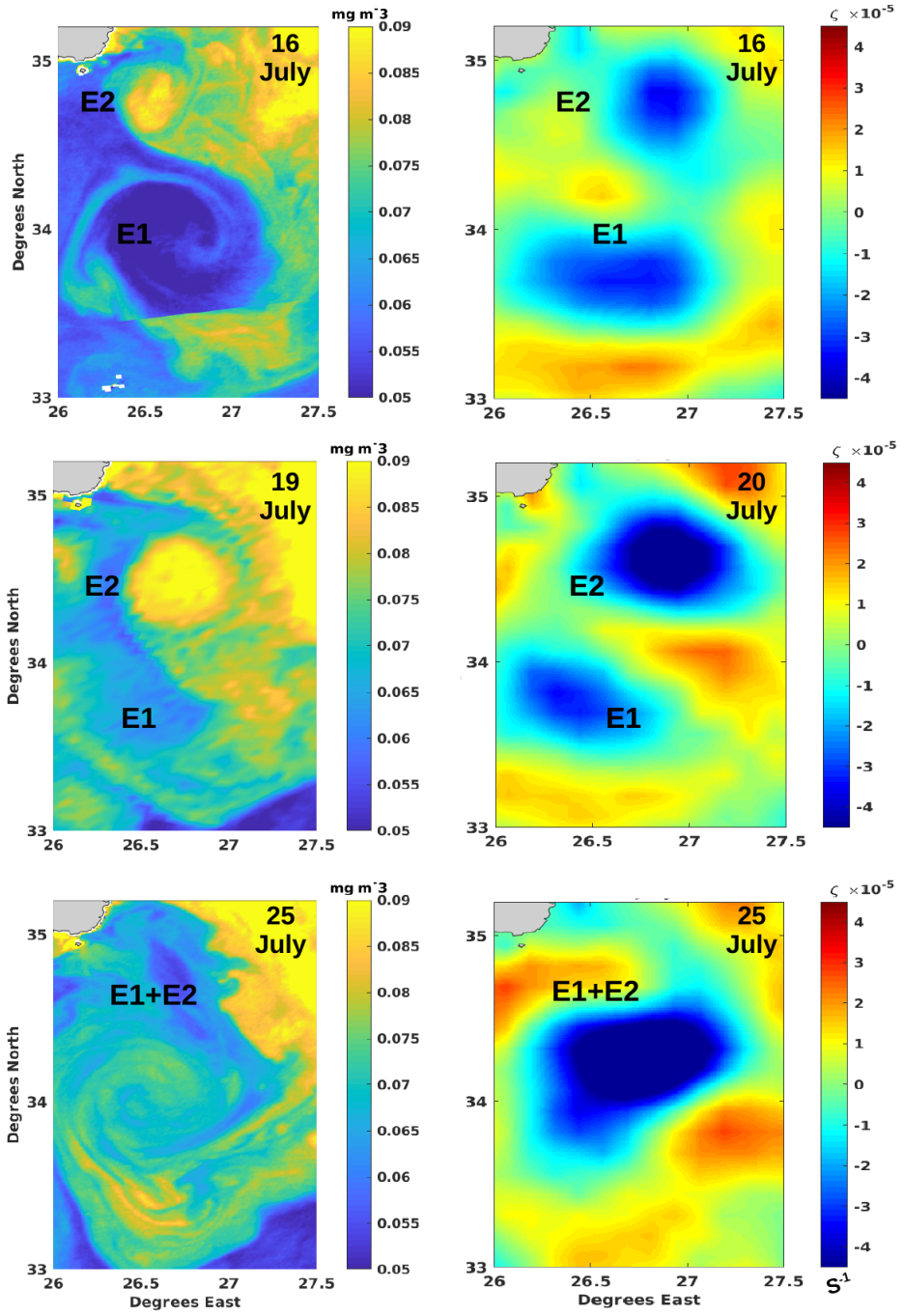

FIGURE 4.14: Daily average relative vorticity (ζ) of the corrected velocities (right) compared with contemporary ocean color chlorophyll images (left). E1 represents the old eddy, while E2 represents the eddy that appeared after 16^{th} of July 2006.

compatible with the daily average ζ, showing two similar eddies in terms of shape and position. On the 19^{th} of July, the chlorophyll image showed that E1 was stable, while E2 extended and drifted toward the south, similarly to the observations of ζ. Afterward, the merging between the two eddies was also observed by the chlorophyll image of the 25^{th} July, showing one spatially extended eddy. Thus, we proved that the corrected

velocities, in agreement with chlorophyll observations, were capable of precisely tracking the newly formed eddy and its merging with the previously existing one causing an increase of its vorticity to values exceeding the standard threshold -*f*.

The corrected velocities allowed us to accurately analyze the mesoscale activity in a highly evolving area in the Southeast of Crete, where the Ierapetra eddy is present. In this area, intense vortices that cold be smoothed or missed by altimetry can appear and then drift and merge with other eddies in a short time scale. Consequently, this particular mesoscale activity increases the dominance of the Ierapetra eddy in the Western Mediterranean, and therefore, its MKE can reach record values exceeding 2000 cm^2/s^2.

4.2.2 Libyo-Egyptian eddy

4.2.2.1 Mean Kinetic Energy

Starting from the 1^{st} of April (denoted as D_0) and until 31^{st} August 2006 (denoted as D_{end}), three drifters were stuck in a high vorticity area off the Libyo-Egyptian coasts (Argo numbers: 59777, 59774, 57312). In fig. 4.15, drifters trajectories during this period were overlaid on the average velocity field before (blue) and after assimilation (red). It could be noticed that in addition to the circular trajectories, the drifters moved zonally (from $\sim 21°$ to $23°$ E) during these five months. The MKE resulting from the corrected and the background velocities were compared to the geostrophic current derived from MFS. In fig. 4.16, the upper panel represents MKE values over all the year 2006, while the lower panel represents MKE during the days of the experiment (from D_0 to D_{end}). The MKE of 2006 shows that only the MFS-derived geostrophic velocities had values exceeding 300 cm^2/s^2, compared to a maximum of 207 cm^2/s^2 for the background and 199 cm^2/s^2 for the corrected velocity field. During the days of the experiment, the density of bins with values exceeding 50 cm^2/s^2 increased after assimilation. For the MFS, around 80% of the bins were 50 cm^2/s^2 or less, while it decreased to less than 60% after correction. The impact of the assimilation was mainly seen by the amplification of bins number with values ≥ 250 cm^2/s^2. The maximum value was recorded by MFS with 379, compared to 316 and 286 cm^2/s^2 for the assimilated and background velocities, respectively.

For all the three velocity fields, the MKE was higher during the period of the eddy activity. However, the assimilation increased the MKE where the density of bins with values $\geq 50\ cm^2/s^2$ increased compared to the background. On the other hand, MFS recorded the highest maxima during all year and the experiment days.

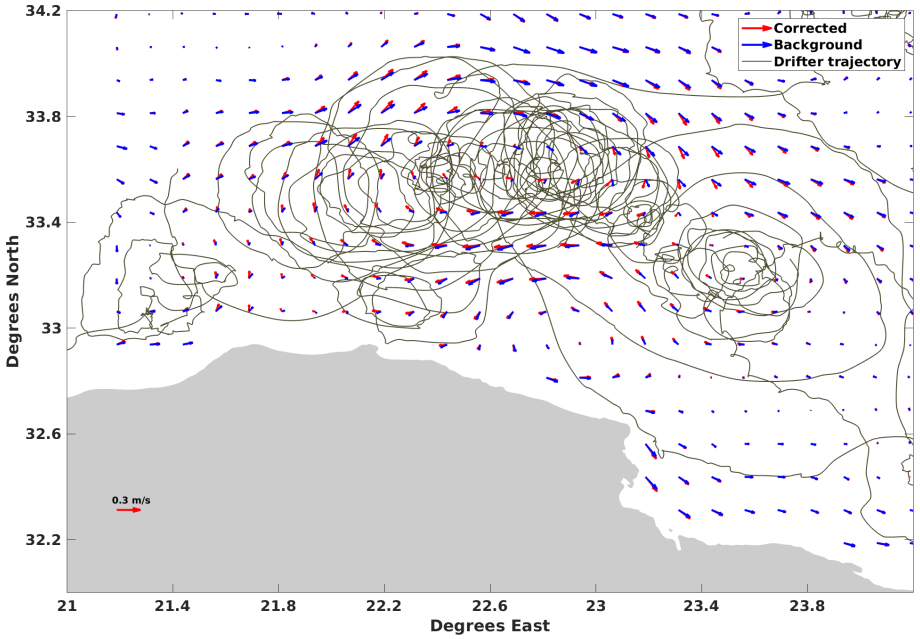

FIGURE 4.15: The three drifters trajectories that were stuck in the coastal eddy off the Libyan coasts. They are overlaid on the average velocity fields from D_0 until D_{end} for the background and assimilation.

4.2.2.2 Eddy Kinetic Energy

Fig. 4.17 shows the EKE over the year 2006 (upper panel) and during the assimilation period (lower panel) off the Libyo-Egyptian coast. For both cases, MFS and assimilation show the highest EKE values.

During the year 2006, the number of bins with values more than 250 cm^2/s^2 was less than $\sim$ 7 % for the background, compared to $\sim$ 24 % after assimilation and $\sim$ 38 % for the MFS (upper panel). The same tendencies were also seen during the experiment days (lower panel), where only $\sim$ 6 % of the bins had values of 300 cm^2/s^2. The number increased to $\sim$ 20 % for the assimilated and $\sim$ 26 % for the MFS. The MFS showed the highest EKE values with 451 cm^2/s^2, followed by the assimilation of 374 cm^2/s^2, while the background only registered 248 cm^2/s^2. During the experiment days, the corrected velocities recorded the highest values with 570 cm^2/s^2, compared to 505 cm^2/s^2 for MFS and 299 cm^2/s^2 for the background.

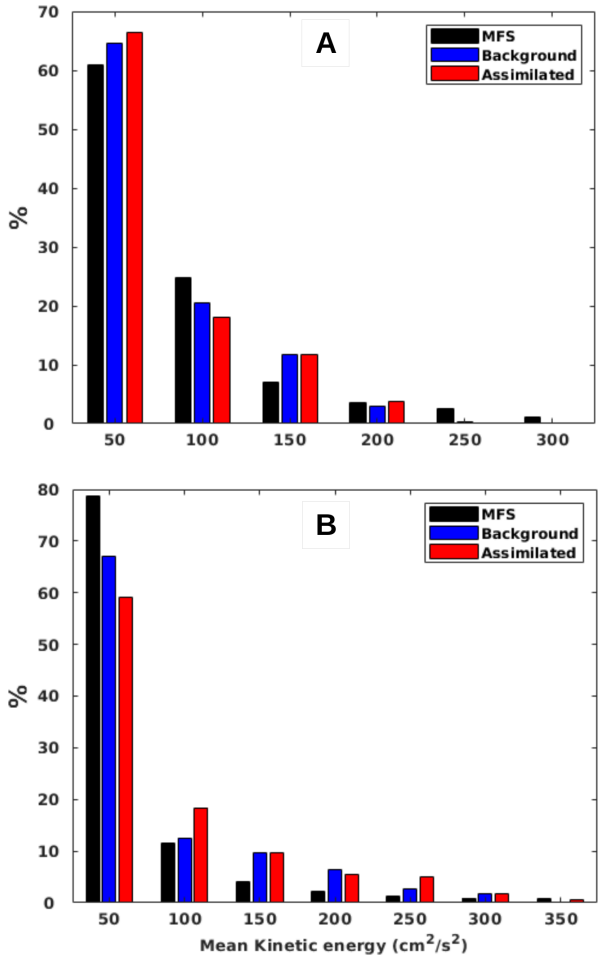

FIGURE 4.16: Histogram of the MKE for the bins off the Libyan coasts (from 22° to 24.1° E, and from 32° to 34° N) resulting from the average velocity field for all the year (upper panel), and from D_0 until D_{end} (lower panel).

EKE was higher off the Libyo-Egyptian coasts, with values reaching 505 cm^2/s^2 for the corrected velocities. It exceeded the MKE during all the year and the assimilation period with a maximum of 286 cm^2/s^2 and 316 cm^2/s^2, respectively. This relative dominance of EKE, contrary to IE, means that the Libyo-Egyptian coasts are a highly variable area, where the mesoscale features are weaker and more unstable compared to IE.

4.2.2.3 Relative vorticity

Fig. 4.18 shows the monthly average variation of ζ in the Libyo-Egyptian coasts during between April and August based on the corrected (left), background (middle), and MFS (right) velocities. The background and corrected velocity fields showed a clear anticyclonic eddy, although it was more intense and extended after correction. Oppositely, the MFS was not able to detect any coherent eddy structure.

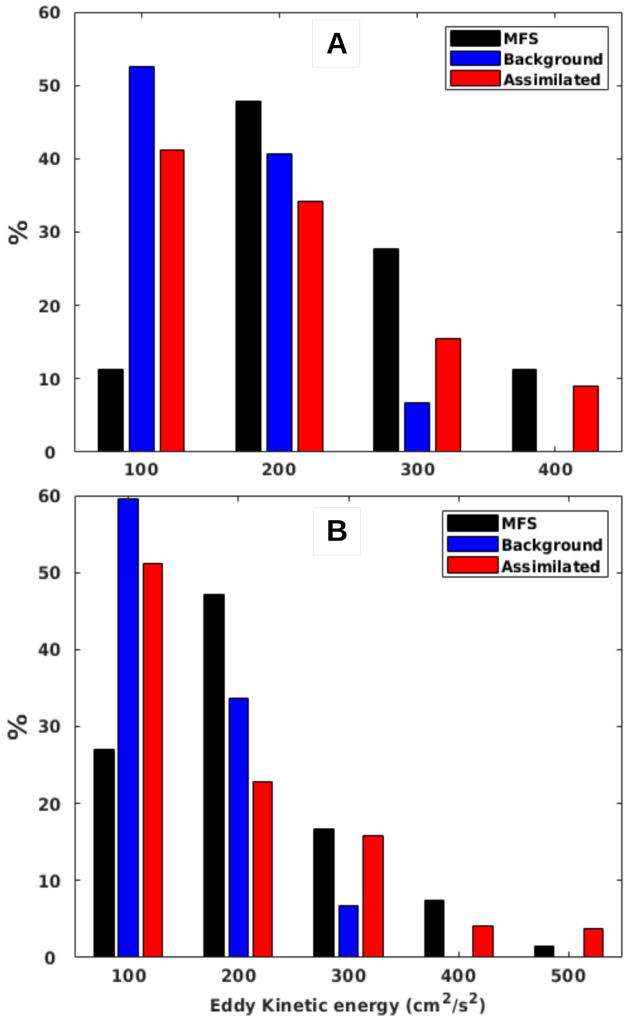

FIGURE 4.17: Histogram of the EKE for the bins off the Libyan coasts (from 22° to 24.1° E, and from 32° to 34° N) resulting from the average velocity field for all the year (upper panel), and from D_0 until D_{end} (lower panel).

To quantify the difference of ζ before and after correction, we tracked the temporal evolution of the eddy core vorticity. Fig. 4.19 (lower panel) shows that the values of ζ after assimilation exceeded those of the background. ζ of the background showed that the eddy core vorticity was fluctuating around -2.5×$10^{-5}s^{-1}$. The assimilation showed similar values at the start before progressively increasing to values exceeding -4×$10^{-5}s^{-1}$ at some periods at the end of May and the start of June. Afterward, ζ decreased progressively, reaching values close to the background at the end of the experiment.

In fig. 4.19 (upper panel), the track of the variation of the eddy core position with time (upper panel) showed a clear westward flow with a short phase of northward flow off the Libyan coast, around 23 °E. These results show that LEE appeared as a coherent

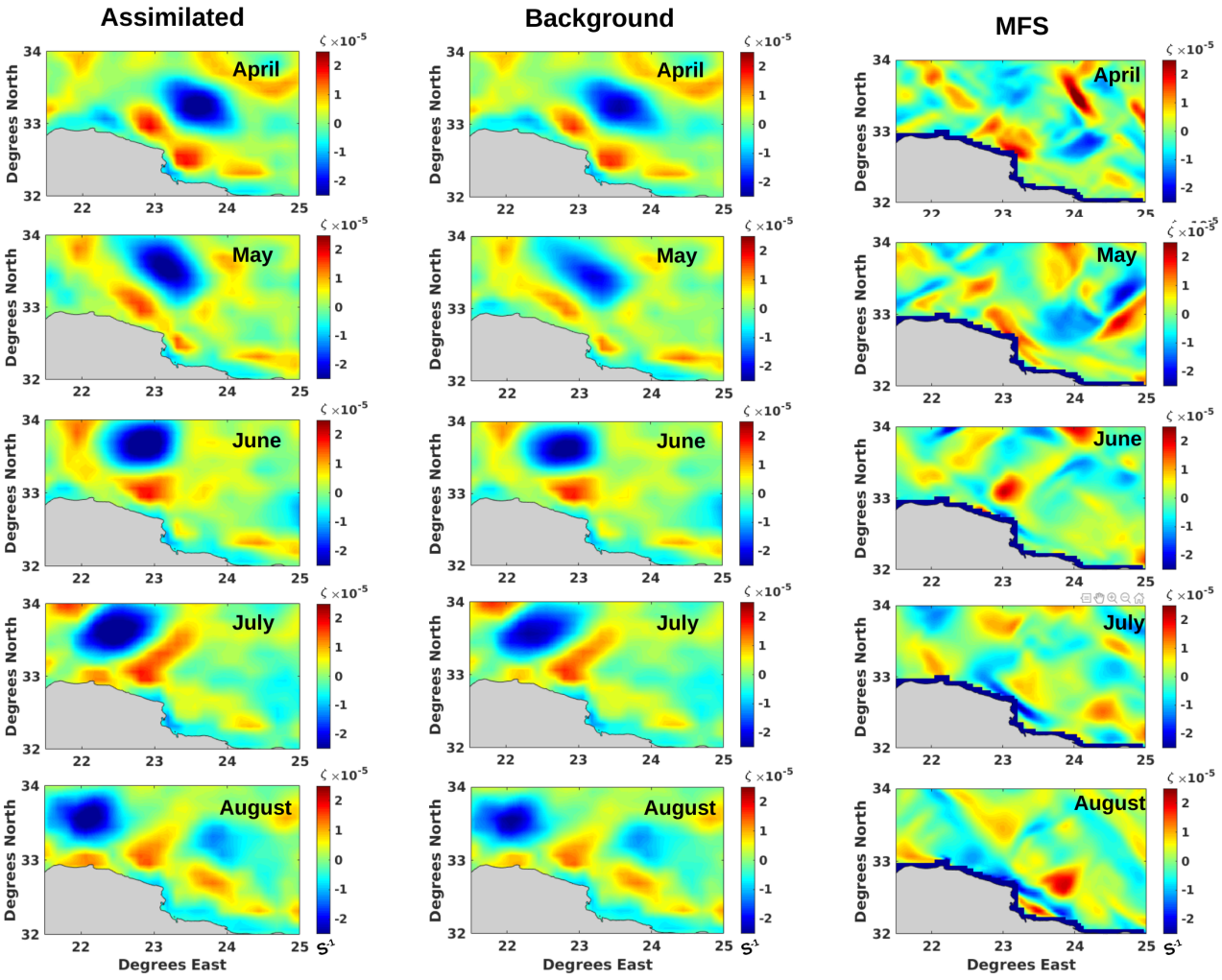

FIGURE 4.18: The monthly average variation of ζ from April until August, based on the assimilated (left), background (middle) and MFS (right) velocities.

structure, flowing towards the west, in an opposite direction of the along-slope eastward circulation. The corrected velocities showed an instant eddy intensification starting from May when the eddies drifted northward. According to Sutyrin et al. (2009), the shallow bathymetry guides the eddy drift, and its center kept a constant distance of 55-65 km from the 200 m bathymetry. Indeed, the deep flow is shifted offshore when the bathymetry changes from the steep continental slope to a gentle continental rise and interacts with the upper layer to provide an additional along-slope vortex drift proportional to the basic drift speed and the steepness. Accordingly, the eddy drift to the west was faster than the β effect, with a mean speed of 1-2 km. Although this abnormal coastal eddies westward drift was observed twice in 2006, no other drifters were available in other years for assimilation (Taupier-Letage, 2008).

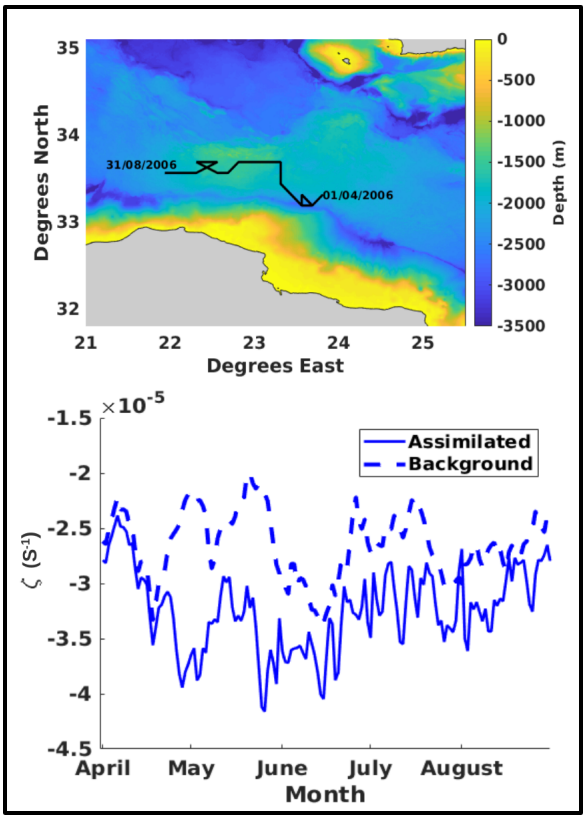

FIGURE 4.19: The lower panel represents the temporal variation of the eddy core intensity before (dashed) and after (thick) assimilation. The upper panel shows the trajectory of the eddy by following the core position evolution with time between D_0 and D_{end}.

4.3 Summary of results

In this chapter, we assimilated the full data set of the drifters deployed in the Western Levantine during the EGYPT/EGITTO campaign to obtain a corrected velocity field in 2006. Then we characterized the two most dominant features in this area; the Ierapetra eddy (IE) and the Libyo-Egyptian eddies (LEE). Because of their high mesoscale activity, they trapped drifters for several weeks. Although IE was a spatially extended structure, we proved that our method is an efficient tool that improves the velocity field of the IE. The assimilation method extends the correction impact for 30 km around drifters trajectories, which helps in better representing the velocities in all the areas around the assimilated drifter, including the maximal velocity contours (V_{max}). This approach is more efficient than observing IE using only drifters' observations. The corrected velocity field showed that the dominance of IE with MKE exceeding 2000 cm^2/s^2, especially in the summer, is enhanced by the fast eddy apparition in the IE area, followed by the merging of the newly formed eddy with the old IE, which drastically increases IE

vorticity. Although those events are potentially more frequent, the limited drifters' deployment did not allow correcting the velocities of IE in other years. Further to the south, the assimilation showed the LEE was active and drifting at a constant distance from the Libyo-Egyptian shoreline. The complex bathymetry in this area increases instabilities, which allowed the LEE to last for several months while drifting westward in an opposite direction of the coastal current. Overall, the assimilation improved the representation of IE and LEE compared to MFS and the background velocities that could be missing or underestimating these structures.

Chapter 5

Characterization of local events in the Eastern Levantine

In this chapter, the assimilation algorithm was applied to study the mesoscale activity in the Eastern Levantine. More specifically, we targeted the most dominant eddies present in the easternmost part of the basin: the Cyprus eddy (CE), the North Sikmona (NSE), and the South Shikmona (SSE) eddies. The new corrected velocity field is used to characterize these eddies based on the diagnostics of the Mean kinetic energy (MKE), eddy kinetic energy (EKE), and relative vorticity (ζ). These results will also be compared with the background (altimetry only) and the geostrophic current derived from the Mediterranean Forecasting system MFS model (reanalysis).

5.1 Mesoscale activity in 2009

Starting from the 5^{th} of August (noted D_0) and until the end of September 2009 (D_{end}), three drifters were circulating off the southern Lebanese coasts (see fig. 5.1), more specifically in SSE. Drifters' positions were assimilated, and the resulting velocities were compared to those of the background and MFS.

5.1.1 MKE

Fig. 5.2 shows the MKE of the background (A), assimilated (B), and the MFS (C) during the days between D_0 and D_{end}. The coastal current was more intense according to MFS, showing a spatially extended flow from the North of Lebanon until the Cyprus eastern coasts. This flow was also observed by the corrected and the background velocities, but it was weaker. This difference between MFS and the background could be related to the altimetry inaccuracies near the coast. Indeed, the background velocities showed an absence of flow closer to the eastern coast of Cyprus. On the other hand, even if there is a slight increase of the MKE after assimilation, the lack of drifters' observations in this area limited the assimilation impact. All the compared velocities agreed on the presence of an along-slope jet in the southern coasts of the basin, perturbed by the mesoscale activity off the Lebanese coasts. Further to the north, there was the re-apparition of an intense coastal jet, especially off the Turkish coasts, known as the Asia minor current (AMC).

MFS shows no clear SSE presence but only meanders instead. After assimilation, the eddy ring shape was observed, with an eddy core of low intensities surrounded by higher

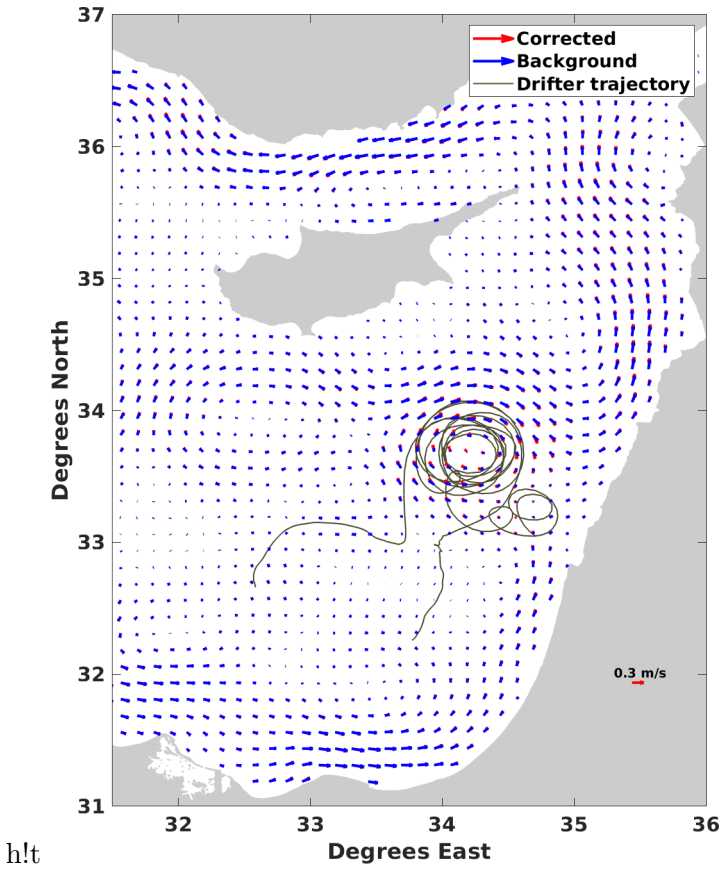

h!t

FIGURE 5.1: Drifters trajectory evolution between 05^{th} August and until 30^{th} September 2009. Positions are overlayed on the averaged velocity field of the assimilated (red) and background (blue) velocity fields.

velocities. To quantify the difference between the compared velocities, we display the MKE value of each bin of SSE as seen in the histogram of fig. 5.3. The assimilation impact was mainly seen by increasing the MKE compared to the background. MFS underestimated MKE where $\sim$ 50 % of the bins had values less than 100 cm^2/s^2. This frequency decreased to $\sim$ 30 % for the background and $\sim$ 24 % for the corrected velocities. MKE with values $\geq$ 300 cm^2/s^2 were almost absent in the MFS and background velocity fields, while it increased to $\sim$ 10 % after assimilation. In terms of local maximum, the highest MKE value was seen after correction with 369 cm^2/s^2, followed by the MFS with 333 cm^2/s^2, and the background (324 cm^2/s^2).

5.1.2 EKE

Fig. 5.4 shows the EKE average of the background (A), assimilated (B), and the MFS (C). MFS showed the highest values in the Latakia Basin. The background and corrected velocities did not reveal high variability in this area. On the other hand, the highest EKE

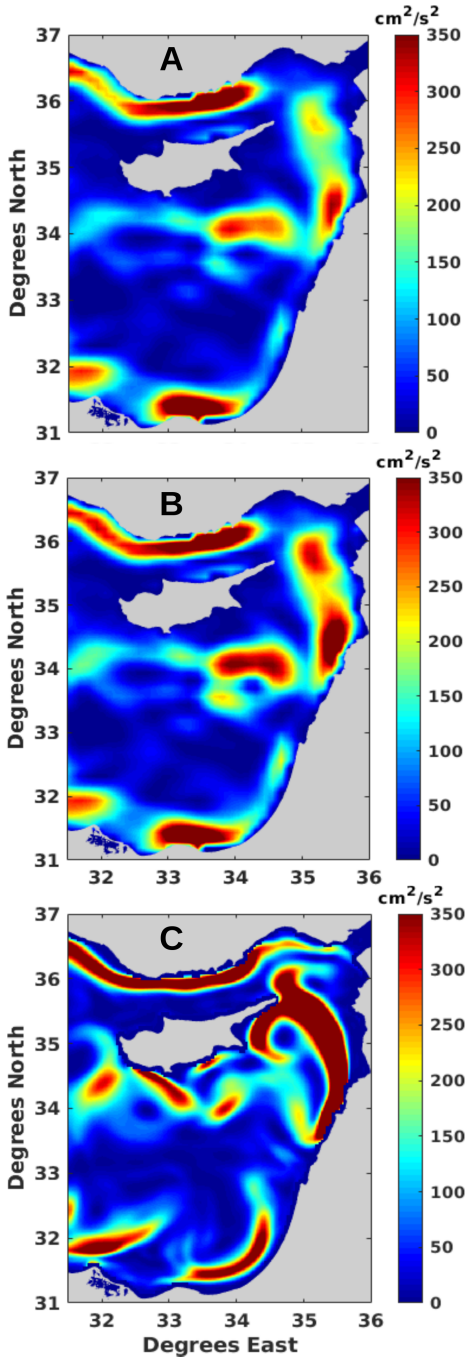

FIGURE 5.2: MKE of the background (A), corrected (B), and MFS (C) velocities for the period of the drifter passage between 05^{th} August until 29^{th} of September 2009.

values in SSE were seen in the corrected velocities. High variations were also observed in MFS but closer to the Lebanese coasts. The higher resolution of MFS showed the variabilities of smaller structures such as filaments and meanders that did not exist or were smoothed in the assimilated and background velocities.

EKE values of SSE are seen in fig. 5.5 (lower panel). Similar to the MKE, the assimilation had the highest variations, where it reduced the frequency of bins with low values and

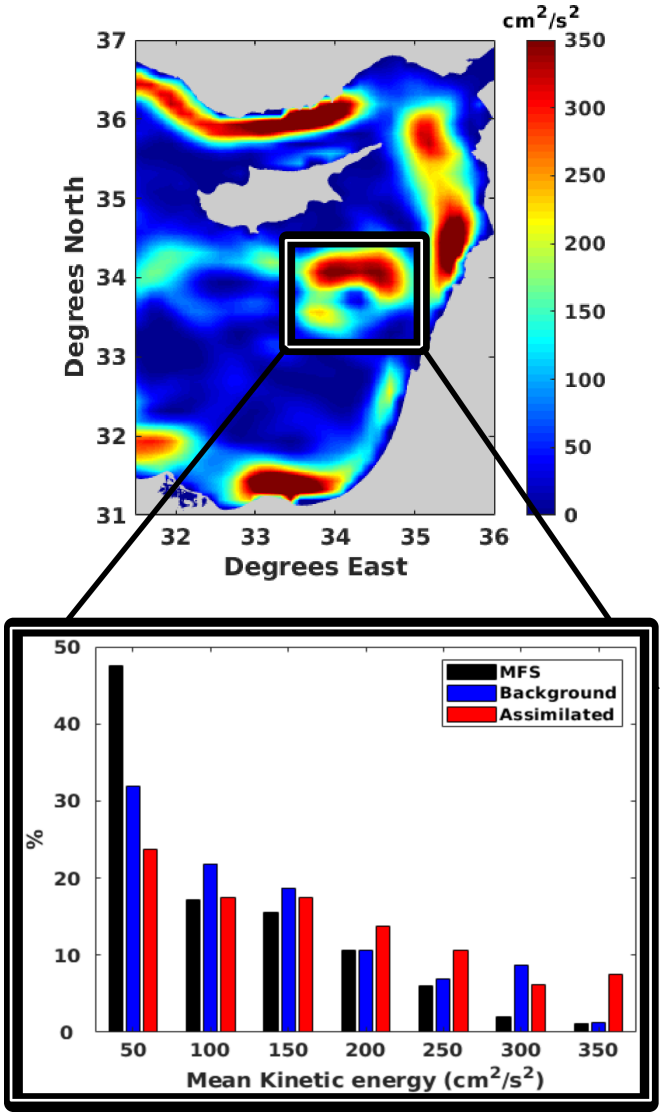

FIGURE 5.3: The area of South Shikmona eddy (SSE) (upper panel) overlayed on MKE derived from corrected velocities. MKE values in each bin are plotted in histograms (lower panel) for the three experimented velocity fields (corrected, background and MFS).

increased those with high values. Moreover, the assimilation increased the maximum from 164 cm^2/s^2 (background) to 232 cm^2/s^2, compared to 206 for the MFS cm^2/s^2

5.1.3 Relative vorticity

The average relative vorticity (ζ) of the background(A), corrected (B), and MFS (C) is presented in fig. 5.6. MFS showed a small anticyclonic with a shift in its position that was closer to the coasts, while the background and corrected velocities showed a

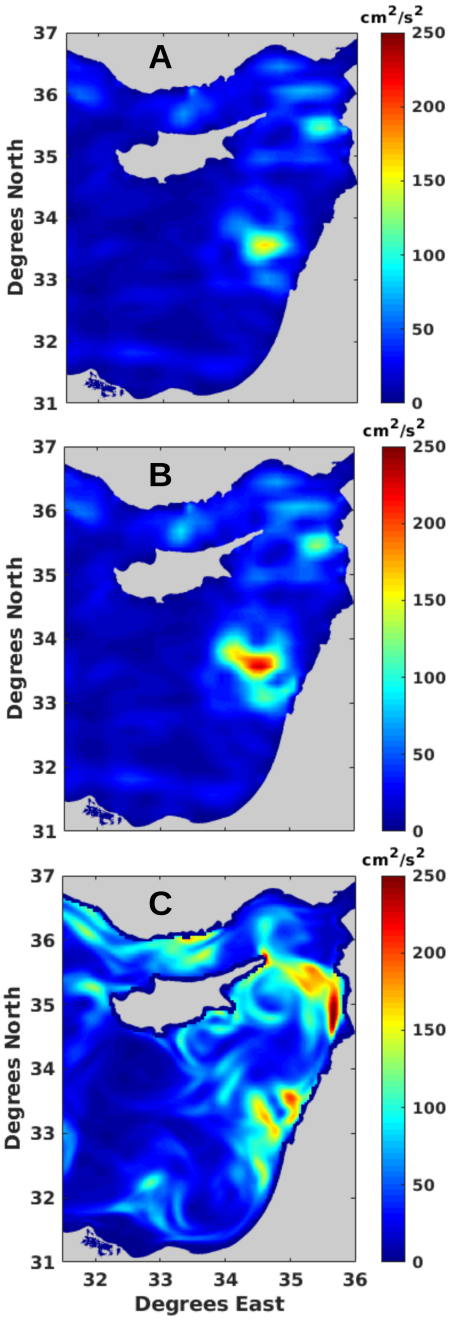

FIGURE 5.4: EKE of the background (A), assimilated (B), and MFS (C) for the period of the drifter passage between 05^{th} August until 29^{th} of September 2009.

larger structure further offshore. Moreover the assimilation increased the intensity of ζ, especially in the eddy core, from $\sim$ -1.4 $\times 10^{-5} s^{-1}$ to $\sim$ -2 $\times 10^{-5} s^{-1}$.

On the 06^{th}, 17^{th}, 22^{nd} and 30^{th} of August 2009, chlorophyll images showing clear SSE pattern were available (see fig. 5.7 (left panel)). These observations were compared with the corresponding daily ζ (right panel), allowing to track the SSE evolution and to evaluate the accuracy of the corrected velocity field. On the 06^{th} of August, ζ showed an

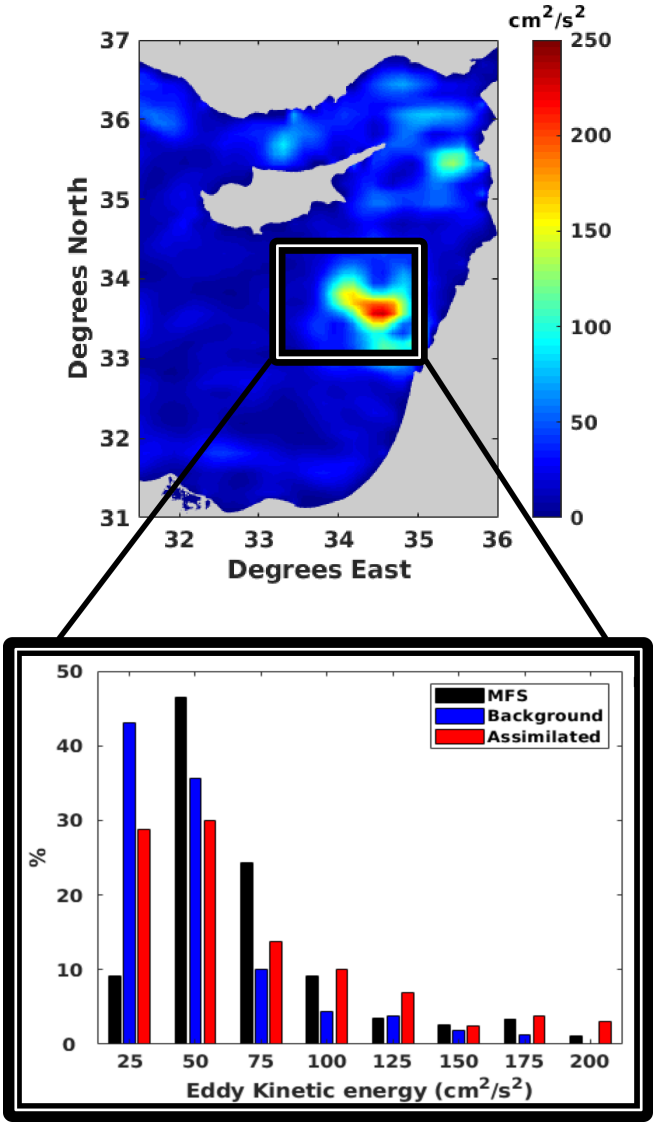

FIGURE 5.5: The area of the Shikmona eddy (upper panel) overlayed on EKE derived from corrected velocities. EKE values in each bin are plotted in histograms (lower panel) for the three experimented velocity fields (corrected, background and MFS).

anticyclonic mesoscale feature (E1) off the Southern Lebanese coasts, with values exceeding -2×$10^{-5}s^{-1}$. Further offshore, there was another anticyclonic eddy (E2), but less developed than E1. After 11 days, more precisely on the 17^{th} of August, the corresponding ζ showed that E1 had drifted offshore towards E2, where a merging between those two eddies occurred. This merging caused the formation of a larger intense mesoscale structure (E1+E2), as seen on the 22^{nd} of August. This anticyclonic eddy continued its intensification where ζ of its core exceeded -3 ×$10^{-5}s^{-1}$. The merging between E1 and E2 was also observed by chlorophyll images showing a coastal eddy, richer in chlorophyll, interacting by a filament with the eddy offshore on the 06^{th} August. Afterward, on the 17^{th} of August, the chlorophyll image showed the formation of a larger feature resulting

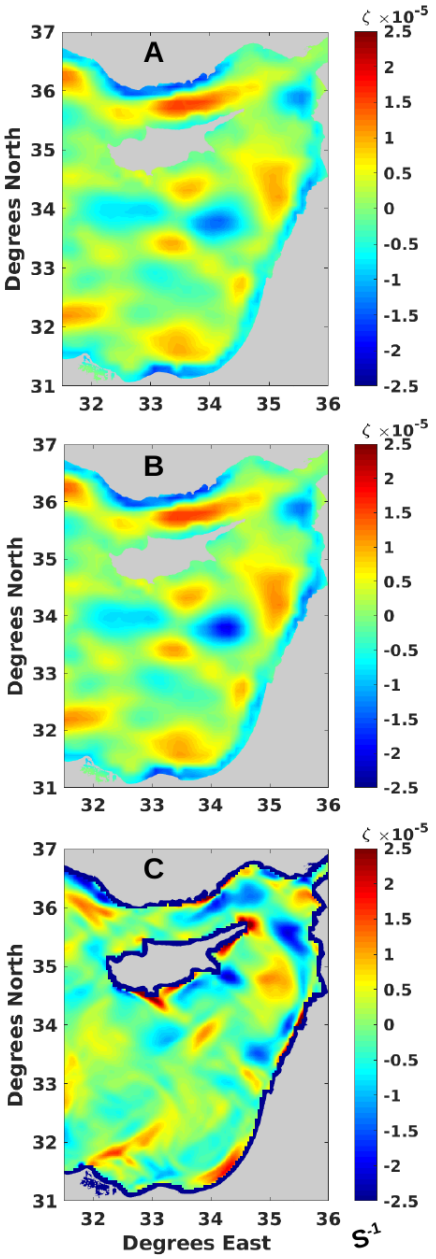

FIGURE 5.6: Average ζ obtained from the background (A), assimilated (B), and MFS (C) velocity fields between the 05^{th} of August and until the 30^{th} September 2009.

from the merging between E2 and E1. The resulting eddy (E1+E2) continued the development and the movement across the basin on the 22^{nd} and 30^{th} of August 2009. The coastal eddy acted as a barrier, trapping the coastal water that was richer in chlorophyll and nutrients. Consequently, the coastal water, richer in chlorophyll flowing along the coast has deviated offshore. The trajectory of SSE, obtained by tracking the eddy center based on the corrected velocities, is presented in fig. 5.8 (upper panel). It shows the pinching-off of SSE from the coast with a westward flow, followed by a merging event and drifting towards the North-West.

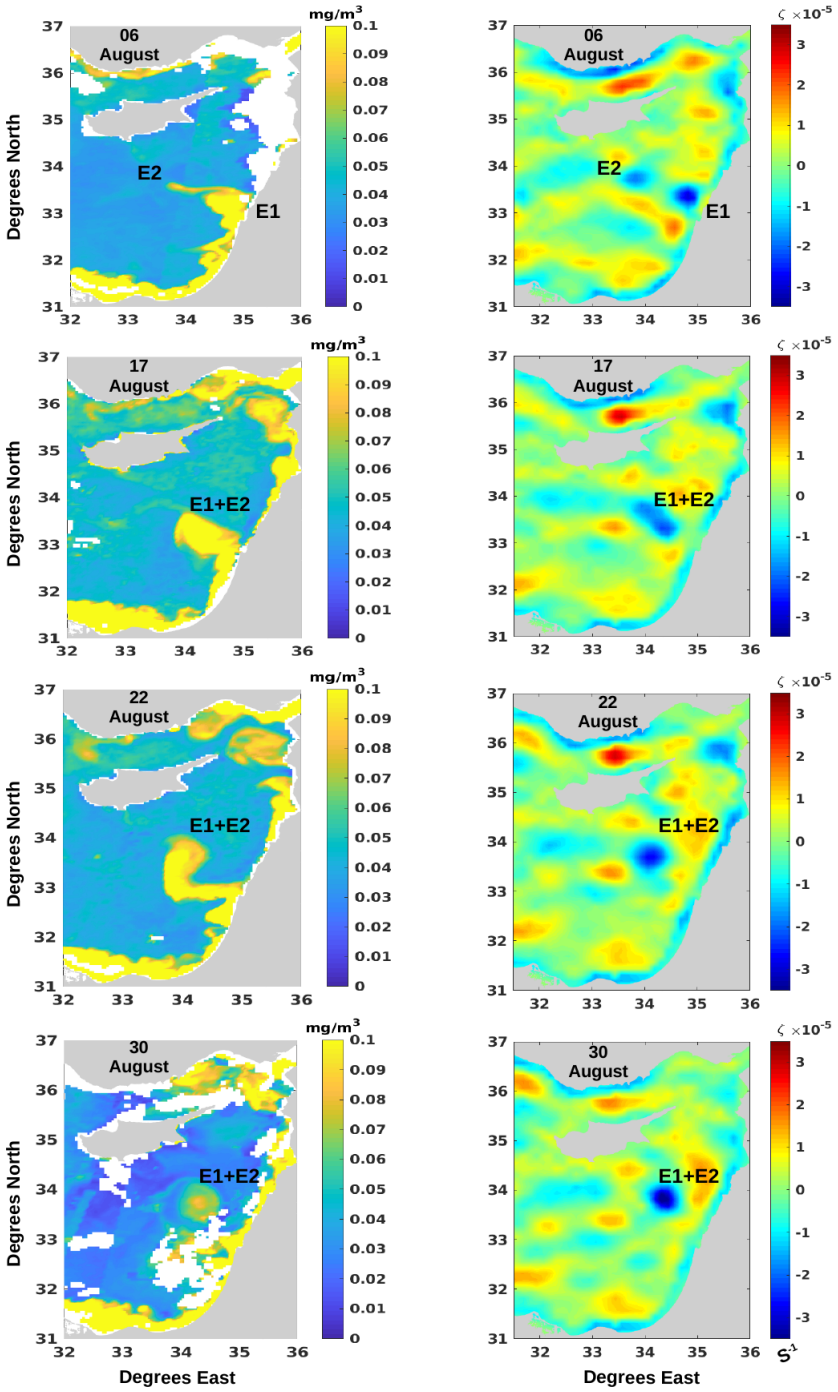

FIGURE 5.7: Daily average ζ variation with time in 06^{th}, 17^{th}, 22^{nd}, and 30^{th} of August 2009 (right side panels). The pinch-off and merging events are compared with contemporary chlorophyll images.

To better quantify the assimilation impact on the representation of SSE activity, we compared the temporal variation of ζ in the E1 core, resulting from the corrected and the background velocities. Fig. 5.8 (lower panel) shows that E1 was stronger after correction during all the assimilation days. The vorticity of E1 was weakening in the first few days, but starting from 16^{th} of August ζ intensified continuously, reaching

values exceeding -4× $10^{-5}s^{-1}$. This intensification, which was underestimated by the background, occurred when E1 started to merge with E2. Accordingly, the assimilation was able to improve SSE representation, especially the merging phase and its impact on increasing SSE intensity.

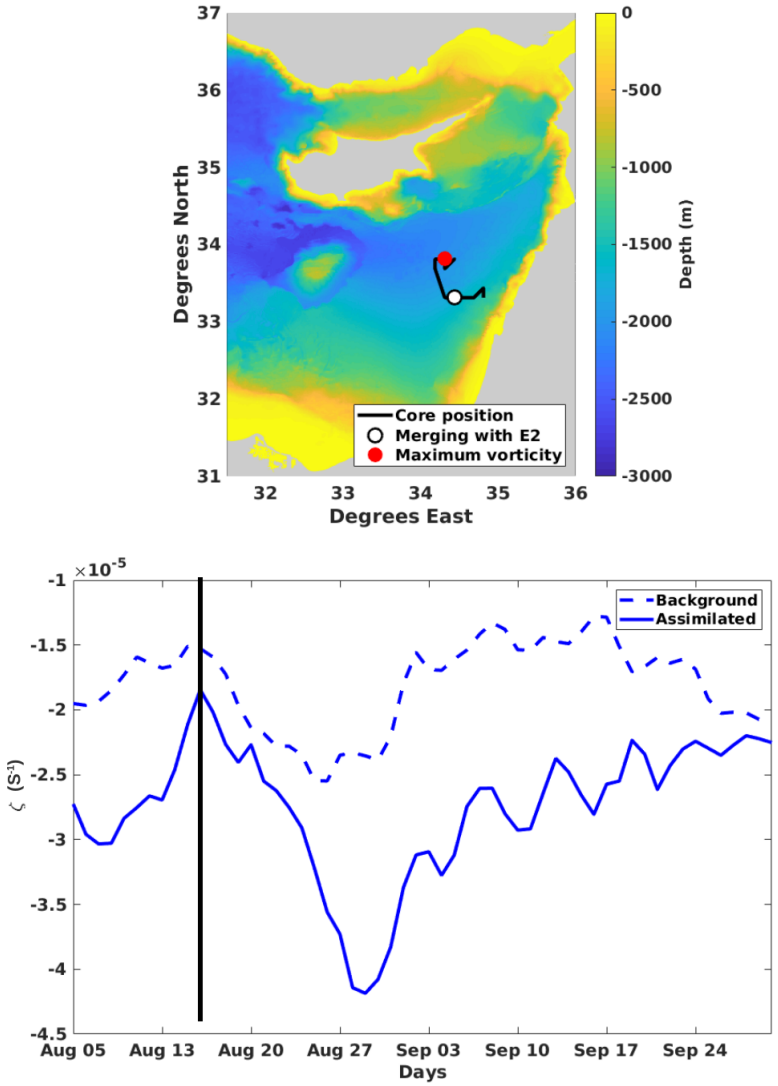

FIGURE 5.8: The upper panel shows the E1 core trajectory after assimilation during these days. The lower panel represents the daily ζ variation of E1 eddy core with time from the 05^{th} of August and until late September 2009, for the background (dashed) and corrected (thick) velocities. The thick dark line represents the merging day with E2.

5.1.4 Historical pinching-off

The coastal SSE blocks and traps the AW along-slope circulation. By pinching off and deviating the coastal water flow offshore, SSE has a direct impact on the coastal water properties. To estimate the frequency of this phenomenon occurring in the south

of Lebanon, we used the DYNED Atlas, a dataset that tracked the intensified eddies in the Meditteranean for 18 years between 2000-2018. Eddies tracking was done using the angular momentum eddy detection and tracking algorithm (AMEDA) (available on https://www1.lmd.polytechnique.fr/dyned/), which is an automated method for eddy detection based on physical parameters and the geometrical properties of the velocity field (Le Vu et al., 2018).

It shows that four pinching-off events occurred in 2000, 2004, 2009, and 2015 (see fig. 5.9). Two of these eddies lasted less than one month (2004 and 2015), while in 2009, SSE lasted more than four months. Three of these events occurred during the summer season, while in 2004, it was observed in winter. In all of these cases, the eddies flowed northward after the pinching off. The maximum of local speed V_{max}, and radius R_{max} variation with time for each eddy is observed in fig. 5.10. SSE_{2009} was the largest and most intense eddy with V_{max} reaching a maximum more than 0.33 m/s and R_{max} exceeding 35 km during most days of its lifetime. The sharp increase of V_{max} occurred when R_{max} increased due to the eddy merging with another one on 17^{th} of August 2009. The second most intense eddy was SSE_{2015} with a maximum $R_{max} \sim 35$ km and V_{max} of 0.2 m/s. SSE_{2000} and SSE_{2004} were the less developed with lifetime that did not exceed three weeks and a maximum of V_{max} around 0.1 m/s while the size of SSE_{2000} was larger with R_{max} reaching ~ 25 km compared to ~ 15 km for the SSE_{2004}.

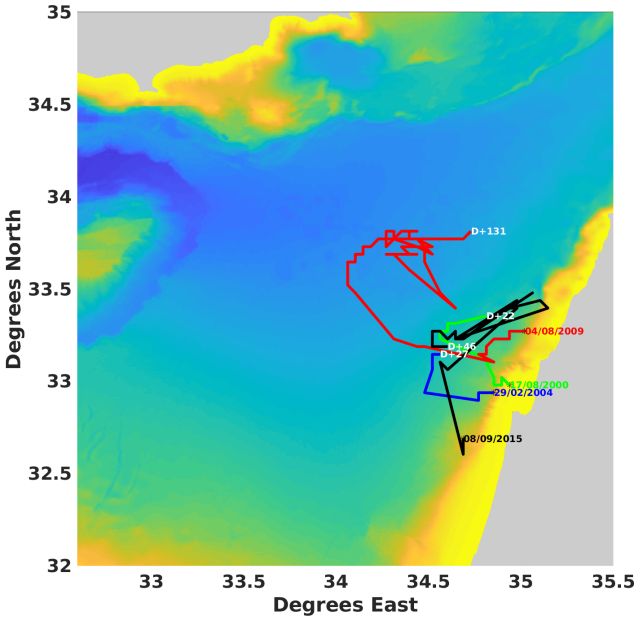

FIGURE 5.9: Trajectory and lifetime of the four eddies that were detected pinching-off from the Southern Lebanese coast between 2000 and 2018, according to the DYNED-Atlas.

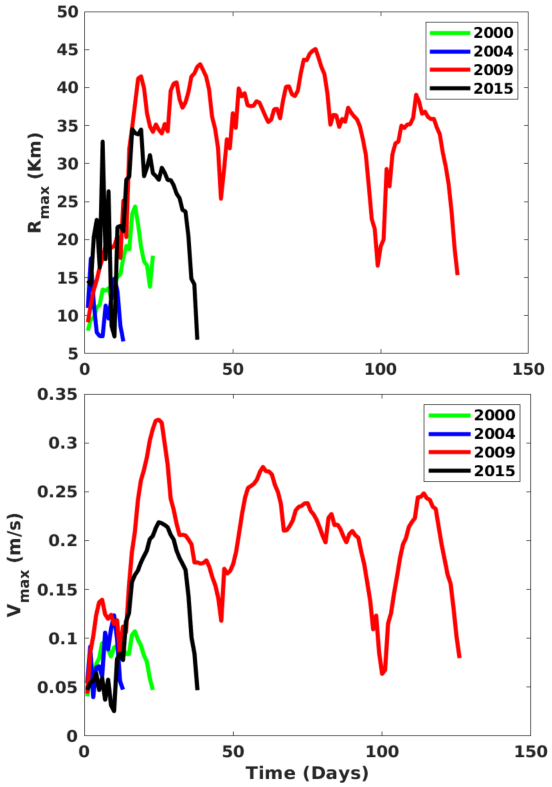

FIGURE 5.10: The V_{max} and R_{max} variations of the four eddies pinching-off from Southern Lebanese coast between 2000 and 2018, according to the DYNED-Atlas.

Overall, the assimilation was able to show the pinching-off then the merging events that caused the intensification of SSE, a highly evolving eddy that plays a significant role in perturbing the coastal currents by deviating the coastal flow towards the shore. However, although its impact, the Ameda data set shows that this pinching off remains rare, observed only 4 times in 18 years.

5.2 Mesoscale activity in 2017

Starting from the 1^{st} of March (denoted as D_0) and until 30^{th} of October 2017 (denoted as D_{end}), a total of six drifters were circulating and forming a ring-shape in two areas: The Cyprus eddy (CE) area (between 32°-34° E and 33°-34.2° N) and the North Shikmona eddy (NSE) (between 34.2°-35.7° E and 34°-35° N).

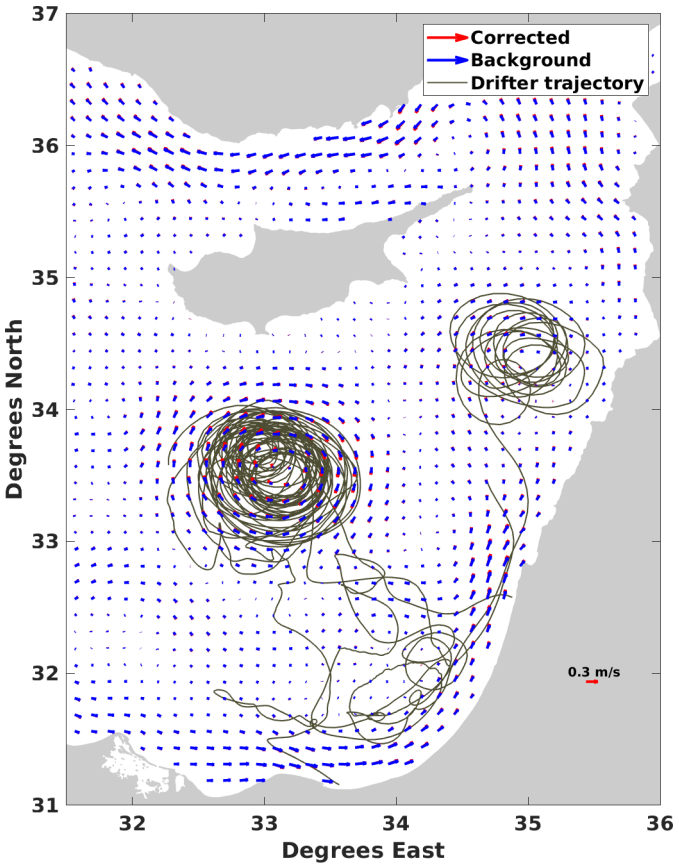

FIGURE 5.11: Trajectories of the drifters mainly circulating in the North Shikmona and Cyprus eddy area between 1^{st} March and until the 26^{th} of October 2017. They are overlaid on the average velocity fields of the background (blue) and assimilation (red).

5.2.1 MKE

In fig. 5.11, drifters' positions are overlaid on the average velocity field between D_0 and D_{end}. The background and the corrected velocities showed differences in NSE and CE. The MKE, resulting from these velocities, is compared with the MFS in fig. 5.12. The assimilation impact was seen especially in the CE, where after correction, the borders of the eddy had a more intense flow that was more similar to those observed by MFS. Oppositely, the MKE of the three velocities did not detect NSE.

A relatively strong coastal jet was observed in the southeasternmost part of the Levantine. However, MFS revealed weaker currents, where the maximum MKE value did not exceed 250 cm^2/s^2, compared to values exceeding 350 cm^2/s^2 in the background and corrected velocities. The coastal jet weakened near the Lebanese coasts, where all the velocities showed that MKE decreased to less than 100 cm^2/s^2. This weakening observed in all the velocities could be related to the presence of the mesoscale eddies in this area, especially the NSE occurring closer to the shore that perturbs and interacts with the coastal flow.

The frequency distribution of the MKE values in CE and NSE bins is seen in fig. 5.13. The lower panel represents the MKE values distribution in CE according to the three compared velocities (assimilated, background, and MFS). The assimilation increased the MKE compared to the background. The frequency of bins with values less than 250 cm^2/s^2 was reduced from $\sim$ 96 % to $\sim$ 75 %, while values exceeding 250 cm^2/s^2 increased from $\sim$ 4 % to $\sim$ 25 %. The MKE distribution of the MFS was more similar to the assimilation than the background, although values exceeding 250 cm^2/s^2 were less frequent. The maximum of MKE was registered by the assimilation with 324 cm^2/s^2, followed by the (MFS 308 cm^2/s^2), and the background (227 cm^2/s^2). In the NSE, more than 95% of all the bins had values lower than 150 cm^2/s^2 in all the velocities. The maximum of MKE was registered by MFS (200 cm^2/s^2), followed by the assimilation (112 cm^2/s^2) and the background (85 cm^2/s^2).

5.2.2 EKE

The EKE average from D_0 to D_{end} is seen in fig. 5.14. In all the velocities, EKE of CE was low. It was the NSE that registered the highest values in the Eastern Levantine during this period. The histograms of EKE in the NSE and CE areas are presented in fig. 5.15. Although the assimilation increased EKE compared to the background, MFS registered the highest values. In NSE the highest EKE recorded for MFS was 260 cm^2/s^2, followed by the assimilation (172 cm^2/s^2) and the background (146 cm^2/s^2) respectively. In CE, the maximum of EKE did not exceed 140 cm^2/s^2 in all of the three velocities (140 cm^2/s^2 assimilation, 102 cm^2/s^2 MFS and 521 cm^2/s^2 for the background).

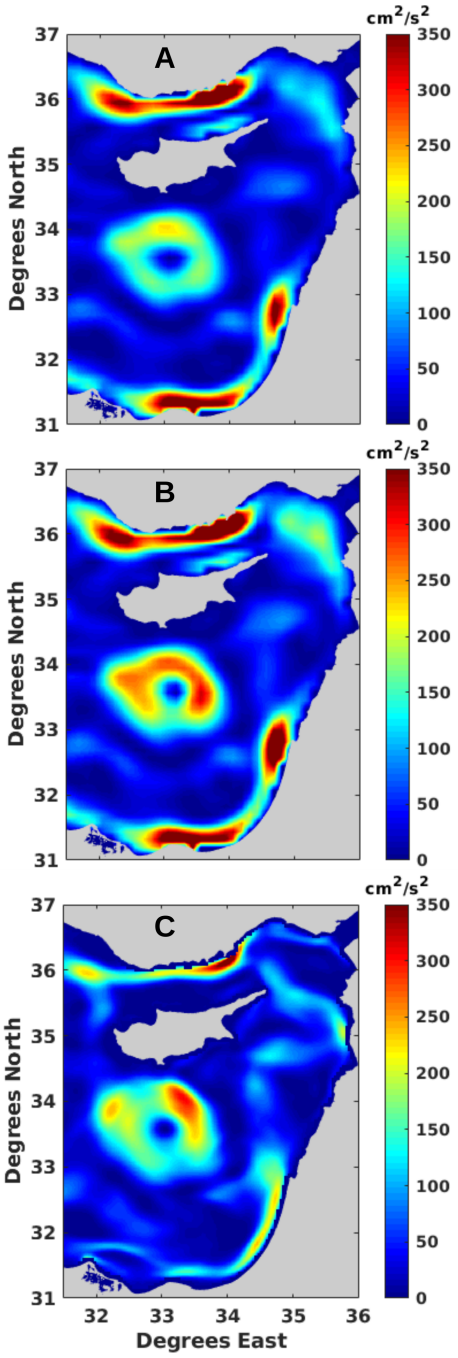

FIGURE 5.12: MKE of the background (A), assimilated (B), and MFS (C) velocities for the period of the drifter passage between 1^{st} March and until the 26^{th} of October 2017.

It can be deduced from all the previous results that the CE was a more stable structure with more intense velocities. Thus it was characterized by low EKE and high MKE. On the other hand, NSE was a highly variable eddy that was weak but not stable (low MKE and high EKE).

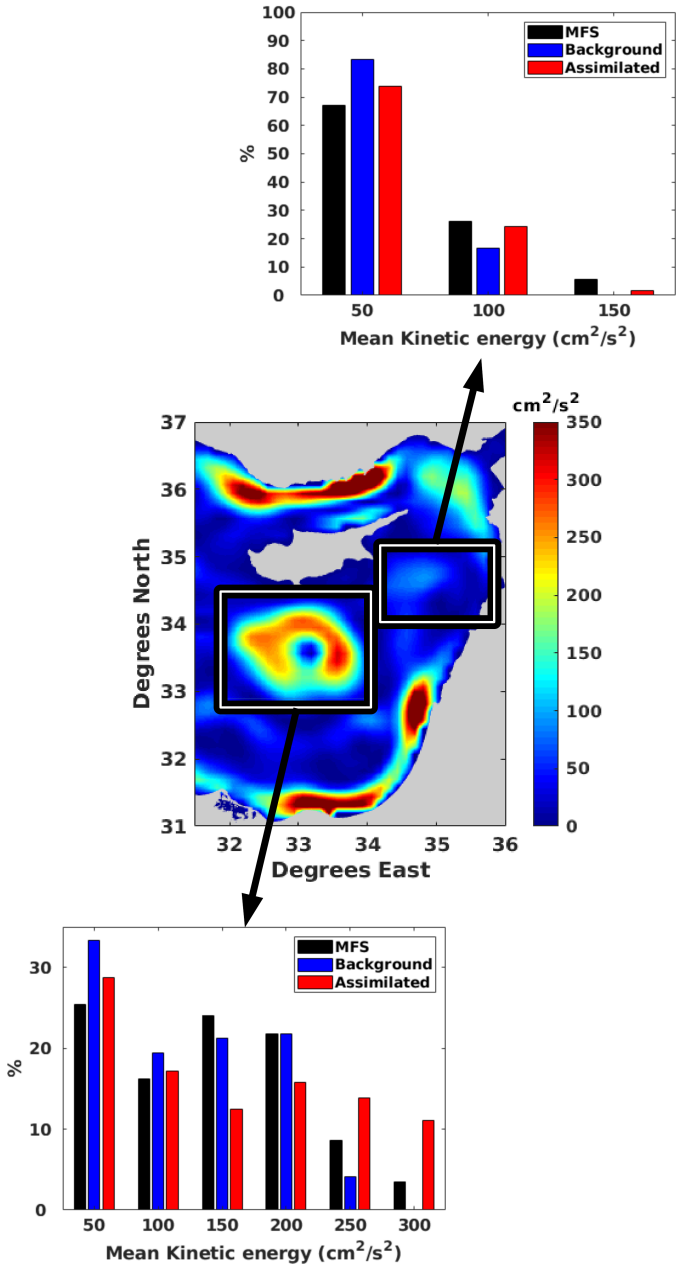

FIGURE 5.13: The middle panel represents the areas of Cyprus eddy (CE) and North Shikmona eddy (NSE) overlayed on MKE derived from corrected velocities. MKE values in NSE (CE) area are plotted in upper (lower) panel histograms for the three experimented velocity fields (corrected, background and MFS).

5.2.3 Relative vorticity

Fig. 5.16, shows the average ζ between D_0 to D_{end}, resulting from the corrected, background and MFS velocity fields. The corrected velocities show a clear CE with negative ζ. Oppositely, the average ζ of the background showed a weaker and less spatially extended pattern, while the MFS was not able to show CE. Closer to the coast, the NSE was not observed by the average ζ in all the three compared velocities.

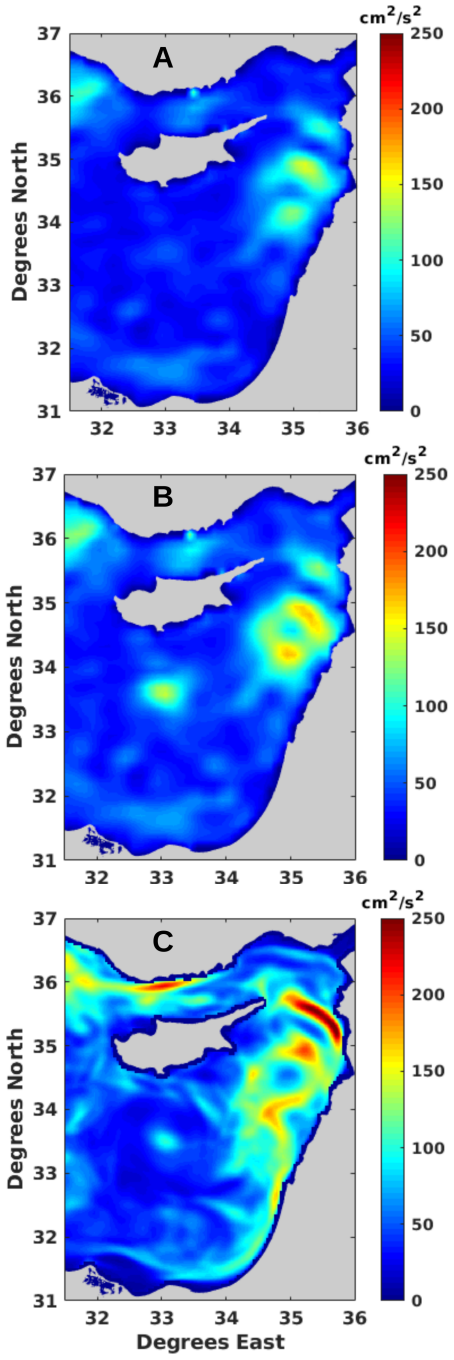

FIGURE 5.14: EKE of the background (A), assimilated (B), and MFS (C) velocities for the period of the drifter passage between 1^{st} March and until the 26^{th} of October 2017.

To quantify the assimilation impact on the representation of CE and NSE, we tracked the temporal variation of ζ in the core of NSE and CE based on the corrected and the background velocities. Fig. 5.17 shows that in CE, ζ was exceeding -3$\times$ $10^{-5}s^{-1}$ starting from the first day. Eddy core was stable until the end of September when there was a decrease of ζ intensity continuously before reaching values of -1.5$\times$ $10^{-5}s^{-1}$ late August.

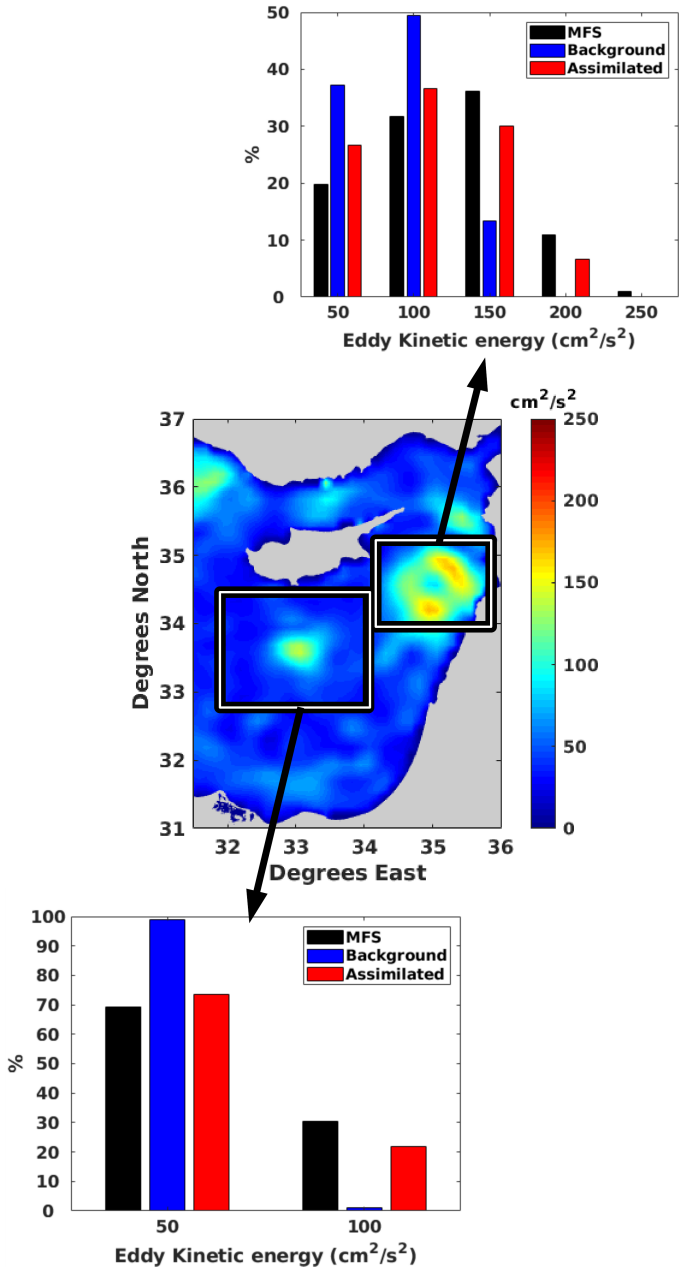

FIGURE 5.15: The areas of Cyprus eddy (CE) and North Shikmona eddy (NSE) overlayed on EKE derived from corrected velocities (middle panel). EKE values in NSE (CE) area are plotted in upper (lower) panel histograms for the three experimented velocity fields (corrected, background and MFS).

On the other hand, the background highly underestimated ζ, as the eddy was weak and barely existed. According to the background, CE exceeded -2$\times$ $10^{-5}s^{-1}$ for few days only. The apparition and intensification of NSE occurred when CE started to weaken, more precisely in late July when there was a shift of the local minimum from -1$\times$ $10^{-5}s^{-1}$ to -3$\times$ $10^{-5}s^{-1}$. Afterward, NSE preserved its activity, although the slight weakening until October. The background velocities also underestimated NSE intensity, where

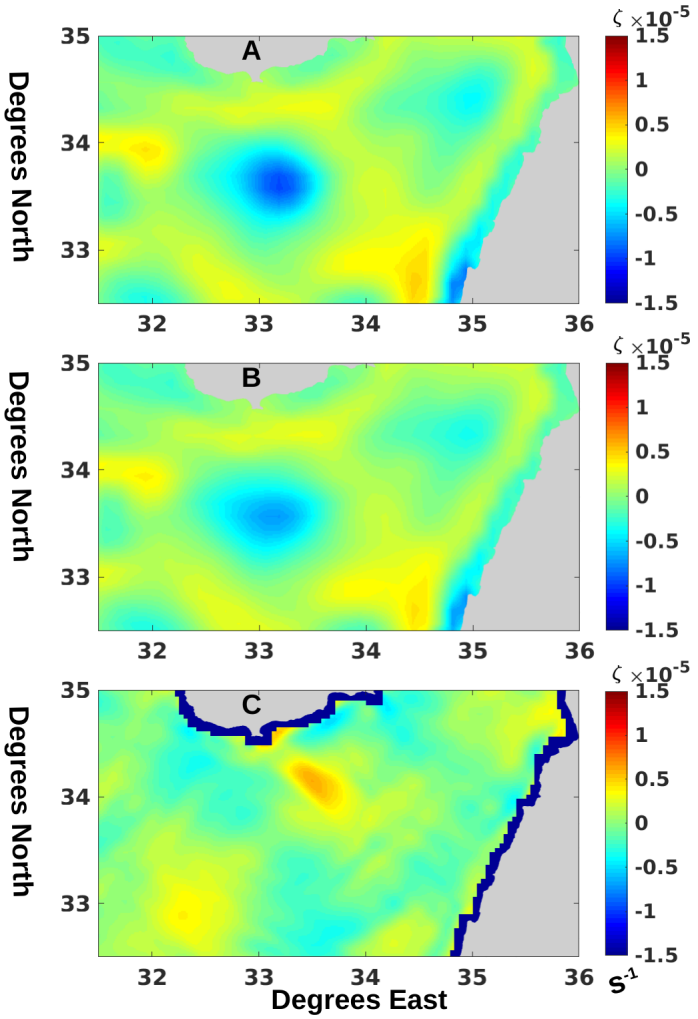

FIGURE 5.16: Average ζ obtained from the background (A), assimilated (B), and MFS (C) velocity fields between 1^{st} March and until the 26^{th} of October 2017.

after assimilation, there was a shift of ζ from -2× $10^{-5}s^{-1}$ to -3× $10^{-5}s^{-1}$, especially in the first days of August.

These results show that CE could affect the activity of NSE. According to Menna et al. (2012), the MMJ could feed the eddies existing in the Levantine Basin, such as NSE. The presence of an intense CE blocks the MMJ and prevents it from interacting with the coastal eddies, which could explain NSE intensification when CE weakened, as observed by the corrected velocities (Mauri et al., 2019).

5.2.4 The impact of satellites tracks

When CE trapped drifters from March to late July, the difference of ζ between the background and assimilation was not consistent. There were periods where the assimilation

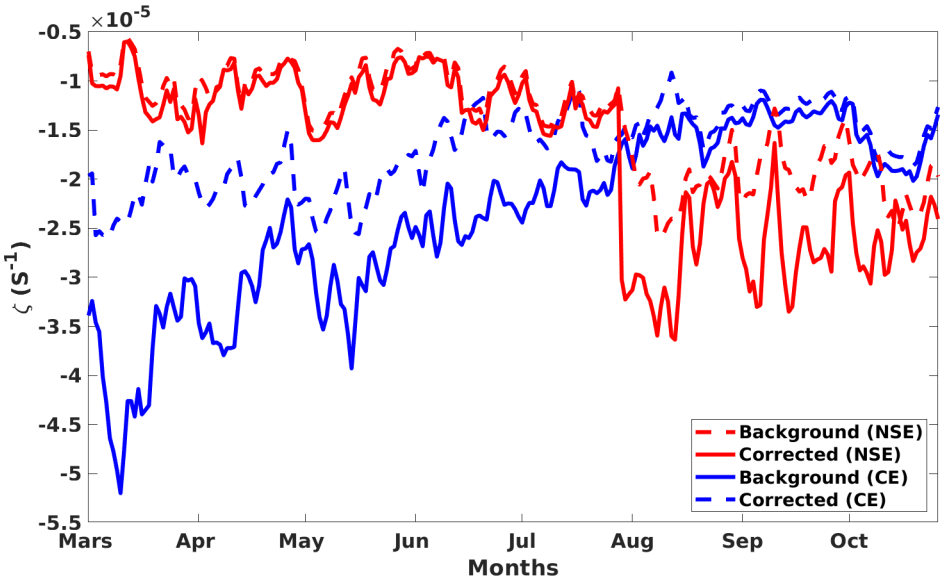

FIGURE 5.17: Temporal variation of the lowest ζ in the Eastern Levantine obtained from the background (dashed) and assimilated (thick) velocity fields.

doubled the intensity of CE compared to the background, such as on the 10^{th} of April (denoted as D_{diff}), while there were some other periods where ζ after the correction was similar to the background, such as on 25^{th} of April (denoted as D_{sim}). The satellite along-track orbits corresponding to these days are shown in fig. 5.18. On D_{diff}, the satellites did not cross CE, and the closet nadir position was more than 40 km far from the eddy border (lower panel). While on D_{sim}, the orbit of one of the satellites crossed the CE core, and another one crossed the border (upper panel). The along-track sampling provides an accurate estimation of the SSH from which the surface circulation is derived. The interpolation of the large gaps (such as in D_{diff}) could underestimate eddies intensities (Ducet et al., 2000), and it is in these cases where there is a maximum of correction by the assimilation. In other terms, when there was a passage of satellite orbits across CE, there was a more accurate description of its intensity and no significant differences between background and assimilation. When there was no satellite passage close to CE, the interpolations tended to underestimate CE activity, and there were high differences between the compared velocities. These observations are consistent with previous studies mentioning that to correctly represent the eddy field, an increase of the satellite tracks number in both time and space is needed, at least for those regions where Rossby radius of deformation is smaller than the global ocean (Amores et al., 2019). These results prove that our method can help to reduce the inaccuracies observed in the altimetric data when interpolating the gaps.

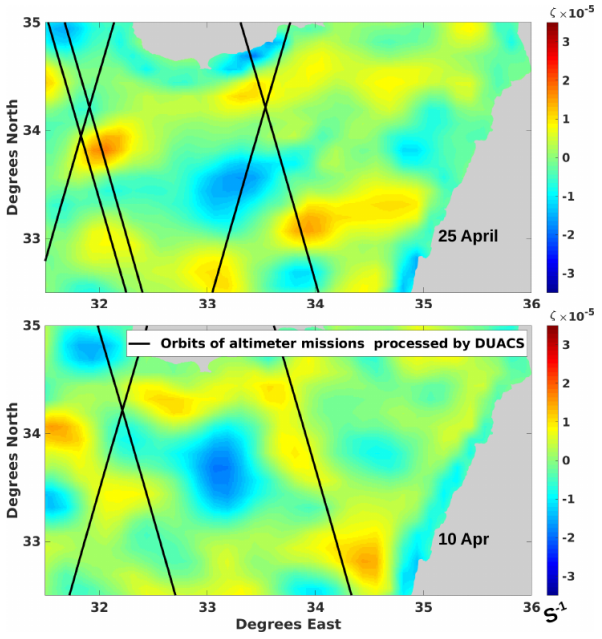

FIGURE 5.18: Orbits of altimeter missions processed by DUACS overlaid on the daily average ζ. The upper layer corresponds to 25/04/2017 (D_{sim}), a day where the background and assimilation were similar, while the lower layer corresponds to 13/05/2017 (D_{diff}) when ζ was highly different between the compared velocity fields.

5.3 Summary of results

In this chapter, we characterized the activity of three eddies present between Cyprus and Lebanon: In 2017, the Cyprus eddy (CE) and the so-called North Shikmona eddy (NSE), while in 2009, the South Shikmona eddy (SSE). We found that SSE was a highly evolving structure that could appear close to the coast, pinch-off, drift offshore, and merge with other eddies in a time scale of a few weeks. The Cyprus eddy (CE) was more stable, characterized by relatively lower Eddy Kinetic Energy (EKE) and higher Mean Kinetic energy (MKE) compared to NSE. CE could affect NSE, where we showed that it was during the weakening of CE when NSE intensified. Indeed, a strong CE could block the Mid-Mediterranean Jet, which prevents the latter from interacting and feeding the NSE. We showed that the corrected velocities improved the representation of the coastal eddies, such as SSE, especially its intensification when merging with another eddy. The highest corrections of altimetric data were observed when the satellite nadir position was more than 40 km far from the eddy border. Accordingly, assimilation helps in efficiently reducing the inaccuracies when interpolating the gaps. From here, it is crucial to increase the drifters' deployment in the Eastern Levantine, especially in

the coastal area where the eddies quickly evolve and the satellite altimetry inaccuracies increases, and models could completely miss these eddies.

The results in chapters 4 and 5 show that the actual altimetric and model observations could be underestimating the eddies in the Levantine Sea. The corrected velocities revealed more intense structures with higher kinetic energy and vorticity. Moreover, the assimilation allowed detecting some quick eddies apparition and merging events that enhance the dominance of these structures. These events were missed by altimetry and models.

Part II

Long-term analysis of the general circulation using machine learning methods

Chapter 6

Data and methods

In the first part of the thesis, the velocities obtained from the variational assimilation highlighted short-term eddies activities lasting several weeks in the Levantine while drifting, merging, or interacting with other eddies. However, the assimilation remains highly dependent on drifters, so we were capable of characterizing only short-term events. Therefore, to analyze the long-term variability of the mesoscale features in the Levantine Sea, we decompose 26 years of altimetric data into clusters reflecting the different circulation patterns. The decomposing of the surface circulation was done using machine learning methods, the self-organizing map (SOM) and the Hierarchical Ascendant Classification (HAC). In this chapter, we present the altimetric data, the machine learning method, and its calibration.

6.1 Data

6.1.1 Altimetry data

The Altimeter satellite gridded Sea Level Anomalies (SLA) is estimated by Optimal Interpolation, merging the measurement from the different altimeter missions available. This product is processed by the DUACS (Data Unification and Altimeter Combination System) multimission altimeter data processing system. It processes data from all altimeter missions: Jason-3, Sentinel-3A, HY-2A, Saral/AltiKa, Cryosat-2, Jason-2, Jason-1, T/P, ENVISAT, GFO, ERS1/2. To produce reprocessed maps in delayed time, the system uses the along-track altimeter missions from products called $SEALEVEL\_*PHY\_L3\_MY\_008*$. The SLA computation provides the Absolute Dynamic Topography (ADT) and the surface geostrophic currents.

6.1.2 Input layer of the SOM

The geostrophic surface velocity fields between 1993 and 2018, from the Herodotus abyssal plain and until the easternmost part of the Levantine sea, form the input layer of the SOM. In addition to the zonal and meridional components of the geostrophic velocities, the fluid parameter of Okubo-Weiss (OW) is included in the input layer (see fig. 6.1). OW measures the relative importance of deformation and rotation at a given point. Positive OW values indicate strain-dominated regions, while negative OW

indicates vortex-dominated. Accordingly, OW is a physical criterion widely used in the methods of eddies detection:

$$OW = s_n^2 + s_s^2 - w^2, \tag{6.1}$$

where s_n and s_s are the normal and the shear components of strain and the relative vorticity of the flow defined respectively by

$s_n = \frac{\partial U}{\partial x} - \frac{\partial V}{\partial y}$; $s_s = \frac{\partial V}{\partial x} + \frac{\partial U}{\partial y}$; $w = \frac{\partial V}{\partial x} - \frac{\partial U}{\partial y}$;

6.2 SOM

The Self-Organizing Map (SOM) is an unsupervised neural network method used for data visualization. It projects higher dimensional data into lower dimensional space leveraging topological similarity properties. By this method, multidimensional data are clustered into neurons clusters automatically associated in orderly fashioned order, where similar neurons are adjacent, and the less similar neurons are situated far from each other in the grid. This way allows obtaining an insight into the topographic relationships of data (Kohonen, 2013).

The SOM is structured in two layers: the input layer (in our case, a 3-D input layer composed of the zonal and meridional components and the Okubo-Weiss parameter) and the resulting neuron grid. Each neuron, representing a cluster with data presenting common characteristics, is associated with a referent vector obtained from a learning data set. Each vector of the input layer will be attributed to the neuron with the closest Euclidean distance with the referent vector. This referent vector is called the best matching unit (BMU), and its associated neuron is the "called" winning neuron. The determination of the referent vectors and the topological order of the SOM maps is done by minimizing the cost function:

$$\mathcal{J}_{SOM}^{T}(\mathcal{X}, W) = \sum_{zi \in D} \sum_{c \in SOM} K^{T}(\delta(c, \mathcal{X}(z_i)))||z_i - w_c||^2 \tag{6.2}$$

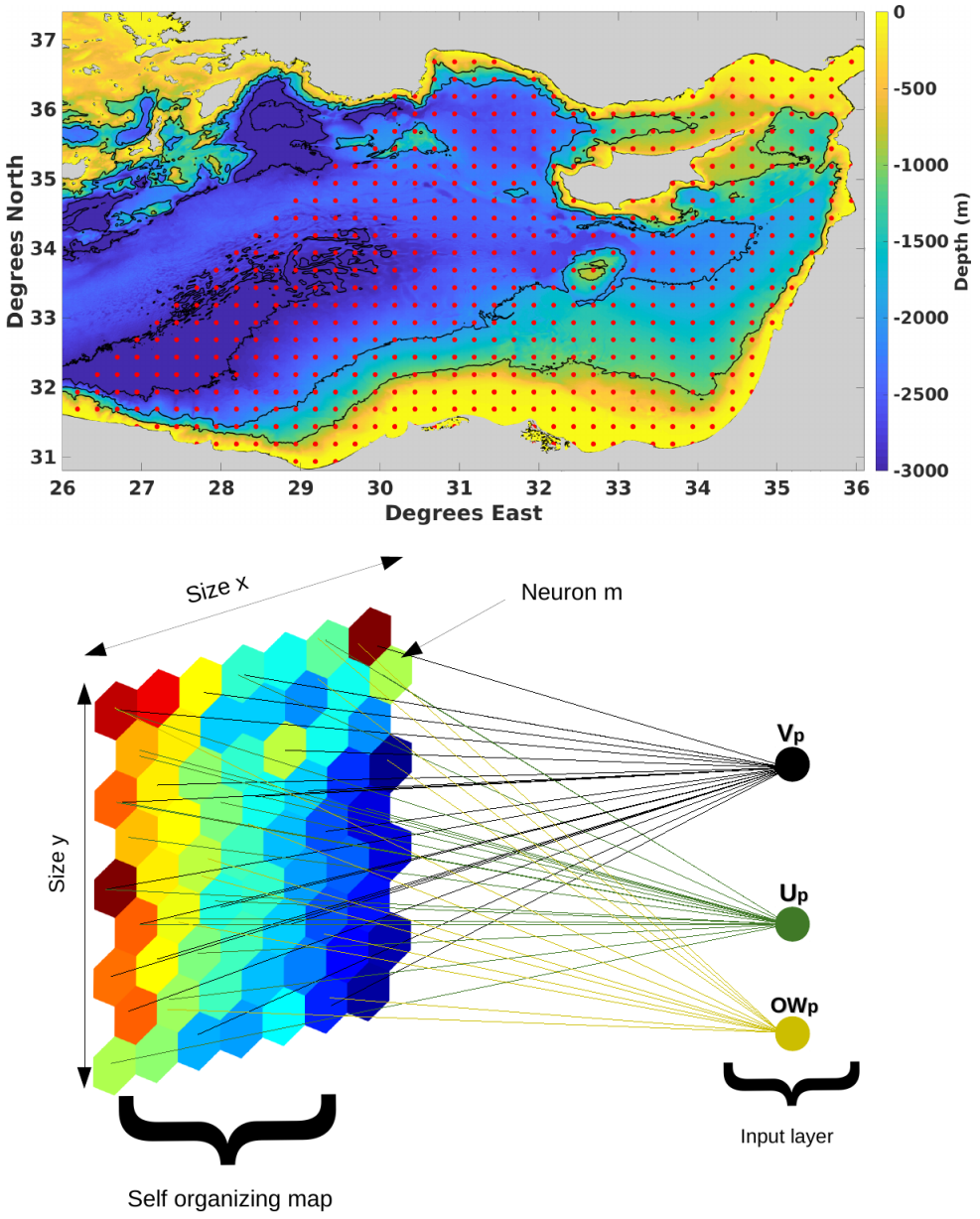

FIGURE 6.1: In the upper panel, the red dots represent the coordinates of the grids providing the input data for the SOM. Each red dot (p) is composed of U and V components and the Okubo-Weiss parameter. The lower panel is a schematic representation of the self-organizing map method: the input layer obtained from the input data and the adaptation layer composed of n neurons automatically associated in orderly fashioned order. Each neuron represents a set of U, V, and OW that represents similarities

where $c \in SOM$ represents the neuron index in the SOM, $\mathcal{X}(z_i)$ represents the allocation function that assigns each element z_i of the input D to the corresponding referent vector $w_{\mathcal{X}(z_i)}$. $\delta(c, \mathcal{X}(z_i))$ represents the discrete distance on the SOM between a neuron c and the neuron allocated to observation z_i. K^T is a kernel function parameterized by T that weights the discrete distance on the map and decreases during the minimization process. During the minimization of the cost function, the topological order is preserved, thus the

more similar neurons are adjacent and the less similar neurons are situated far from each other. To provide an equal weights distribution of the input parameters, the variables were normalized with their variances.

It should be mentioned that the SOM algorithm was applied on Matlab, using the software library SOM Toolbox 2.0 Copyright (C) 1999 by Esa Alhoniemi, Johan Himberg, Jukka Parviainen, and Juha Vesanto and accessible at https://github.com/ilarinieminen/SOMToolbox.

Sensivity tests

Several tests were conducted to precise the SOM size (m) that gives the best representation by repeating the training phase with different sizes m (350, 700, 1050, 1400, and 1750 neurons). For each m value, we show the corresponding mean quantization errors (qe), where qe is the Euclidean distance between input data D and their corresponding Best matching unit (BMU):

$$qe = 1/N \sum_{i=1}^{N} ||D_{(i)} - BMU_{(i)}|| \tag{6.3}$$

The results in fig. 6.2 show that expanding the SOM size decreases qe sharply when shifting m from 350 to 700 neurons. Afterward, the decreases in the error become progressively less intense with increasing m. Accordingly, we opted for a SOM size of 1400.

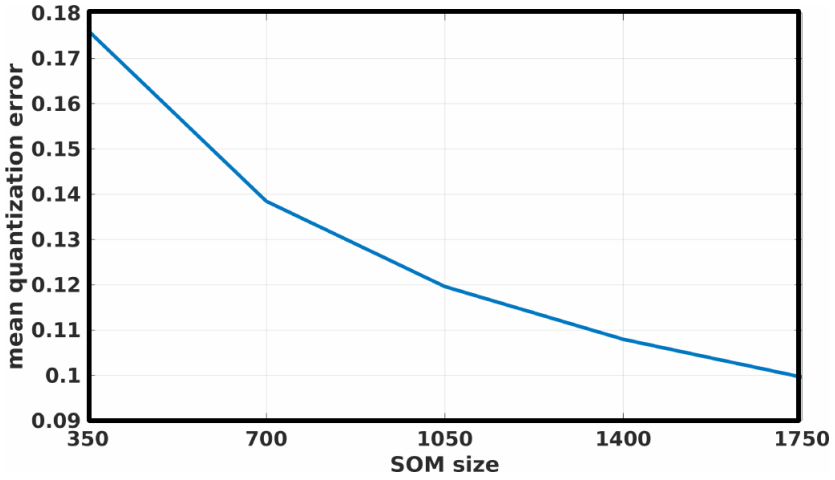

FIGURE 6.2: Variation of the mean quantization errors (qe) with varying SOM size.

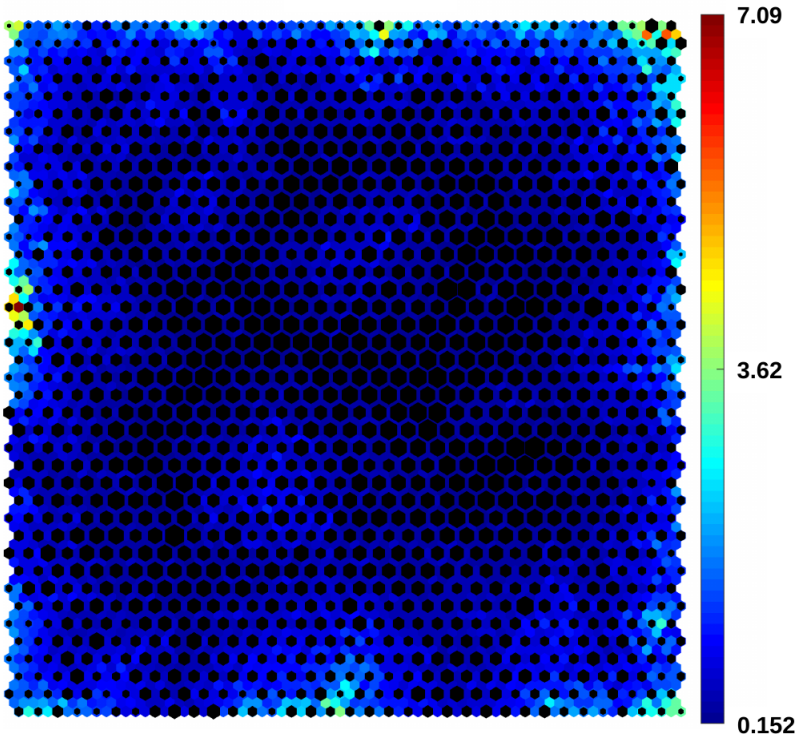

FIGURE 6.3: Distribution of training data in the trained SOM (hitmap) based on their similarity. Each hexagon is a neuron in the SOM and the size of the black points within each hexagon is proportional to the number of training data associated to that node during the training phase. The colorbar represents the distances between the neighboring referents on one hand, and the averages of these distances on the other.

The distribution of the training data in the trained SOM (hit map) is presented in fig. 6.3. It shows that the neurons associated with the highest training data are mostly located in the middle of the SOM, while the number decreases in the neurons located closer to the borders. The resulting organization of the three variables of the input layer (U, V, OW) is presented in fig. 6.4. It reveals a good organization of these variables, where there is a gradient of zonal and meridional velocities, with the highest values mostly located at the borders. This distribution of U and V well-reflected the OW variation. The OW in SOM shows clusters of intense positive or negative values (see fig. 6.4). These extreme values represent the characteristics of a vortex (positive) or strain (negative) dominance.

6.3 HAC

The SOM allowed classifying the velocity field into neurons that represent the different circulation patterns of the targeted grid, based on U, V, and OW. For an improved representation of the physical processes obtained from the different situations, we applied

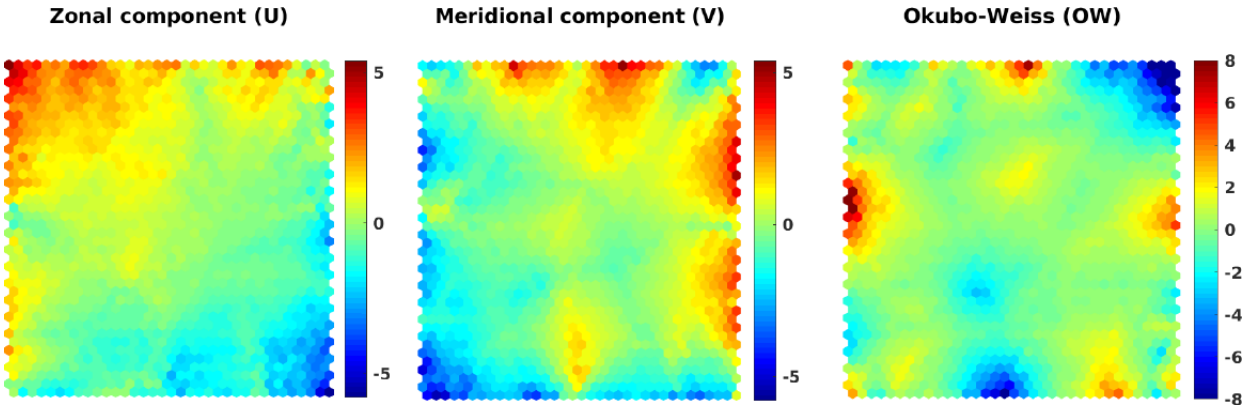

FIGURE 6.4: Topological maps showing the organization of the three variables (U, V, and OW) on the SOM after the training phase. Each map shows the normalized recorded values by each neuron for the three variables.

the HAC (Hierarchical Ascendant Classification) to group these neurons into a reduced number of clusters. HAC is a cluster analysis that seeks to build a bottom-up hierarchy of clusters. From the initial partition containing the neuron groups of the SOM map, two neurons of the same neighborhood were clustered at each iteration. The used criterion was Ward's minimum variance method, which provides a partition that minimizes the within-cluster inertia (Randriamihamison et al., 2021). As a result, the neurons were separated into five different clusters (see fig. 6.5, upper panel). Consequently, clusters 4 and 5 (denoted as C4 and C5) were characterized by a negative OW, compared to positive OW for C1 and C2, while C3 had an average OW of 0. MKE boxplots of the neurons in each cluster show that C3 had the weakest flow intensity, while C4 and C1 represented the highest MKE intensities, followed by C2 and C5. In summary, C1 and C2 are clusters of a strong-flow with positive OW, C4 and C5 are clusters of a strong-flow with negative OW, while C3 is the cluster of the weakest velocities (fig. 6.5, lower panel).

SOM

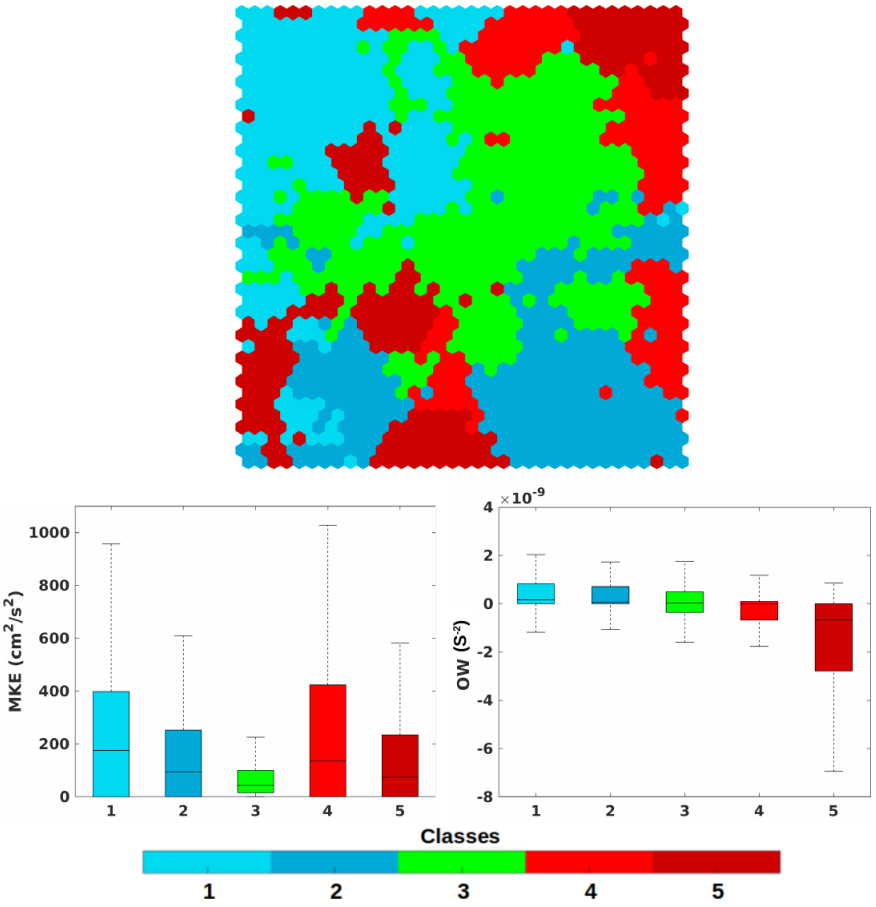

FIGURE 6.5: The upper panel shows the topological map of neurons representing the different clusters obtained from the SOM and HAC method. The resulting MKE and OW values of each cluster are presented in the boxplots of the lower panel.

Chapter 7

Long-term analysis of the Eastern Mediterranean surface circulation

In this chapter, we decompose the surface currents of the Levantine Basin between 1993 and 2018 into the five different clusters obtained using SOM and HAC methods, as explained in chapter 6. Then we analyze the variability of these clusters to improve the understanding of the main mesoscale features activities and the factors driving their behaviors.

7.1 Studied area

The eddies usually reveal elevations (anticyclones) or depressions of the sea surface. Accordingly, to study the variation in the activity of the main mesoscale structures in the Levantine after decomposing the surface circulation into five clusters reflecting the different circulation patterns, we delimited the spatial area of each eddy by computing the Mean Dynamic Topography (MDT) map obtained from averaging Absolute Dynamic Topography (ADT) for over 26 years between 1993 and 2018. In fig 7.1, the iso-MDT (upper panel) closed lines show several eddies structures consistently present in the basin. The Positive MDT values, revealing anticyclonic circulation structures, were around the Eratosthenes seamount and the Herodotus Abyssal Plain depth. On the other hand, negative MDT values, hosting cyclonic circulation, were observed between Cyprus and the Asia minor and in the Shikmona area between the South of Lebanon and Egypt. The representation of MDT variation (lower panel) shows similar mesoscale structures with additionally two active zones, observed offshore the Lebanese coasts and the west of the Eratosthenes Seamount. Depending on these results revealed by the average and the variation of the Dynamic topography, we divided the basin's mesoscale activity into several boxes: the Beirut box off the Lebanese coast (Bei), Cyprus Eddy that includes the Eratosthenes seamount (CE), Mersa-Matruh eddy above the Herodotus plain (MME), Nile, Shikmona (Shik) and the Asia Minor Current box (AMC).

7.2 Results

In this section, we present the results of decomposing the surface circulation of the Levantine Basin into the five clusters obtained by the HAC and SOM methods.

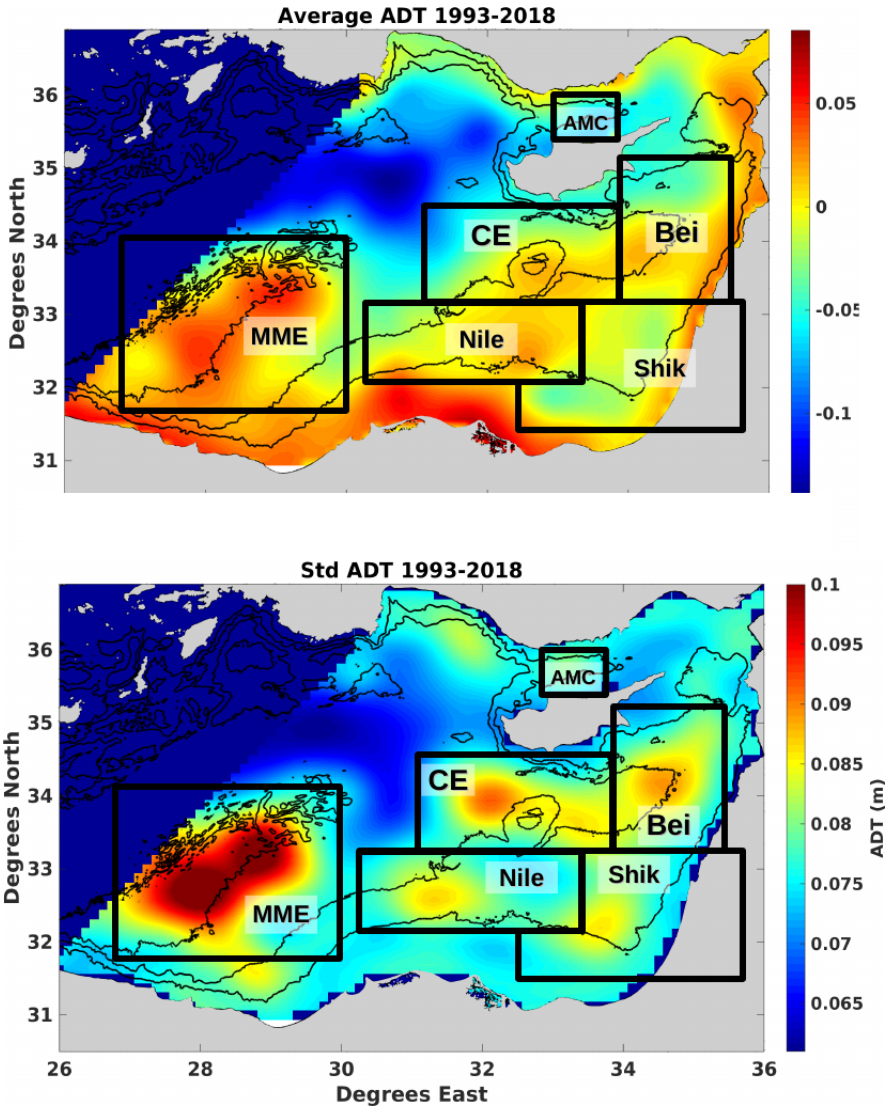

FIGURE 7.1: The upper panel shows Mean Dynamic Topography (MDT) between 1993 and 2018 in the Eastern Levantine, while the lower panel shows the standard deviation of the Absolute Dynamic topography (ADT) for the same periods. Both includes the names and borders of the six delimited sub-regions or boxes (MME: Mersa-Matruh Eddy, CE: Cyprus Eddy, Nile, Shik: Shikmona, Bei: Beirut, AMC: Asia Minor Current).

7.2.1 Temporal analysis

The frequency variation of the five clusters in each of the selected boxes, Bei, Shik, MME, AMC, Nile, and CE, is seen in fig. 7.2. Except for C4 in the AMC, all the clusters permanently occurred, with different proportions highly variable with time in each box. Moreover, clusters frequency significantly varies from one box to another. Although clusters of strain-dominated flow (C1 and C2) were not frequent everywhere, C1 and C2 were frequently observed in MME and AMC, respectively, during all the period. Such a high frequency occurred at the expense of other clusters, especially the

cluster of weak flow C3 that was less observed in these two boxes. Regarding the vortex-dominated clusters (C4 and C5), C5 was the most frequent. C4 was quasi-absent in AMC and scarcely existed in the other boxes. When comparing between boxes, C5 was most frequent in the MME. Overall, all the clusters occurrences were highly fluctuating with time. To better analyze these variations, we presented the daily dominant cluster in each box in fig. 7.3. On the one hand, C3 was the main cluster in CE, Nile, Bei, and Shik boxes. Moreover, between 1993 and 2000, C3 was almost exclusively dominating CE. On the other hand, C3 dominance was rare or quasi-nonexistent in the MME and AMC, where instead, C1 and C2 were, respectively, the most frequent clusters. While C2 dominance was not observed in MME, an increasing periodic C1 domination was observed in AMC, starting from 2000. C5 was frequently dominating all the boxes, but intermittently. This dominance was rare in the CE, Nile, and AMC, compared to the MME, Bei, and Shik. Indeed, in these last three boxes, C5 dominance was frequent and showed a long lifetime that lasts for several months, such as observed in Bei in 2003 and 2014 and Shik in 2005.

These results showed that MME and AMC are two zones of a special regime of flow. This latter is represented by clusters of intense current, the so-called C1, and C2. The other boxes are zones of relatively weaker currents. In all the boxes, there were sporadic events of intense eddy activity, exhibited by the intermittent periods of C5 dominance.

To quantify the flow intensity variation, the daily mean kinetic energy of the mean flow per unit of mass (MKE) is computed in each box (see fig. 7.4). It shows that the lowest MKE was observed in the boxes of C3 domination (CE, Nile, Shik, and Bei). In these boxes, MKE values were less than 150 cm^2/s^2. On the other hand, the highest values were in AMC and MME, with values consistently exceeding 300 cm^2/s^2. Hence, the boxes, dominated by C1 and C2, had MKE values double those dominated by C3.

The tendency of the dominant cluster could change with time, where for example, previous results show that between 1993 and 1997, C5 was rare in Bei before being more frequently observed as a dominant cluster. Fig. 7.5 shows the seasonal variation of the C1 (left panel), C3 (middle panel), and C5 (right panel) averages frequencies in all the boxes between 1993 and 2018. The general trend of C5 frequency was increasing with time. The most intense C5 positive tendency was in MME, where C5 increased by 10 % in 26 years. In all the seasons, the C5 frequency average increased from 25 % in 1993

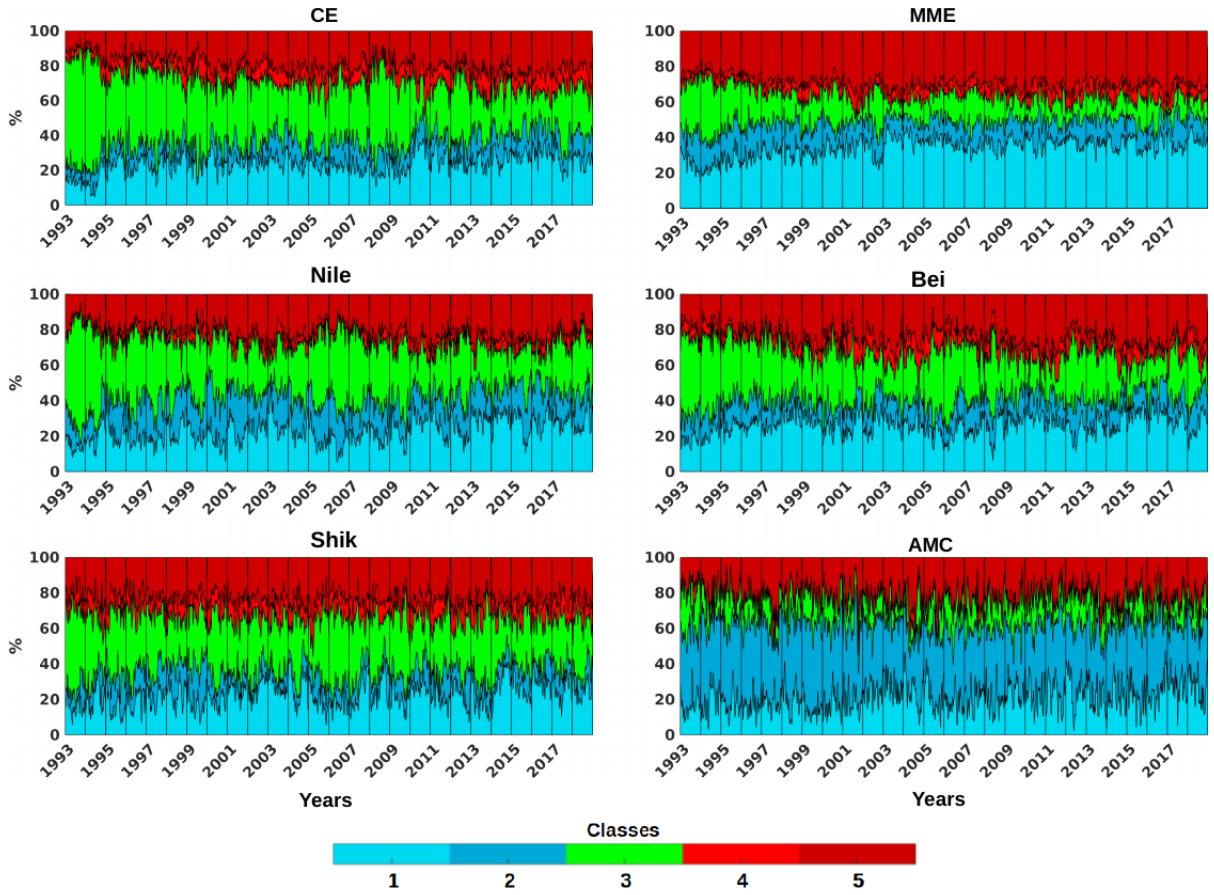

FIGURE 7.2: The temporal variation of each cluster frequency in the selected boxes, between the start of 1993 and until late 2018.

to 35 % in 2018. There was a similar increase in all the seasons in the Bei, MME, and Nile boxes. The weakest increasing tendency was in AMC and Shik. In terms of seasonality, there was no significant difference of C5 frequency between seasons, except in CE, where in summer and fall, the values were higher with values closer to the MME. MME registered the highest seasonal average frequency of C1 (see left panel), meaning that this box is the most dominant in terms of intensity and vorticity (C5 and C1). In terms of trends, C1 showed similar results to C5. MME and Nile boxes showed the sharpest increases, followed by AMC, Nile, CE, and Bei, while C3 was continuously decreasing in all the boxes (see middle panel).

These results show that the activity of the dominant mesoscale features is increasing with time. Previous altimetric data observations from 1993-2003 revealed increasing variability of the Mediterranean Sea activity that is maximal in the Levantine Sea, especially in the Mersa-Matruh area, where increasing energetic structures were observed (Pujol and Larnicol, 2005). Studies have discovered evidence that eddies are becoming

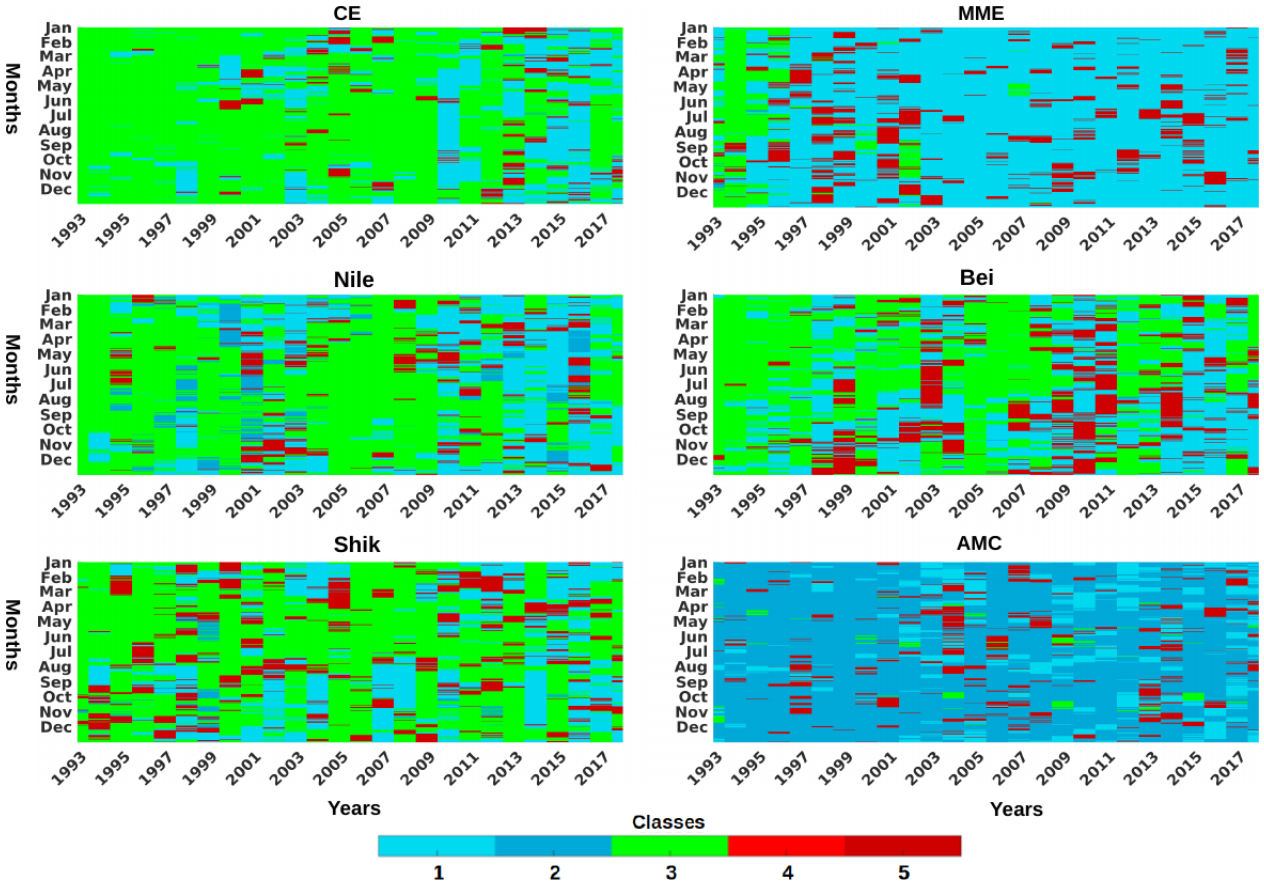

FIGURE 7.3: The daily dominant cluster in each box from 1993 and 2018.

more energetic. This increase was related to several reasons, such as the changes in winds or large-scale horizontal temperature gradients or the changes in the shear of the ocean currents (Martínez-Moreno et al., 2021). This current evolution is well highlighted where C3 is being progressively replaced by C1. Nevertheless, we should not exclude the impact of the altimetry increasing accuracy in describing the surface circulation, with an increasing number of satellite tracks in both time and space. Indeed, combining satellite altimeters proved its efficiency in providing a better representation of the mesoscale activity (Amores et al., 2019; Pascual et al., 2006). In terms of seasonality, there was no significant difference of C5 frequency between seasons, except in CE, where in summer and fall, the values were higher with values closer to the MME. Although previous studies have mentioned that eddies in MME are mainly formed in summer and spring (Hamad et al., 2005; Mkhinini et al., 2014), there was no clear seasonality of C5 frequency. It is explained by the frequent eddies apparition and their relatively long lifetime. Consequently, eddies permanently occur in the MME box (Taupier-Letage, 2008).

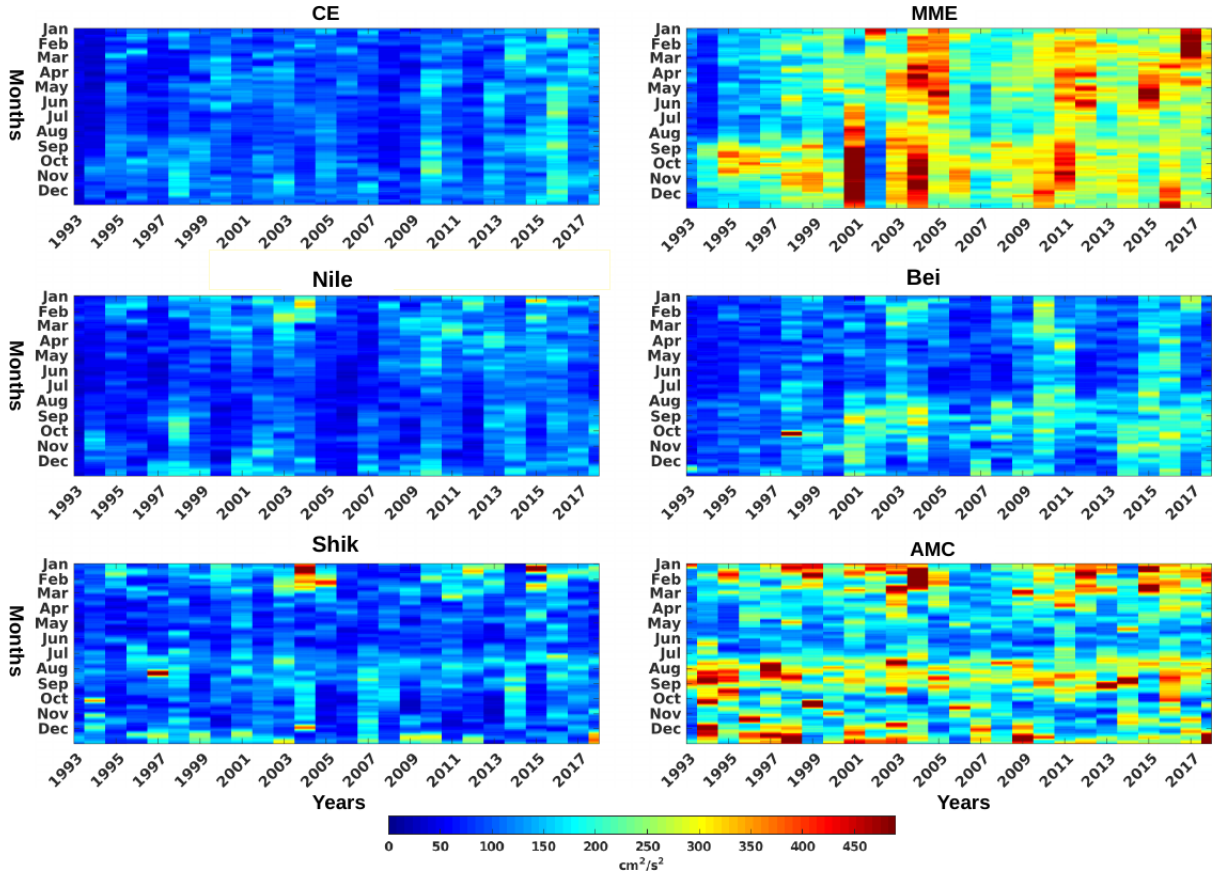

FIGURE 7.4: The variation of the daily average Kinetic energy (MKE cm^2/s^2), in each box from 1993 to late 2018.

It should be mentioned that C2 and C4 did not show a clear tendency. However, C2 was only significantly present in AMC with values around 40%, while in all other boxes, the frequency was less than 20% (see fig. 7.6).

7.2.2 Saptial analysis

The spatial variation of clusters' frequencies is shown in fig. 7.7. The along-slope coastal circulation in the Eastern Levantine did not reveal consistent clusters frequencies. The high kinetic energy clusters, C1 and C2, were highly persistent off the Libyo-Egyptian coasts and between Turkey and Cyprus, respectively, with a frequency exceeding 50%, before being replaced by the weak flow cluster C3 in the easternmost part of the basin. The C5 predominance is mostly situated in the western part, revealing that the mesoscale activity is more intense in that area. No clear jet was observed in the middle of the basin, including the MMJ pathway, where C1 dominance was disconnected by high C3 occupancy, more specifically between 30 and 32°E (see C1 in fig. 7.7).

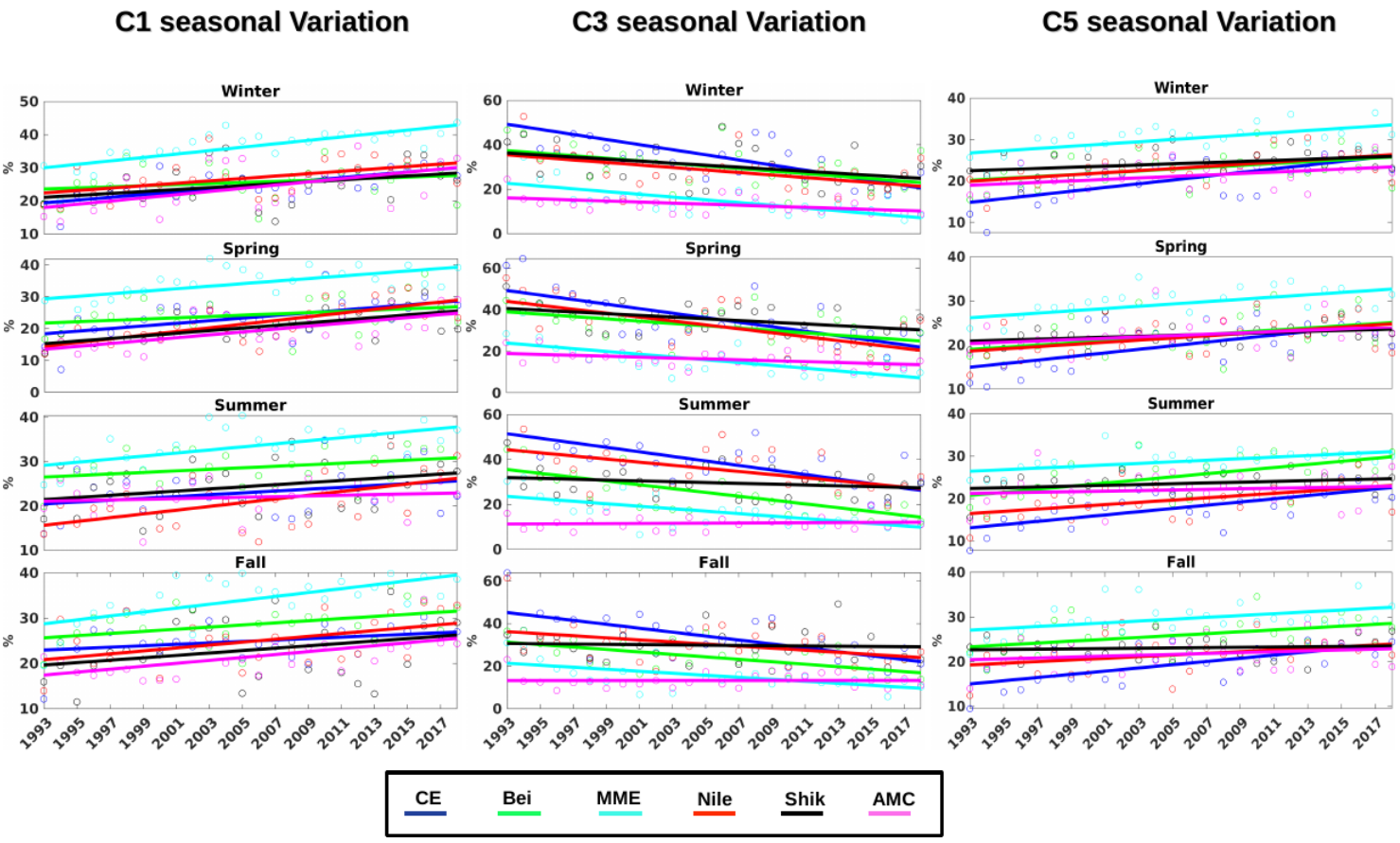

FIGURE 7.5: The seasonal variation of the C1 (high kinetic energy), C5 (high vorticity), and C3 (low KE and low vorticity) average in each box and their resulting linear regression.

7.2.3 MMJ

To further investigate the time evolution of the potentially existing MMJ, we present in fig. 7.8 (the upper panel) a Hovmoeller diagram (along longitude 31.5625 °E) that shows the temporal variation of the clusters along its potential path. The longitude selection was based on the previous results showing area dominated by weak flow cluster C3 in the MMJ potential pathway between the Eratosthenes Seamount and Cyprus coast (see C1 frequency in fig. 7.7). Although frequent C3 domination, there were years where clusters revealing higher KE were frequently occurring, such as C1 in 2015 or C5 between 2013 and 2014. An example of this variation is presented in fig. 7.8 (the lower panel), which shows the clusters frequencies distribution during the EGYPT/EGITTO (September 2005-July 2007) CINEL campaigns (September 2016-August 2017) that provided in-situ drifters observations in MMJ potential pathway. During EGYPT/EGITTO campaign, C3 frequency was more than 50 %, and the other clusters did not exceed 15 %, while

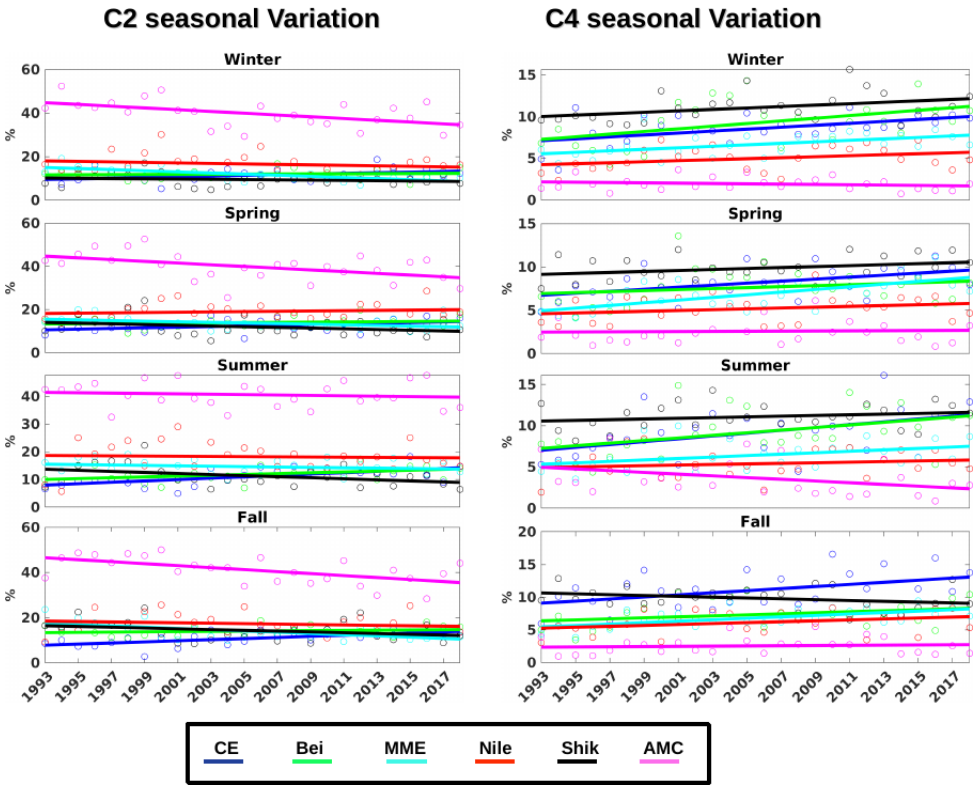

FIGURE 7.6: The seasonal variation of the C2, C4, and C3 average in each box and their resulting linear regression

through the CINEL campaign, clusters of stronger KE increased at the expanse of C3, decreasing to 27 %. All these results reveal that in the middle of the basin, the MMJ is present, but sporadically and not as one of the most remarkable features, where the strong flow clusters were frequently observed but masked by C3, the dominant cluster there. In Millot and Gerin (2010), the drifter data set used from the EGYPT/EGITTO campaign that showed no distinct jet was between 2005 and 2007, a period of C3 domination. On the other hand, in Mauri et al. (2019) the drifter tracks that showed a clear MMJ crossing the basin from west to east was between late 2016 and 2017, a period when there was a sharp shift in C3 frequency, decreasing by more than half compared to EGYPT/EGITTO. The Hovmoeller diagram also showed that MMJ variability was without any seasonal or periodic nature, in agreement with Ciappa (2021).

7.2.4 C5 analysis

Both of C4 and C5 are vortex-dominated clusters. However, the previous results showed that C4 is a peripheral cluster scarcely observed, dominating only very few pixels close to the coast. C5 was the main cluster that mainly reflected the eddies' presence. Here

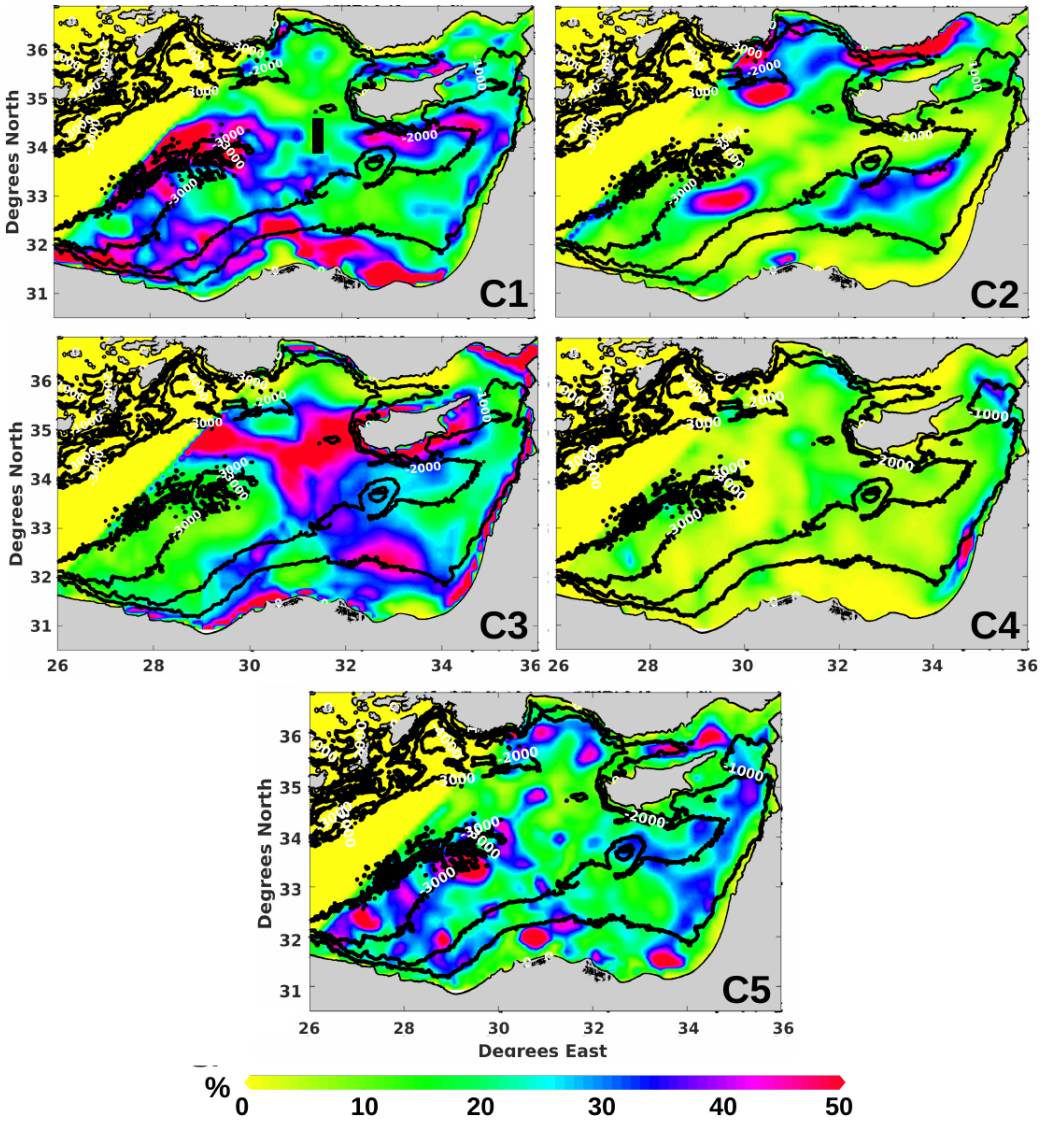

FIGURE 7.7: Percentage of C1, C2, C3, C4, C5 occurrence between 1993 and 2018, overlayed on the main bathymetric iso-lines of -1000, -2000, and -3000 m. The dark line in panel A shows the position of the Hovmoller diagram in sec. 7.2.3

we present a more detailed analysis of the C5 evolution that reveals eddies activity in the Levantine sea.

Fig. 7.9 (upper panel) shows the spatial distribution of C5 whose occurrence exceeded 40 % (C5P). The highest persistent C5P number was at the borders of the Herodotus plain. In addition, another group of C5P occurred in areas of the extended continental shelf, more precisely the shelf located offshore Egypt and between Cyprus and Turkey in the northern part of the basin. A small number of C5P followed the bathymetric iso-bath of 1000 m in the western part of the basin. On the other hand, C5P was absent in the eastern part of the Levantine. In the lower panel, we present the variation

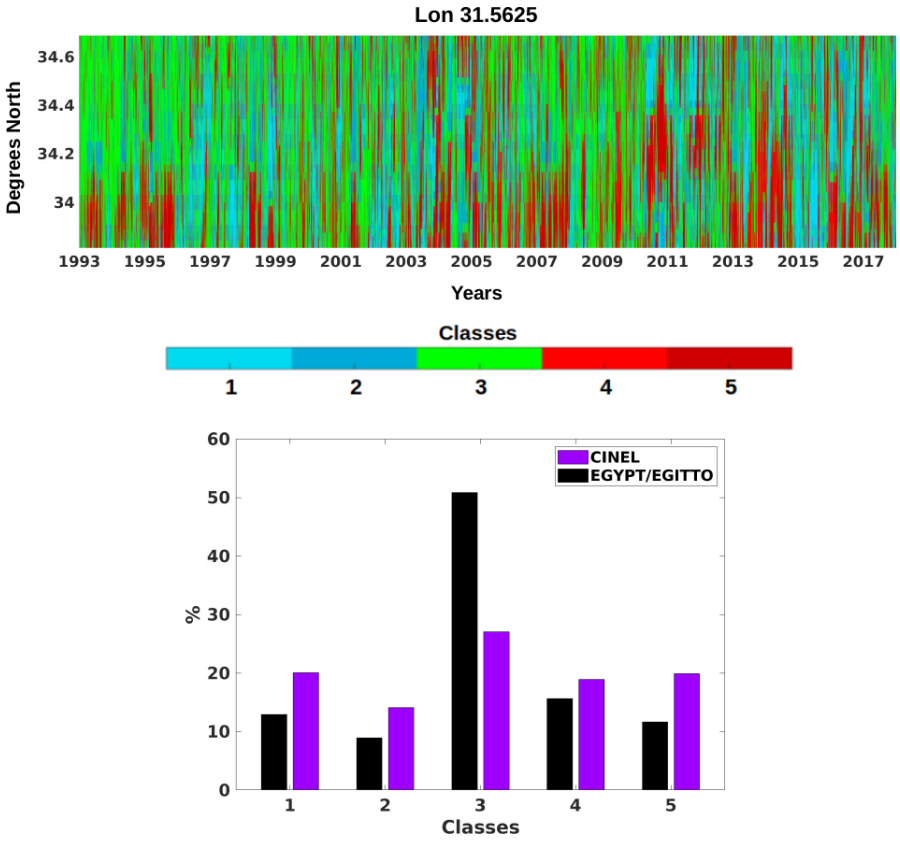

FIGURE 7.8: The upper panel shows the Hovmoeller diagram of daily clusters variation along the MMJ potential pathway, at the longitude 31.5 °E (right). The resulting clusters frequencies during the EGYPT/EGITTO (September 2005-July 2007) and CINEL campaigns (September 2016-August 2017) are shown in the lower panel.

of C5P numbers regarding their distances with the main bathymetric structures (isolines of 1000, 2000, and 3000 m). More than 80 % of C5P were located at a distance less than 60 km from these main features. In the zones of extended continental shelf, such as offshore the Libyo-Egyptian coasts, there is a strong flow dominated by C2 and C1. Previous studies have shown that a current becomes unstable when wider than the bathymetry. Thus it favors the eddies formation conditions (Wolfe and Cenedese, 2006). The C5P absence off the Lebanese coasts is explained by the tight continental shelf almost absent. Indeed, the weak current dominated by C3 near the coastline is not strong enough to permanently create instabilities. The group of C5P observed in MME is due to the Herodotus abyssal plain impact. The vertically extended eddies pinch off from the coast and propagate to the east before being trapped, thus accumulating eddies (Alhammoud et al., 2005; Elsharkawy et al., 2017). These results show that the main bathymetric features could potentially influence eddies creation and persistence.

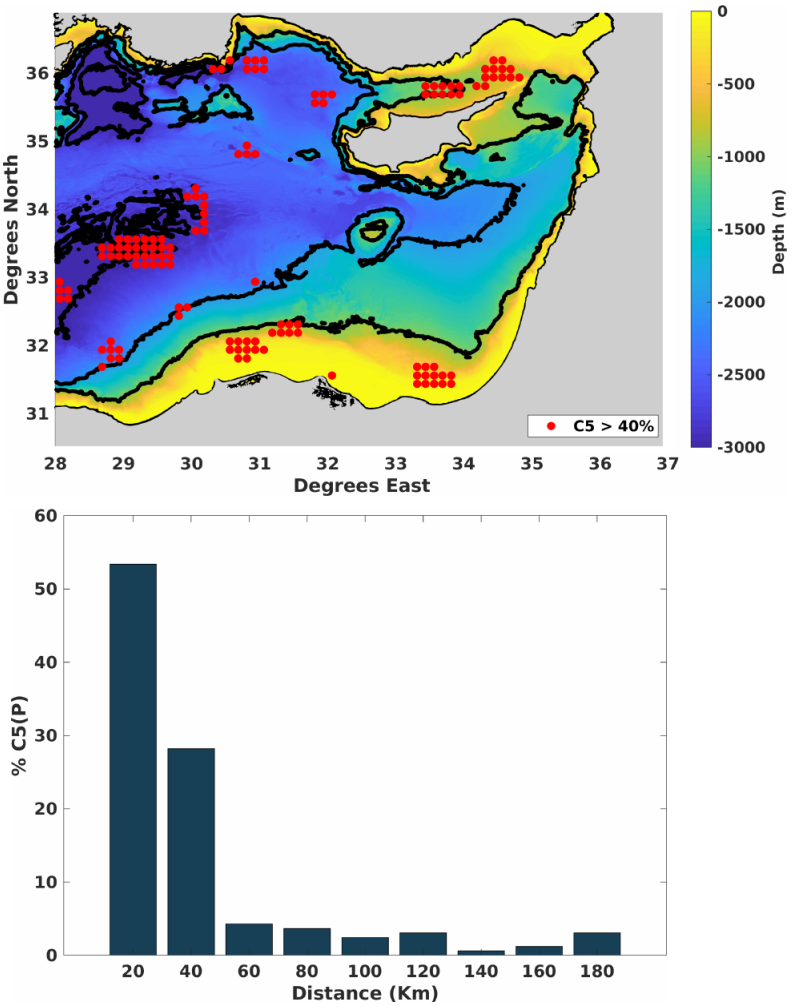

FIGURE 7.9: In the upper panel, the red dots show the positions of C5P, which are the pixels where C5 existed more than 40 % of the time. The dark line represents the main bathymetric iso-lines (1000, 2000, and 3000 m). The lower panel shows the variations of C5P frequency compared to their distance with these iso-lines.

7.2.5 Sensivity of the method to the used model

Because of the coarse resolution in both space and time of the altimeters, and to the fact that mesoscale structures move continuously, eddies can be missed or artificially created, smoothed, misplaced, or be aliased into larger features compared to the true eddies (Amores et al., 2019; Ioannou et al., 2017; Mkhinini et al., 2014). To evaluate if the previously observed results are sensitive to the accuracy and the resolution of the altimetric data, we used a method to assimilate drifters with altimetry to obtain an improved representation of the surface circulation. We took advantage of three drifters, released during the CINEL campaign in 2017, and trapped in the Cyprus eddy for several months between 7^{th} of March (denoted as D_0) and until 31 st of July 2017 (denoted as D_{end}) to assimilate them with altimetry (drifters OGS id: 5321, 5318, 5312).

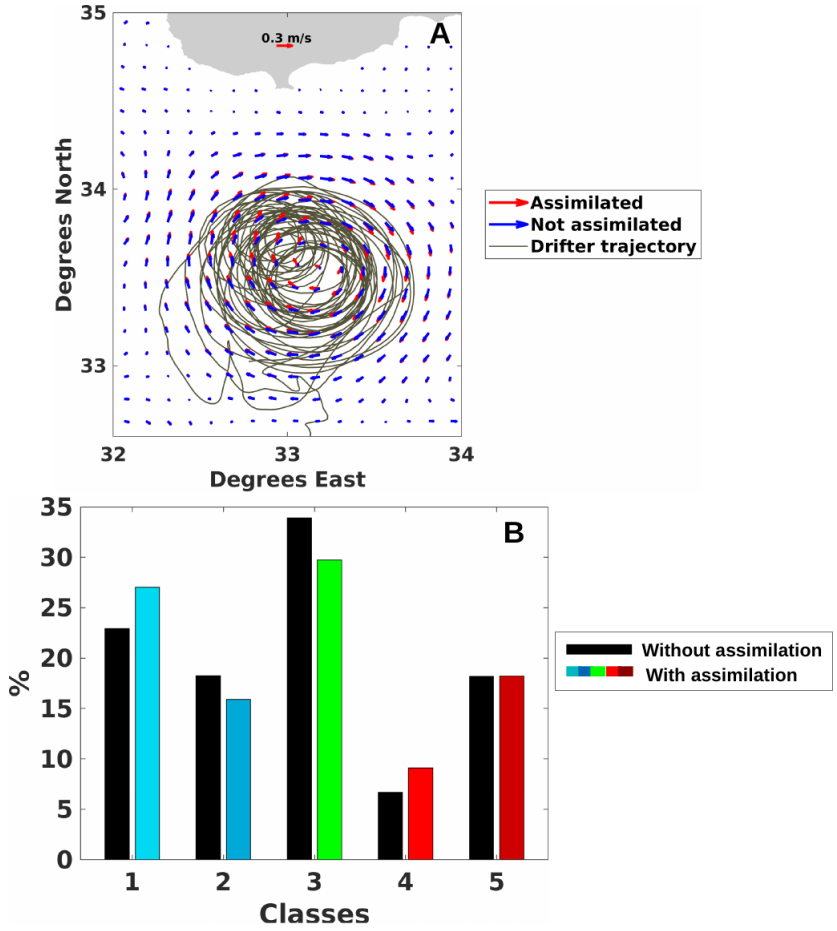

FIGURE 7.10: Panel A shows the average velocity field obtained before (blue) and after assimilating (red) the drifters' trajectories represented by the grey lines, circulating in CE from the start of March until late July. B represents the percentage of pixels assigned to the clusters from 1 to 5 before (dark bars) and after assimilation (colored bars).

The average velocity field shows differences in CE after assimilation (see fig.7.10, A). To evaluate assimilation impact on the surface circulation decomposition, we assigned each velocity observation, before and after being affected by the assimilation, to a cluster using the trained SOM and HAC methods. In panel B we compared between the resulting clusters frequencies of the observed velocities before and after assimilation. It reveals that the assimilation slightly modifies the clusters proportions, except for C5, where C1 and C4 increased while C2 and C3 decreased. Hence clusters that are characterized by a strong MKE flow slightly increased at the expense of the other. Indeed, although altimetry is a coherent tool, assimilation showed that eddies intensities in the Levantine could be underestimated. Besides that, the surface circulation could be less accurate closer to the coast, where previous studies have shown a declining altimetry accuracy in the Levantine Basin (Fifani et al., 2021). Accordingly, the use of higher spatio-temporal

resolution products, such as accurate models, or the upcoming altimetry missions like SWOT that will provide more reliability close to the coast (Barceló-Llull et al., 2021; dOvidio et al., 2019; Morrow et al., 2019), will improve the decomposition of the surface circulation by our method, without changing the main conclusions.

7.3 Summary of results

In this study, we analyzed the surface circulation of the Levantine Basin using the SOM + HAC method that allows decomposing 26 years data set of surface geostrophic velocities into five clusters representing the different surface current flowing types. By tracking the clusters variability, we showed that the surface circulation is complex and divided into several energetic boxes. We highlighted the increasing mesoscale activity in the basin, where these eddy-rich boxes are showing a positive trend with time. The cluster of weak flow is being progressively substituted by those of higher kinetic energy and vorticity. We were able to show the sporadic occurrence of the MMJ, which could explain the contradictory statements about the MMJ's existence. We highlighted the crucial role of bathymetry and the coastal flow intensity in increasing instabilities and eddies formation in the Levantine sea. Accordingly, the most persistent eddies occurred in areas characterized by a strong coastal flow and an extended continental shelf or around Herodotus Abyssal plain, explaining thus the disproportions of eddies frequencies and persistence in the Levantine. It is a promising method that will undoubtedly benefit from more accurate and higher resolution of future altimetric missions. Also, it could be associated with other parameters such as Sea Surface Temperature and chlorophyll to study the interactions between the physical and biogeochemical water properties. Further work should expand the studied area to the entire Mediterranean to investigate whether these increasing trends are only observed in the Eastern Levantine or extend to a larger scale.

Chapter 8

Conclusions, limitations and perspectives

8.1 Conclusions

An accurate estimation of the surface circulation is crucial because of its direct impact on physical and bio-geochemical water properties. Despite the high kinetic energy observed in the Eastern Mediterranean, the activity of some main features is still debated or unknown because of the relative scarceness and/or the inaccuracies of data. Indeed, the altimetry observations could be inaccurate in the Mediterranean for several reasons, such as the small Rossby radius ($\sim$ 10 km), which is similar to the AVISO resolution, and the degradation of the satellite information near the coastal areas, within 20-50 km from the land. Consequently, eddies can be missed, artificially created, smoothed, or misplaced. Due to these problems, a precise description of the mesoscale activity in the Levantine Sea could be lacking. In the first part of the thesis, we present an improved estimation of the surface circulation in the Levantine sea by reducing the altimetric errors using variation assimilation.

In the first part of the thesis, we presented the variational assimilation method that merges satellite altimetry with drifter observations to improve the representation of the surface circulation of short-term and local events in the eastern and western parts of the Levantine Basin. In chapter 2, we described the method used and its calibration. Then, we proved, in chapter 3, the assimilation's efficiency by comparing the corrected velocities with independent in situ observations and ocean color images available in the Levantine Basin. We found that the method was particularly efficient in high vorticity areas. Indeed, by extending the correction impact for 30 km around drifters trajectories, the assimilation helps in better representing the velocities in all the areas around the assimilated drifter, including all the eddy velocity contours. Our method was more efficient than observing eddies using only drifters or altimetry. Accordingly, we used the assimilation to analyze the activity of evolving eddies in the Levantine Basin in chapters 4 and 5. In chapter 4, the corrected velocities obtained after assimilating EGYPT/EGITTO drifters in 2006, showed that previous observations underestimated the strength of Ierapetra eddy (IE), and it was the only eddy in the basin whose relative vorticity exceeded minus the planetary vorticity (-f). Such an exclusive dominance could be due to the merging of eddies occurring in the IE area. Further to the South, the corrected velocities showed that the Libyo-Egyptian eddies (LEE) are also strong vortices. Because of the bathymetry that increases instabilities, LEE could drift westward in an opposite

direction of the along-slope coastal flow at a constant distance from the Libyo-Egyptian shoreline. In chapter 5, we characterized the activity of three eddies between Cyprus and Lebanon: Cyprus eddy (CE), the so-called North Shikmona eddy (NSE), and South Shikmona eddy (SSE). SSE was shown as a highly variable structure that pinched off from the coast and could merge with smaller eddies in a time scale of a few weeks. The Cyprus Eddy (CE) appeared in the spring at the surface as a stable mesoscale structure with low Eddy Kinetic Energy (EKE) and high Mean Kinetic Energy (MKE) values, contrary to the NSE that registered high EKE and low MKE. The intensification of the NSE occurred when the CE started to weaken. The intense CE blocked the Mid-Mediterranean Jet (MMJ), which prevented the latter from interacting and feeding NSE, thus blocking its development and intensification. Overall, CE was a stable anticyclonic structure offshore exerting control on NSE dynamics, while SSE was more likely related to the instabilities of the coastal circulation.

We showed that the altimetry and the MFS model underestimate the intensity of the eddies in the Levantine Sea. Especially the highly evolving eddies, such as the Ierapetra eddies or coastal eddies close to southern Lebanon that can pinch off and merge in a short time scale. We proved the assimilation capacity ability to detect these quick and short-term mesoscale activities.

Yet, we applied the assimilation method to characterize only some intermittent and short-term local events occurring in the Levantine Basin. Because of the significant spatio-temporal gaps in drifters' coverage, the assimilation could not allow further investigation of the overall mesoscale patterns and their long-term variabilities. To analyze the long-term variability of the surface dynamics, we used machine learning techniques to decompose the different circulation patterns into separated clusters and build a catalog of the several regimes of circulation. While previous studies showed average patterns, emphasizing active and permanent eddies, with less focus on interannual variability or other patterns, this machine learning method can efficiently show the variability of the different structures, including jets and weak flows, on a large temporal scale.

In chapter 7, we presented the machine learning method, which is the self-organizing map (SOM), and the Hierarchical Ascendant Classification (HAC) used to decompose the surface circulation velocity field into five different clusters representing the different circulation patterns. As a result, four clusters were associated with the relatively strong

flow, with either strain (C1 and C2) or vortex (C4 and C5) dominance, while C3 reflected the weakest flowing features, with low MKE and OW. In chapter 8, we decomposed 26 years data set of surface geostrophic velocities of the Eastern Levantine into these five different clusters. We analyzed the variation of the clusters in control boxes that include the main mesoscale features: the Nile box, Mersa-Matruh eddies (MME), Asia Minor current (AMC), Cyprus eddy (CE), Beirut (Bei), and Shikmona eddies (Shke) boxes. The results showed that C4 was rare, while the other clusters permanently occurred in all the boxes. The clusters frequencies varied from one box to another without seasonal or inter-annual variability, and the weak flow cluster C3 dominated the boxes of Nile, Beirut, Shikmona, and Cyprus Eddy. Oppositely, strong flow clusters C2 and C1 dominated AMC and MME, respectively. We highlighted the increasing mesoscale activity in the basin, where eddy-rich boxes are showing a positive trend with time. The cluster of weak flow C3 is being progressively substituted by those of higher kinetic energy and vorticity. We could reveal the sporadic occurrence of the MMJ, which might explain the contradictory statements about the MMJ's existence. We highlighted the crucial role of bathymetry in increasing instabilities and eddies formation Levantine Basin, where most intense and persistent eddies occurred in areas of the extended continental shelf and around Herodotus Abyssal plain. This is a main reason behind the higher mesoscale activity in the Western Levantine Basin, where the bathymetry is more complex than in the East.

8.2 Limitations and perspectives

The assimilation method is dependent on drifters' trajectories, so it is only applied when drifters are available, correcting around and along drifters' trajectories. The method proved its efficiency in providing a more accurate representation of the surface circulation locally and temporarily. When it comes to an extended analysis of the mesoscale activity, assimilation impact will diminish as the corrected velocities are insignificant compared to the total background velocity field. This is why we were limited to eddies in such studies, i.e., because the eddies were trapping drifters in a restricted area for several weeks or months, thus providing a continuous correction of their velocities. Regarding jet or meanders, such an analysis is impossible unless there is a regular deployment of drifters, otherwise, it leads to spatio-temporal gaps and discontinuity. From here, there

is a necessity for efficient drifters deployment strategies. In future works, the use of other in-situ data for assimilation will help to increase the method's accessibility. Argo floats are one of the potentially available instruments. Their positions at deeper depths could be assimilated with models to provide a new representation of Mediterranean deeper currents.

In the second part of the thesis, the self-organizing map (SOM) is based on a large database composed of the zonal and meridional components of the geostrophic current and the Okubo-Weiss parameter, but does not consider biogeochemical properties. In future works, adding other parameters such as temperature, salinity, and chlorophyll would help to understand the biogeochemical processes in the Levantine and the current impact on these parameters. Moreover, the role of climate change in increasing the mesoscale activity in the Eastern Mediterranean would be better understood when adding hydrographic parameters (e.g., temperature, salinity).

SOM has also been efficient in the characterization of the coastal areas by combining high-resolution numerical models with radars observations (Ren et al., 2020) or radar with ADCP datasets, such as in the West Florida Shelf (Liu et al., 2007) and the Long Island Sound tidal estuary (Mau et al., 2007). In the Mediterranean, SOM was applied in the Adriatic Sea using the HF radar measurements (Mihanović et al., 2011). In the future Levantine Sea, specific areas should be targeted, such as the south of Lebanon, where South Shikmona eddy pinched off from the coast, to understand the frequency and the mechanisms driving such events.

We targeted the mesoscale activity between the Herodotus plain and the easternmost part of the Levantine Basin while excluding the Ierapetra eddy and Rhodes Gyre because these would dominate the other features in the Eastern Mediterranean. Extending the analysis to all the Eastern Mediterranean in future work is crucial. Besides considering these eddies with the highest kinetic energy in the East Mediterranean, this extension of the studied area will also include the Libyan coasts, where eddies can flow in an opposite direction of the along-slope eastward circulation, thus perturbing the coastal circulation. This step would help in better understanding the interactions between the main mesoscale features and evaluating the variability of the coastal flow near the Libyan shoreline and its impact on the other part of the basin.

Finally, the actual altimetric velocity field spatial resolution is insufficient to capture the small details (less than $\sim$ 100-150 km), and eddies can be, therefore, missed, artificially created, smoothed, or misplaced. This problem increases near the coast, where satellite information is degraded in areas within 20-50 km from land. When decomposing the surface circulation, we could be missing classes or features. In the future, using higher spatio-temporal resolution products, such as accurate models, or upcoming altimetry missions like SWOT that will provide more reliability close to the coast, will enhance our study by improving the decomposition of the surface circulation by our method.

8.2.1 SWOT mission

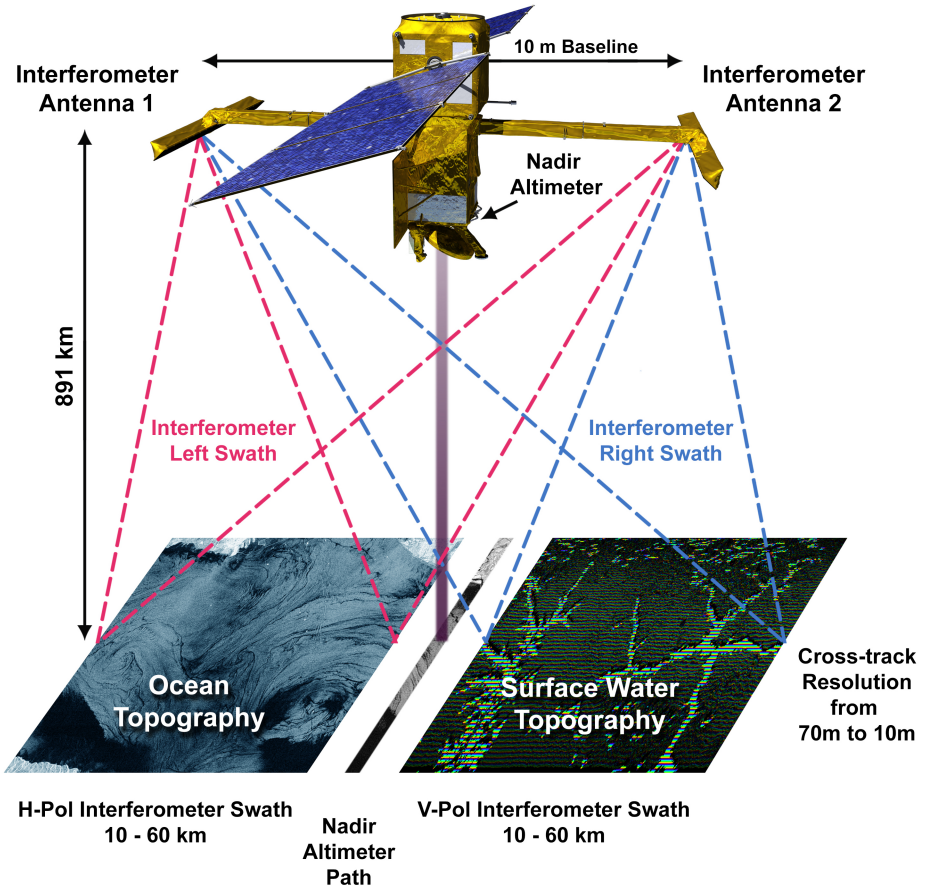

FIGURE 8.1: Schematic representation of the SWOT measurement system (Vignudelli et al., 2019).

The international Surface Water and Ocean Topography (SWOT) is a non-sun-synchronous satellite orbit that will carry a Ka-band Radar Interferometer (KaRIN), providing two swaths of 50 km with a 20-km gap centered at the nadir track (see fig. 8.1) . Such

a central gap can be filled by an additional conventional nadir altimeter, Jason-class. The SWOT mission, considered to be the next generation altimetry, will be launched in November 2022. It will cover a region of 420 km in 60 seconds, supplying a synoptic snapshot of 2D SSH variations, with a temporal resolution of 21 days unaffected by the cloud coverage. Accordingly, the 2-D spatial resolution will increase to values reaching 15-30 km. Such enhancement is revolutionary to resolve small-scale energetic processes maintaining and dissipating the ocean circulation energy, the global heat, nutrients, carbon budgets, and biogeochemical processes. SWOT extends to within 0.5-1.0 km of the coast, which will allow estimating the impact of these small-scale variabilities on the mesoscale activity close to the shore (Fu et al., 2012; Morrow et al., 2019; Wang et al., 2018)

This will provide an upgraded dataset for statistical and machine learning methods. The higher resolution velocities will allow improved decomposition of the surface circulation by potentially detecting classes missed by the actual altimetry, especially in areas of small-scale variation playing a crucial role in coastal eddies formation, such as we saw in the Mersa-Matruh area and Shikmona. However, we should mention that the SWOT mission does not prevent the assimilation importance. On the contrary, it will allow having a better background to assimilate with drifters.

Thesis work presentation and journal papers

The thesis work was presented through:

- a participation (Poster) to the Journées Nationales SWOT in CNES in Toulouse, France (20 - 21 November 2018)

- a participation (Poster) to World Ocean Circulation User Consultation meeting 2019 in ESA-ESRIN in Frascati (Rome, Italy, 21 - 22 February 2019)

- a participation (forum) to European Geo-sciences Union (EGU 2020)

During the thesis, we were able to publish the following journal papers (peer-review):

- Baaklini, G., Issa, L., Fakhri, M., Brajard, J., Fifani, G., Menna, M., Taupier-Letage, I., Bosse, A. and Mortier, L., 2021. Blending drifters and altimetric data to estimate surface currents: Application in the Levantine Mediterranean and objective validation with different data types. *Ocean Modelling*, p.101850.

Résumé de la thèse

Introduction générale

Les courants de surface ont un impact continu et direct sur les propriétés physiques et biogéochimiques de l'eau. Par exemple, la circulation de surface peut transporter des produits chimiques provenant des rivières et des eaux riches vers la mer ouverte oligotrophe. (Escudier et al., 2016; Lehahn et al., 2007; Levy and Martin, 2013; Taupier-Letage et al., 2003). Cette circulation de surface est perturbée par des structures en forme de boucle avec des lignes de courant presque fermées qui sont les tourbillons océaniques. Les tourbillons dont l'échelle horizontale dépasse le rayon de déformation local appartiennent à la méso-échelle. À l'intérieur de ces tourbillons, les propriétés physiques et biogéochimiques, comme la température, la salinité et le carbone, peuvent différer de celles des eaux environnantes. L'eau à l'intérieur du tourbillon peut donc être transportée par la déplacement du tourbillon sans mélange significatif sur de grandes distances (Bonaduce et al., 2021; Chelton et al., 2011, 2007; Zhao et al., 2018). De plus, la dynamique à méso-échelle est associée à des échanges verticaux qui sont importants pour le transport de chaleur de l'atmosphère vers l'océan profond et pour la production primaire (Escudier et al., 2013; Griffies et al., 2015; Pascual et al., 2004).

La surveillance de la circulation de surface à méso-échelle est ainsi cruciale et fait face à des défis importants. Contrairement aux grandes échelles qui sont suivies avec précision grâce à l'altimétrie satellitaire, l'étude de la méso-échelle n'est toujours pas résolue de manière adéquate par l'altimétrie qui pourrait manquer de précision dans les zones à petite échelle et près des côtes. La mer Méditerranée est un exemple de régions où la dynamique de fine échelle domine la circulation actuelle et est mal résolue par les satellites altimétriques actuels.

La mer Méditerranée

La mer Méditerranée est un bassin quasi fermé entouré par le Moyen-Orient et l'Asie mineure à l'est, l'Afrique du Nord au sud, et le continent européen au nord. Elle est formée de deux parties, la Méditerranée orientale et la Méditerranée occidentale, qui sont

reliées par le canal de Sicile. Le courant de surface est caractérisé par une circulation anti-estuarienne, avec un système de flux entrant en surface et de flux sortant en profondeur (Bergamasco and Malanotte-Rizzoli, 2010). Ce dernier est entraîné par le taux d'évaporation qui dépasse les précipitations (Tanhua et al., 2013). Par conséquent, la circulation est directement affectée par le réchauffement climatique. Bien que représentant 0,82 % de l'océan mondial, il abrite entre 4 % et 18 % des espèces marines. Elle est considérée comme un "hot-spot de la biodiversité et du réchauffement climatique" (Bianchi and Morri, 2000), fortement exposée à de nombreuses menaces notamment en raison des côtes très peuplées. En effet, outre le réchauffement qui affecte ses propriétés hydrographiques (température et salinité), la Méditerranée est également soumise à la pollution marine d'origine humaine qui est principalement transportée par les courants. Les mesures hydrographiques précédentes ont montré que trois masses d'eau sont présentes en permanence en Méditerranée orientale (voir fig. 1.1). La première couche est l'eau atlantique modifiée (MAW), formée par l'eau de l'Atlantique entrant dans le bassin et occupant la subsurface entre 30 et 200 m de profondeur, avec une salinité de 38,6. La masse d'eau la plus profonde, située en dessous de 800 m dans la partie orientale, est appelée Eastern Mediterranean Deep Water (EMDW). Elle est froide (13,6 °C), et sa salinité est d'environ 38,7. L'EMDW est principalement formée par le fort refroidissement de l'Adriatique et de la mer Égée. Dans la partie occidentale, l'eau profonde est connue sous le nom d'eau profonde de la Méditerranée occidentale (WMDW), caractérisée par une température de 12,7 °C et une salinité de 38,4. Elle se forme principalement dans le golfe du Lion et est déclenchée par l'atmosphère avec des vents locaux forts (Rixen et al., 2005). La masse d'eau qui sépare l'AW et l'eau profonde est l'eau intermédiaire levantine (LIW). Cette dernière occupe toute la mer et représente $\sim$ 26 % de l'eau totale. Elle a la salinité la plus élevée (38,8-39,0) et est formée par l'évaporation intense qui augmente la salinité de MAW en été. Le LIW interagit avec l'océan Atlantique par le détroit de Gibraltar (Alhammoud et al., 2005; Lascaratos et al., 1999; Ovchinnikov, 1984).

Cette particularité de la Méditerranée est principalement due à un bilan hydrique négatif, où l'évaporation dépasse les précipitations. Il y a donc une entrée continue de l'eau de l'Atlantique (AW) par le détroit de Gibraltar pour compenser la perte d'eau. En s'écoulant vers l'est, l'eau de l'Atlantique devient plus salée et plus dense.

En conséquence, la Méditerranée présente une petite réplique de la circulation thermohaline entraînée par l'échange de chaleur et d'eau douce en surface. En raison de l'effet de Coriolis, l'AW circule dans le sens inverse des aiguilles d'une montre le long du talus continental, formant un grand gyre cyclonique. Ce cournat côtier est perturbé par des tourbillons côtiers, comme dans le bassin algérien, où de petites instabilités et la bathymétrie abrupte augmentent l'énergie cinétique et la vorticité potentielle (Sutyrin et al., 2009; Testor et al., 2005). Les tourbillons formés peuvent atteindre un diamètre de 50-100 km et s'étendre à des milliers de mètres jusqu'au fond (Taupier-Letage et al., 2003). Ils peuvent perturber l'écoulement le long de la pente en bloquant ou en étalant l'AW côtière plus au large. Ensuite, la partie de l'AW qui atteint les côtes tunisiennes se divise en deux branches, où une partie pénètre dans la mer Tyrrhénienne, tandis que l'autre partie progresse dans le canal de Sicile (Jouini et al., 2016). C'est un détroit d'environ 150 km de large et 600 m de profondeur qui joue un rôle crucial dans la connexion et la régulation des échanges entre les bassins de la Méditerranée occidentale et orientale (Menna et al., 2019).

Dans la partie orientale, l'AW côtière continue son écoulement dans le sens inverse des aiguilles d'une montre et interagit avec plusieurs structures intenses caractérisées par leur énergie cinétique élevée (plus de 700 cm^2/s^2)(Gerin et al., 2009; Poulain et al., 2013; Pujol and Larnicol, 2005). Ces caractéristiques de méso-échelle sont décrites comme des blocs distincts : le tourbillon anticyclonique d'Ierapetra (au sud-est de la Crète), les tourbillons de Mersa-Matruh au large des côtes égyptiennes, les tourbillons de Shikmona, le tourbillon de Chypre et le tourbillon cyclonique de Rhodes.

Tourbillon d'Ierapetra (IE)

Le tourbillon d'Ierapetra (IE), situé au sud-est de la Crète, est l'un des tourbillons de mésoéchelle les plus importants et les plus durables de la Méditerranée orientale. Le tourbillon IE est principalement généré par la tension du vent étésien (Larnicol et al., 2002). Il se forme et s'intensifie de la fin de l'été au début de l'automne et peut persister pendant plusieurs mois ou durer toute l'année avant de fusionner avec le nouvel anticyclone formé l'été suivant. Par conséquent, cette fusion peut augmenter la durée de vie de l'IE, qui peut dépasser deux ans (comme l'IE formé en 2005). Nous notons

que parmi les 20 années de surveillance, la formation d'un IE n'était absente que pendant trois années (Ioannou et al., 2017; Mkhinini et al., 2014). L'IE peut soit rester stationnaire, soit se déplacer vers le versant libyen (Hamad et al., 2005). En raison de sa structure robuste et cohérente et des signaux significatifs de température et de hauteur de la surface de la mer, l'IE peut être identifiée à l'aide de différents outils d'observation, notamment l'altimétrie par satellite, les mesures in situ et les images de température de la surface de la mer. Elle peut également être reproduite par des modèles à haute résolution (Alhammoud et al., 2005).

Tourbillons de Mersa-Matruh (MME)

Les tourbillons de Mersa-Matruh (MME), également connus sous le nom de Herodotus Trough Eddies (HTE), se forment au large des côtes libyennes et égyptiennes. Les courants dans cette zone sont instables, générant de grands tourbillons Mersa-Matruh qui perturbent la circulation le long de la pente et alimentent parfois l'IE (Hamad et al., 2005). Ces tourbillons se forment principalement au printemps et en été et peuvent atteindre de grands diamètres (jusqu'à $\sim$ 100-250 km). Lorsque MME dérivent vers le large, la plaine d'Hérodote de 3000 m piège et empêche les tourbillons côtiers à extension verticale de se propager plus loin vers l'est, provoquant ainsi une accumulation de ces tourbillons dans cette zone (Alhammoud et al., 2005; Elsharkawy et al., 2017). Nous constatons que la MME et l'IE sont les tourbillons les plus dominantes dans la Méditerranée orientale (Menna et al., 2012).

Tourbillons de Shikmona (Shke)

Les tourbillons de Shikmona (Shke) représentent un système complexe composé de plusieurs tourbillons cycloniques et anticycloniques dont la taille, la position et l'intensité varient (Gertman et al., 2007; Mauri et al., 2019; Menna et al., 2012). Comme dans le cas de MME, Shke n'est pas une zone de formation de tourbillons, mais une zone où les tourbillons précédemment formés ont tendance à s'accumuler et/ou à fusionner (Hamad et al., 2005). Les instabilités proches du rivage peuvent propager l'AW vers le large pour alimenter le Shke ou générer de petits tourbillons qui peuvent se détacher de la côte et se propager vers le centre du bassin levantin (Alhammoud et al., 2005; Millot and Taupier-Letage, 2005). L'apparition et la disparition continues de tels tourbillons

renforcent la dominance de Shke. Cependant, le suivi de ces tourbillons reste complexe en raison de leur nature évolutive et de la couche chaude de surface qui peut couvrir leurs signatures thermiques.

Tourbillon de Chypre (CE)

Le tourbillon de Chypre (CE) est une autre caractéristique remarquable dans le bassin oriental du Levant et son influence s'étend jusqu'à environ 400 m de profondeur. Contrairement à la MME et au Shke, il ne s'agit pas d'une zone d'accumulation de tourbillons (Zodiatis et al., 2005) et quand CE est actif, il pourrait s'étendre vers l'est, engendrant une grande structure anticyclonique de $\sim$ 100 km de diamètre (Menna et al., 2012).

Notons que d'autres structures de méso-échelle existent dans l'est du Levantin mais sont moins fréquemment observées. Parmi celles-ci, nous mentionnons le tourbillon de Lattakia (LE) qui prend place entre Chypre et la Syrie. LE est un tourbillon cyclonique généré par l'interaction du courant de nord le long des côtes libanaises et syriennes avec le Mid-Mediterranean Jet (Zodiatis et al., 2003), et/ou entre Shke et la côte (Hamad et al., 2005), et/ou par la topographie (Gerin et al., 2009).

Mid-Mediterranean Jet (MMJ)

Le "Mid-Mediterranean Jet" (MMJ) est un écoulement transversal de l'AW au large de l'est du Levant dont la présence a déjà fait l'objet d'évaluations contradictoires. Certains auteurs considèrent le MMJ comme un artefact causé par la déviation de l'AW côtier, entraîné d'un tourbillon à l'autre. En d'autres termes, il s'agit du "paddle-wheel effect" dû à la forte activité mésoéchelle à travers le Levant oriental. Par conséquent, aucun jet remarquable n'a été observé par le programme Mediterranean Forecast System (MFS) (Manzella et al., 2001) ou par les campagnes XBT (Horton et al., 1994; Zervakis et al., 2003) ou par l'important ensemble de données publiées au cours du programme EGYPT/EGITTO entre septembre 2005 et juillet 2007 (Millot and Gerin, 2010), ou même en utilisant des modèles numériques à haute résolution (Alhammoud et al., 2005).

Néanmoins, d'autres observations ont montré un flux transversal clair au milieu du bassin avec une vitesse moyenne comprise entre 10-19 cm/s (Amitai et al., 2010; Poulain et al., 2012). Plus récemment, les images d'anomalies de SST, les traces de bouées et

les courants géostrophiques calculés à partir des champs ADT ont montré un MMJ occasionnel s'écoulant vers le nord des côtes libanaises entre 2016 et 2017 (Mauri et al., 2019). L'investigation des images SST et altimétriques entre 2000 et 2015 a considéré que le MMJ est déclenché par les eaux froides de surface poussées par le vent du nord, atteignant la périphérie nord des côtes lybio-égyptiennes et la forte vorticité au large du LEE qui injectent le MMJ au milieu du bassin levantin oriental (Ciappa, 2021).

Outils d'observation

Les estimations actuelles restent difficiles car le champ de courants est affecté par des flux à petite échelle qui changent rapidement. De plus, les tourbillons sont des structures très énergétiques qui peuvent interagir, se diviser ou fusionner et induire des structures à plus petite échelle (d'Ovidio et al., 2004; Laxenaire et al., 2018; Le Vu et al., 2018; Taupier-Letage et al., 2003). Historiquement, Nielsen (1912) a été le pionnier dans la description de la circulation de surface en Méditerranée comme un simple gyre clonique à l'échelle du bassin dans lequel le courant le plus fort est proche de la côte. L'augmentation des outils d'observation disponibles a permis d'améliorer la description de la circulation de surface et la compréhension des mécanismes générant les caractéristiques de méso-échelle. Ces outils d'observation sont des observations in-situ ou par satellite.

Observations in-situ

Les mesures in situ sont des outils d'observation utilisés pour évaluer avec précision des paramètres tels que la température, la salinité, la pression, la vitesse et la direction des courants marins, la hauteur d'eau, l'état de la mer, la turbidité et les propriétés physico-chimiques.

Les bouées de surface sont des plateformes autonomes in-situ. Elles sont utilisées pour étudier les courants océaniques et d'autres paramètres comme la température ou la salinité. Une fois libérées, elles suivent le courant océanique. En raison de leur flottabilité positive, ces outils lagrangiens les retiennent en même temps que l'écoulement bidimensionnel à la surface ou près de la surface de l'océan. Les bouées ont l'avantage de fournir une description précise de la circulation actuelle.

Observations par satellite

L'altimétrie par satellite est une technique radar qui mesure la distance entre le satellite et la surface de l'océan à l'aide d'un signal radar. L'altimètre est placé sur un satellite et émet une onde radar (signal) vers la surface de la terre. La surface de la terre reflète le signal émis puis le satellite reçoit le signal réfléchi. Le temps écoulé entre l'émission et la réception du signal radar est proportionnel à la hauteur du satellite. La distance avec la surface instantanée de l'océan est déterminée par le traitement des données. Avec une orbite précisément déterminée, les distances calculées donnent la hauteur de la surface de la mer (SSH) par rapport à un ellipsode de référence.

L'altimétrie par satellite est considérée comme révolutionnaire pour les systèmes mondiaux d'observation des océans et est utilisée dans diverses applications. L'un des principaux objectifs de l'altimétrie par satellite est de surveiller les courants océaniques, fournissant ainsi un enregistrement continu de la topographie de la surface de l'océan mondial depuis 1991. En effet, la couverture spatio-temporelle ininterrompue fournie par l'altimétrie permet aux océanographes d'étudier les changements du niveau de la mer, de l'échelle méso à l'échelle globale, depuis plus de 25 ans : (Bosch et al., 2014; Fu and Cazenave, 2000; Hamlington et al., 2013; Willis, 2010).

Comme l'altimétrie fournit un ensemble de données très étendu, différentes méthodes peuvent être appliquées pour caractériser la circulation de surface. L'une de ces approches est la Self Organizing Map, (SOM) une méthode de regroupement très performante. Il s'agit d'un outil efficace pour classer et extraire des caractéristiques, déjà appliqué dans différents domaines. Dans le domaine océanographique, le SOM a été appliqué pour caractériser la variabilité interannuelle, saisonnière et événementielle des vents et des températures de surface de la mer Richardson et al. (2003), et des concentrations de pigments de phytoplancton El Hourany et al. (2019). L'outil s'est également avéré efficace pour la caractérisation des zones côtières en combinant des modèles numériques à haute résolution avec des observations radars (Ren et al., 2020), ou un radar avec un ensemble de données ADCP, comme dans le West Florida Shelf Liu et al. (2007), et l'estuaire tidal de Long Island Sound (Mau et al., 2007). En Méditerranée, SOM a été appliqué dans la mer Adriatique en utilisant les mesures radar HF (Mihanović et al., 2011), et dans le canal de Sicile, en utilisant 46 ans de modèle

haute résolution (Jouini et al., 2016). Cette approche a permis de décomposer la circulation de surface dans le canal de Sicile en modes reflétant la variabilité de la circulation dans l'espace et le temps aux échelles saisonnière et interannuelle. SOM a également été capable de fournir une prédiction du courant de surface dans la zone côtière peu profonde (Kalinić et al., 2017) et d'identifier les types fonctionnels de phytoplancton dans la mer Méditerranée en utilisant une approche de biorégionalisation (Basterretxea et al., 2018; El Hourany et al., 2019).

Limitations de l'atimétrie

Bien que la fusion des altimètres contribue à améliorer la représentation des caractéristiques de méso-échelle (Pascual et al., 2007), la résolution réelle reste insuffisante pour traiter la circulation océanique à petite échelle. De plus, d'autres erreurs et imprécisions apparaissent, notamment près des zones côtières où les informations satellitaires sont dégradées (à moins de 20-50 km de la terre, Cipollini et al. (2010)). De nombreux facteurs sont à l'origine de ces inexactitudes, comme la contamination des terres, les corrections inexactes des marées et de la géophysique, la topographie dynamique moyenne inexacte et la suppression incorrecte des effets atmosphériques à haute fréquence à la surface de la mer (Caballero et al., 2013). Le problème s'accentue en Méditerranée où la connaissance précise de la MDT reste un problème, en raison de la présence de détroits étroits et d'un nombre élevé d'îles, et du faible rayon de déformation de Rossby en Méditerranée (environ 10 km) qui rend l'altimétrie insuffisante pour capturer les petits détails (Rio et al., 2014). En raison de la résolution grossière à la fois dans l'espace et dans le temps des altimètres et du fait que les structures à méso-échelle se déplacent continuellement, les tourbillons peuvent être manqués, créés ou mal placés (Mkhinini et al. (2014), Ioannou et al. (2017)).

Assimilation de données

L'utilisation de l'altimétrie pour étudier les courants de surface est efficace, mais il subsiste parfois un certain manque de précision. D'autre part, les observations in-situ ne fournissent pas une couverture spatio-temporelle continue. Ainsi, différentes approches sont utilisées pour améliorer les vitesses eulériennes (obtenues par altimétrie) basées sur des observations lagrangiennes. Une des méthodes les plus utilisées est

l'approche statistique, qui est conditionnée par la disponibilité de grands ensembles de données. La combinaison de l'altimétrie avec des observations de grandes données bouées a déjà été réalisée avec succès : par exemple dans le Golfe du Mexique Berta et al. (2015); Carrier et al. (2014); Muscarella et al. (2015), la Mer Noire Kubryakov and Stanichny (2011); Stanichny et al. (2016), le Pacifique Nord Uchida and Imawaki (2003). Dans la mer Méditerranée, Poulain et al. (2012), Menna et al. (2012) ont appliqué des statistiques pseudo-eulériennes en utilisant des modèles de régression pour améliorer la représentation de la circulation de surface.

Une autre méthode courante consiste à utiliser les positions d'observation in-situ pour modifier l'état du modèle dynamique. Dans ce contexte, il existe deux approches principales de l'assimilation de données : L'assimilation variationnelle, basée sur la théorie du contrôle optimal, ou statistique, basée sur l'estimation statistique optimale. Les méthodes séquentielles reposant sur l'interpolation optimale ont été testées avec succès dans l'assimilation de données de position in-situ et de plusieurs types de modèles opérationnels, tels que les modèles de circulation générale avec stratification simplifiée (Molcard et al., 2005, 2003). Dans l'approche d'assimilation variationnelle, les corrections de vitesse sont obtenues en minimisant une fonction objectif mesurant la différence entre les observations et les variables correspondantes du modèle. Le gradient de cette fonction objectif est calculé par l'intégration du modèle adjoint. Les méthodes variationnelles reposant sur des calculs adjoints et prenant en compte la variation temporelle des observations sont appelées 4D-Var (Kamachi and O'Brien, 1995; Mead, 2005; Nodet, 2006). D'autres méthodes assimilent les vitesses des bouées au lieu de leurs positions (Carrier et al., 2014; Muscarella et al., 2015).

En mer Méditerranée, Taillandier et al. (2006b) a utilisé un modèle d'advection pour obtenir les positions des bouées en supposant que les vitesses étaient indépendantes du temps. Cette méthode a permis le développement de l'algorithme d'analyse variationnelle lagrangienne (LAVA). Il a été appliqué pour corriger les champs de vitesse du modèle à l'aide de trajectoires de bouées (Taillandier et al., 2006a, 2008) et plus tard adapté à plusieurs autres applications telles que l'assimilation de modèles (Chang et al., 2011; Taillandier et al., 2010). Il a également été appliqué à l'estimation des courants de surface dans le Golfe du Mexique (Berta et al., 2015).

Plus récemment, Issa et al. (2016) a utilisé l'assimilation variationnelle qui mélange

l'altimétrie avec les observations des bouées. Elle a prouvé son efficacité dans la région du Levant oriental, plus précisément entre le Liban et Chypre. Elle était basée sur la mise en correspondance des positions des bouées observées avec celles prédites par un modèle d'advection simple, prenant en compte l'effet du vent et imposant une condition sans divergence sur la correction de vitesse. La correction de la vitesse s'est faite de manière continue dans le temps en assimilant en une seule fois une trajectoire entière des bouées, en utilisant une fenêtre de temps glissante. Les analyses de sensibilité ont montré que la vitesse s'améliorait de manière significative même avec seulement quelques bouées, et qu'elle nécessitait très peu de ressources informatiques et convergeait rapidement.

Motivation et objectifs de la thèse

La circulation de surface de la Méditerranée est énergique et très variable à la fois aux échelles spatiale et temporelle. Par conséquent, l'écoulement de surface ne peut pas être facilement caractérisé en termes de moyennes temporelles ou de variabilité saisonnière (Menna et al., 2012). Bien qu'une énergie cinétique élevée soit observée dans tous les bassins, la partie orientale est encore moins étudiée que son homologue occidentale. De plus, dans le bassin levantin, des controverses subsistent car les observations altimétriques pourraient être biaisées en Méditerranée en raison du faible rayon de déformation de Rossby d'environ 10 km, ce qui rend la résolution altimétrique insuffisante pour capturer les petits détails. De plus, l'information satellitaire se dégrade près des zones côtières à moins de 20-50 km des terres (Cipollini et al., 2010; Rio et al., 2014). Ce manque de précision de l'altimétrie n'est pas compensé par l'augmentation des observations in-situ en Méditerranée orientale. Malgré quelques campagnes d'observation, telles que EGITTO/EGYPT (2006), NEMED (2009), Altifloat (2011), et CINEL (2017), la densité des observations in-situ reste insuffisante. Par conséquent, certaines des principales caractéristiques sont encore débattues, comme le Mid-Mediterranean Jet. De même, le fonctionnement de certains structures est encore inconnu, comme le courant proche des côtes Libanaises. En effet, les seules observations de ce courant ont été limitées aux images de température de surface de la mer sans considérer son comportement dynamique. Dans cette thèse, nous présentons un produit hybride qui fusionne l'observation des bouées déployés avec l'altimétrie satellitaire pour améliorer la représentation de la circulation de surface dans le bassin levantin après avoir testé

l'efficacité de la méthode en comparant les champs de vitesse résultants avec d'autres observations in-situ. Cette approche permettra une caractérisation plus précise des événements locaux se produisant dans le Bassin du Levant. Cependant, il existe des lacunes spatio-temporelles importantes dans la couverture des bouées où pendant plusieurs années, aucune bouée n'a été déployée dans toute la Méditerranée orientale, et lorsqu'elles ont été déployées, la zone qu'elles ont couverte était limitée par rapport à la zone totale (voir fig. 1.9). Ainsi, l'assimilation permettrait d'étudier l'activité mésoéchelle intermittente et à court terme.

Pour analyser la variabilité à long terme de la dynamique de surface, nous avons décomposé un jeu de données altimétriques étendu en groupes révélant les différents schémas de circulation à l'aide d'une technique d'apprentissage automatique, la self-organizing map (SOM). Il s'agit d'une méthode de clustering non supervisée qui permettra de construire un catalogue des différents régimes de circulation et de comprendre les principaux facteurs affectant la dynamique de surface.

Chapitre 2

Dans ce chapitre, nous présentons la méthode d'assimilation utilisée dans la première partie de la thèse pour l'analyse des événements à court terme de l'activité mésoéchelle dans le bassin levantin. Elle est basée sur une approche variationnelle (Issa et al., 2016) qui minimise une fonction de coût $\mathcal{J}$, qui mesure les distances entre les positions des observations (drifter) et celles prédites par un modèle d'advection. L'algorithme d'assimilation mélange l'altimétrie, le vent et les positions des bouées pour obtenir un champ de vitesse de surface corrigé. Dans un premier temps, nous présentons les données utilisées dans l'algorithme, puis nous détaillons la méthode elle-même et sa calibration.

Chapitre 3

Nous présentons une validation objective de l'assimilation variationnelle appliquée dans le bassin levantin. L'évaluation est faite en comparant les champs de vitesse corrigés avec d'autres observations indépendantes. Ces observations sont des données in-situ (courantomètre, glider, et bouée indépendante) et des images de la couleur de l'océan.

Les métriques utilisées pour la validation ont prouvé que l'algorithme était capable d'améliorer la représentation de la circulation de surface même dans une zone de haute vorticité. La Figure 3.1 montre qu'après avoir assimilé les positions des bouées piégées dans un tourbillon détecté au même moment à partir d'images à haute résolution de la chlorophylle, les lignes de courant résultant du champ de vitesse corrigé sont plus cohérentes avec la forme et l'emplacement du tourbillon tel que révélé par l'image de la couleur de l'océan. Une présentation détaillée de ces validations est présentée dans le Baaklini et al. (2021) de l'annexe A.

Chapitre 4

Dans ce chapitre, nous assimilons l'ensemble des données des bouees déployés dans le Levantin occidental pendant la campagne EGYPT/EGITTO pour obtenir un champ de vitesse corrigé en 2006. Ensuite on caractérise les deux tourbillons les plus dominantes dans cette zone : le tourbillon d'Ierapetra (IE) et le tourbillon Libyo-Egyptien (LEE), qui en raison de leur forte activité à méso-échelle, ils ont piégé des bouées pendant plusieurs semaines. Bien que l'IE soit une structure spatialement étendue et que les caractéristiques de ses contours de vitesse varient significativement avec leur distance au centre, nous avons pu prouver dans ce chapitre que notre méthode est un outil efficace qui améliore le champ de vitesse de l'IE. La méthode d'assimilation étend l'impact de la correction à 30 km autour des trajectoires des bouées, ce qui permet de mieux représenter les vitesses dans toutes les zones autour des ces bouées, y compris les contours de vitesse maximale (V_{max}). Cette approche est plus efficace que l'observation de l'IE en utilisant uniquement les observations des bouées ou par l'altimétrie ou des modèles qui ont tendances à sous-estimer ces tourbillons. Le champ de vitesse corrigé montre que la dominance de l'IE avec MKE dépassant 2000 cm^2/s^2, surtout en été, est renforcée par l'apparition rapide des tourbillons dans cette zone, suivie par leur fusion avec l'ancien IE, ce qui augmente drastiquement la vorticité de ce dernier. Bien que ces événements soient potentiellement plus fréquents, le déploiement limité des bouées ne permet pas de corriger les vitesses de l'IE les autres années. Plus au sud, on montre par l'assimilation que le LEE est actif et peut se déplaçer à une distance constante du littoral libyo-égyptien. Ceci est dû à la bathymétrie complexe de cette zone qui augmente les

instabilités, ce qui permet au LEE de rester actif plusieurs mois tout en se déplaçant vers l'ouest dans une direction opposée au courant côtier.

Chapitre 5

Dans ce chapitre, après assimilation nous caractérisons l'activité de trois tourbillons présents entre Chypre et le Liban: en 2017, le tourbillon de Chypre (CE) et le tourbillon dit de Shikmona Nord (NSE), et en 2009, le tourbillon de Shikmona Sud (SSE). SSE se montre comme une structure hautement évolutive qui peut apparaître près de la côte, se pincer, dériver vers le large et fusionner avec d'autres tourbillons sur une échelle de temps de quelques semaines. Alors que nous montrons que le tourbillon de Chypre (CE) est plus stable, caractérisé par une variabilité de l'énergie cinétique (EKE) relativement plus faible et une énergie cinétique moyenne (EKE) plus élevée par rapport à NSE. CE pourrait affecter NSE, où nous montrons que c'est pendant l'affaiblissement de CE que NSE s'est intensifié. En effet, un CE fort pourrait bloquer le MMJ, ce qui empêche ce dernier d'interagir et d'alimenter NSE, empêchant ainsi son développement et son intensification. Nous montrons dans ce chapitre que les vitesses corrigées amélioraient la représentation des tourbillons côtiers, tels que le SSE, notamment son intensification lorsqu'il fusionne avec un autre tourbillon. Les corrections les plus élevées des données altimétriques se produit lorsque la position du nadir du satellite était à plus de 40 km de la périphérie du tourbillon. En conséquence, l'assimilation permet de réduire efficacement les imprécisions de l'atimétrie lors de l'interpolations. De là, on surligne la nécessité d'augmenter le déploiement de bouées dans l'est du Levantin, en particulier dans la zone côtière où les tourbillons évoluent rapidement et où les incertitudes altimétriques du satellite augmentent, et où les modèles pourraient complètement manquer ces tourbillons.

Chapitre 6

Dans la première partie de la thèse, les vitesses obtenues à partir de l'assimilation variationnelle ont mis en évidence des activités tourbillonnaires à court terme, durant plusieurs semaines dans le Levantin, en se déplaant, fusionnant, ou en interagissant avec d'autres tourbillons. Cependant, puisque l'assimilation reste fortement dépendante des

bouées, nous n'avons donc pu caractériser que des événements de court terme. Par conséquent, pour analyser la variabilité à long terme de la dynamique de surface dans le bassin du Levantin, nous avons utilisé une autre approche basée sur des méthodes de machine learning et utilisant des données altimétriques. Il s'agit d'une méthode de classification non supervisée, la "self organizing map" (SOM), et "Hierarchical Ascendant Classification" (HAC) qui permet de décomposer les courants de surface en clusters reflétant différents régimes de circulation. Dans ce chapitre, nous présentons les données, et nous introduisons la méthode d'apprentissage automatique utilisée ainsi que sa calibration.

Chapitre 7

Dans ce chapitre, nous décomposons les courants de surface du bassin levantin entre 1993 et 2018 en cinq différents clusters qui sont obtenus par les méthodes SOM et HAC, comme expliqué dans le chapitre précédent. Ensuite, nous analysons la variabilité de ces clusters afin d'améliorer la compréhension de l'activité des principales structures à méso-échelle et des facteurs qui régissent leurs comportements. En suivant la variabilité des clusters, nous montrons que la circulation de surface est complexe et divisée en plusieurs boîtes énergétiques. On met en évidence l'activité mésoéchelle croissante dans le bassin, où ces boîtes riches en tourbillons montrent une tendance positive avec le temps. Le cluster représentant de flux faibles sont progressivement remplacés par ceux d'énergie cinétique et de vorticité plus élevées. Nous montrons l'occurrence sporadique du MMJ, ce qui pourrait expliquer les évaluations contradictoires sur l'existence du MMJ. On met en évidence le rôle crucial de la bathymétrie et de l'intensité du flux côtier dans l'augmentation des instabilités et la formation de tourbillons dans la mer du Levant. En conséquence, les tourbillons les plus persistants apparaît dans les zones caractérisées par un fort flux côtier et un plateau continental étendu ou autour de la plaine abyssale d'Hérodote, expliquant ainsi les disproportions de fréquences et de persistance des tourbillons dans le Levantin

Limitations et perspectives

La méthode d'assimilation dépend des trajectoires des bouées, elle n'est donc appliquée que lorsque les bouées sont disponibles, en corrigeant autour et le long des leurs trajectoires. Par conséquent, cette méthode conduit à des lacunes et des discontinuités spatio-temporelles. La méthode a prouvé son efficacité en fournissant une représentation plus précise de la circulation de surface localement et temporairement. Lorsqu'il s'agit d'une analyse étendue de l'activité à méso-échelle, l'impact de l'assimilation diminuera car les vitesses corrigées sont insignifiantes par rapport au champ de vitesse de l'altimétrie. C'est pourquoi nous nous sommes limités aux tourbillons dans ces études, car ils piégeaient les bouées dans une zone restreinte pendant plusieurs semaines ou mois, fournissant ainsi une correction continue de leurs vitesses. Lorsqu'il s'agit de jets ou de méandres, une telle analyse est impossible à moins d'un déploiement régulier de bouées, d'où la nécessité de stratégies efficaces de déploiement. Dans les travaux futurs, l'utilisation d'autres données in-situ pour l'assimilation permettra d'augmenter l'accessibilité de la méthode. Les flotteurs Argo sont l'un des instruments potentiellement disponibles. En effet, les positions des flotteurs Argo à grande profondeur pourraient être assimilées à des modèles pour fournir une nouvelle représentation des courants profonds de la Méditerranée.

Dans la deuxième partie, la carte SOM est basée sur une grande base de données composée des composantes zonales et méridionales du courant géostrophique et du paramètre d'Okubo-Weiss, sans tenir compte des propriétés biogéochimiques. Dans les travaux futurs, l'ajout d'autres paramètres tels que la température, la salinité et la chlorophylle aiderait à comprendre les processus biogéochimiques dans le Levantin et l'impact actuel sur ces paramètres. De plus, le rôle du changement climatique dans l'augmentation de l'activité mésoéchelle en Méditerranée orientale serait mieux compris en ajoutant les paramètres de température et de salinité. Nous avons ciblé l'activité mésoéchelle entre la plaine d'Hérodote et la partie la plus orientale du bassin levantin, en excluant le tourbillon d'Ierapetra et le gyre de Rhodes, car ils domineraient les autres caractéristiques de la Méditerranée orientale. Il est crucial d'étendre l'analyse à toute la Méditerranée orientale dans les travaux futurs. Outre le fait que les tourbillons ayant l'énergie cinétique la plus élevée émergent, cette zone inclut également les côtes libyennes, où les tourbillons peuvent circuler dans une direction opposée à la circulation vers l'est le long de

la pente, perturbant ainsi la circulation côtière. L'extension de la zone étudiée permettrait de mieux comprendre les interactions entre les principales caractéristiques de méso-échelle et d'évaluer la variabilité de la circulation côtière près de la côte libyenne et son impact sur l'autre partie du bassin. De plus, la résolution spatiale du champ de vitesse est limitée à 0,125° × 0,125°. Une telle résolution est insuffisante pour capturer les petits détails, et les tourbillons peuvent être manqués, créés artificiellement, lissés ou mal placés. Ce problème s'accentue près de la côte, où les informations satellitaires sont dégradées près des zones côtières situées à moins de 20-50 km de la terre. Lors de la décomposition de la circulation de surface, nous pouvons manquer des classes ou des caractéristiques. Dans le futur, l'utilisation de produits à plus haute résolution spatio-temporelle, tels que des modèles précis, ou les prochaines missions altimétriques comme SWOT qui fourniront plus de fiabilité près de la côte, amélioreront la décomposition de la circulation de surface par notre méthode.

Appendix A

Blending drifters and altimetric data to estimate surface currents: Application in the Levantine Mediterranean and objective validation with different data types

Ocean Modelling 166 (2021) 101850

Contents lists available at ScienceDirect

Ocean Modelling

journal homepage: www.elsevier.com/locate/ocemod

Blending drifters and altimetric data to estimate surface currents: Application in the Levantine Mediterranean and objective validation with different data types

Georges Baaklini [a,b], Leila Issa [c,*], Milad Fakhri [b], Julien Brajard [a,d], Gina Fifani [a,b], Milena Menna [f], Isabelle Taupier-Letage [e], Anthony Bosse [e], Laurent Mortier [a]

[a] Sorbonne University, UPMC Univ Paris 06 CNRS-IRD-MNHN, LOCEAN Laboratory, 4 place Jussieu, 75005 Paris, France
[b] National Centre for Marine Sciences-CNRSL, P.O. Box 189, Jounieh, Lebanon
[c] Department of Computer Science and Mathematics, Lebanese American University, Beirut, Lebanon
[d] Nansen Environmental and Remote Sensing Center, Bergen, Norway
[e] Aix Marseille Univ., Universite de Toulon, CNRS, IRD, MIO UM 110, 13288, Marseille, France
[f] National Institute of Oceanography and Applied Geophysics (OGS) Borgo Grotta Gigante, 42/c 34010 Sgonico (Trieste), Italy

ARTICLE INFO

Keywords:
Altimetry
Lagrangian data
Data assimilation
Drifters
Surface velocity field
Levantine Mediterranean

ABSTRACT

An improved estimation of the surface currents in the Levantine Basin of the Mediterranean sea is crucial for a wide range of applications, including pollutants transport and nutrients distribution. This estimation remains challenging due to the scarcity or shortcomings of various data types used for this purpose. In this paper, we present an objective validation of a variational assimilation algorithm that blends geostrophic velocities derived from altimetry, wind-induced velocities, and drifter positions, to continuously obtain velocity corrections. The assessment of the validation impact was based on available independent in-situ data (current meters, gliders, and independent drifters) and satellite ocean color images. In all cases, the improvement was shown either qualitatively (position of the eddies) or quantitatively.

1. Introduction

The surface circulation in the southern part of the Mediterranean sea along the North African coasts is characterized by the presence of unstable currents that generate mesoscale eddies (see, e.g, Robinson et al. (1992), Millot and Taupier-Letage (2005), Amitai et al. (2010) and Schroeder et al. (2012)). These eddies have diameters of 10–100 km and lifetimes that can span several months to years (see, e.g, Puillat et al. (2002), Hamad et al. (2006), Mkhinini et al. (2014) and Pessini et al. (2020)). Mesoscale activity in the Eastern Mediterranean is intense with high eddy kinetic energy (more than 700 cm^2/s^2) recorded historically (see, e.g, Robinson et al. (1992), Pujol and Larnicol (2005) and Gerin et al. (2009)). Mesoscale eddies can interact, split or merge, and induce smaller-scale structures (shear-eddies and filaments). Thus tracking them is a real challenge (see, e.g, Taupier-Letage et al. (2003), d'Ovidio et al. (2004), Laxenaire et al. (2018) and Le Vu et al. (2018)). All these structures can transport coastal waters, trap and advect on large distances tracer anomalies. Such activity has a continuous and direct impact on biogeochemical water properties, especially in the redistribution of nutrient-rich coastal waters into the oligotrophic open sea (see, e.g, Taupier-Letage et al. (2003), Lehahn et al. (2007), Levy and Martin (2013) and Escudier et al. (2016)) and the dispersion of pollutants. An accurate and continuous estimation of surface circulation is therefore needed, but remains challenging.

Even though more and more data, in particular, operational products from the Copernicus Marine Service (marine.copernicus.eu) are available for estimating surface currents at (sub)mesoscale, each on their own, have their limitations. A powerful tool that is widely used to describe the mesoscale features of surface circulation is the state of the art satellite altimetry. Multi-mission gridded altimeter products originated from Copernicus Marine Service have the advantage of providing uninterrupted and continuous global surface velocities (Caballero et al., 2013). Nevertheless, there are still uncertainties associated with these products: relative low spatial resolution of current radar altimetry; satellite information is degraded near the coastal areas within 20–50 km from land (Cipollini et al., 2010); incorrect removal of high-frequency atmospheric effects that exist at the sea surface (Caballero et al., 2013), Mean Dynamic Topography (MDT) is not always precisely known in the basin. Moreover, the problem accentuates in the

* Corresponding author.
E-mail address: leila.issa@lau.edu.lb (L. Issa).

https://doi.org/10.1016/j.ocemod.2021.101850
Received 15 May 2021; Received in revised form 6 July 2021; Accepted 23 July 2021
Available online 3 August 2021

Mediterranean Sea where a precise knowledge of MDT is still an issue, due to the presence of narrow straits and a high number of islands, and the small Rossby radius of deformation of around 10 km that makes the altimeter-resolution insufficient to capture the small details (Rio et al., 2014). Due to the coarse resolution in both space and time of the altimeters, and to the fact that mesoscale structures move continuously, eddies can be missed, artificially created, smoothed or misplaced (Mkhinini et al., 2014; Ioannou et al., 2017). Characterizing eddies using altimetry can lead to an underestimation of the eddies' density, especially the small ones. These eddies may be not captured by altimetry or tend to be aliased into larger structures compared to the true eddies (Amores et al., 2018).

In-situ observations are used as a tool to complement and/or validate altimetry (Le Traon and Hernandez, 1992). Drifters have the advantage of being autonomous and relatively inexpensive. They are in-situ Lagrangian tools following the ocean current once they are released and adequately equipped with a drogue (Poulain et al., 2012). Characterized by positive buoyancy, this restrains them along with the two-dimensional flow at the surface or near-surface of the ocean. Even though they help in providing a precise description of the surface circulation, their spatio-temporal distribution is not continuous, because they are typically short-lived and their spatial distribution is intrinsically uneven.

When large data sets are available, combining altimetric and drifter data can be done using statistical approaches (see, e.g, Niiler (2003), Uchida and Imawaki (2003), Poulain et al. (2009), Maximenko et al. (2009), Poulain et al. (2012), Menna et al. (2012) and Stanichny et al. (2016)). Alternatively, data can be assimilated in a variational approach in which corrections of the velocity are obtained by minimizing an objective function measuring the difference between observations and their corresponding model variables. Variational methods that take into account the temporal variation within the optimization are called 4D-Var (Kamachi and O'Brien, 1995; Mead, 2005; Nodet, 2006; Carrier et al., 2014; Muscarella et al., 2015). A more detailed review of various assimilation methodologies can be found in Issa et al. (2016).

From the application point of view, merging altimetry and in-situ data for a better estimation of the sea surface circulation has previously had several successful applications: for example in the Gulf of Mexico (Carrier et al., 2014; Muscarella et al., 2015; Berta et al., 2015), the Black Sea (Kubryakov and Stanichny, 2011; Stanichny et al., 2016), the North Pacific (Uchida and Imawaki, 2003), and the Mediterranean Sea (Taillandier et al., 2006; Menna et al., 2012; Issa et al., 2016), each of them using different methodologies for merging.

Validating these merged data sets using in-situ current meter data was done in Taillandier et al. (2006), where the comparison focused on the net transport time series representing the total volume flux over a selected area. Referring to long-term current meter measurements available across the Corsica Channel, the assimilation showed a 10% increase of the estimated net transport leading to instantaneous transport values that are closer to those observed by the current meter.

The variational assimilation algorithm used by Issa et al. (2016) proved its efficiency in the Eastern Levantine Mediterranean region, specifically along the Lebanese coast and in the region between Lebanon and Cyprus. Sensitivity analyses showed that the velocity estimation can be improved significantly even with only a small number of drifters. The algorithm that was developed relies on continuously correcting the altimetry-derived velocity by matching the observed drifters positions with those predicted by an advection model, taking into account the wind effect and imposing a divergence-free condition on the correction. The algorithm needed very few computational resources and converged quickly.

The contribution of the current work is two-fold: (i) a further extension of the application of the previous algorithm by Issa et al. (2016) in the Levantine Mediterranean and (ii) an objective validation of the algorithm, using reliable tools/data independent of the algorithm itself. In particular, we use four different types of independent data: first, a current meter moored off Libya is used to validate the algorithm results in terms of velocity intensity and direction. Second, a glider-derived near-surface absolute geostrophic velocity perpendicular to its trajectory is compared with the projected velocities obtained after assimilation. Third, we reproduce the path of a non-assimilated drifter by the simulation of its position using velocities obtained by the assimilation of two other drifters. Finally, we compare streamlines of the corrected velocity field with the shape of an eddy obtained by an ocean color satellite image. This offers a qualitative but useful comparison. Except for products from Copernicus operational forecast models or reanalysis, we believe that no other surface current data are available in the Levantine region for such a comparison.

The paper is structured as follows: we introduce the data used in the assimilation and validation in Section 2. In Section 3, we provide a brief recap of the algorithm used for the assimilation, as well as the sensitivity test done to optimally choose the parameters. In Section 4, we present the metrics used for validation. Finally, in Section 5, we show the results of the assimilation experiments, as compared with in-situ current meter data, ocean color satellite images, gliders. We also show the results of the independent drifters experiment.

2. Data

The study focuses on the Eastern part of the Mediterranean, that is less investigated than its western counterpart, more specifically on the Levantine basin. The data used for this study are listed in Sections 2.1–2.7:

2.1. Drifters data

The EGYPT/EGITTO program (Eddies and Gyres Paths Tracking, Taupier-Letage et al. (2007)) focused on the Eastern Mediterranean southern part spanning the period 2005–2007. It provided an extensive deployment of satellite-tracked drifters which helps in characterizing mesoscale and sub-mesoscale structures. (see the ~2-years trajectories animation on southeastern Mediterranean surface drifter database: nettuno.ogs.trieste.it/doga/sire/egitto/database_egitto/movies/sep05-oct07.avi). These drifters were tracked by the global Argos System. Their time series were interpolated at 0.5 h (Poulain et al., 2013). Data were then low-pass filtered using a Hamming filter with a cut-off period at 36 h to eliminate high-frequency current components (tidal and inertial currents).

In addition to those, we used drifters from the Surface Circulation in the Northeastern Mediterranean (NEMED) project from 2009 to 2010. NEMED is an observational program releasing drifters between Cyprus and the Middle East. Drifters time series were interpolated at 6 h. From this large drifters data set (97 drifters from EGYPT/EGITTO and 31 drifters from NEMED) (Menna et al., 2018), we selected drifters depending on each validation experiment. All drifters used in the assimilation are equipped with a positioned drogue located at 15 m depth, which reduces the wind forcing impact.

2.2. Altimetry data

Geostrophic surface velocity fields are processed by the DUACS (Data Unification and Altimeter Combination System) multi-mission altimeter data processing system and distributed by E.U. Copernicus Marine Service Information (CMEMS). The SLA computation provides the Absolute Dynamic Topography (ADT) and geostrophic currents. The gridded products are estimated by an optimal interpolation that merges measurements from several altimeter missions: HY-2 A, Jason-2, Jason-1, T/P, ENVISAT, GFO, ERS1/2. The interpolation provides a consistent and homogeneous database. Data were daily mapped at a resolution of 1/8°.

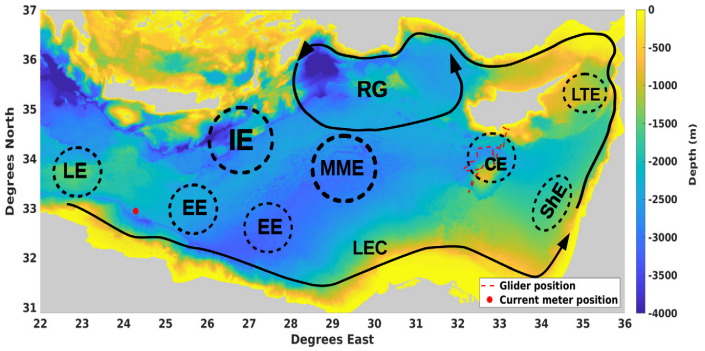

Fig. 1. A schematic representation of the main current structures based on the observations of Gerin et al. (2009) and Menna et al. (2012) in the Levantine basin (RG: Rhodes gyre, IE: Ierapetra eddy, LE: Libyan eddies, EE: Egyptian eddies, LEC: Libyo-Egyptian current, MME: Mersa-Matruh eddies (also known as Herodotus trough eddies), CE: Cyprus eddies, ShE: Shikmona eddies, LTE: Lattakia eddy). The location of the in-situ data used for validation is compared to these structures. The red star represents the mooring C_3 location off the Libyo-Egyptian coasts, during the EGYPT/EGITTO program, supporting the 60m-deep current meter used for the validation. The red dashed line south of Cyprus represents the glider trajectory. All is overlayed on a bathymetry map.

2.3. Wind data

Six-hourly wind data were obtained from ECMWF ERA-Interim products (Dee et al., 2011) at 10 m above the surface. Data was re-sampled on a half an hour time step. The product spatial resolution is approximately 0.7 degrees. Wind velocities were interpolated at a resolution of 1/8° at the same grid point as the AVISO background data although the actual resolution is much coarser.

2.4. Current meter

The first comparison focused on the area of the Libyo-Egyptian coast, where the anticyclonic eddies generated by the Libyo-Egyptian Current move offshore (Hamad et al., 2006). Between April 2006 and April 2007, 7 moorings each equipped with current meters were deployed off Libya during the EGYPT/EGITTO program (Taupier-Letage et al., 2007) to provide information on the circulation of the water masses. However, since only sub-surface moorings could be used because of safety issues, the surface layer of Atlantic Water was sampled at 60–100 m deep, and used to compare with the drifter (~15 m deep).

We selected the current meter that met the following criteria: a long record (since some moorings have been cut accidentally), fixed at ~60–100 m deep, and located on a mooring with a contemporary drifter passage. The shallowest current meter of the C_3 mooring (see Fig. 1) was the only one to meet all the criteria, as the mooring C3 was located near the passage path of the 1st selected drifter (Argos number: 57306) and providing data at less than 100 m depth.

2.5. Mediterranean Forecasting system (MFS)

The Mediterranean Forecasting System is a coupled hydrodynamic (from NEMO v3.6) and wave (provided by WaveWatch-III) model with data assimilation components implemented over the Mediterranean Basin. In-situ vertical profiles of temperature and salinity (from XBT, CTD, Argo floats) are assimilated with satellite Sea Level Anomaly along-track data (from Jason1&2, Cryosat, Envisat, Altika). The product quality assessment is done by comparing with quasi-independent satellite and in-situ observations. The model spatial resolution is 1/16°, and the product is computed on 72 unevenly-spaced vertical levels. The depths levels are unevenly spaced and the thickness varies from 3 m at the surface to 300 m at the bottom. The first level depth is at 1.5 m while the deepest one is at 5000 m (Tonani et al., 2008). The model outputs were used to evaluate the comparability between the current vector velocity fields at the current meter and the drifters depth as detailed in Section 4.1.

2.6. Gliders

Gliders are a type of robotic underwater vehicle that perform saw-tooth trajectories (Testor et al., 2019). The movement of the internal weights allows the glider to change its buoyancy. Thus, it dives or climbs in the water column. Moreover, the lift generated by the wings moving through the water converts vertical force into forwarding motion. In the context of the "Eye of the Levantine" experiment, gliders were deployed south of Cyprus in November and December 2010. Targeting the Cyprus warm core eddy, the transects followed a butterfly pattern near the Eratosthenes Seamount, extending to a maximum depth of 1000 m, collecting seawater characteristics such as temperature and salinity (Hayes et al., 2011). The water density sections and the depth-averaged current data derived from these glider positions are used to estimate profiles of absolute geostrophic velocity perpendicular to their trajectories (Eriksen et al., 2001). During the campaign, six gliders were deployed off Limassol towards the Cyprus eddy. From these gliders, we used the geostrophic velocities from the named "TRIESTE-1" glider. It was a coastal glider that dived at 200 m depth maximum and was circulating close to a drifter (Argos number: 92060). The obtained velocities used for the comparison corresponded to the near-surface absolute geostrophic velocities perpendicular to the glider track and averaged in the upper 20 m. The glider sampled the upper 200 m, and geostrophic shear was integrated to the surface from a low-pass filtered density section, where variability smaller than 15 km corresponding to unbalanced isopycnal displacement was removed by a moving average. This approach was applied in numerous studies in the past (see e.g. Bosse and Fer (2019)).

2.7. Ocean color

Eddies are oceanic structures with high vorticity able to modify the seawater physical distribution properties, thus affecting the distribution of marine phytoplankton communities (McGillicuddy Jr, 2016). Previous high-resolution chlorophyll images have shown that even small swirling and filamentary patterns of chlorophyll could be determined from satellite imagery. Therefore high resolution ocean color images could be an efficient tool for mesoscale features monitoring such as eddies. Their shape and location could be detected from chlorophyll-a concentration images, leading to a better understanding of these physical processes (Sarangi, 2012). These chlorophyll-a images detected the shape of an eddy trapping a contemporary drifter (Argos number: 57307). MODIS-Aqua chlorophyll level-2 data, at 1 km spatial resolution, corresponding to the days of assimilation for comparison were acquired from GSFC-NASA.

3. Assimilation algorithm

The correction is based on a variational assimilation method described in Issa et al. (2016). Observations of drifter's positions are available every Δt. We denote the background surface velocity field by

$$\mathbf{u}_m^b = \mathbf{u}^b(m\Delta t),\ m = 1, 2, \ldots, M, \tag{1}$$

where this field is two dimensional $\mathbf{u}_m^b = (u_m^b, v_m^b)$, and where m is the integer time index. This field is corrected by matching observed drifter's positions with those predicted by an advection model.

The background velocity field ($\mathbf{u}_m^b$) used is the sum of a geostrophic component provided by altimetry ($\mathbf{u}_m^{\text{geos}}$) and an ageostrophic component accounting for the effect induced by the wind ($\mathbf{u}_m^{\text{wind}}$)

$$\mathbf{u}_m^b = \mathbf{u}_m^{\text{geos}} + \mathbf{u}_m^{\text{wind}}. \tag{2}$$

This wind-induced velocity is computed by the equation of Poulain et al. (2009) (for drifters that are attached with a drogue).

$$\mathbf{U}_m^{wind} = 0.007\exp(-27^\circ i) \times \mathbf{U}_m^{10} \tag{3}$$

where $\mathbf{U}_m^{wind} = u_m^{\text{wind}} + iv_m^{\text{wind}}$ is the drifter velocity due to the wind effect, and $\mathbf{U}_m^{10} = u_m^{10} + iv_m^{10}$ represents the wind velocity at 10 m above the surface. Both are expressed as complex numbers. The wind speed above the sea surface varies considerably at a very short time scale. Thus the wind-induced velocity field contribution to the total velocity depends on the varying weathering conditions.

An incremental approach (Talagrand and Courtier, 1987) is used so that the minimization is done for the incremental corrections $\boldsymbol{\delta}\mathbf{u}$ invariant in time within the time window of size T_w. The objective function to be minimized is:

$$\mathcal{J}(\delta\mathbf{u}) = \sum_{i=1}^{N_f} \sum_{m=1}^{\lfloor T_w/\Delta t \rfloor} \left\| \mathbf{r}_i^b(\mathbf{u}_m^b) + \delta\mathbf{r}_i(\delta\mathbf{u}) - \mathbf{r}_{i,m}^{\text{obs}} \right\|^2 + \alpha_1 \|\delta\mathbf{u}\|_{\mathbf{B}}^2 + \alpha_2 \sum_{j,k} (\nabla \cdot \delta\mathbf{u})^2, \tag{4}$$

where N_f is the number of drifters, i is the index of the drifter and Δt is the sampling time of the observations. $\mathbf{r}_{i,m}^{\text{obs}}$ represents the observed position of drifter i at time $m\Delta t$. The term $\mathbf{r}_i^b$ (resp. $\delta\mathbf{r}_i$) is the position of the drifter i estimated by an advection model calculated from the background field $\mathbf{u}_m^b$ (resp. from the incremental correction $\boldsymbol{\delta}\mathbf{u}$). The advection model consists of a numerical integration of the advection equation, for example, using an Euler scheme. The first term measures the misfit between the observations and the positions of drifters simulated considering the advection by the surface velocity field. The second component requires the corrected field to stay close to the background velocity. Here the $\mathbf{B}$-norm is defined as $\|\psi\|_{\mathbf{B}}^2 \equiv \psi^T\mathbf{B}^{-1}\psi$, where $\mathbf{B}$ is the error covariance matrix. The error covariance matrix $\mathbf{B}$ is obtained using the diffusion filter method of Weaver and Courtier (2001). The choice of the length scale R of the correction that enters in the error covariance matrix can be done in the context of the sensitivity analyses. The last component is a constraint on the geostrophic part of the velocity, required to stay divergence free. This term is added to ensure a physical correction, avoiding artifacts especially near the coasts. The weights α_1 and α_2 correspond to the confidence given to the respective terms of the cost function, relative to the observation error term. Because the cost function is defined within a multiplicative constant, it is safe to set a standard confidence of one to the observation error term, assuming that each observation error is equal and de-correlated from the other. The relative confidence in the background α_1, and in the non-divergent constraint α_2 cannot be objectively determined. So they are determined empirically using sensitivity analyses (see Section 3.1). After the minimization, we compute a corrected velocity field:

$$\mathbf{u}_{\text{m}}^{\text{corr}} = \mathbf{u}_m^b + \delta\mathbf{u} \tag{5}$$

Because $\delta\mathbf{u}$ is constant inside a time window and to obtain a smooth, time-dependent velocity field, a sliding window T_w, of time shift σ is used to obtain smoother corrections in time. A detailed description of the algorithm is found in Issa et al. (2016).

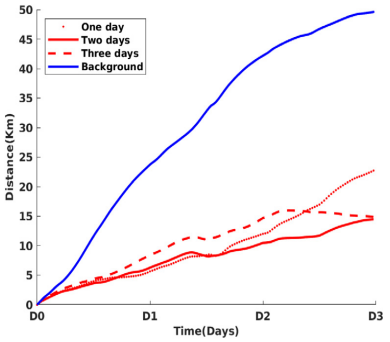

Fig. 2. Distance variation $d(t)$ as in Eq. (6) between the simulated positions and real observations. The red lines represent the simulations after assimilation using a temporal window size T_w of one, two, and three days. The blue line represents the distance between the observed drifter and the one simulated by the background velocity field.

3.1. Sensitivity tests

Sensitivity tests allow to tune the following parameters of the algorithm: the temporal size of the window (T_w), the divergence coefficient (α_2) and the length scale R of the correction that enters in the error covariance matrix. In Fig. 10, we show the setup of the sensitivity experiment: three drifters were circulating close to each other near the Libyan coast. Two drifters, shown in colors, are assimilated to produce a corrected velocity field. The resulting corrected velocity field is used to simulate the trajectory of the third independent drifter (shown in black). The metric used is the mean separation distance between the simulated and observed trajectories:

$$d(t) = \frac{1}{N_w} \sum_{j=1}^{N_w} \|\mathbf{r}_j(t) - \mathbf{r}_j^{obs}(t)\|^2, \tag{6}$$

where N_w is the number of windows used during the simulation.

Temporal window sizes T_w of 1, 2, and 3 days were compared. Fig. 2 reveals that a window size of 2 days maximally reduces distances. The improvement reaches around 70% compared to the background, 5% and 9% more when compared to T_w of 1 and 3 days respectively. To produce a smooth time-dependent velocity, we use a sliding window of time-shift σ. We opted for σ of half a day to have a smoother correction.

The other two parameters seem not to have a significant impact on the assimilation. For example, if the value of α_2 is changed from 5×10^{-6} to null, the solution is modified by only around 0.7%. For the length scale parameter, varying R from 20 to 30 km improves the correction by around 3% only.

Consequently, in the further experiments we apply the algorithm with the following parameters: T_w = 2 days, σ = half-day, $\alpha_2 = 5\times10^{-6}$, and R = 30 km.

4. Validation method

4.1. Current meter

On the 1st of June 2006, the 1st selected drifter (OGS drifter identification number: 3627) circulated near the C_3 mooring at a distance shorter than 30 km. This passage allows us to apply the algorithm to the area containing C_3. The drifter trajectory is assimilated starting from this day, denoted by D_0. The experiment extends until the 14th of June (D_{13}).

The current meter was fluctuating around 73 m deep during the drifter passage, as is revealed by its pressure reading. On the other hand, drifters track the current at ~15 m. To assess the validity of the comparison with these two different depths, we computed the temporal

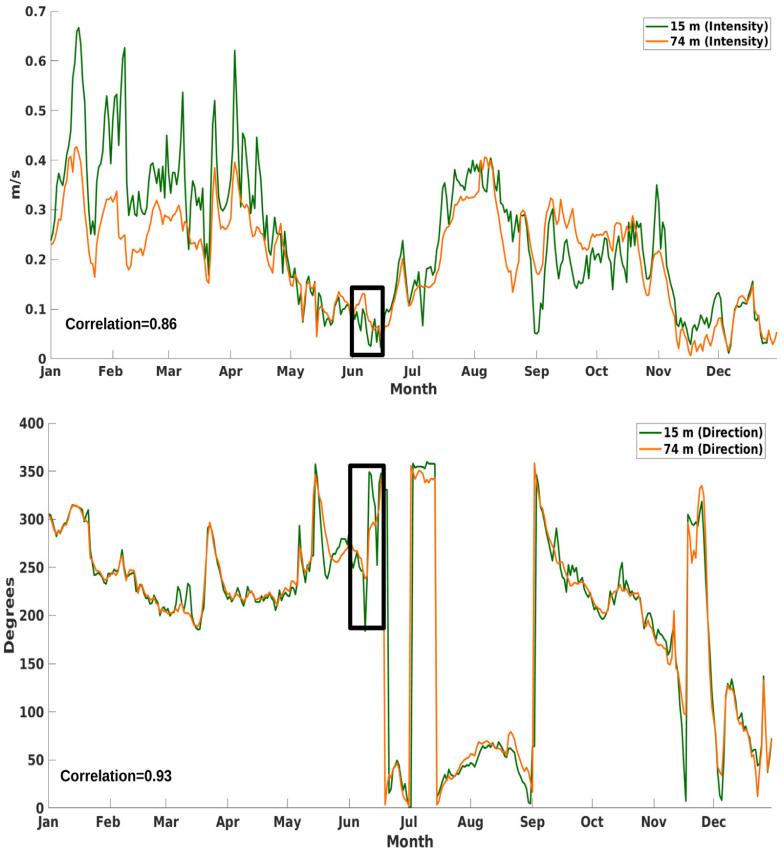

Fig. 3. Temporal variations of the current velocity (upper panel) and the direction (lower panel) at 74 (orange) & 15 m (green) depth, as shown by MFS. The period of the experiment (1–14 Jun 2006) is indicated by the black rectangle.

variation of the velocity field (intensity and angle) at both depths using the products derived from the Mediterranean Forecasting System.

The variation of the intensity and direction of the current in the year 2006 is presented in Fig. 3 at 15 m and 74 m depth. It includes the days of the experiments dating from the 1st and the 14th of June. The jumps in the direction (from mid-June, until mid-July) are due to the periodic definition of the direction. During the experiment, the difference between the velocities at the two depths is 0.033 m/s on average (with a standard deviation of 0.074 m/s); the difference in the direction is ~ 0.3° on average (with a standard deviation of 37°). These differences are small compared with the natural variability of the signal (standard deviation of 0.23 m/s for the velocity and 97° for the angle). Moreover, there is a high correlation existing between both levels, with a correlation of 0.93 for the direction and 0.86 for the intensity.

It should be mentioned that the mixed layer was not deep enough to include the current meter ~ 70 m depth, so the comparison between the drifter and the current meter underneath could induce a bias. However, as discussed above, the MFS results show the currents at the two different depths agree well in terms of direction and intensity during the time of the experiment. Thus, the current meter measurements at 73 m depth can still be used to validate the corrected surface velocity estimated at 15 m depth.

Let us denote the current meter velocity by $\mathbf{u}_m^{\text{ref}}$, and use $\mathbf{u}_m$ for the fields associated with the assimilation experiment (either the background or the corrected one). The zonal and meridional components are: $\mathbf{u}_m^{\text{ref}} = (u_m^{\text{ref}}, v_m^{\text{ref}})$, and $\mathbf{u}_m = (u_m, v_m)$. Similarly, we use θ^{ref} for the current-meter velocity angle variation and θ for either the background or the corrected velocities.

For an overall quantification of the assimilation impact, we calculated the L_2 norm error between $\mathbf{u}_m^{\text{ref}}$ and $\mathbf{u}_m$ velocity fields.

$$E_m = \sqrt{(u_m^{\text{ref}} - u_m)^2 + (v_m^{\text{ref}} - v_m)^2}. \tag{7}$$

Low values of E_m^2 reveal a similarity in both intensity and direction between the compared vectors.

4.2. Comparison with glider

A drifter from the NEMED project was circulating close to a glider providing geostrophic velocities perpendicular to its trajectories. We use the glider-derived velocities ($\mathbf{u}_m^{\text{ref}}$), averaged between 0 and 20 m, as observations to be compared with the experimented velocity fields ($\mathbf{u}_m$). The experimented velocities are interpolated and orthogonally projected to the glider trajectory as explained in the data section.

To assess the assimilation efficiency, we compute the average error (E_a) between the projected experimented velocities and the glider-derived velocities.

$$E_a = \frac{1}{M_g}\left(\frac{\sum_{m=1}^{m=M_g} \|\mathbf{u}_m\| - \|\mathbf{u}_m^{ref}\|}{\sum_{m=1}^{m=M_g} \|\mathbf{u}_m^{ref}\|}\right) \times 100, \tag{8}$$

where M_g represents the total glider positions used for comparison, $\|\mathbf{u}_m\|$ the norm of the background and assimilated projected velocities at each glider position and $\|\mathbf{u}_m^{ref}\|$ represents the glider-derived velocities norm at each position.

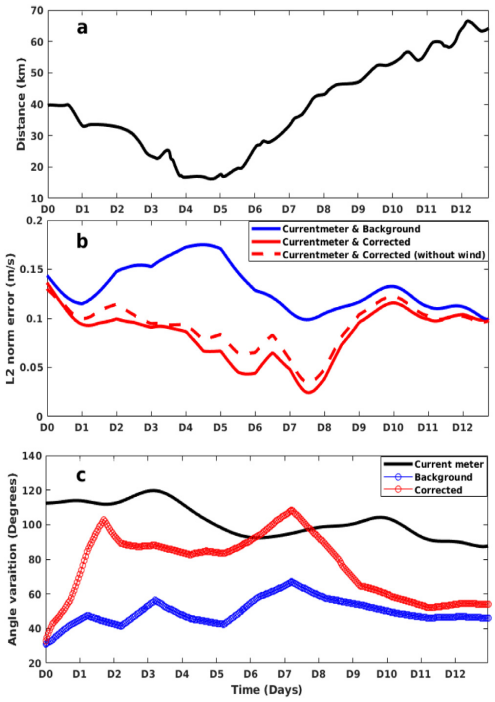

Fig. 4. The upper panel shows the distance evolution between the drifter and the current meter C_3 location. The middle panel shows the L_2 norm error variation of the background (blue) compared to the corrected velocity field with (solid) and without (dashed) adding the ageostrophic component during the assimilation. The lower panel represents the time series of the current direction as derived from the current meter C_3 (black line), the background (blue line), and the corrected (red line) currents.

4.3. Comparison with ocean color data

A drifter that was circulating in a high vorticity area is assimilated from the 1st of February 2006 until 28th of June 2006. The mesoscale structure trapping the drifter was also well defined in terms of shape and location by a contemporary chlorophyll image. A visual observation of the eddy is possible by drawing the streamlines resulting from the background and assimilated velocity fields. So the eddy shape could be represented by the flow lines of the resulting velocity fields. A better agreement with the eddy as observed from the chlorophyll image is expected after correction (in terms of shape and location).

5. Results

In this section we show all the results of the comparisons from the background, the corrected velocity field and the independent current measurements derived from different sources (current meter, glider, ocean color, drifters).

5.1. Comparison with current meter

The first comparison focused on the area off the Libyo-Egyptian coast (see Fig. 1).

In the period between the 1st (D0) and the 14th (D13) of June 2006, the drifter 57306 (Argos number), that collects data close to and concurrently to the C3 current meter, is selected for the assimilation.

Fig. 4c shows the temporal variation of the current direction as recorded by C_3. This change in the angle current direction of C_3 was then compared to the variations of the background and corrected velocity fields. Significant improvements are seen starting from D_0 until D_{12}. During this period, the direction of the corrected velocity is close to the one measured by C_3. Furthermore, the improvement in direction reaches more than 40 degrees after correction, especially between D_2 and D_8. A significant shift in the current direction is detected between D_0 and D_2, varying from 60 to 140 degrees within only a few hours during these dates. This adjustment corresponds to the time when the drifter gets closer to C_3, from ~ 40 to ~ 30 km (see Fig. 4a).

Fig. 4b confirms the previous results and demonstrates how the assimilation reduces the overall L_2 error. This error is reduced after correction starting from D_0. During D_4, and D_5, the largest improvement from the background is observed. In fact, the amplitude of the corrections depends on two main factors: the initial error of the background and the distance between the drifter and the point of interest (here the C_3 location). The difference between the background and the corrected velocity field increases with decreasing distances. When the drifter gets far away again (>30 km), the impact of the assimilation diminishes progressively.

Excluding the ageostrophic component from the background during the assimilation does not have a significant impact on the resulting corrected velocity field. As Fig. 4b shows, adding the wind component to the background velocity slightly reduces the overall $L2$ error between the corrected and current-meter velocity fields. During the experiment, the wind forcing was oriented towards the South-Southeast and had an average speed of 7 m/s.

The average velocity field during the days of the experiments (from D_0 until D_{12}) is presented in Fig. 5. After the drifter passage, the resulting assimilated velocity vectors (red vectors) are modified in a way that is consistent with the mean-field recorded by the current meter (dark vector).

Fig. 6 shows the daily average velocity field on the $4^{th}(D_3)$, $6^{th}(D_5)$, $8^{th}(D_7)$, $12^{th}(D_{11})$ of June 2006. On D_3, when the circulating drifter is still far from the current meter location, the corrected velocity field near C_3 is close to the background. Both velocity fields are different from the current meter. The average current as recorded by C_3 is oriented to the North-Northwest, while both velocity fields are oriented North-Northeast. In D_5 when the drifter gets closer to C_3, an important shift of the corrected velocity field vectors is noticed. The agreement between the C_3 and the corrected current vectors improves, up to the best match on D_7. In D_{11}, when the drifter becomes distant, there is no more impact of the correction on the velocity field around C_3. As a result, the background and the assimilated velocity fields are again similar.

5.2. Comparison with glider

We targeted a drifter from the Surface Circulation in the Northeastern Mediterranean (NEMED) project releasing drifters between Cyprus and the Middle East from summer 2009 to spring 2010.

Fig. 7a shows that starting from December 3rd (the glider deployment date) and until the 21st of December 2006, there was a drifter circulating near the deployment location in the South of Cyprus. Although they were many intersections between the glider and drifter trajectories, most of these intersections occurred at different times. Only between the 10th and 11th of December 2009, the TRIESTE-1 glider circulated at a distance less than 30 km with the drifter 92060 (see red square). We assimilate the latter, and obtain corrected velocities around the glider location.

The glider surfaces approximately every hour, with three observations starting from 7 pm on the 10th and seventeen observations on the 11th. That is a total of twenty observations during these two days (Fig. 7b). The background and the assimilated velocity fields are then interpolated at these glider positions (P). Because the derived geostrophic velocities are perpendicular to the glider trajectory, the interpolated background and assimilation are orthogonally projected onto the glider trajectory.

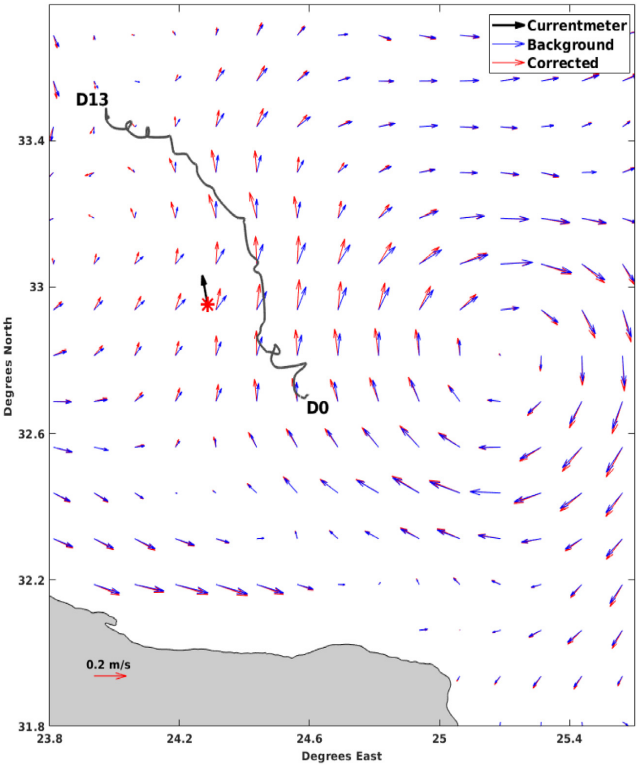

Fig. 5. Average velocity field during the 14 days of the experiment between the 1st and the 14th of June 2006. The drifter trajectory is represented by the solid black line moving from the South to the North. The black vector represents the average current recorded by C_3 (represented by the red star).

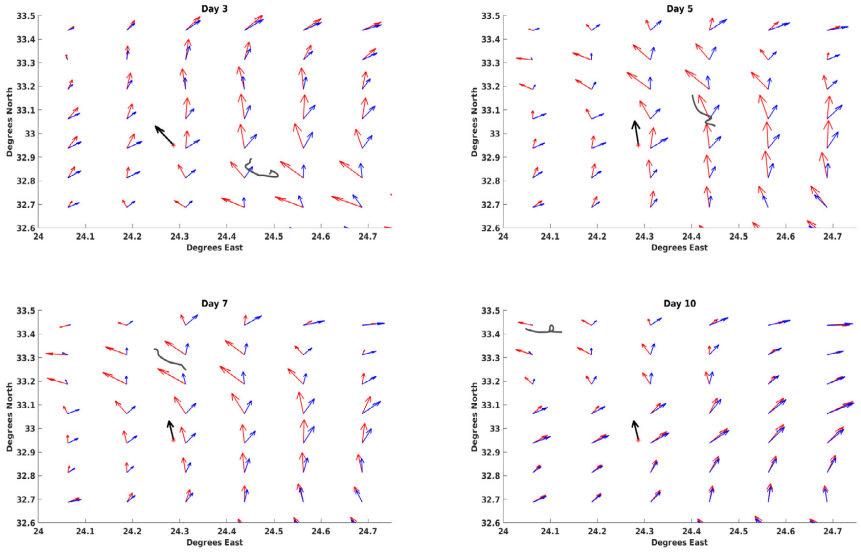

Fig. 6. The daily average velocity field on the 4th, 6th, 8th, 12th of June 2006 of the current meter C_3 (black), the background (blue) and the corrected (red) together with the drifter trajectory (black curve).

In Fig. 7c, we show the background and corrected fields, together with the velocity computed using the glider data. It can be seen that the projected velocity norm shows how the background tends to underestimate the intensity with a maximum value reaching 0.08 m/s. After correction, the resulting velocity norm increases. When we compare it with the glider results (around 0.14 m/s), the corrected

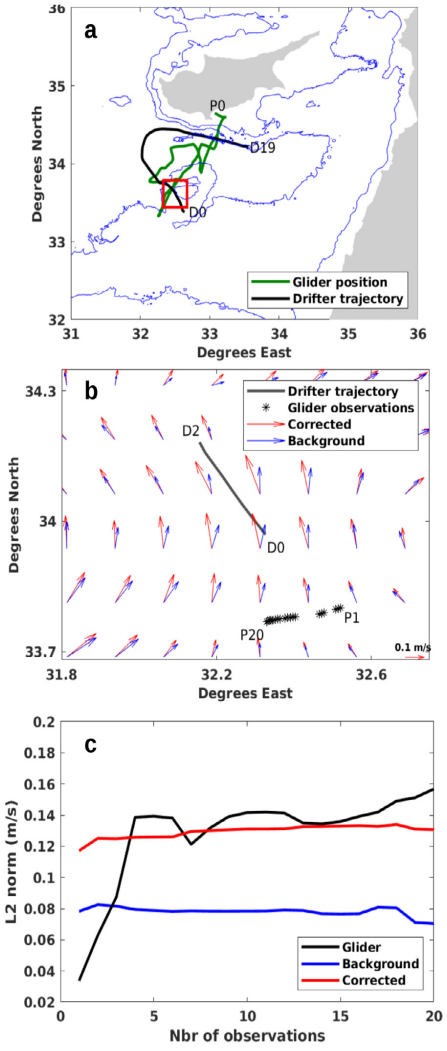

Fig. 7. Glider (green) and drifter (dark) trajectories between the 10th and 11th of December 2009. The red rectangle represents the location where the intersection between the glider and drifter trajectories is contemporary. The two days of the glider passage near the drifter are schematized in the middle panel. The glider positions are represented by black stars. All of this is overlaid on the average velocity field of the background and the assimilation. The lower panel represents average velocity norm of the vectors orthogonally projected at the glider positions of the background (blue) and the corrected (red) velocity field. They are compared with the glider-derived velocity norm (dark).

values are closer (0.12 m/s) than the background values (0.08 m/s). The overall error E_a has been reduced by more than 20% by the assimilation. This improvement is important despite two factors that could tend to penalize the assimilation. First, the different time scale of observation, where the sampling time of the gliders is hourly while the sampling frequency of the drifter is every six hours. The second factor is the distance between the assimilated drifter and the observed glider positions (P). The distance between the nearest sample drifter position and P1 is more than 25 km. This distance increases continuously and reduces the correction impact.

5.3. Comparison with high resolution ocean color images

We targeted a drifter (Argos number: 57307) that was released in 20.85°E, 33.055°N from the 1st of February 2006 until 28th of June 2006. This drifter was stuck in one of the highly active eddies off the Egyptian coasts (see Fig. 8) for several weeks starting May 17, 2006. A contemporary chlorophyll image was available during this period, specifically on May 20, showing the eddy shape and location.

The assimilation experiment was done for 6 days, starting from the 17th of May. The streamlines of the velocity fields before and after correction were compared with the simultaneous chlorophyll-a concentration image in Fig. 9. The observed streamlines of the velocity field after correction (red) are close to the chlorophyll-a image in terms of shape and location, while the background velocity field presents a shift in location and difference in size. The latter reveals an extension of the eddy towards the southeast.

5.4. Reconstruction of independent drifter trajectory

As explained in Section 3.1, we used three drifters trapped in the anticyclone noted LE1 off Libya (see Figs. 2 and 5 in Gerin et al. (2009); see also Fig. 1 in Sutyrin et al. (2009)). Between the 8th and the 27th of May 2006, we assimilated the positions of the Argo numbers 59777 and 59774 to simulate the position evolution of the third one (57312) based on the surrounding velocity field (see Fig. 10).

The prediction of the future drifter positions after correcting the velocity field is closer to the real trajectory during the 20 days of the experiment (as shown in Fig. 11). Predicted positions after correction (in red) reveal trends that are similar to the real ones. On the other hand, predictions based on the background velocities differ from the real observations as they do not show circular patterns.

The lower panel presents the evolution in time of the distance $d(t)$ as in Eq. (6), between the observed position and the simulated position of the independent drifter before and after correction. The simulated drifter position is reinitialized every 2 days to the position of the real drifter. The distance is computed for each of these 2 days windows (T_w) and then averaged to produce the average position error in time. Fig. 11 shows a decrease of this error after the correction. The distance between the expected and the real observation reaches around 40 km using the background velocities. The assimilation reduces these distances to less than 9 km. Moreover, the correction lowers the uncertainties (standard deviation of the error over each of the 10 windows) as compared to those of the background (see Fig. 11). The standard deviation of the background distances increases continuously with time reaching more than 19 km at the end of the window after two days. After correction, these variations are significantly reduced and barely increase with time, and do not exceed 3.7 km. In other words, on average, the assimilation allows us to reduce the error from 40 to less than 9 km after two days when simulating the positions of independent drifter not included in the assimilation.

6. Perspectives

When in-situ drifters data are available, the assimilation could be applied on a larger spatio-temporal scale. From all the 97 drifters of the EGYPT/EGITTO campaign, 29 drifters covering the area between the Libyo-Egyptian coasts and Crete (between ~21° to ~31°E, and ~30° to ~36°N in 2006 have been assimilated. In general, altimetry strongly underestimates the Mean Kinetic energy (MKE) and Eddy Kinetic Energy (EKE) of the velocity field (Pujol and Larnicol, 2005; Gerin et al., 2009; Poulain et al., 2012). So we expect the assimilation to improve those estimates obtained from altimetry. Fig. 12 reveals that the MKE increases after assimilation, especially when targeting a main regional mesoscale feature such as Ierapetra eddy (IE) (Amitai et al., 2010; Ioannou et al., 2017). After correction, the MKE in IE is more than 700 cm^2/s^2 on all sides with a maximum of ~760 cm^2/s^2. For the

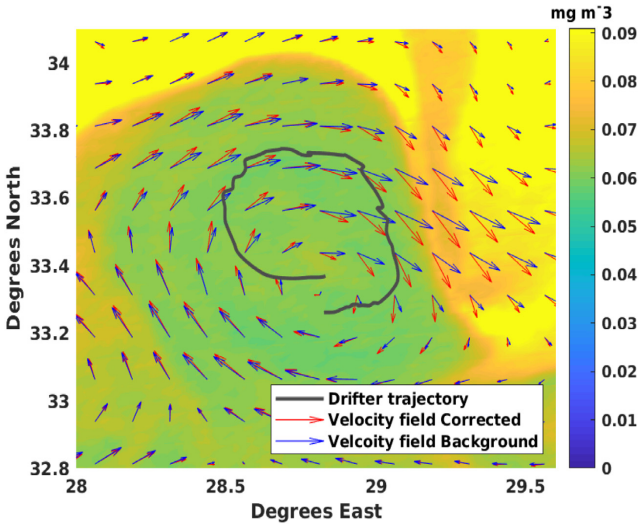

Fig. 8. Average of the background (blue) and the corrected (red) velocity fields after six days of assimilation starting from the 17th of May 2006. Drifter trajectory is represented in gray. All of them are overlaid on a high-resolution chlorophyll-a image of 20 May 2006.

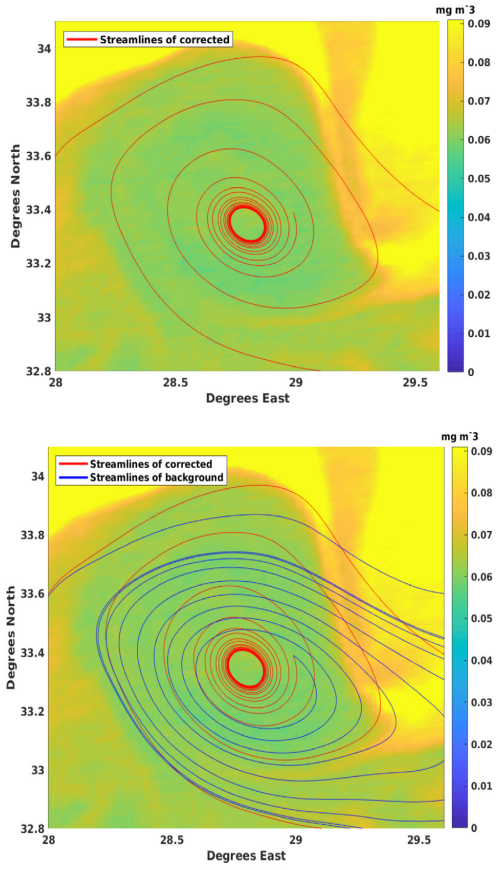

Fig. 9. Velocity field streamlines after correction (upper panel) compared with the background (lower panel) overlaid on chlorophyll-a image of 20 May 2006.

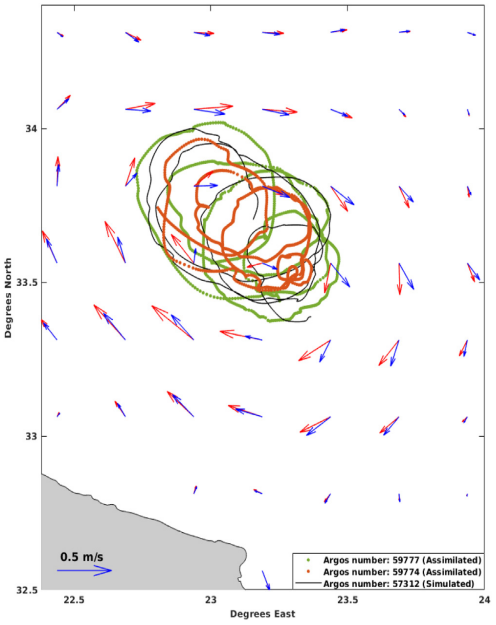

Fig. 10. The trajectory of the three drifters circulating close to each other between 8th and the 27th of May 2006. The dark line represents the real trajectory of the non-assimilated drifter, while the lines in green and orange represent the trajectories of the assimilated drifters. These trajectories are overlayed on the resulting average velocity field before (blue) and after assimilation (red).

background, MKE reaches a maximum of ~630 cm^2/s^2 but only locally. The eastern and the western sides of the eddy have low values of MKE as they do not exceed ~350 cm^2/s^2.

Moreover, EKE (see Fig. 13) reveals a higher variability after assimilation, especially in the Ierapetra area and near the Libyan coast. After assimilation, all sides of the IE structure reach more than 500 cm^2/s^2 with a maximum of ~1100 cm^2/s^2. For the background, values over

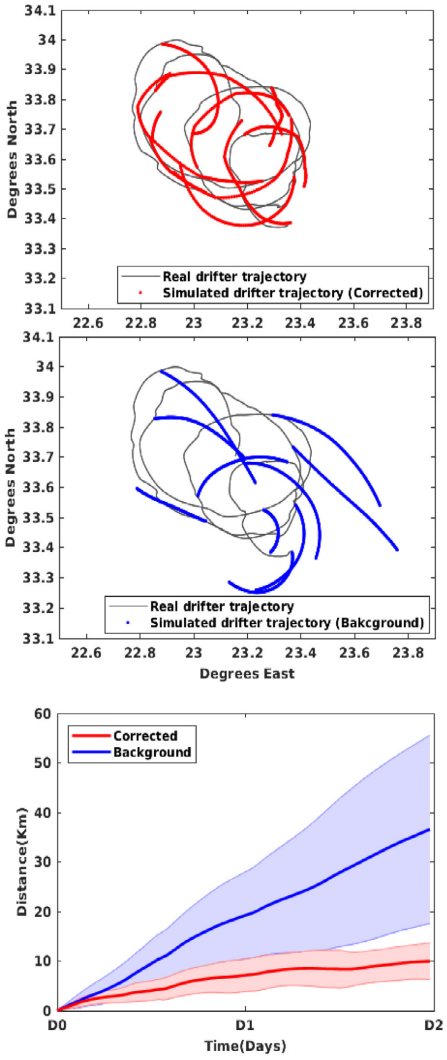

Fig. 11. The red lines (blue) represent the simulated drifter position using the corrected (background) velocity field. Both trajectories are compared with the real observations (dark). In the lower panel, the red (blue) line represents the distance evolution ($d(t)$ as in Eq. (6)) between the simulated trajectory using the corrected field (background) and the real observations, averaged over 10 simulations. Shades around the lines represent the standard deviation over the 10 simulations.

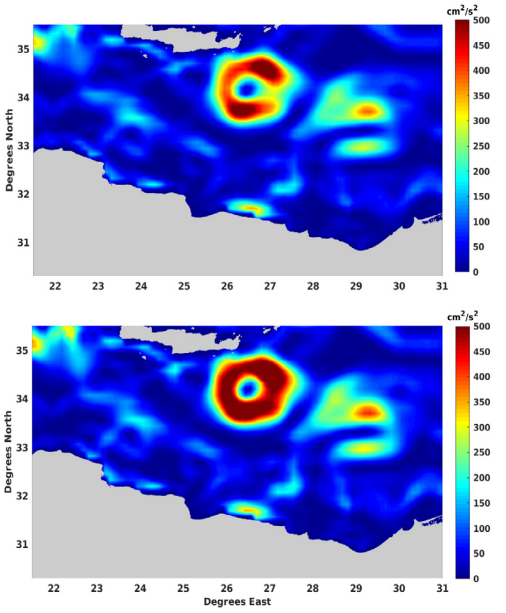

Fig. 12. The annual Mean Kinetic Energy (MKE) in 2006 resulting from background (upper panel) and the assimilated velocity fields (lower panel).

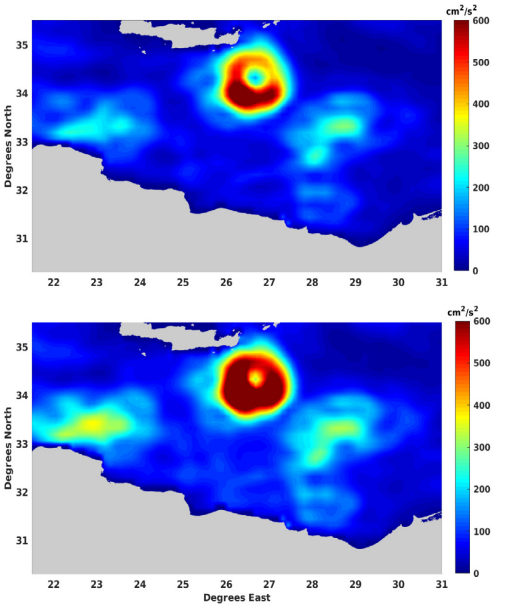

Fig. 13. The annual Eddy Kinetic Energy (EKE) in 2006 resulting from background (upper panel) and the assimilated velocity fields (lower panel).

500 cm^2/s^2 are limited to the southern part of IE with a maximum of ~860 cm^2/s^2.

The differences in MKE and EKE reveal that the algorithm can help in revising the quantification of surface velocity features, mainly in the Ierapetra area and off the Libyan coast, where intense mesoscale features are found permanently. A further detailed study of these areas based on this method could help investigate some oceanographic questions that are unclear, especially off Libya where the Libyo-Egyptian Current generates instabilities and thus a very high variability which paves the way to differing interpretations.

7. Conclusion

This paper has extended the application and objectively validated the assimilation algorithm developed in Issa et al. (2016). When compared with in-situ contemporary current meter data located in the assimilated area, the modified velocity field is in better agreement with

the current meter records. Significant improvements are seen when the assimilated drifter reaches a distance less than 30 km from the current meter location. This spatial extension of correction is larger than the internal Rossby radius in the Mediterranean that is on the order of 10–14 km (Robinson et al., 2001). We have shown that the corrected velocity field is closer to current meter data in both direction and intensity.

The application of the assimilation in high vorticity areas gives more realistic results than the altimetric product. After assimilating drifter positions trapped in an eddy detected at the same time from high-resolution chlorophyll images, the resulting streamlines from the corrected velocity field are consistent with the eddy shape and location, as shown by the ocean color image.

To quantify the assimilation efficiency, we showed that the error between the real and simulated drifter positions decreases after assimilation, from 40 km without assimilation to less than 10 km with assimilation after two days. Also, the correction reduces the uncertainties during all the experiments.

Further to the East, gliders from the "Eye of the Levantine" campaign deployed in the south of Cyprus were used for further validation. The resulting perpendicular velocity norm has values closer to the glider-derived velocities after assimilation. Despite the difference in the sampling time-scale and the considerable distances, the assimilation was able to reduce the error by more than 20%.

The results obtained pave the way for further investigations and larger spatio-temporal applications in the Eastern Mediterranean, where many drifter positions are available. This application can provide a precise and detailed description, improving the understanding of the mesoscale and sub-mesoscale activity.

CRediT authorship contribution statement

Georges Baaklini: Writing – original draft, Software, Formal analysis, Visualization. **Leila Issa:** Conceptualization, Methodology, Writing – review & editing, Project administration, Validation, Supervision. **Milad Fakhri:** Funding acquisition, Writing – review & editing, Supervision. **Julien Brajard:** Conceptualization, Methodology, Writing – review & editing, Project administration, Validation, Supervision. **Gina Fifani:** Software, Writing – review. **Milena Menna:** Writing – review & editing, Resources. **Isabelle Taupier-Letage:** Writing – review & editing, Resources. **Anthony Bosse:** Writing – review & editing, Resources. **Laurent Mortier:** Conceptualization, Funding acquisition, Writing – review & editing, Validation, Supervision.

Declaration of competing interest

The authors declare that they have no known competing financial interests or personal relationships that could have appeared to influence the work reported in this paper.

Acknowledgments

We would like to acknowledge the National Council for Scientific Research of Lebanon (CNRS-L) for granting a doctoral fellowship to Georges Baaklini. This work was partially funded by the ALTILEV program in the framework of the PHC-CEDRE project. We would like to thank Professor Alexandre Stegner (CNRS) for helping in data interpretation.

Drifters data were provided from: doi:data/10.6092/7a8499bc-c5ee-472c-b8b5-03523d1e73e9. We thank Pierre-Marie Poulain (CMRE) for his contribution in providing the drifters data.

EGYPT/EGITTO(Eddies and GYres Paths Tracking) program received funding from CNRS INSU LEFE IDAO and Mercator programs

Glider data are available on http://www.ifremer.fr/co/ego/ego/v2/trieste-1/trieste-1_20091124/. They were collected and made freely available by the Coriolis project and programmes that contribute to it (http://www.coriolis.eu.org)

The altimeter products were produced by Ssalto/Duacs and distributed by AVISO, with support from CNES (http://www.aviso.altimetry.fr/duacs/).The drifter data are distributed by OGS (http://nodc.ogs.trieste.it/). Chlorophyll image was provided by NASA Goddard Space Flight Center, Ocean Ecology Laboratory, Ocean Biology Processing Group. Moderate-resolution Imaging Spectroradiometer (MODIS) Aqua Chlorophyll Data; 2018 Reprocessing. NASA OB.DAAC, Greenbelt, MD, USA. doi:data/10.5067/AQUA/MODIS/L3B/CHL/2018.

The MIO has received funding from European FEDER Fund under project 1166–39417.

Bathymetry data are provided by GEBCO Compilation Group (2020) GEBCO 2020 Grid (doi:10.5285/a29c5465-b138-234d-e053-6c86abc040b9).

Appendix

If u and v are the zonal and meridional velocities respectively, the Mean Kinetic Energy (MKE, cm^2/s^2) is computed:

$$MKE = \frac{1}{2}\left(|u|^2 + |v|^2\right)$$

where | | is the time averaging of the component in a given bin.

The Eddy Kinetic Energy (EKE) is:

$$EKE = \frac{1}{2}\left(|u'u'| + |v'v'|\right)$$

$|u'u'|$ and $|v'v'|$ are the variances in the zonal and meridional directions, respectively.

References

Amitai, Y., Lehahn, Y., Lazar, A., Heifetz, E., 2010. Surface circulation of the eastern Mediterranean Levantine basin: Insights from analyzing 14 years of satellite altimetry data. J. Geophys. Res. Oceans 115 (C10).

Amores, A., Jordà, G., Arsouze, T., Le Sommer, J., 2018. Up to what extent can we characterize ocean eddies using present-day gridded altimetric products? J. Geophys. Res. Oceans 123 (10), 7220–7236.

Berta, M., Griffa, A., Magaldi, M.G., Özgökmen, T.M., Poje, A.C., Haza, A.C., Olascoaga, M.J., 2015. Improved surface velocity and trajectory estimates in the Gulf of Mexico from blended satellite altimetry and drifter data. J. Atmos. Ocean. Technol. 32 (10), 1880–1901.

Bosse, A., Fer, I., 2019. Mean structure and seasonality of the Norwegian Atlantic Front Current along the Mohn Ridge from repeated glider transects. Geophys. Res. Lett. 46 (22), 13170–13179.

Caballero, I., Gómez-Enri, J., Cipollini, P., Navarro, G., 2013. Validation of high spatial resolution wave data from Envisat RA-2 altimeter in the Gulf of Cádiz. IEEE Geosci. Remote Sens. Lett. 11 (1), 371–375.

Carrier, M.J., Ngodock, H., Smith, S., Jacobs, G., Muscarella, P., Ozgokmen, T., Haus, B., Lipphardt, B., 2014. Impact of assimilating ocean velocity observations inferred from Lagrangian drifter data using the NCOM-4DVAR. Mon. Weather Rev. 142 (4), 1509–1524.

Cipollini, P., Benveniste, J., Bouffard, J., Emery, W., Gommenginger, C., Griffin, D., Høyer, J., Madsen, K., Mercier, F., Miller, L., et al., 2010. The role of altimetry in coastal observing systems. Proc. OceanObs 9, 181–191.

Dee, D.P., Uppala, S.M., Simmons, A., Berrisford, P., Poli, P., Kobayashi, S., Andrae, U., Balmaseda, M., Balsamo, G., Bauer, d.P., et al., 2011. The ERA-Interim reanalysis: Configuration and performance of the data assimilation system. Q. J. R. Meteorol. Soc. 137 (656), 553–597.

d'Ovidio, F., Fernández, V., Hernández-García, E., López, C., 2004. Mixing structures in the Mediterranean Sea from finite-size Lyapunov exponents: Mixing structures in the Mediterranean Sea. Geophys. Res. Lett. 31 (17), http://dx.doi.org/10.1029/2004GL020328, URL: http://doi.wiley.com/10.1029/2004GL020328.

Eriksen, C.C., Osse, T.J., Light, R.D., Wen, T., Lehman, T.W., Sabin, P.L., Ballard, J.W., Chiodi, A.M., 2001. Seaglider: A long-range autonomous underwater vehicle for oceanographic research. IEEE J. Ocean. Eng. 26 (4), 424–436.

Escudier, R., Mourre, B., Juza, M., Tintoré, J., 2016. Subsurface circulation and mesoscale variability in the Algerian subbasin from altimeter-derived eddy trajectories: Algerian Eddies propagation. J. Geophys. Res. Oceans 121 (8), 6310–6322. http://dx.doi.org/10.1002/2016JC011760, URL: http://doi.wiley.com/10.1002/2016JC011760.

Gerin, R., Poulain, P.-M., Taupier-Letage, I., Millot, C., Ben Ismail, S., Sammari, C., 2009. Surface circulation in the Eastern Mediterranean using drifters (2005–2007). Ocean Sci. 5 (4), 559–574. http://dx.doi.org/10.5194/os-5-559-2009, URL: https://os.copernicus.org/articles/5/559/2009/.

Hamad, N., Millot, C., Taupier-Letage, I., 2006. The surface circulation in the eastern basin of the Mediterranean Sea. Sci. Mar. 70 (3), 457–503.

Hayes, D., Zodiatis, G., Konnaris, G., Hannides, A., Solovyov, D., Testor, P., 2011. Glider transects in the Levantine Sea: Characteristics of the warm core Cyprus eddy. In: OCEANS 2011 IEEE-Spain. IEEE, pp. 1–9.

Ioannou, A., Stegner, A., Le Vu, B., Taupier-Letage, I., Speich, S., 2017. Dynamical evolution of intense Ierapetra eddies on a 22 year long period. J. Geophys. Res. Oceans 122 (11), 9276–9298.

Issa, L., Brajard, J., Fakhri, M., Hayes, D., Mortier, L., Poulain, P.-M., 2016. Modelling surface currents in the Eastern Levantine Mediterranean using surface drifters and satellite altimetry. Ocean Model. 104, 1–14.

Kamachi, M., O'Brien, J., 1995. Continuous data assimilation of drifting buoy trajectory into an equatorial Pacific Ocean model. J. Mar. Syst. 6 (1–2), 159–178.

Kubryakov, A., Stanichny, S., 2011. Mean dynamic topography of the black sea, computed from altimetry, drifter measurements and hydrology data. Ocean Sci. 7 (6), 745.

Laxenaire, R., Speich, S., Blanke, B., Chaigneau, A., Pegliasco, C., Stegner, A., 2018. Anticyclonic eddies connecting the western boundaries of Indian and Atlantic Oceans. J. Geophys. Res. Oceans 123 (11), 7651–7677.

Le Traon, P., Hernandez, F., 1992. Mapping the oceanic mesoscale circulation: Validation of satellite altimetry using surface drifters. J. Atmos. Ocean. Technol. 9 (5), 687–698.

Le Vu, B., Stegner, A., Arsouze, T., 2018. Angular Momentum Eddy Detection and tracking Algorithm (AMEDA) and its application to coastal eddy formation. J. Atmos. Ocean. Technol. 35 (4), 739–762.

Lehahn, Y., d'Ovidio, F., Lévy, M., Heifetz, E., 2007. Stirring of the northeast Atlantic spring bloom: A Lagrangian analysis based on multisatellite data. J. Geophys. Res. 112 (C8), C08005. http://dx.doi.org/10.1029/2006JC003927, URL: http://doi.wiley.com/10.1029/2006JC003927.

Levy, M., Martin, A.P., 2013. The influence of mesoscale and submesoscale heterogeneity on ocean biogeochemical reactions: Influence of heterogeneity. Glob. Biogeochem. Cycles 27 (4), 1139–1150. http://dx.doi.org/10.1002/2012GB004518, URL: http://doi.wiley.com/10.1002/2012GB004518.

Maximenko, N., Niiler, P., Centurioni, L., Rio, M.-H., Melnichenko, O., Chambers, D., Zlotnicki, V., Galperin, B., 2009. Mean dynamic topography of theRapp. Comm. Int. Mer. Medit., 38 pp., 2007. ocean derived from satellite and drifting buoy data using three different techniques. J. Atmos. Ocean. Technol. 26 (9), 1910–1919.

McGillicuddy Jr, D.J., 2016. Mechanisms of physical-biological-biogeochemical interaction at the oceanic mesoscale. Annu. Rev. Mar. Sci. 8, 125–159.

Mead, J., 2005. Assimilation of simulated float data in Lagrangian coordinates. Ocean Model. 8 (4), 369–394.

Menna, M., Poulain, P.-M., Bussani, A., Gerin, R., 2018. Detecting the drogue presence of SVP drifters from wind slippage in the Mediterranean Sea. Measurement 125, 447–453.

Menna, M., Poulain, P.-M., Zodiatis, G., Gertman, I., 2012. On the surface circulation of the levantine sub-basin derived from Lagrangian drifters and satellite altimetry data. Deep Sea Res. I 65, 46–58.

Millot, C., Taupier-Letage, I., 2005. Circulation in the Mediterranean Sea. In: Saliot, A. (Ed.), The Mediterranean Sea, Vol. 5K. Springer Berlin Heidelberg, Berlin, Heidelberg, pp. 29–66. http://dx.doi.org/10.1007/b107143, URL: http://link.springer.com/10.1007/b107143.

Mkhinini, N., Coimbra, A.L.S., Stegner, A., Arsouze, T., Taupier-Letage, I., Béranger, K., 2014. Long-lived mesoscale eddies in the eastern Mediterranean Sea: Analysis of 20 years of AVISO geostrophic velocities. J. Geophys. Res. Oceans 119 (12), 8603–8626.

Muscarella, P., Carrier, M.J., Ngodock, H., Smith, S., Lipphardt Jr, B., Kirwan Jr, A., Huntley, H.S., 2015. Do assimilated drifter velocities improve Lagrangian predictability in an operational ocean model? Mon. Weather Rev. 143 (5), 1822–1832.

Niiler, P.P., 2003. Near-surface dynamical structure of the Kuroshio Extension. J. Geophys. Res. 108 (C6), 3193. http://dx.doi.org/10.1029/2002JC001461, URL: http://doi.wiley.com/10.1029/2002JC001461.

Nodet, M., 2006. Variational assimilation of Lagrangian data in oceanography. Inverse Problems 22 (1), 245.

Pessini, F., Cotroneo, Y., Olita, A., Sorgente, R., Ribotti, A., Jendersie, S., Perilli, A., 2020. Life history of an anticyclonic eddy in the Algerian basin from altimetry data, tracking algorithm and in situ observations. J. Mar. Syst. 207, 103346. http://dx.doi.org/10.1016/j.jmarsys.2020.103346, URL: https://linkinghub.elsevier.com/retrieve/pii/S0924796320300427.

Poulain, P.-M., Bussani, A., Gerin, R., Jungwirth, R., Mauri, E., Menna, M., Notarstefano, G., 2013. Mediterranean surface currents measured with drifters: From basin to subinertial scales. Oceanography 26 (1), 38–47.

Poulain, P.-M., Gerin, R., Mauri, E., Pennel, R., 2009. Wind effects on drogued and undrogued drifters in the eastern Mediterranean. J. Atmos. Ocean. Technol. 26 (6), 1144–1156.

Poulain, P.-M., Menna, M., Mauri, E., 2012. Surface geostrophic circulation of the Mediterranean Sea derived from drifter and satellite altimeter data. J. Phys. Oceanogr. 42 (6), 973–990.

Puillat, I., Taupier-Letage, I., Millot, C., 2002. Algerian eddies lifetime can near 3 years. J. Mar. Syst. 31 (4), 245–259.

Pujol, M.-I., Larnicol, G., 2005. Mediterranean sea eddy kinetic energy variability from 11 years of altimetric data. J. Mar. Syst. 58 (3–4), 121–142.

Rio, M.H., Pascual, A., Poulain, P.-M., Menna, M., Barceló-Llull, B., Tintoré, J., 2014. Computation of a new mean dynamic topography for the Mediterranean Sea from model outputs, altimeter measurements and oceanographic in situ data. Ocean Sci. 10 (4), 731–744.

Robinson, A.R., Leslie, W.G., Theocharis, A., Lascaratos, A., 2001. Mediterranean sea circulation. Ocean Curr. 1, 19.

Robinson, A.R., Malanotte-Rizzoli, P., Hecht, A., Michelato, A., Roether, W., Theocharis, A., Ünlüata, U., Pinardi, N., Artegiani, A., Bergamasco, A., et al., 1992. General circulation of the Eastern Mediterranean. Earth-Sci. Rev. 32 (4), 285–309.

Sarangi, R.K., 2012. Observation of oceanic eddy in the northeastern arabian sea using multisensor remote sensing data. Int. J. Oceanogr. 2012, 1–9. http://dx.doi.org/10.1155/2012/531982, URL: https://www.hindawi.com/journals/ijocean/2012/531982/.

Schroeder, K., Garcìa-Lafuente, J., Josey, S.A., Artale, V., Nardelli, B.B., Carrillo, A., Gacic, M., Gasparini, G.P., Herrmann, M., Lionello, P., et al., 2012. Circulation of the Mediterranean Sea and its variability. In: Lionello, P. (Ed.), The Climate of the Mediterranean Region. Elsevier, pp. 187–256.

Stanichny, S.V., Kubryakov, A.A., Soloviev, D.M., 2016. Parameterization of surface wind-driven currents in the Black Sea using drifters, wind, and altimetry data. Ocean Dyn. 66 (1), 1–10.

Sutyrin, G., Stegner, A., Taupier-Letage, I., Teinturier, S., 2009. Amplification of a surface-intensified eddy drift along a steep shelf in the Eastern Mediterranean Sea. J. Phys. Oceanogr. 39 (7), 1729–1741.

Taillandier, V., Griffa, A., Poulain, P.-M., Béranger, K., 2006. Assimilation of Argo float positions in the north western Mediterranean Sea and impact on ocean circulation simulations. Geophys. Res. Lett. 33 (11), L11604. http://dx.doi.org/10.1029/2005GL025552.

Talagrand, O., Courtier, P., 1987. Variational assimilation of meteorological observations with the adjoint vorticity equation. I: Theory. Q. J. R. Meteorol. Soc. 113 (478), 1311–1328.

Taupier-Letage, I., Barbanti, R., El Gindy, A., Emelianov, M., Fuda, J.-L., Font, J., Gerin, R., Guillerm, C., Julia, A., Mauri, E., Millot, C., Poulain, P.-M., Notarstefano, G., Rougier, G., Said, M., 2007. New Elements on the Surface Circulation in the Eastern Basin of the Mediterranean, Vol. 38. Technical Report, CIESM 38th Congress, Rapp. Comm. Int. Mer Medit., Istanbul, Turkey, p. 204, April 2007.

Taupier-Letage, I., Puillat, I., Raimbault, P., Millot, C., 2003. Biological response to mesoscale eddies in the Algerian Basin. J. Geophys. Res. 108 (C8), 3245–3267. http://dx.doi.org/10.1029/1999JC000117, URL: http://doi.wiley.com/10.1029/1999JC000117.

Testor, P., de Young, B., Rudnick, D.L., Glenn, S., Hayes, D., Lee, C.M., Pattiaratchi, C., Hill, K., Heslop, E., Turpin, V., et al., 2019. Oceangliders: a component of the integrated GOOS. Front. Mar. Sci. 6, 422.

Tonani, M., Pinardi, N., Dobricic, S., Pujol, I., Fratianni, C., 2008. A high-resolution free-surface model of the Mediterranean Sea. Ocean Sci. Eur. Geosci. Union 4 (1), 1–14.

Uchida, H., Imawaki, S., 2003. Eulerian mean surface velocity field derived by combining drifter and satellite altimeter data: Eulerian mean surface velocity field. Geophys. Res. Lett. 30 (5), 1229. http://dx.doi.org/10.1029/2002GL016445, URL: http://doi.wiley.com/10.1029/2002GL016445.

Weaver, A., Courtier, P., 2001. Correlation modelling on the sphere using a generalized diffusion equation. Q. J. R. Meteorol. Soc. 127 (575), 1815–1846.

Bibliography

Alhammoud, B., Béranger, K., Mortier, L., Crépon, M., and Dekeyser, I. (2005). Surface circulation of the levantine basin: comparison of model results with observations. *Progress in Oceanography*, 66(2-4):299–320.

Amitai, Y., Lehahn, Y., Lazar, A., and Heifetz, E. (2010). Surface circulation of the eastern mediterranean levantine basin: Insights from analyzing 14 years of satellite altimetry data. *Journal of Geophysical Research: Oceans*, 115(C10).

Amores, A., Jordà, G., and Monserrat, S. (2019). Ocean eddies in the mediterranean sea from satellite altimetry: Sensitivity to satellite track location. *Frontiers in Marine Science*, 6:703.

Baaklini, G., Issa, L., Fakhri, M., Brajard, J., Fifani, G., Menna, M., Taupier-Letage, I., Bosse, A., and Mortier, L. (2021). Blending drifters and altimetric data to estimate surface currents: Application in the levantine mediterranean and objective validation with different data types. *Ocean Modelling*, page 101850.

Barceló-Llull, B., Pascual, A., Sánchez-Román, A., Cutolo, E., d'Ovidio, F., Fifani, G., Ser-Giacomi, E., Ruiz, S., Mason, E., Cyr, F., et al. (2021). Fine-scale ocean currents derived from in situ observations in anticipation of the upcoming swot altimetric mission. *Frontiers in Marine Science*, page 1070.

Basterretxea, G., Font-Muñoz, J. S., Salgado-Hernanz, P. M., Arrieta, J., and Hernández-Carrasco, I. (2018). Patterns of chlorophyll interannual variability in mediterranean biogeographical regions. *Remote sensing of environment*, 215:7–17.

Bergamasco, A. and Malanotte-Rizzoli, P. (2010). The circulation of the mediterranean sea: a historical review of experimental investigations. *Advances in Oceanography and Limnology.*, 1(1):11–28.

Berta, M., Griffa, A., Magaldi, M. G., Özgökmen, T. M., Poje, A. C., Haza, A. C., and Olascoaga, M. J. (2015). Improved surface velocity and trajectory estimates in the gulf of mexico from blended satellite altimetry and drifter data. *Journal of Atmospheric and Oceanic Technology*, 32(10):1880–1901.

Bianchi, C. N. and Morri, C. (2000). Marine biodiversity of the mediterranean sea: situation, problems and prospects for future research. *Marine pollution bulletin*, 40(5):367–376.

Bonaduce, A., Cipollone, A., Johannessen, J. A., Staneva, J., Raj, R. P., and Aydogdu, A. (2021). Ocean mesoscale variability: a case study on the mediterranean sea from a re-analysis perspective.

Bosch, W., Dettmering, D., and Schwatke, C. (2014). Multi-mission cross-calibration of satellite altimeters: Constructing a long-term data record for global and regional sea level change studies. *Remote Sensing*, 6(3):2255–2281.

Bosse, A. (2015). *Circulation générale et couplage physique-biogéochimie á (sous-) mésoéchelle en Méditerranée Nord-Occidentale á partir de données in situ.* PhD thesis, Paris 6.

Caballero, I., Gómez-Enri, J., Cipollini, P., and Navarro, G. (2013). Validation of high spatial resolution wave data from envisat ra-2 altimeter in the gulf of cádiz. *IEEE Geoscience and Remote Sensing Letters*, 11(1):371–375.

Carrier, M. J., Ngodock, H., Smith, S., Jacobs, G., Muscarella, P., Ozgokmen, T., Haus, B., and Lipphardt, B. (2014). Impact of assimilating ocean velocity observations inferred from lagrangian drifter data using the ncom-4dvar. *Monthly Weather Review*, 142(4):1509–1524.

Chang, Y., Hammond, D., Haza, A., Hogan, P., Huntley, H., Kirwan Jr, A., Lipphardt Jr, B., Taillandier, V., Griffa, A., and Özgökmen, T. (2011). Enhanced estimation of sonobuoy trajectories by velocity reconstruction with near-surface drifters. *Ocean Modelling*, 36(3-4):179–197.

Chelton, D. B., Schlax, M. G., and Samelson, R. M. (2011). Global observations of nonlinear mesoscale eddies. *Progress in oceanography*, 91(2):167–216.

Chelton, D. B., Schlax, M. G., Samelson, R. M., and de Szoeke, R. A. (2007). Global observations of large oceanic eddies. *Geophysical Research Letters*, 34(15).

Ciappa, A. (2021). A study on causes and recurrence of the mid-mediterranean jet from 2003 to 2015 using satellite thermal and altimetry data and ctd casts. *Journal of Operational Oceanography*, 14(1):37–47.

Cipollini, P., Benveniste, J., Bouffard, J., Emery, W., Gommenginger, C., Griffin, D., Høyer, J., Madsen, K., Mercier, F., Miller, L., et al. (2010). The role of altimetry in coastal observing systems. *Proceedings of OceanObs*, 9:181–191.

De Dominicis, M., Leuzzi, G., Monti, P., Pinardi, N., and Poulain, P.-M. (2012). Eddy diffusivity derived from drifter data for dispersion model applications. *Ocean Dynamics*, 62(9):1381–1398.

Dee, D. P., Uppala, S. M., Simmons, A., Berrisford, P., Poli, P., Kobayashi, S., Andrae, U., Balmaseda, M., Balsamo, G., Bauer, d. P., et al. (2011). The era-interim reanalysis: Configuration and performance of the data assimilation system. *Quarterly Journal of the royal meteorological society*, 137(656):553–597.

Della Penna, A. and Gaube, P. (2019). Overview of (sub) mesoscale ocean dynamics for the naames field program. *Frontiers in Marine Science*, 6:384.

Ding, M., Lin, P., Liu, H., Hu, A., and Liu, C. (2020). Lagrangian eddy kinetic energy of ocean mesoscale eddies and its application to the northwestern pacific. *Scientific reports*, 10(1):1–11.

d'Ovidio, F., Fernndez, V., Hernndez-Garca, E., and Lpez, C. (2004). Mixing structures in the Mediterranean Sea from finite-size Lyapunov exponents: MIXING STRUCTURES IN THE MEDITERRANEAN SEA. *Geophysical Research Letters*, 31(17).

Ducet, N., Le Traon, P.-Y., and Reverdin, G. (2000). Global high-resolution mapping of ocean circulation from topex/poseidon and ers-1 and-2. *Journal of Geophysical Research: Oceans*, 105(C8):19477–19498.

dOvidio, F., Pascual, A., Wang, J., Doglioli, A. M., Jing, Z., Moreau, S., Grégori, G., Swart, S., Speich, S., Cyr, F., et al. (2019). Frontiers in fine-scale in situ studies: Opportunities during the swot fast sampling phase. *Frontiers in Marine Science*, 6:168.

El Hourany, R., Abboud-abi Saab, M., Faour, G., Aumont, O., Crépon, M., and Thiria, S. (2019). Estimation of secondary phytoplankton pigments from satellite observations using self-organizing maps (soms). *Journal of Geophysical Research: Oceans*, 124(2):1357–1378.

El Hourany, R., Abboud-abi Saab, M., Faour, G., Mejia, C., Crépon, M., and Thiria, S. (2019). Phytoplankton diversity in the mediterranean sea from satellite data using self-organizing maps. *Journal of Geophysical Research: Oceans*, 124(8):5827–5843.

Elsharkawy, M. S., Radwan, A. A., and Sharaf El-Din, S. H. (2017). General characteristics of current in front of Port Said, Egypt. *The Egyptian Journal of Aquatic Research*, 43(2):123–128.

Escudier, R., Bouffard, J., Pascual, A., Poulain, P.-M., and Pujol, M.-I. (2013). Improvement of coastal and mesoscale observation from space: Application to the northwestern mediterranean sea. *Geophysical Research Letters*, 40(10):2148–2153.

Escudier, R., Mourre, B., Juza, M., and Tintor, J. (2016). Subsurface circulation and mesoscale variability in the Algerian subbasin from altimeter-derived eddy trajectories: ALGERIAN EDDIES PROPAGATION. *Journal of Geophysical Research: Oceans*, 121(8):6310–6322.

Fakhri, M., Romano, J.-C., and Abboud-Abi Saab, M. (2011). Impact of wind on the dispersion of contaminants in the lebanese northern marine area. *Journal of the Black Sea/Mediterranean Environment*, 17(1).

Fifani, G., Baudena, A., Fakhri, M., Baaklini, G., Faugère, Y., Morrow, R., Mortier, L., and dOvidio, F. (2021). Drifting speed of lagrangian fronts and oil spill dispersal at the ocean surface. *Remote Sensing*, 13(22):4499.

Fu, L.-L., Alsdorf, D., Morrow, R., Rodriguez, E., and Mognard, N. (2012). Swot: The surface water and ocean topography mission: Wide-swath altimetric elevation on earth. Technical report, Pasadena, CA: Jet Propulsion Laboratory, National Aeronautics and Space .

Fu, L.-L. and Cazenave, A. (2000). *Satellite altimetry and earth sciences: a handbook of techniques and applications*. Elsevier.

Gerin, R., Poulain, P.-M., Taupier-Letage, I., Millot, C., Ben Ismail, S., and Sammari, C. (2009). Surface circulation in the eastern mediterranean using drifters (2005–2007). *Ocean Science*, 5(4):559–574.

Gertman, I., Zodiatis, G., Murashkovsky, A., Hayes, D., and Brenner, S. (2007). Determination of the locations of southeastern levantine anticyclonic eddies from ctd data. *Rapp. Commun. Int. Mer. Mediterr*, 38:151.

Griffies, S. M., Winton, M., Anderson, W. G., Benson, R., Delworth, T. L., Dufour, C. O., Dunne, J. P., Goddard, P., Morrison, A. K., Rosati, A., et al. (2015). Impacts on ocean heat from transient mesoscale eddies in a hierarchy of climate models. *Journal of Climate*, 28(3):952–977.

Groom, S., Sathyendranath, S., Ban, Y., Bernard, S., Brewin, R., Brotas, V., Brockmann, C., Chauhan, P., Choi, J.-k., Chuprin, A., et al. (2019). Satellite ocean colour: current status and future perspective. *Frontiers in Marine Science*, 6:485.

Haine, T. W. (2008). Numerical modeling of ocean circulation.

Hamad, N., Millot, C., and Taupier-Letage, I. (2005). A new hypothesis about the surface circulation in the eastern basin of the mediterranean sea. *Progress in Oceanography*, 66(2-4):287–298.

Hamlington, B., Leben, R., Strassburg, M., Nerem, R., and Kim, K.-Y. (2013). Contribution of the pacific decadal oscillation to global mean sea level trends. *Geophysical Research Letters*, 40(19):5171–5175.

Horton, C., Kerling, J., Athey, G., Schmitz, J., and Clifford, M. (1994). Airborne expendable bathythermograph surveys of the eastern mediterranean. *Journal of Geophysical Research: Oceans*, 99(C5):9891–9905.

Ioannou, A., Stegner, A., Le Vu, B., Taupier-Letage, I., and Speich, S. (2017). Dynamical evolution of intense ierapetra eddies on a 22 year long period. *Journal of Geophysical Research: Oceans*, 122(11):9276–9298.

Isern-Fontanet, J., Ballabrera-Poy, J., Turiel, A., and García-Ladona, E. (2017). Remote sensing of ocean surface currents: A review of what is being observed and what is being assimilated. *Nonlinear Processes in Geophysics*, 24(4):613–643.

Issa, L., Brajard, J., Fakhri, M., Hayes, D., Mortier, L., and Poulain, P.-M. (2016). Modelling surface currents in the eastern levantine mediterranean using surface drifters and satellite altimetry. *Ocean Modelling*, 104:1–14.

Jayne, S. R., Roemmich, D., Zilberman, N., Riser, S. C., Johnson, K. S., Johnson, G. C., and Piotrowicz, S. R. (2017). The argo program: present and future. *Oceanography*, 30(2):18–28.

Jouini, M., Béranger, K., Arsouze, T., Beuvier, J., Thiria, S., Crépon, M., and Taupier-Letage, I. (2016). The sicily channel surface circulation revisited using a neural clustering analysis of a high-resolution simulation. *Journal of Geophysical Research: Oceans*, 121(7):4545–4567.

Kalinić, H., Mihanović, H., Cosoli, S., Tudor, M., and Vilibić, I. (2017). Predicting ocean surface currents using numerical weather prediction model and kohonen neural network: a northern adriatic study. *Neural Computing and Applications*, 28(1):611–620.

Kamachi, M. and O'Brien, J. (1995). Continuous data assimilation of drifting buoy trajectory into an equatorial pacific ocean model. *Journal of Marine Systems*, 6(1-2):159–178.

Kloosterziel, R. and Van Heijst, G. (1991). An experimental study of unstable barotropic vortices in a rotating fluid. *Journal of fluid mechanics*, 223:1–24.

Kohonen, T. (2013). Essentials of the self-organizing map. *Neural networks*, 37:52–65.

Kubryakov, A. and Stanichny, S. (2011). Mean dynamic topography of the black sea, computed from altimetry, drifter measurements and hydrology data. *Ocean Science*, 7(6):745.

Lacorata, G., Palatella, L., and Santoleri, R. (2014). Lagrangian predictability characteristics of an o cean m odel. *Journal of Geophysical Research: Oceans*, 119(11):8029–8038.

Larnicol, G., Ayoub, N., and Le Traon, P.-Y. (2002). Major changes in mediterranean sea level variability from 7 years of topex/poseidon and ers-1/2 data. *Journal of Marine Systems*, 33:63–89.

Lascaratos, A., Roether, W., Nittis, K., and Klein, B. (1999). Recent changes in deep water formation and spreading in the eastern mediterranean sea: a review. *Progress in oceanography*, 44(1-3):5–36.

Laxenaire, R., Speich, S., Blanke, B., Chaigneau, A., Pegliasco, C., and Stegner, A. (2018). Anticyclonic eddies connecting the western boundaries of indian and atlantic oceans. *Journal of Geophysical Research: Oceans*, 123(11):7651–7677.

Lazar, A., Stegner, A., and Heifetz, E. (2013). Inertial instability of intense stratified anticyclones. part 1. generalized stability criterion. *Journal of Fluid Mechanics*, 732:457–484.

Le Vu, B., Stegner, A., and Arsouze, T. (2018). Angular momentum eddy detection and tracking algorithm (ameda) and its application to coastal eddy formation. *Journal of Atmospheric and Oceanic Technology*, 35(4):739–762.

Lehahn, Y., d'Ovidio, F., Lvy, M., and Heifetz, E. (2007). Stirring of the northeast Atlantic spring bloom: A Lagrangian analysis based on multisatellite data. *Journal of Geophysical Research*, 112(C8):C08005.

Levy, M. and Martin, A. P. (2013). The influence of mesoscale and submesoscale heterogeneity on ocean biogeochemical reactions: INFLUENCE OF HETEROGENEITY. *Global Biogeochemical Cycles*, 27(4):1139–1150.

Liu, Y., Weisberg, R. H., and Shay, L. K. (2007). Current patterns on the west florida shelf from joint self-organizing map analyses of hf radar and adcp data. *Journal of Atmospheric and Oceanic Technology*, 24(4):702–712.

Lumpkin, R. and Pazos, M. (2007). Measuring surface currents with surface velocity program drifters: the instrument, its data, and some recent results. *Lagrangian analysis and prediction of coastal and ocean dynamics*, 39:67.

Manzella, G., Cardin, V., Cruzado, A., Fusco, G., Gacic, M., Galli, C., Gasparini, G., Gervais, T., Kovacevic, V., Millot, C., et al. (2001). Eu-sponsored effort improves monitoring of circulation variability in the mediterranean. *Eos, Transactions American Geophysical Union*, 82(43):497–504.

Martínez-Moreno, J., Hogg, A. M., England, M. H., Constantinou, N. C., Kiss, A. E., and Morrison, A. K. (2021). Global changes in oceanic mesoscale currents over the satellite altimetry record. *Nature Climate Change*, 11(5):397–403.

Matteoda, A. M. and Glenn, S. M. (1996). Observations of recurrent mesoscale eddies in the eastern mediterranean. *Journal of Geophysical Research: Oceans*, 101(C9):20687–20709.

Mau, J.-C., Wang, D.-P., Ullman, D. S., and Codiga, D. L. (2007). Characterizing long island sound outflows from hf radar using self-organizing maps. *Estuarine, Coastal and Shelf Science*, 74(1-2):155–165.

Mauri, E., Sitz, L., Gerin, R., Poulain, P.-M., Hayes, D., and Gildor, H. (2019). On the variability of the circulation and water mass properties in the eastern levantine sea between september 2016–august 2017. *Water*, 11(9):1741.

Mead, J. (2005). Assimilation of simulated float data in lagrangian coordinates. *Ocean Modelling*, 8(4):369–394.

Menna, M., Gerin, R., Bussani, A., and Poulain, P.-m. (2017). The ogs mediterranean drifte r dataset: 1986-2016. *Rel. OGS*, 92.

Menna, M., Poulain, P.-M., Ciani, D., Doglioli, A., Notarstefano, G., Gerin, R., Rio, M.-H., Santoleri, R., Gauci, A., and Drago, A. (2019). New insights of the sicily channel and southern tyrrhenian sea variability. *Water*, 11(7):1355.

Menna, M., Poulain, P.-M., Zodiatis, G., and Gertman, I. (2012). On the surface circulation of the levantine sub-basin derived from lagrangian drifters and satellite altimetry data. *Deep Sea Research Part I: Oceanographic Research Papers*, 65:46–58.

Mihanović, H., Cosoli, S., Vilibić, I., Ivanković, D., Dadić, V., and Gačić, M. (2011). Surface current patterns in the northern adriatic extracted from high-frequency radar data using self-organizing map analysis. *Journal of Geophysical Research: Oceans*, 116(C8).

Millot, C. and Gerin, R. (2010). The mid-mediterranean jet artefact. *Geophysical research letters*, 37(12).

Millot, C. and Taupier-Letage, I. (2005). Circulation in the mediterranean sea. In *The Mediterranean Sea*, pages 29–66. Springer.

Mkhinini, N., Coimbra, A. L. S., Stegner, A., Arsouze, T., Taupier-Letage, I., and Béranger, K. (2014). Long-lived mesoscale eddies in the eastern mediterranean sea: Analysis of 20 years of aviso geostrophic velocities. *Journal of Geophysical Research: Oceans*, 119(12):8603–8626.

Molcard, A., Griffa, A., and Özgökmen, T. M. (2005). Lagrangian data assimilation in multilayer primitive equation ocean models. *Journal of Atmospheric and Oceanic Technology*, 22(1):70–83.

Molcard, A., Piterbarg, L. I., Griffa, A., Özgökmen, T. M., and Mariano, A. J. (2003). Assimilation of drifter observations for the reconstruction of the eulerian circulation field. *Journal of Geophysical Research: Oceans*, 108(C3).

Morrow, R., Fu, L.-L., Ardhuin, F., Benkiran, M., Chapron, B., Cosme, E., dOvidio, F., Farrar, J. T., Gille, S. T., Lapeyre, G., et al. (2019). Global observations of fine-scale ocean surface topography with the surface water and ocean topography (swot) mission. *Frontiers in Marine Science*, 6:232.

Muscarella, P., Carrier, M. J., Ngodock, H., Smith, S., Lipphardt Jr, B., Kirwan Jr, A., and Huntley, H. S. (2015). Do assimilated drifter velocities improve lagrangian predictability in an operational ocean model? *Monthly Weather Review*, 143(5):1822–1832.

Nodet, M. (2006). Variational assimilation of lagrangian data in oceanography. *Inverse problems*, 22(1):245.

Ovchinnikov, I. (1984). The formation of intermediate water in the mediterranean. *Oceanology*, 24(2):168–173.

Pascual, A., Faugère, Y., Larnicol, G., and Le Traon, P.-Y. (2006). Improved description of the ocean mesoscale variability by combining four satellite altimeters. *Geophysical Research Letters*, 33(2).

Pascual, A., Gomis, D., Haney, R. L., and Ruiz, S. (2004). A quasigeostrophic analysis of a meander in the palamós canyon: vertical velocity, geopotential tendency, and a relocation technique. *Journal of Physical Oceanography*, 34(10):2274–2287.

Pascual, A., Pujol, M.-I., Larnicol, G., Le Traon, P.-Y., and Rio, M.-H. (2007). Mesoscale mapping capabilities of multisatellite altimeter missions: First results with real data in the mediterranean sea. *Journal of Marine Systems*, 65(1-4):190–211.

Poulain, P.-M. (1999). Drifter observations of surface circulation in the adriatic sea between december 1994 and march 1996. *Journal of Marine Systems*, 20(1-4):231–253.

Poulain, P.-M., Barbanti, R., Font, J., Cruzado, A., Millot, C., Gertman, I., Griffa, A., Molcard, A., Rupolo, V., Le Bras, S., et al. (2007). Medargo: a drifting profiler program in the mediterranean sea. *Ocean Science*, 3(3):379–395.

Poulain, P.-M., Bussani, A., Gerin, R., Jungwirth, R., Mauri, E., Menna, M., and Notarstefano, G. (2013). Mediterranean surface currents measured with drifters: From basin to subinertial scales. *Oceanography*, 26(1):38–47.

Poulain, P.-M., Gerin, R., Mauri, E., and Pennel, R. (2009). Wind effects on drogued and undrogued drifters in the eastern mediterranean. *Journal of Atmospheric and Oceanic Technology*, 26(6):1144–1156.

Poulain, P.-M., Menna, M., and Mauri, E. (2012). Surface geostrophic circulation of the mediterranean sea derived from drifter and satellite altimeter data. *Journal of Physical Oceanography*, 42(6):973–990.

Pujol, M.-I. and Larnicol, G. (2005). Mediterranean sea eddy kinetic energy variability from 11 years of altimetric data. *Journal of Marine Systems*, 58(3-4):121–142.

Randriamihamison, N., Vialaneix, N., and Neuvial, P. (2021). Applicability and interpretability of wards hierarchical agglomerative clustering with or without contiguity constraints. *Journal of Classification*, 38(2):363–389.

Ren, L., Chu, N., Hu, Z., and Hartnett, M. (2020). Investigations into synoptic spatiotemporal characteristics of coastal upper ocean circulation using high frequency radar data and model output. *Remote Sensing*, 12(17):2841.

Richardson, A. J., Risien, C., and Shillington, F. A. (2003). Using self-organizing maps to identify patterns in satellite imagery. *Progress in Oceanography*, 59(2-3):223–239.

Rio, M.-H., Pascual, A., Poulain, P.-M., Menna, M., Barceló, B., and Tintoré, J. (2014). Computation of a new mean dynamic topography for the mediterranean sea from

model outputs, altimeter measurements and oceanographic in situ data. *Ocean Science*, 10(4):731–744.

Rio, M.-H., Poulain, P.-M., Pascual, A., Mauri, E., Larnicol, G., and Santoleri, R. (2007). A mean dynamic topography of the mediterranean sea computed from altimetric data, in-situ measurements and a general circulation model. *Journal of Marine Systems*, 65(1-4):484–508.

Rixen, M., Beckers, J.-M., Levitus, S., Antonov, J., Boyer, T., Maillard, C., Fichaut, M., Balopoulos, E., Iona, S., Dooley, H., et al. (2005). The western mediterranean deep water: a proxy for climate change. *Geophysical Research Letters*, 32(12).

Sánchez-Román, A., Ruiz, S., Pascual, A., Mourre, B., and Guinehut, S. (2017). On the mesoscale monitoring capability of argo floats in the mediterranean sea. *Ocean Science*, 13(2):223–234.

Sarangi, R. (2012). Observation of oceanic eddy in the northeastern arabian sea using multisensor remote sensing data. *International Journal of Oceanography*, 2012.

Stanichny, S. V., Kubryakov, A. A., and Soloviev, D. M. (2016). Parameterization of surface wind-driven currents in the black sea using drifters, wind, and altimetry data. *Ocean Dynamics*, 66(1):1–10.

Stone, P. H. (1966). On non-geostrophic baroclinic stability. *Journal of the Atmospheric Sciences*, 23(4):390–400.

Sutyrin, G., Stegner, A., Taupier-Letage, I., and Teinturier, S. (2009). Amplification of a surface-intensified eddy drift along a steep shelf in the eastern mediterranean sea. *Journal of physical oceanography*, 39(7):1729–1741.

Taillandier, V., Dobricic, S., Testor, P., Pinardi, N., Griffa, A., Mortier, L., and Gasparini, G. P. (2010). Integration of argo trajectories in the mediterranean forecasting system and impact on the regional analysis of the western mediterranean circulation. *Journal of Geophysical Research: Oceans*, 115(C3).

Taillandier, V., Griffa, A., and Molcard, A. (2006a). A variational approach for the reconstruction of regional scale eulerian velocity fields from lagrangian data. *Ocean Modelling*, 13(1):1–24.

Taillandier, V., Griffa, A., Poulain, P., Signell, R., Chiggiato, J., and Carniel, S. (2008). Variational analysis of drifter positions and model outputs for the reconstruction of surface currents in the central adriatic during fall 2002. *Journal of Geophysical Research: Oceans*, 113(C4).

Taillandier, V., Griffa, A., Poulain, P.-M., and Béranger, K. (2006b). Assimilation of argo float positions in the north western mediterranean sea and impact on ocean circulation simulations. *Geophysical research letters*, 33(11).

Talagrand, O. and Courtier, P. (1987). Variational assimilation of meteorological observations with the adjoint vorticity equation. i: Theory. *Quarterly Journal of the Royal Meteorological Society*, 113(478):1311–1328.

Tanhua, T., Hainbucher, D., Schroeder, K., Cardin, V., Álvarez, M., and Civitarese, G. (2013). The mediterranean sea system: a review and an introduction to the special issue. *Ocean Science*, 9(5):789–803.

Taupier-Letage, I. (2008). On the use of thermal images for circulation studies: applications to the eastern mediterranean basin. In *Remote sensing of the European seas*, pages 153–164. Springer.

Taupier-Letage, I., Barbanti, R., El Gindy, A., Emelianov, M., Fuda, J.-L., Font, J., Gerin, R., Guillerm, C., Julia, A., Mauri, E., Millot, C., Poulain, P.-M., Notarstefano, G., Rougier, G., and Said, M. (2007). New elements on the surface circulation in the eastern basin of the mediterranean. Technical report, CIESM 38th Congress, Istanbul, Turkey, April 2007, Rapp. Comm. Int. Mer Medit., 38:204.

Taupier-Letage, I., Puillat, I., Raimbault, P., and Millot, C. (2003). Biological response to mesoscale eddies in the algerian basin. *J. Geophys. Res.*, VOL. 108(NO. C8):3245–3267.

Teinturier, S., Stegner, A., Didelle, H., and Viboud, S. (2010). Small-scale instabilities of an island wake flow in a rotating shallow-water layer. *Dynamics of atmospheres and oceans*, 49(1):1–24.

Testor, P., de Young, B., Rudnick, D. L., Glenn, S., Hayes, D., Lee, C. M., Pattiaratchi, C., Hill, K., Heslop, E., Turpin, V., et al. (2019). Oceangliders: a component of the integrated goos. *Frontiers in Marine Science*, 6:422.

Testor, P., Send, U., Gascard, J.-C., Millot, C., Taupier-Letage, I., and Béranger, K. (2005). The mean circulation of the southwestern mediterranean sea: Algerian gyres. *Journal of Geophysical Research: Oceans*, 110(C11).

Thomas, L. N., Taylor, J. R., Ferrari, R., and Joyce, T. M. (2013). Symmetric instability in the gulf stream. *Deep Sea Research Part II: Topical Studies in Oceanography*, 91:96–110.

Tintoré, J., Pinardi, N., Álvarez-Fanjul, E., Aguiar, E., Álvarez-Berastegui, D., Bajo, M., Balbin, R., Bozzano, R., Nardelli, B. B., Cardin, V., et al. (2019). Challenges for sustained observing and forecasting systems in the mediterranean sea. *Frontiers in Marine Science*, page 568.

Tonani, M., Pinardi, N., Dobricic, S., Pujol, I., and Fratianni, C. (2008). A high-resolution free-surface model of the mediterranean sea. *Ocean Science, European Geosciences Union*, 4(1):1–14.

Uchida, H. and Imawaki, S. (2003). Eulerian mean surface velocity field derived by combining drifter and satellite altimeter data. *Geophysical Research Letters*, 30(5).

Van Sebille, E., Griffies, S. M., Abernathey, R., Adams, T. P., Berloff, P., Biastoch, A., Blanke, B., Chassignet, E. P., Cheng, Y., Cotter, C. J., et al. (2018). Lagrangian ocean analysis: Fundamentals and practices. *Ocean Modelling*, 121:49–75.

Vignudelli, S., Birol, F., Benveniste, J., Fu, L.-L., Picot, N., Raynal, M., and Roinard, H. (2019). Satellite altimetry measurements of sea level in the coastal zone. *Surveys in geophysics*, 40(6):1319–1349.

Wang, J., Fu, L.-L., Qiu, B., Menemenlis, D., Farrar, J. T., Chao, Y., Thompson, A. F., and Flexas, M. M. (2018). An observing system simulation experiment for the calibration and validation of the surface water ocean topography sea surface height measurement using in situ platforms. *Journal of Atmospheric and Oceanic Technology*, 35(2):281–297.

Weaver, A. and Courtier, P. (2001). Correlation modelling on the sphere using a generalized diffusion equation. *Quarterly Journal of the Royal Meteorological Society*, 127(575):1815–1846.

Willis, J. K. (2010). Can in situ floats and satellite altimeters detect long-term changes in atlantic ocean overturning? *Geophysical research letters*, 37(6).

Wolfe, C. L. and Cenedese, C. (2006). Laboratory experiments on eddy generation by a buoyant coastal current flowing over variable bathymetry. *Journal of Physical Oceanography*, 36(3):395–411.

Wunsch, C. (1999). Where do ocean eddy heat fluxes matter? *Journal of Geophysical Research: Oceans*, 104(C6):13235–13249.

Zervakis, V., Papadoniou, G., Tziavos, C., and Lascaratos, A. (2003). Seasonal variability and geostrophic circulation in the eastern mediterranean as revealed through a repeated xbt transect. In *Annales Geophysicae*, volume 21, pages 33–47. Copernicus GmbH.

Zhao, J., Bower, A., Yang, J., Lin, X., and Penny Holliday, N. (2018). Meridional heat transport variability induced by mesoscale processes in the subpolar north atlantic. *Nature communications*, 9(1):1–9.

Zodiatis, G., Drakopoulos, P., Brenner, S., and Groom, S. (2005). Variability of the cyprus warm core eddy during the cyclops project. *Deep Sea Research Part II: Topical Studies in Oceanography*, 52(22-23):2897–2910.

Zodiatis, G., Lardner, R., Lascaratos, A., Georgiou, G., Korres, G., and Syrimis, M. (2003). High resolution nested model for the cyprus, ne levantine basin, eastern mediterranean sea: implementation and climatological runs. In *Annales Geophysicae*, volume 21, pages 221–236. Copernicus GmbH.